

UNDERSTANDING AND MITIGATING DEGRADATION IN LI-ION  
BATTERIES

by

Eric Logan

Submitted in partial fulfilment of the requirements  
for the degree of Doctor of Philosophy

at

Dalhousie University  
Halifax, Nova Scotia  
August, 2022

© Copyright by Eric Logan, 2022

# TABLE OF CONTENTS

TABLE OF CONTENTS.....	ii
LIST OF TABLES.....	vii
LIST OF FIGURES.....	viii
ABSTRACT.....	xv
LIST OF ABBREVIATIONS AND SYMBOLS USED.....	xvi
ACKNOWLEDGEMENTS.....	xxiii
CHAPTER 1 INTRODUCTION.....	1
1.1 MOTIVATION.....	1
1.2 LI-ION CELLS.....	1
1.3 POSITIVE ELECTRODE MATERIALS.....	10
1.3.1 LiCoO <sub>2</sub> (LCO) and Li[Ni <sub>x</sub> Mn <sub>y</sub> Co <sub>1-x-y</sub> ]O <sub>2</sub> (NMC).....	10
1.3.2 LiFePO <sub>4</sub> (LFP).....	12
1.3.3 LiMn <sub>2</sub> O <sub>4</sub> (LMO).....	13
1.4 NEGATIVE ELECTRODE MATERIALS.....	14
1.5 ELECTROLYTE.....	18
1.5.1 Solvents.....	20
1.5.2 Salts.....	21
1.5.3 The Solid Electrolyte Interphase (SEI).....	24
1.5.4 Electrolyte Additives.....	25
1.6 SCOPE OF THIS THESIS.....	29

CHAPTER 2 LI-ION CELL DEGRADATION AND ISOTHERMAL MICROCALORIMETRY.....	33
2.1 COULOMBIC EFFICIENCY AND CHARGE ENDPOINT SLIPPAGE .....	33
2.2 PARASITIC REACTIONS.....	38
2.2.1 Electrolyte reduction and SEI formation .....	38
2.2.2 Electrolyte Oxidation .....	43
2.2.3 Cross-talk and shuttle reactions .....	45
2.2.4 Transition Metal Dissolution .....	47
2.3 IMPEDANCE GROWTH.....	49
2.4 ACTIVE MATERIAL LOSS .....	52
2.5 LITHIUM PLATING .....	53
2.6 ISOTHERMAL MICROCALORIMETRY .....	55
CHAPTER 3 EXPERIMENTAL.....	60
3.1 POUCH CELLS.....	60
3.2 ELECTROLYTE MATERIALS .....	64
3.3 POUCH CELL FILLING AND FORMATION.....	65
3.4 CYCLING AND STORAGE PROTOCOLS.....	65
3.4.1 Long-term Cycling.....	65
3.4.2 Ultra-High Precision Coulometry (UHPC).....	66
3.4.3 OCV Storage.....	67
3.5 WATER CONTENT MEASUREMENTS .....	69
3.6 EX-SITU GAS MEASUREMENTS .....	72
3.7 ELECTROCHEMICAL IMPEDANCE SPECTROSCOPY (EIS).....	72

3.8	MICRO X-RAY FLUORESCENCE SPECTROSCOPY ( $\mu$ -XRF).....	75
3.9	SCANNING ELECTRON MICROSCOPY (SEM) .....	77
3.10	POUCH BAG CONSTRUCTION.....	78
3.11	ISOTHERMAL MICROCALORIMETRY .....	79
3.11.1	Measurement principles .....	80
3.11.2	Cycling protocols .....	84
3.11.3	OCV experimental protocols .....	84
	CHAPTER 4 INITIAL SURVEY OF THE PERFORMANCE OF LIFEPO <sub>4</sub> /GRAPHITE CELLS .....	86
4.1	INTRODUCTION .....	86
4.2	WATER CONTAMINATION AND MECHANICAL INTEGRITY AFTER DRYING.....	88
4.3	SURVERY OF ELECTROLYTE ADDITIVES.....	93
4.4	FE DISSOLUTION AND DEPOSITION .....	104
4.5	MEASURING PARASITIC REACTIONS WITH ISOTHERMAL MICROCALORIMETRY... 114	
4.5.1	Measuring the Entropy change of Li intercalation into Graphite and Mean Field Theory Calculations.....	114
4.5.2	Measuring parasitic heat flow for LFP/graphite cells with different electrolyte additives and different levels of water contamination .....	120
4.6	DISCUSSION .....	132
4.7	COMPARING THE PERFORMANCE OF LFP TO NMC .....	139
4.8	CONCLUSIONS.....	142
	CHAPTER 5 STRATEGIES FOR IMPROVING THE PERFORMANCE OF LFP/GRAPHITE CELLS.....	145

5.1	INTRODUCTION .....	145
5.2	STUDYING THE EFFECT OF LFP PARTICLE SIZE ON LIFETIME .....	146
5.2.1	Water content and cycling results .....	147
5.2.2	Understanding the differences between low, medium, and high BET LFP	150
5.2.3	Further considerations on the effects of residual water in LFP cells .....	157
5.2.4	Discussion and conclusions .....	159
5.3	IMPACT OF DIFFERENT LI SALTS AND ELECTROLYTE ADDITIVES .....	163
5.3.1	Introduction.....	163
5.3.2	Results.....	165
5.3.3	Discussion.....	187
5.4	IMPACT OF DIFFERENT GRAPHITE MATERIALS .....	192
5.5	SUMMARY AND OUTLOOK .....	202
CHAPTER 6 LONG-TERM STORAGE STUDIES OF LFP/GRAPHITE AND NMC811/GRAPHITE POUCH CELLS.....		206
6.1	INTRODUCTION .....	206
6.2	RESULTS .....	209
6.2.1	Full cell storage.....	209
6.2.2	Pouch bags .....	220
6.2.3	Isothermal Microcalorimetry .....	233
6.3	DISCUSSION AND CONCLUSION .....	239
6.3.1	Full cell versus pouch bag gas evolution .....	239
6.3.2	Capacity fade dominated by Li inventory loss .....	242
6.3.3	Conclusion .....	245
CHAPTER 7 CONCLUSIONS .....		249
7.1	CONCLUSION.....	249

7.2	FUTURE WORK .....	254
7.2.1	LFP future directions .....	254
7.2.2	Isothermal microcalorimetry future directions .....	256
7.2.3	Blended NMC/LFP positive electrodes .....	259
7.2.4	Increasing energy density with $\text{LiMn}_x\text{Fe}_{1-x}\text{PO}_4$ (LMFP).....	262
	REFERENCES .....	266
	APPENDIX A ADDITIONAL FIGURES .....	302
	APPENDIX B COPYRIGHT PERMISSIONS .....	315

## LIST OF TABLES

Table 1.1: Common solvents used in Li-ion battery electrolytes. ....	21
Table 1.2: Names and structures of some common Li salts used in electrolyte solutions for Li-ion batteries. ....	24
Table 1.3: Names and structures of some common electrolyte additives used in Li-ion batteries. ....	28
Table 3.1: Specifications and compositions of the different Li-ion pouch cells used in this thesis. ....	62
Table 3.2: Properties of electrodes obtained from Li-ion pouch cells used in this thesis. ....	63
Table 3.3: List of chemicals used for electrolyte preparation in this thesis. ....	64
Table 5.1: Physical properties of the different LFP materials studied in this work. ....	147
Table 5.2: Physical properties of the different artificial graphites (AG) studied. ....	193
Table 6.1: Matrix of different positive electrode/negative electrode/electrolyte combinations used in Chapter 6. ....	209
Table A.1: [Fe] detected on the anode, capacity loss, cycle number, and cycle time for the cells disassembled for $\mu$ XRF measurements referenced in Figure 6 in the main text. ....	305

## LIST OF FIGURES

Figure 1.1: Schematic of a full Li-ion cell during charge.....	3
Figure 1.2: Voltage (vs Li metal) versus specific capacity for various relevant positive electrode materials. ....	5
Figure 1.3: Specific energy of various positive electrode materials for Li-ion batteries....	7
Figure 1.4: Crystal structures for different positive and negative electrode materials. ....	8
Figure 1.5: Illustrating how a full cell voltage curve is constructed from individual half cell curves. ....	9
Figure 1.6: Cross-section schematic of the repeating double sided cell stack.....	10
Figure 1.7: Pictures of different Li-graphite structures. ....	16
Figure 1.8: Voltage versus specific capacity for an artificial graphite (AG) electrode versus Li metal. ....	18
Figure 1.9: Conductivity as a function of salt concentration for a common alkyl carbonate electrolyte mixture, ethylene carbonate (EC):dimethyl carbonate (DMC) 3:7 (by weight) with LiPF <sub>6</sub> as the conducting salt. ....	19
Figure 1.10: Differential capacity (dQ/dV) versus cell voltage during the first charge of a LiFePO <sub>4</sub> /graphite pouch cell, zoomed in on the SEI formation region. ....	29
Figure 2.1: Illustrating the concept of coulombic efficiency (CE). ....	35
Figure 2.2: Voltage curves over several cycles for an LiFePO <sub>4</sub> /Graphite pouch cell. ....	37
Figure 2.3: Schematic depicting the formation of SEI products on the negative electrode of a cell, reducing electrolyte components (S) and irreversibly consuming lithium.....	39
Figure 2.4: Voltage curve for the first full cycle of an LFP/graphite pouch cell, illustrating how much lithium is consumed in the initial formation of the graphite SEI layer. ...	40
Figure 2.5: Example of a simple model of $t^{1/2}$ SEI growth.....	42
Figure 2.6: Schematic of electrolyte oxidation in a Li-ion cell. ....	44
Figure 2.7: Schematics of related reaction mechanisms: (a) non-reversible cross-talk, and (b) reversible shuttle reactions. ....	46
Figure 2.8: Schematic illustrating a cell in open circuit experiencing transition metal dissolution. ....	48
Figure 2.9: Demonstrating voltage polarization in an LFP/graphite pouch cell.....	51



Figure 2.10: Cartoon schematic of active material loss in a positive active material particle. .....	53
Figure 2.11: Examples of different degrees of severity of lithium metal deposition in Li-ion batteries. ....	55
Figure 3.1: Photograph of one of the the 204035-sized pouch cells used throughout this thesis, before and after disassembly.....	61
Figure 3.2: Example of the “smart” storage protocol for an LFP/graphite pouch cell. ....	69
Figure 3.3: Schematic of a Karl Fischer (KF) coulometric titration setup. ....	71
Figure 3.4: Simple model of impedance in a Li-ion cell. ....	75
Figure 3.5: Flow chart outlining how separated electrode pouch bags are constructed from full pouch cells. ....	79
Figure 3.6: Cartoon of the reference and sample ampoules in a single calorimeter channel. .....	81
Figure 3.7: A picture of the TAM III at Dalhousie University and the individual lifters.	82
Figure 3.8: Temperature stability of the TAM III microcalorimeter over time. ....	83
Figure 4.1: Water content in LFP electrodes as a function of vacuum drying temperature as measured by Karl Fischer (KF) titration.....	89
Figure 4.2: Ultra-high Precision Coulometry (UHPC) cycling measurements for LFP cells with different electrolytes and different levels of water contamination. ....	93
Figure 4.3: CE versus cycle number for LFP cells vacuum dried at different temperatures cycled using the UHPC cycler at 40°C and a rate of C/20. ....	95
Figure 4.4: Zeroed (at cycle 2) charge endpoint capacity as a function of cycle number for LFP cells vacuum dried at different temperatures cycled using the UHPC system at 40°C and a rate of C/20.....	97
Figure 4.5: Normalized (cycle 2) discharge capacity versus cycle number for LFP cells vacuum dried at different temperatures cycled using the UHPC system at 40°C and a rate of C/20. ....	98
Figure 4.6: Long-term cycling results for LFP cells at 40°C and a rate of C/3:C/3. Normalized capacity versus cycle number for cells with different additive systems. .....	100

Figure 4.7: Normalized voltage polarization versus cycle number for cells cycling at 40°C, C/3:C/3 rate.....	101
Figure 4.8: High temperature OCV storage results for LFP cells vacuum dried at different temperatures.....	104
Figure 4.9: Visualizing the deposition of Fe on graphite electrodes.....	107
Figure 4.10: Different measurements as a function of cycle number for cells that were eventually disassembled for $\mu$ XRF measurements.....	109
Figure 4.11: Comparison of Fe dissolution for LFP cells at different vacuum drying temperatures.....	111
Figure 4.12: Plotting Fe deposition as a function of capacity loss.....	113
Figure 4.13: Voltage and measured heat flow versus capacity for an LFP/graphite cell.....	115
Figure 4.14: Phase diagram for $\text{Li}_x\text{C}_6$ at different temperatures.....	117
Figure 4.15: Demonstrating the lattice sites A, B, and C for the intercalation of lithium into graphite.....	118
Figure 4.16: Full cycling protocol to determine parasitic heat flow in LFP/graphite cells.....	121
Figure 4.17: Extracted components of the heat flow for an LFP/graphite cell.....	122
Figure 4.18: Parasitic heat flow versus relative state of charge for all cycles with the control electrolyte.....	124
Figure 4.19: Parasitic heat flow versus relative state of charge for LFP cells with different electrolyte additives.....	126
Figure 4.20: Comparing parasitic heat flow at different vacuum drying temperatures for LFP cells with 2VC in the electrolyte.....	130
Figure 4.21: Summary of average parasitic heat flow versus cycle number for LFP/graphite cells vacuum dried at different temperatures with different electrolyte additives..	132
Figure 4.22: Summary of cycling and storage tests for key additives in cells with different vacuum drying temperatures.....	134
Figure 4.23: Comparing LFP/Graphite pouch cells to commercial LFP cells and NMC/Graphite pouch cells.....	142

Figure 5.1: Water content detected in different LFP electrodes by Karl Fischer (KF) titration after vacuum drying at different temperatures. ....	149
Figure 5.2: Capacity retention and voltage polarization results for cells cycled at 55°C, C/3 rate, between 2.5 V and 3.65 V. ....	150
Figure 5.3: Fe deposition per hour for LFP/graphite cells cycled at different temperature with different electrolytes used. ....	152
Figure 5.4: SEM images of low and high BET LFP electrodes before and after cycling at 55°C, C/3 rate. ....	155
Figure 5.5: Average parasitic heat flow as a function of cycle number for low, medium, and high BET LFP/AG cells. ....	157
Figure 5.6: XRF results and capacity retention for LFP cells vacuum dried at different temperatures. ....	159
Figure 5.7: Examining differential voltage for C/20 check-up cycles at beginning of life and end of life for LFP/graphite cells with 2VC+1DTD electrolyte cycled at 40°C, C/3 rate. ....	163
Figure 5.8: Long-term cycling for LFP/AG cells cycled at 40°C and a rate of C/3. ....	166
Figure 5.9: Long-term cycling for LFP/AG cells cycled at 55°C and a rate of C/3. ....	168
Figure 5.10: $\mu$ XRF measurements of deposited Fe on the negative electrode extracted from LFP/graphite cells with different electrolytes aged under different conditions. ....	170
Figure 5.11: Ultra high-precision coulometry cycles for LFP/AG cells with different Li salts in the electrolyte. ....	172
Figure 5.12: Parasitic heat flow results extracted from cycles in the isothermal microcalorimeter at 40.0000°C and a rate of $\sim$ C/220. ....	174
Figure 5.13: Parasitic heat flow results for LFP/AG cells with 2VC electrolyte. ....	175
Figure 5.14: Summary of isothermal microcalorimetry results. ....	177
Figure 5.15: OCV storage experiments at 60°C for LFP cells with different electrolytes. ....	179
Figure 5.16: Volumes of gas formation versus time for pouch bags constructed from disassembled LFP/AG pouch cells stored at 60°C. ....	181
Figure 5.17: Isothermal microcalorimetry measurements for pouch bags extracted from full LFP/graphite cells. ....	186

Figure 5.18: Correlation of formation quantities to the first cycle efficiency. ....	195
Figure 5.19: Long-term cycling results for LFP cells with different graphite negatives cycling at C/3 rate at 55°C. ....	196
Figure 5.20: Reversible and irreversible capacity losses in 60°C storage experiments..	198
Figure 5.21: Average parasitic heat flow versus cycle number for LFP/AG cells with different graphites. ....	200
Figure 5.22: Average parasitic heat flow for LFP/AG-A and LFP/AG-C cells, comparing full cells in OCV mode and the sum of separate pouch bags. ....	201
Figure 5.23: Normalized discharge capacity versus cycling time for various LFP cells presented throughout the thesis. ....	205
Figure 6.1: Voltage versus time over five 500 hr OCV storage periods at 60°C. ....	210
Figure 6.2: Discharge capacity and normalized capacity versus storage time for different cell types. ....	214
Figure 6.3: Charge-transfer resistance versus storage time for (a) LFP/AG cells at 3.65 V, and (b) NMC811/AG cells at 4.06 V. ....	217
Figure 6.4: Gas volume evolved as a function of storage time for (a) LFP/AG cells at 3.65 V, and (b) NMC811/AG cells at 4.06 V with different electrolytes and negative electrodes. ....	219
Figure 6.5: Specific gas volumes evolved in charged positive electrode pouch bags at different temperatures from cells with different positive electrode/negative electrode pairings. ....	222
Figure 6.6: Specific gas volumes evolved in charged negative electrode pouch bags at different temperatures from cells with different positive electrode/negative electrode pairings. ....	224
Figure 6.7: Gas produced in pouch bags containing only electrolyte stored at different temperatures. ....	227
Figure 6.8: Arrhenius plot showing average initial specific gas production rate for NMC811 positive electrode pouch bags. ....	229
Figure 6.9: Arrhenius plot comparing the initial specific gas production rate for graphite pouch bags extracted from different LFP/AG cells with different electrolytes. ....	231

Figure 6.10: Arrhenius plot comparing initial specific gas production rate for AG-A pouch bags extracted from either LFP/AG-A or NMC811/AG-A cells.....	232
Figure 6.11: Arrhenius plot comparing initial specific gas production rate for AG-C pouch bags extracted from either LFP/AG-C or NMC811/AG-C cells..	233
Figure 6.12: Measured heat flow versus time for pouch bags and full pouch cells (in OCV mode) in the microcalorimeter.....	235
Figure 6.13: Average parasitic heat flow for full cells and pouch bags for different positive/negative electrode/ electrolyte combinations.....	236
Figure 6.14: Average parasitic heat flow for artificial graphite pouch bags originating from pouch cells with different positive electrodes and electrolytes.....	237
Figure 6.15: Comparing gas evolution in pouch bags and full cells.....	241
Figure 6.16: Correlating capacity fade in full LFP/AG pouch cells to initial specific gas evolution rate in negative electrode pouch bags aged at 80°C.....	244
Figure 6.17: Correlating capacity fade in full LFP/AG cells to parasitic heat flow in graphite pouch bags using IMC.....	245
Figure 7.1: Parasitic heat flow versus inverse temperature measured in different pouch bags as a function of temperature.....	259
Figure 7.2: Studies of blended LFP-NMC positive electrodes.....	262
Figure 7.3: Normalized discharge capacity versus cycle number for $\text{LiMn}_{0.8}\text{Fe}_{0.2}\text{PO}_4$ (LMFP)/AG-A cells with different electrolytes compared to the best LFP/AG-A cell with LiFSI + 2VC electrolyte.....	264
Figure 7.4: Bar graph showing parasitic heat flow measured in full cells and pouch bags in the TAM calorimeter.....	265
Figure A.1: DSC traces of separator samples taken from pouch cells as received, heated at 130°C and heated at 140°C.....	302
Figure A.2: Capacity retention of LFP/AG cells vacuum dried at different temperatures.....	303
Figure A.3: TGA thermograms of carboxymethylcellulose (CMC) carried out in Ar atmosphere.....	304

Figure A.4: Parasitic heat flow versus relative state-of-charge (SOC) over the different cycles in the isothermal microcalorimetry protocol.....	306
Figure A.5: Cross-sectional SEM image of an LFP electrode extracted from one of the low BET LFP/graphite cells that underwent cycling tests in the microcalorimeter. ....	307
Figure A.6: Heat flow versus time measured in the microcalorimeter for pouch bags filled with 1.0 mL each of electrolyte. ....	307
Figure A.7: Voltage versus capacity curves measured at 40°C, C/20 rate for LFP/graphite pouch cells with different artificial graphite negative electrodes. ....	308
Figure A.8: Isothermal microcalorimetry results for LFP/AG cells with different graphites. ....	308
Figure A.9: Nyquist plots for different cells after each storage period. ....	309
Figure A.10: Measured specific gas volume data for LFP positive electrode pouch bags aged at different temperatures with linear fits to initial gas production. ....	310
Figure A.11: Measured specific gas volume data for LFP negative electrode pouch bags aged at different temperatures with linear fits to initial gas production. ....	311
Figure A.12: Measured specific gas volume data for NMC811 positive electrode pouch bags aged at different temperatures with linear fits to initial gas production. ....	312
Figure A.13: Measured specific gas volume data for NMC811 negative electrode pouch bags aged at different temperatures with linear fits to initial gas production. ....	313
Figure A.14: Fits to normalized capacity versus cycle time for LFP/AG cells cycled at C/3 rate at 55°C. ....	314

## ABSTRACT

The market for Li-ion batteries has seen unprecedented growth in recent years due to the adoption of electric vehicles (EVs) and growth of grid-level energy storage. For these applications to be sustainable, inexpensive and long-lasting Li-ion batteries are required. This thesis considers  $\text{LiFePO}_4$  (LFP) as a positive electrode material for use in long-lifetime Li-ion batteries. Already a commercially used material, LFP is seeing a renewed interest in many applications due to the cost and relative scarcity of commonly used transition metals in Li-ion batteries, Ni and Co.

Initial studies of LFP/graphite cells considered the impact of water contamination and different electrolyte additives on lifetime, and an optimal electrolyte composition was determined. Isothermal microcalorimetry techniques were used to rank the lifetime of cells with different electrolyte additives.

Next, different approaches were taken to improve the lifetime of LFP/graphite cells, including considering the surface area of LFP, different Li salts in the electrolyte, and different graphite materials. Combining the results of these studies led to an LFP cell with greatly improved capacity retention. Isothermal microcalorimetry techniques were developed to observe parasitic reactions separately at the positive and negative electrodes, and to infer the degree of “cross-talk” reactions in the cell.

Finally, the storage performance, gas evolution, and parasitic heat flow for Li-ion cells with different positive electrodes, negative electrodes, and electrolytes were studied. The results of these experiments highlighted the complex interactions that occur between different components of the cell. In LFP cells, capacity loss was correlated with the reactivity of the negative electrode.

The results presented in this thesis demonstrate significant lifetime improvements for LFP/graphite cells by targeting different cell components. Additional insights into the role of parasitic reactions on the lifetime of Li-ion cells have been developed. This work should contribute to the future development of Li-ion cells with extremely long lifetimes.

## LIST OF ABBREVIATIONS AND SYMBOLS USED

$\dot{q}_p$	Parasitic heat flow
$\dot{q}_{av}$	Average heat fow
$\dot{q}_{chg}$	Heat flow on charge
$\dot{q}_{dis}$	Heat flow on discharge
$\dot{q}_F$	Full cell parasitic heat flow (OCV)
$\dot{q}_N$	Negative electrode parasitic heat flow
$\dot{q}_{p,av}$	Average parasitic heat flow
$\dot{q}_P$	Positive electrode parasitic heat flow
$\dot{q}_s$	Entropic heat flow
$D_0$	Initial discharge capacity
$D_1$	First discharge capacity after storage
$D_2$	Second discharge capacity after storage
$Q_0$	Initial capacity
$Q_C$	Charge capacity
$Q_D$	Discharge capacity
$q_{Li}$	Li capacity loss (SEI)
$q_{ox}^a$	Oxidation reaction charge
$\dot{q}$	Heat flow
$R_{CT}$	Charge-transfer resistance
$R_{el}$	Solution resistance
$V_r$	Reference voltage



$V_s$	Sample voltage
$Z_C$	Imaginary impedance
$Z_R$	Real impedance
$\Delta_C$	Charge-endpoint capacity slippage
$\Delta_D$	Discharge-endpoint capacity slippage
$^{\circ}\text{C}$	Degrees celcius
2H	Hexagonal graphite
3R	Rombohedral graphite
AG	Artificial graphite
B	Base
BET	Brunauer-Emmett-Teller
BP	Boiling point
$C$	Capacitance
$C/x$	“C-rate” charging rate
CB	Carbon black
CC	Current collector/constant current
CCCV	Constant current constant voltage
CE	Coulombic efficiency
CEI	Cathode electrolyte interphase
CMC	Carboxymethyl cellulose
cP	Centipoise
CTRL	Control
$D_{50}$	Mass median particle diameter

DEC	Diethyl carbonate
DMC	Dimethyl carbonate
DSC	Differential scanning calorimetry
DTD	Ethylene sulfite
<i>e</i>	Elementary charge
EC	Ethylene carbonate
EIS	Electrochemical impedance spectroscopy
EMC	Ethyl methyl carbonate
EU	European Union
EV	Electric vehicle
FCE	First cycle coulombic efficiency
FEC	Fluoroethylene carbonate
<i>g</i>	Gram
<i>g</i>	Gravitational acceleration
hr	Hour
<i>I</i>	Current
<i>i</i>	Imaginary number
IMC	Isothermal microcalorimetry
<i>K</i>	Arbitrary constant
K	Degrees kelvin
KF	Karl Fischer
Kg	Kilogram
kPa	kilopascal

L	Liter
LCO	Lithium cobalt oxide, $\text{LiCoO}_2$
LEDC	Lithium ethylene dicarbonate
LEMC	Lithium ethylene mono-carbonate
LFO	$\text{LiPO}_2\text{F}_2$
LFP	Lithium iron phosphase, $\text{LiFePO}_4$
LiBOB	lithium bis(oxolato)borate
LiDFOB	lithium difluoro(oxalate)borate
LiFSI	lithium bis(fluorosulfonyl)imide
LiTFSI	lithium bis(trifluoromethanesulfonyl)imide
LMFP	$\text{Li}[\text{Mn}_{0.8}\text{Fe}_{0.2}]\text{PO}_4$
LMO	Lithium manganese oxide, $\text{LiMn}_2\text{O}_4$
LTO	Lithium titanate, $\text{Li}_4\text{Ti}_5\text{O}_{12}$
m	Meter
MA	Methyl acetate
mAh	Milliamp-hour
MFT	Mean Field Theory
MP	Melting point
$n$	Number of electrons
NCA	$\text{Li}[\text{Ni}_x\text{Co}_y\text{Al}_{1-x-y}]\text{O}_2$
NG	Natural graphite
NMC	$\text{Li}[\text{Ni}_x\text{Mn}_y\text{Co}_{1-x-y}]\text{O}_2$
OCV	Open-circuit voltage

P	Turbostratic disorder probability
PE	polyethylene
PP	polypropylene
Ppm	Parts per million
PVDF	polyvinylidene fluoride
Q	Capacity or charge
<i>R</i>	Resistance
ROH	Alcohol
RT	Room temperature
S	Generic electrolyte component
<i>s</i>	Entropy per site
<i>S</i>	Entropy
SBR	Styrene-butadiene rubber
SEI	Solid electrolyte interphase
SEM	scanning electron microscopy
SOC	State of charge
SP	Super-P
SSA	Specific surface area
STO	OCV Storage
<i>t</i>	Time
<i>T</i>	Temperature
TGA	Thermogravimetric analysis
TM	Transition metal

TMB	trimethyl borate
TOC	Top of charge
TPFPB	tris(pentafluorophenyl) borane
UHPC	Ultra-high precision coulometry
$V$	Cell voltage
V	Volt
VC	Vinylene carbonate
W	Watt
Wh	Watt-hour
$x$	Lithium occupation (concentration)
XPS	X-ray photoelectron spectroscopy
$Z$	Complex Impedance
$\Delta\dot{q}$	Cross-talk parasitic heat flow
$\Delta G$	Gibbs free energy change
$\Delta V$	Voltage polarization
$\Delta v$	Change in volume
$\Delta w$	Change in weight
$\epsilon$	Calibration constant (IMC)
$\eta$	Overpotential
$\mu$	Chemical potential
$\mu\text{XRF}$	Micro X-ray fluorescence
$\rho$	Density
$\tau$	Calorimeter time constant

$\omega$

Frequency

$\Omega$

Ohm/multiplicity of states

## ACKNOWLEDGEMENTS

For financial support I would like to thank the Natural Sciences and Engineering Research Council (NSERC), the Nova Scotia Graduate Scholarship (NSGS) program, Dalhousie University, and Tesla Canada.

I would like to thank Connor Aiken, Jessie Harlow, Ahmed Eldesoky, Dr. David Hall, Dr. Stephen Glazier, and many others for their support over the years, and good times had both in and out of the lab. I would also like to thank Helena Hebecker, Aidan Luscombe and Ethan Eastwood for helping to complete the work presented in this thesis. I also need to thank Mike Johnson for his encyclopedic knowledge of all equipment in the lab, and keeping the lab from burning down over the years.

Thanks to Laura for always being there for me, even through the hardest parts of this process. I am looking forward to our next chapter, and all of the ups and downs it will bring.

Finally, I would like to thank Jeff for all his support and supervision over the years. Jeff makes sure that each and every one of his students learn and grow to their fullest potential, and it was no different in my experience. Thank you, Jeff, for everything.

## CHAPTER 1 INTRODUCTION

### 1.1 MOTIVATION

Li-ion batteries have been ubiquitous in consumer electronics since their first commercialization more than 30 years ago. Now, Li-ion batteries are being adopted for much larger scale applications such as electric vehicles (EVs)<sup>1</sup> and grid energy storage projects<sup>2</sup>. The EV market in particular has seen meteoric growth in the last decade. New full electric and plug-in hybrid electric vehicle sales in the European Union (EU) have gone from only 700 in 2007 to over 1.3 million in 2020<sup>3</sup>. The number of new registrations of full electric and plug-in hybrid electric vehicles in the EU represented 10% of all new vehicle sales in 2020<sup>3</sup>, and in the coming years demand for EVs will increase even further. In an effort to fight climate change, the EU has proposed legislation to ban the sale of new internal combustion vehicles by 2035<sup>4</sup>, with similar legislation being considered in the State of California<sup>5</sup> and in Canada<sup>6</sup>.

With the continued adoption of Li-ion batteries in these large-scale and long-term applications, maximizing the lifetime of batteries is of paramount importance for sustainability, reliability, and cost. Li-ion batteries have finite lifetimes as cyclable lithium is consumed by parasitic side reactions between charged electrodes and the electrolyte, limiting the total available capacity. Broadly, it will be the goal of this thesis to understand the degradation mechanisms of Li-ion cells, and using this understanding to develop strategies to extend the lifetimes of cells.

### 1.2 LI-ION CELLS



Figure 1.1 shows a schematic of a typical Li-ion cell during a charge cycle, highlighting the primary components. A cell consists of two electrodes, electrically isolated by a porous separator. The separator is usually made of polyethylene (PE), polypropylene (PP), or a combination of the two<sup>7</sup>. Solid electrodes consist of “active” material, where lithium is stored in the charged or discharged state, and “inactive” materials that serve key purposes other than storing lithium. The active and inactive materials are mixed and coated onto a metallic current collector. Active material particles are represented by the large spheres in Figure 1.1. Common inactive materials in a Li-ion electrode are binders (typically polyvinylidene fluoride, PVDF) to promote adhesion of active particles to each other and to the current collector during cycling, and conductive additives (typically carbon black, CB) to bolster electrical conductivity between the active particles<sup>8</sup>. In some cases, active material particles can be coated in a small layer of carbon to further promote electrical conductivity<sup>9-11</sup>, especially for materials that have inherently poor electrical conductivity. The transport of Li ions between electrodes during charge and discharge is facilitated by a conducting electrolyte. Different classes of electrolytes exist in the Li-ion battery space, but this thesis will solely focus on non-aqueous liquid electrolytes. These electrolytes consist of a solvent or blend of solvents, a conducting Li-salt, and possibly some other additives. The electrolyte will be discussed in more detail below.

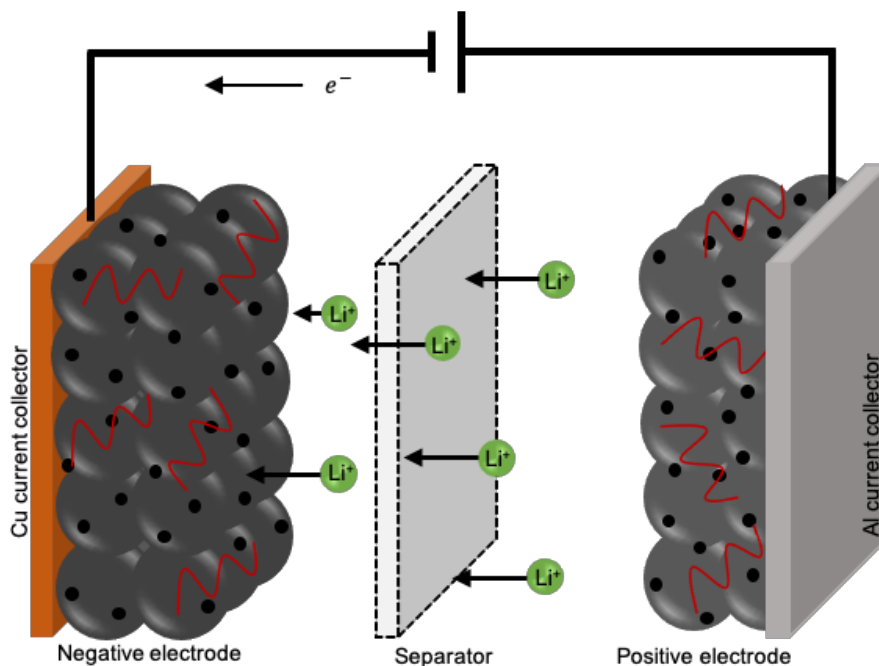


Figure 1.1: Schematic of a full Li-ion cell during charge. The large spheres represent particles of active material in the positive and negative electrodes, which are adhered to the Al and Cu current collectors, respectively. These active materials are held together with the aid of the binder (red lines), and electrical connectivity of the electrode is promoted with the conductive additive (black dots). The two electrodes are electrically isolated by the porous separator. Liquid electrolyte is filled throughout the cell, and allows Li-ion conduction between the electrodes.

Energy is stored and released in a Li-ion cell by shuttling Li ions between the positive and negative electrode. In the discharged state, nearly all Li-ions are stored in the positive electrode. When the cell is charged, Li ions de-intercalate from the positive electrode and intercalate into the negative electrode, where they are stored until the cell is discharged. The porous separator ensures the electrodes do not come into direct electrical contact, while still allowing for the flow of ionic current.

When a cell is charged, for example, Li ions are forced from the positive electrode to the negative electrode. At the same time, an equivalent charge of electrons flow through the external circuit (see Fig 1.1) to maintain charge balance. In this process, an amount of

electrical work  $neV$  is done where  $n$  is the number of electrons (or ions) transferred,  $e$  is the electron charge, and  $V$  is the cell voltage. This corresponds to the change in free energy of the cell, so that

$$\Delta G = -\Delta neV \quad 1.1$$

So, the cell voltage is

$$V = -\frac{\Delta G}{\Delta ne} \quad 1.2$$

Equation 1.2 can be written in terms of the individual half reactions:

$$V = -\frac{1}{e} \left( \frac{\Delta G_{pos}}{\Delta n} - \frac{\Delta G_{neg}}{\Delta n} \right) \quad 1.3$$

The cell voltage can also be related to the chemical potential of the electrodes, defined as

$$\left( \frac{\partial G}{\partial n_i} \right)_{T,P} = \mu_i \quad 1.4$$

where  $i$  represents one of the electrode half-reactions, at constant entropy  $S$  and volume  $v$ .

Then, the cell voltage can be written

$$V = -\frac{1}{e} (\mu_{pos} - \mu_{neg}) \quad 1.5$$

The cell voltage is given by the difference between chemical potential of the positive and negative electrodes. The chemical potential of an active material is dependent on the Li occupancy  $x$ , defined as the ratio of filled sites to available sites in the material. As lithium is intercalated into or deintercalated from the material, the chemical potential will change,

giving the characteristic “voltage curve” of the material. Voltage curves for several common positive electrode materials are shown in Figure 1.2.

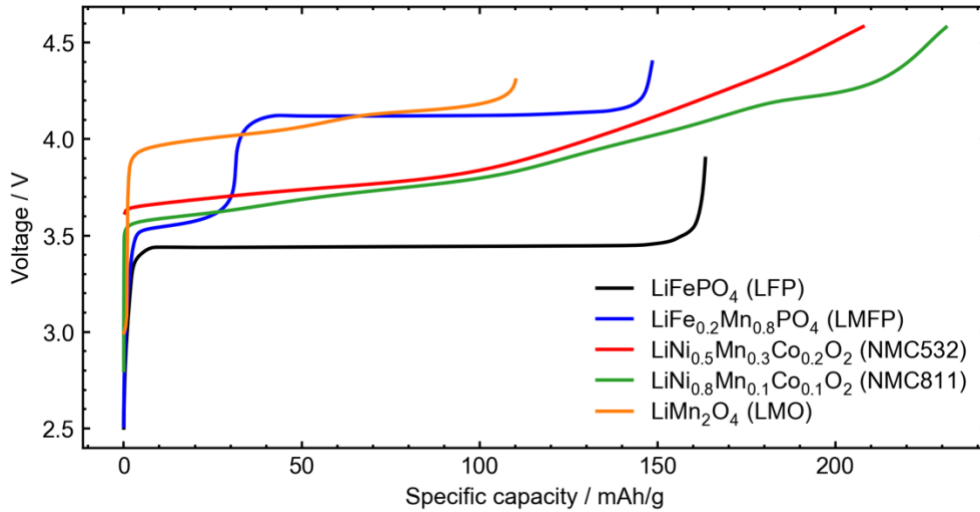
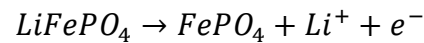


Figure 1.2: Voltage (vs Li metal) versus specific capacity for various relevant positive electrode materials.

While the shape of the voltage curve for a material is determined by the chemical environment and crystal structure of the material, the capacity of the material is often determined by the stoichiometry of the material. Take  $\text{LiFePO}_4$  for an example. Assume all of the Li is removed from the material, i.e.



This process gives us 1 mol of electrons (or 1 mol Li ions). The molar mass of  $\text{LiFePO}_4$  is 157.8 g/mol, so using Faraday’s constant, the expected specific capacity for LFP should be 169.9 mAh/g. Looking at the LFP voltage curve in Figure 1.2, the accessible capacity is about 163 mAh/g, quite close to the calculated theoretical capacity. This simple calculation can be used to understand the expected capacity for a given battery material. The capacity

of a material gives the amount of charge that can be stored. Perhaps a more practical metric is the amount of *energy* that can be stored in a material. Figure 1.3 shows the specific energy (in units of Wh/kg) of the different positive electrode materials shown in Figure 1.2. These numbers were obtained by integrating the voltage vs specific capacity curves for each positive electrode material shown in Figure 1.2. The integration was completed over the full voltage curve unless otherwise noted in Figure 1.3. Note that these numbers only consider the active material itself. Practical values for specific energy in a full Li-ion cell account for both the negative electrode and inactive components and will be lower than the numbers shown here. Additionally, the operating voltage of a cell may be constrained in order to limit parasitic reactions with the electrolyte, among other reasons. As a result, not all of the capacity may be utilized. The impact of cutoff voltage on the resulting specific energy is demonstrated for one of the materials described.

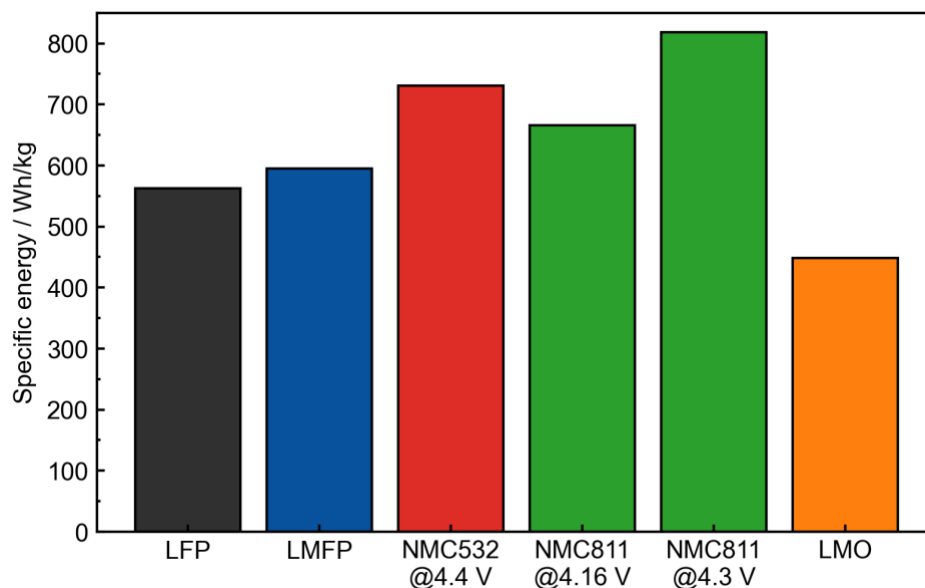


Figure 1.3: Specific energy of various positive electrode materials for Li-ion batteries. LFP and LMFP materials are taken to be completely delithiated, and specific energy of the NMC materials is calculated up to the voltages specified (vs Li metal).

Many different classes of Li energy storage materials exist. Commonly used positive electrode materials are: (1) layered transition metal oxides, (2) olivine materials including  $\text{LiFePO}_4$ , and (3) spinel materials, including  $\text{LiMn}_2\text{O}_4$ . Crystal structures of different materials are shown in Figure 1.4. The most common negative electrode in Li-ion batteries is graphite. Lithiated graphite ( $\text{LiC}_6$ ) is illustrated in Figure 1.4d. These materials will be discussed in more detail in the following sections.

An example of positive and negative electrode voltage curves (vs lithium metal) and the corresponding full cell voltage curve is shown in Figure 1.5. In this example, the positive electrode is  $\text{LiFePO}_4$  (LFP), and the negative electrode is graphite. Practical Li-ion cells are designed with excess capacity in the negative electrode, as depicted in Figure 1.5. This is primarily done to prevent catastrophic failure if the cell is slightly over-charged. The

ratio of negative electrode capacity to positive electrode capacity is known as the N/P ratio.

Typical N/P ratios in both lab scale and commercial cells is around 1.05 – 1.15.

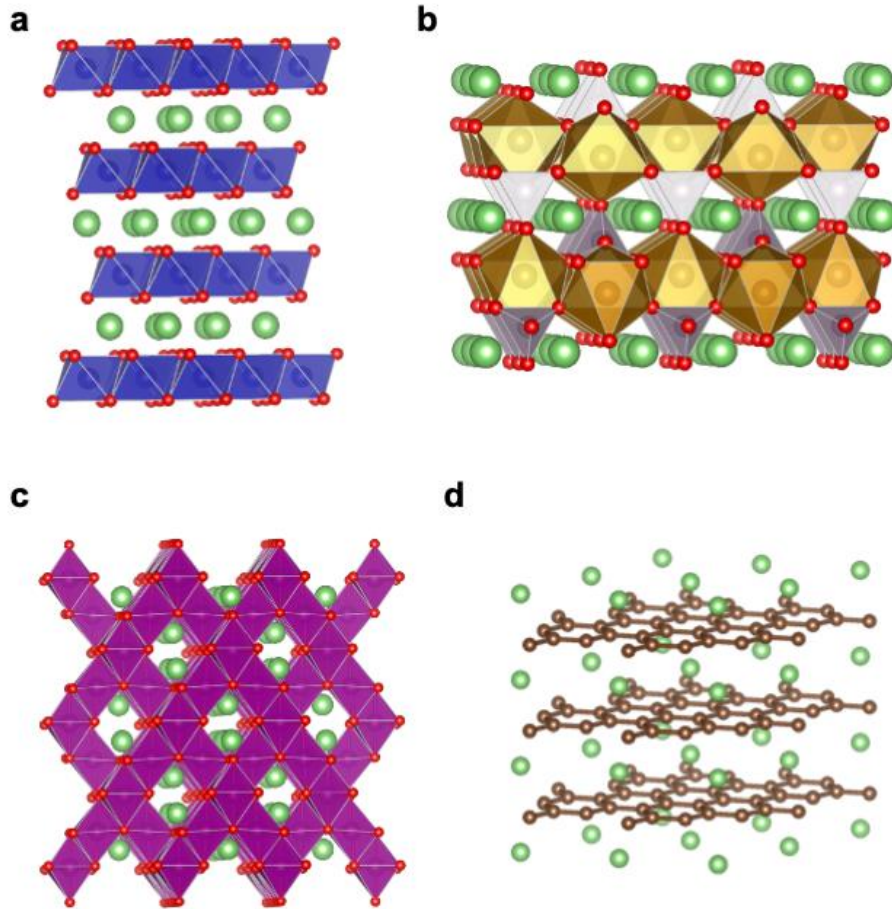


Figure 1.4: Crystal structures for (a) a generic  $\text{LiMO}_2$  layered material, (b) olivine  $\text{LiFePO}_4$  (LFP), (c) spinel  $\text{LiMn}_2\text{O}_4$  (LMO), and (d) fully lithiated graphite ( $\text{LiC}_6$ ). In these pictures, lithium atoms are green, oxygen is red, the generic transition metal M in (a) is blue, Fe is orange/brown, Mn is purple, and carbon is brown.

Full Li-ion cells – including the lab scale cells used in this lab and commercial cells – consist of alternating layers of positive electrode, negative electrode, and separator. In

many cases the positive and negative current collectors are coated on both sides to maximize energy density. Figure 1.6 shows a cartoon of a repeating unit of a cell stack, illustrating the double side coated positive and negative electrodes kept apart by separator layers. Also illustrated is another practical aspect of Li-ion cell design, the so-called “overhang” region. The negative electrode coating is typically wider than the positive electrode coating (~0.2 cm wider in the lab-scale cells used in this thesis). In addition to providing some of the excess negative electrode capacity, it also allows for minor misalignments between positive and negative electrodes in cell assembly and prevents the deposition of lithium metal on the current collector edges during charge.

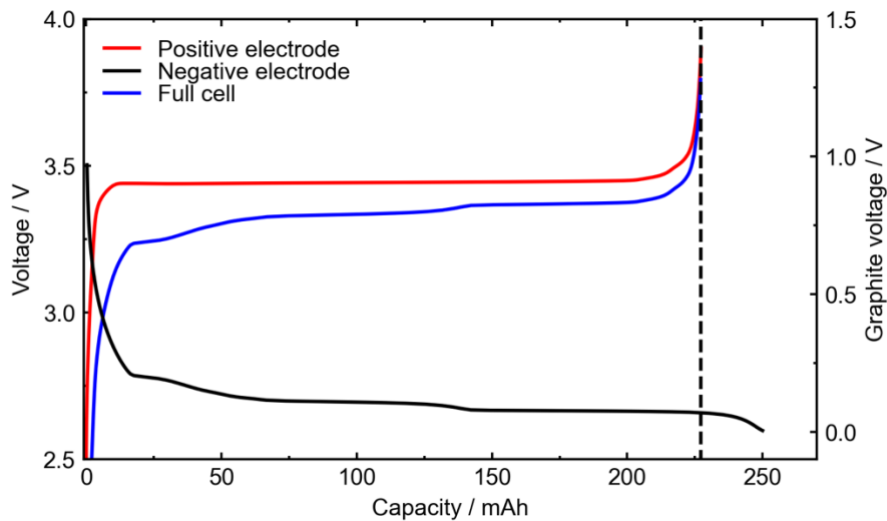


Figure 1.5: Illustrating how a full cell voltage curve is constructed from individual half cell curves. The dashed line is drawn at the end of the full cell capacity, indicating the excess graphite capacity loading. The positive electrode and the full cell voltages are plotted on the left axis, while the graphite voltage curve is plotted on the right axis.



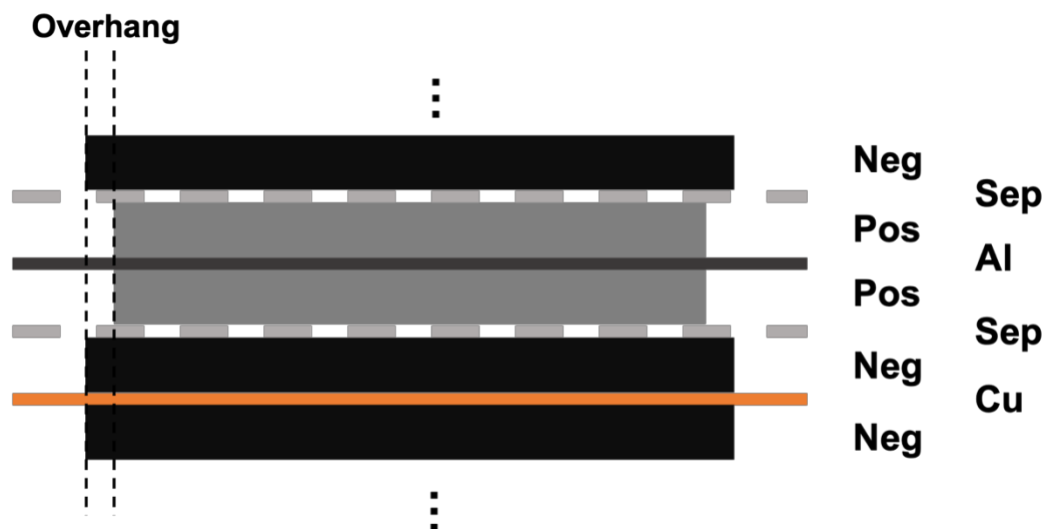


Figure 1.6: Cross-section schematic of the repeating double sided cell stack. Positive electrode (Pos) and negative electrode (Neg) coatings are labelled, as well as the current collectors (Cu and Al) and the separator (Sep). The overhang region is specified by the vertical dashed lines.

### 1.3 POSITIVE ELECTRODE MATERIALS

Positive electrode materials for Li-ion batteries contain lithium in the structure in the discharged state. When the cell is charged, lithium is deintercalated from the positive electrode, and stored in the negative electrode. Many different classes of positive electrode materials exist<sup>12,13</sup>, all with different advantages and disadvantages given different applications. The three main classes of positive electrode materials are described here.

#### 1.3.1 $\text{LiCoO}_2$ (LCO) and $\text{Li}[\text{Ni}_x\text{Mn}_y\text{Co}_{1-x-y}]\text{O}_2$ (NMC)

Some of the earliest positive electrode materials used in Li-ion batteries, and by far the most popular by market share, are a class of materials known as transition metal oxides (generic formula  $\text{LiMO}_2$  where M is a transition metal or a mixture of transition metals).

The crystal structure of a generic  $\text{LiMO}_2$  material is shown above in Figure 1.4a. These materials have a hexagonal lattice (space group R-3m) consisting of alternating layers of  $\text{MO}_6$  octahedra and lithium. The lithium in the structure occupies the octahedral sites between “slabs” of  $\text{MO}_6$ . These materials exhibit high potentials when lithium is removed ( $>4.0$  V vs lithium), and have high specific capacities ( $>150$  mAh/g).

The first practical material of this class that was discovered was  $\text{LiCoO}_2$  (LCO), first published in 1980 by John Goodenough and co-workers<sup>14</sup> (In 2019, John Goodenough would share the Nobel Prize in Chemistry for his contributions to the development of Li-ion batteries). The first commercial Li-ion cell, put to market in 1991 by Sony<sup>12</sup> used an LCO positive electrode. Since then, LCO became the material of choice for batteries for consumer electronics, and is still widely used today. However, the continued use of cobalt in the rapidly growing battery industry faces a number of problems, including supply, ethical questions surrounding its mining and production<sup>15,16</sup>, as well as an extremely volatile price which in turn impacts the cost of the final battery product<sup>17</sup>. Great efforts have been made to move the industry towards positive electrode materials that use less cobalt<sup>18,19</sup>.

Layered oxide materials with mixtures of Ni, Mn, Co were first reported in 2001<sup>20,21</sup>, leading to the development of so-called “NMC” materials with stoichiometry  $\text{Li}[\text{Ni}_x\text{Mn}_y\text{Co}_{1-x-y}]\text{O}_2$ . These materials, in addition to using less cobalt than LCO have higher specific capacities (and thus higher specific energy), and are safer than pure LCO<sup>22</sup>. Since the initial development of NMC and related NCA<sup>23</sup> (A = Al) materials, a major

research objective was to continue to increase the Ni content and reduce Mn, Co, and Al contents, primarily to maximize the specific capacity of the material. By the end of the 2010s, extremely high Ni NMC materials were developed such that the other transition metals in the material could almost be considered “dopants” to a pure Ni LiNiO<sub>2</sub><sup>24–26</sup>. Recently Li et al. questioned whether cobalt was required at all, showing minimal impact on the electrochemical cycling performance of high nickel materials<sup>27</sup>. That said, all Ni rich NMC materials suffer from large volume changes at high states of charge leading to particle cracking and capacity loss<sup>28</sup>.

Reducing the amount of Co required in state-of-the-art Li-ion batteries was a significant achievement. However, the Co that is removed from these materials has largely been replaced with Ni. While Ni is more abundant, cheaper, and less associated with unethical mining practices, the unprecedented growth of the Li-ion battery industry (primarily driven by the EV sector) has put pressure on the Ni supply as well. It has been suggested that with the advent of commercial Ni rich NMC materials, the overall cost of Li-ion batteries with NMC positive electrodes are much more sensitive to increases in the price of Ni compared to Co<sup>29</sup>. Therefore, alternative positive electrode materials that do not contain Ni or Co should be considered.

### 1.3.2 LiFePO<sub>4</sub> (LFP)

LiFePO<sub>4</sub> (LFP) is one of a number of compounds that exhibit the olivine structure. As opposed to the layered structure of LCO and NMC, lithium atoms in LFP are stored in 1-dimensional “tunnels” in the lattice, which can be seen in Figure 1.4b. LFP was shown to

be a useful electrode material in 1997 by Padhi et al.<sup>30</sup> (also from John Goodenough's research group). It has a relatively high specific capacity of 170 mAh/g (although less than NMC materials) and a redox potential of around 3.5 V vs Li<sup>+</sup>/Li (also lower than NMC). While it cannot achieve the same energy density as Ni-rich layered oxides, it possesses superior safety<sup>31,32</sup> and inexpensive precursor materials including no Co or Ni, resulting in commercial interest in LFP. As of 2018, LFP made up 34% of cathode material production in the Li-ion battery industry<sup>33</sup>. LFP is attractive for grid energy storage systems, where energy density is less of a priority.

The use of LFP has practical issues, however. Both the lithiated and delithiated phases have inherently sluggish Li diffusion, severely inhibiting the rate capability of the material. However, this issue has largely been overcome by using carbon coatings to enhance electronic conductivity and small LFP particles to reduce the Li diffusion length within the particle<sup>11,34,35</sup>. Perhaps ironically, with these improvements to LFP, the resulting carbon-coated, nanostructured material is known as an excellent choice for high-power applications<sup>36-40</sup>. As well, other transition metals can be substituted in place of Fe in the olivine structure<sup>41</sup>. One common substitution is for Mn, i.e. LiFe<sub>x</sub>Mn<sub>1-x</sub>PO<sub>4</sub> (LMFP)<sup>42,43</sup>. These materials have similar specific capacities to LFP, but a higher redox potential, thus increasing the specific energy of the material. The voltage curve of a LiFe<sub>0.2</sub>Mn<sub>0.8</sub>PO<sub>4</sub>/Li half cell is shown in Figure 1.3.

### 1.3.3 LiMn<sub>2</sub>O<sub>4</sub> (LMO)

$\text{LiMn}_2\text{O}_4$  (LMO) spinel materials are another potential Co- and Ni- free alternative to NMC positive electrode materials. LMO has a cubic lattice, with the oxygen atoms forming a close-packed structure<sup>44</sup>. Li and Mn are arranged in such a way that the lithium has three-dimensional diffusion pathways, leading to extremely high charge and discharge rate capability in this material<sup>45</sup>. However, LMO suffers from extremely poor high temperature cycle performance<sup>46</sup>, which is usually attributed to large amounts of Mn dissolution (see CHAPTER 2) from the material and subsequent deposition on the negative electrode<sup>47,48</sup>. As well, LMO has a lower specific capacity compared to both the layered oxides and olivines. LMO positive electrodes will not be considered in this thesis.

#### **1.4 NEGATIVE ELECTRODE MATERIALS**

The negative electrode in a Li-ion cell stores lithium when the cell is charged. Graphite is by far the most widely used negative electrode material for Li-ion batteries. It has a very high theoretical specific capacity (370 mAh/g) and low operating potential versus lithium (average voltage 0.125 V<sup>49</sup>) leading to high full cell potentials and high specific and volumetric energy densities. As well, graphite has other desirable properties such as high coulombic efficiency, relatively low volume expansion when Li is cycled, and high energy efficiency<sup>50</sup>.

Graphite is made up of repeating layers of  $\text{sp}^2$ -bonded carbon known as graphene. Sheets of graphene are held together with Van der Waals forces to form graphite. Two main phases of graphite exist, hexagonal (2H) and rhombohedral (3R). 2H graphite consists of graphene sheets arranged such that the carbon atoms of subsequent layers are shifted by one C-C

bond length relative to the previous layer. This is known as ABAB stacking. 3R graphite has three layers of graphene in a repeating unit, known as ABCABC stacking. When lithium is inserted into graphite, it occupies the space between the graphene layers. Regardless of the graphite phase, neighbouring graphene layers become aligned when lithium is inserted, such that carbon atoms in adjacent layers are directly above and below each other. Lithium atoms intercalate into the center of the hexagonal carbon structures in the graphite, avoiding nearest neighbour interactions when the layer is full. Figure 1.7 shows cartoon images of both pristine 2H graphite and completely lithiated graphite ( $\text{LiC}_6$ ). Both the stacking of adjacent graphene layers and the positions of the intercalated lithium can be seen in these images.

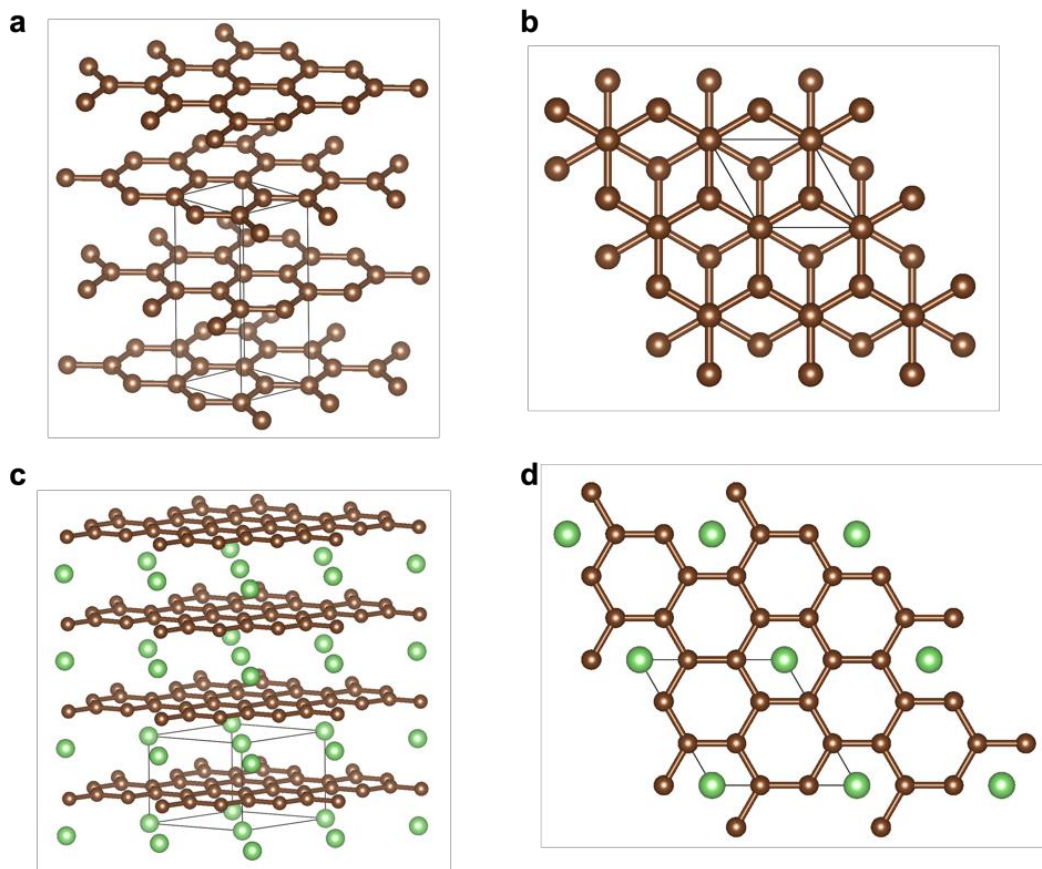


Figure 1.7: Pictures of different graphite structures. (a) Pristine 2H graphite (front view), (b) pristine 2H graphite (top view), (c) fully lithiated graphite LiC<sub>6</sub> (front view), and (d) fully lithiated graphite (top view). In this picture, lithium atoms are green and carbon atoms are brown.

The Li-graphite system has a rich phase diagram of distinct phases or “stages” as a function of lithium concentration<sup>51</sup>, that in turn influence the electrochemical profile of graphite. Figure 1.8 shows the voltage profile of an artificial graphite electrode versus a lithium metal anode as Li was intercalated into graphite. The approximate locations of coexistence regions between different stages are indicated in the Figure. In this nomenclature, the stage number specified the number of graphene layers between the next layer of lithium, e.g. in “stage 2”, there are 2 graphene layers between each lithium layer. The “L” modifier to some of the stages specifies that the lithium atoms on a given layer are randomly placed, i.e. a “liquid” arrangement of lithium in a layer. Stages without the “L” modifier consist of

ordered lithium layers. Some consequences of this lithium ordering will be considered later in this thesis.

In reality, not all graphite is perfectly 2H or 3R. In practice, graphite possesses mistakes in the graphene stacking known as turbostratic disorder. The probability  $P$  is defined as the probability of turbostratic rotation between adjacent graphene sheets. Perfect graphite where  $P=0$  would be 2H graphite. Zheng et al. showed a strong negative correlation between  $P$  and the achievable Li storage capacity in a given graphite material, i.e. the more turbostratic disorder in a graphite sample, the lower the attainable capacity<sup>52</sup>. Turbostratic disorder in graphite essentially “blocks” Li intercalation between layers, thus limiting the amount of Li that can be stored.

Graphite materials used in Li-ion batteries can be classified into two main groups: natural graphites (NGs) and artificial graphites (AGs). NGs, as the name would suggest, are mined from the Earth’s crust already in graphitic form. AGs are synthesized from soft carbon precursors such as petroleum pitch or tar at extremely high temperatures of  $>2500^{\circ}\text{C}$ <sup>50</sup>. NG materials typically have lower degrees of turbostratic misalignment ( $P$  close to 0), while AGs have higher  $P$  values that are strongly dependent on the heat-treatment temperature of the given sample<sup>52</sup>. While NGs have higher specific capacities due to being close to perfect graphite, AGs typically have better capacity retention because the turbostratically misaligned layers effectively “pin” adjacent graphene layers, preventing degradation of the material as lithium is inserted and removed from cycle to cycle<sup>53,54</sup>. In this thesis, only artificial graphites are considered.



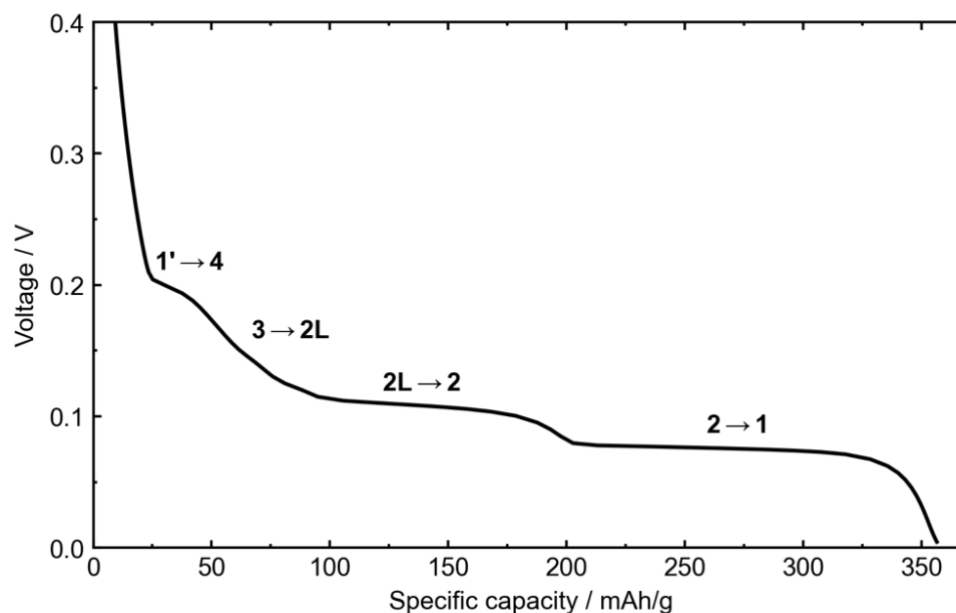


Figure 1.8: Voltage versus specific capacity for an artificial graphite (AG) electrode versus Li metal. Approximate locations of coexistence regions of “stages” in the Li-Gr phase diagram are labelled, with the different stages listed.

Materials other than graphite can be used as the negative electrode in Li-ion cells, including silicon-containing materials<sup>49,55</sup>, metallic lithium<sup>56,57</sup> or other Li-containing compounds such as  $\text{Li}_4\text{Ti}_5\text{O}_{12}$  (LTO)<sup>58</sup>. Apart from LTO, these negative electrode materials typically achieve higher energy densities than graphite but tend to suffer from lifetime issues, a discussion of which is beyond the scope of this thesis.

## 1.5 ELECTROLYTE

The electrolyte plays many crucial roles in a Li-ion cell. Its primary function is to transport Li ions between the positive and negative electrodes during charge and discharge. Li-ion transport is especially important when considering fast charging applications, where electrolyte transport may become the limiting factor<sup>59,60</sup>. The ionic conductivity versus

lithium salt concentration for a typical electrolyte solution is shown in Figure 1.9. The typical range in lithium salt concentration is highlighted in the Figure. While it is generally desirable for the electrolyte to be as resistant to reactions with the charged electrode as possible, specific reactions between the electrolyte and electrodes are key in the formation of passivating interphases that extend the lifetime of the cell. Without these electrolyte-electrode reactions, long lifetime Li-ion cells would not be possible. While many different types of electrolytes exist, the cells used in this thesis exclusively used non-aqueous liquid electrolytes. The various components of the electrolyte, as well as key interfacial reactions, are described below.

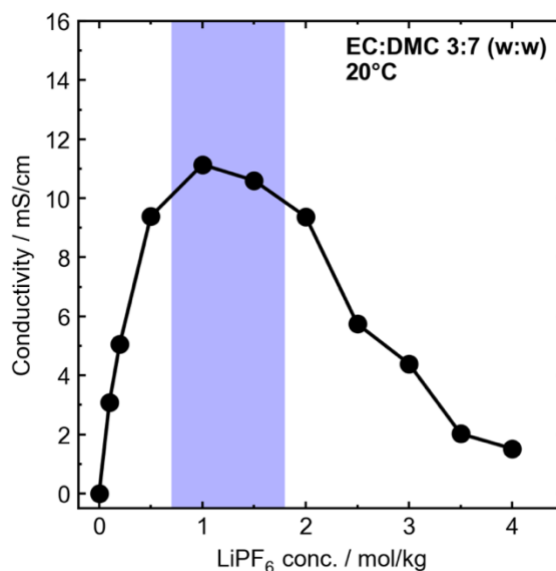
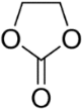
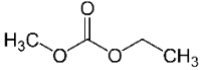
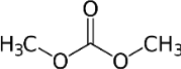
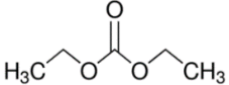


Figure 1.9: Conductivity as a function of salt concentration for a common alkyl carbonate electrolyte mixture, ethylene carbonate (EC):dimethyl carbonate (DMC) 3:7 (by weight) with LiPF<sub>6</sub> as the conducting salt. Conductivity was measured at 20°C.

### 1.5.1 Solvents

Non-aqueous electrolyte solutions typically use alkyl carbonate solvents as they tend to possess an ideal combination of electrochemical stability, ability to dissociate Li salts, relatively low toxicity, high flash points (ideal for safety), and low cost<sup>61,62</sup>. Further, different carbonate solvents can be blended to further optimize the physical and electrochemical properties of the solution. A common solvent blend that is used throughout industry, academia, and this thesis is a mixture of the cyclic ethylene carbonate (EC) and a linear carbonate such as dimethyl carbonate (DMC) or ethyl methyl carbonate (EMC). These solvents combine the high dielectric constant of EC as well as its passivating film-forming properties (more on this below) with the low viscosity and low melting point of either DMC or EMC. Some physical properties of some common carbonate solvents are shown in Table 1.1.

Table 1.1: Common solvents used in Li-ion battery electrolytes. Basic physical properties of these solvents are shown, as well as their molecular structure. Typically, blends of these solvents are used in practice.

Name	Melting point (°C)	Boiling point (°C)	Dielectric constant at 25°C	Viscosity at 25°C (cP)	Structure
Ethylene carbonate (EC)	36.4	248	89.78 (40°C)	1.93 (40°C)	
Ethyl methyl carbonate (EMC)	-53	110	2.958	0.65	
Dimethyl carbonate (DMC)	4.6	90	3.1075	0.59	
Diethyl carbonate (DEC)	-74.3	126	2.805	0.75	

### 1.5.2 Salts

The Li salt in the electrolyte facilitates the conduction of lithium ions between the electrodes during charge and discharge.

Table 1.2 shows a number of common Li salts.  $\text{LiPF}_6$  has long been the salt of choice for Li-ion batteries due to its balance of low cost, high ionic conductivity in alkyl carbonate solutions, relative stability against electrochemical reactions, moderate thermal stability, and relatively high degree of dissociation in polar solution<sup>61</sup>. Despite this,  $\text{LiPF}_6$  can thermally decompose at relatively low temperatures<sup>63</sup>, and is prone to hydrolysis, forming acidic species which can interact with various components of the cell<sup>64-67</sup>.


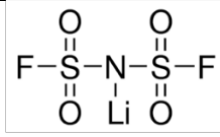

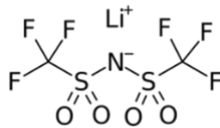
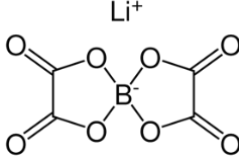
The related imide salts lithium bis(trifluoromethanesulfonyl)imide ( $\text{LiTFSI}$ ) and lithium bis(fluorosulfonyl)imide ( $\text{LiFSI}$ ) demonstrate high ionic conductivity and excellent dissociation in carbonate solvents<sup>61,68,69</sup>, as well as high thermal stability<sup>70</sup>. However, nagging issues exist with these salts as well, notably corrosion of the Al current collector when used in high-voltage chemistries<sup>69,71-73</sup>. Electrolytes with  $\text{LiFSI}$  salt are considered in CHAPTER 5.

Lithium bis(oxolato)borate ( $\text{LiBOB}$ ) is able to passivate the Al current collector in cells that operate at high voltages in a similar way to  $\text{LiPF}_6$ <sup>74</sup>. Several works have reported promising improvements in cell lifetime when  $\text{LiBOB}$  was used, where it was shown to form favorable species on the negative electrode<sup>75-77</sup>. One downside of  $\text{LiBOB}$  is its low solubility in alkyl carbonate solutions ( $<0.8 \text{ M}$ )<sup>62</sup>.

Another common salt for Li-ion batteries is  $\text{LiBF}_4$ .  $\text{LiBF}_4$  has higher thermal stability than  $\text{LiPF}_6$ <sup>61</sup>. Electrolyte solutions with  $\text{LiBF}_4$  have lower ionic conductivities than when  $\text{LiPF}_6$

is used<sup>78</sup> due to the stronger association between  $\text{Li}^+$  and  $\text{BF}_4^-$ . The use of  $\text{LiBF}_4$  has been shown in some cases to improve the high voltage cycling of NMC/graphite cells<sup>79</sup>.

Table 1.2: Names and structures of some common Li salts used in electrolyte solutions for Li-ion batteries.

Common name	Chemical formula	Chemical structure
LiPF <sub>6</sub>	LiPF <sub>6</sub>	Li <sup>+</sup> 
LiFSI	LiN(FSO <sub>2</sub> ) <sub>2</sub>	
LiBF <sub>4</sub>	LiBF <sub>4</sub>	Li <sup>+</sup> 
LiTFSI	LiN(CF <sub>3</sub> SO <sub>2</sub> ) <sub>2</sub>	
LiBOB	LiB(C <sub>2</sub> O <sub>4</sub> ) <sub>2</sub>	Li <sup>+</sup> 

### 1.5.3 The Solid Electrolyte Interphase (SEI)

Most components of a typical non-aqueous electrolyte are inherently unstable in the voltage ranges that a Li-ion cell operates within. When in contact with the charged negative electrode, the electrolyte will react readily, consuming Li and rapidly decreasing the capacity of the cell. However, some electrolyte-electrode reactions have favorable products, producing a film on the active material particle surface that is electrically insulating to prevent further reactions, but still ionically conductive so lithium can reach

the active material. This film is known using the umbrella term solid electrolyte interphase (SEI). This film is not made up of a single continuous component, but rather consists of a mixture of different organic and inorganic species, each providing different properties to the film. The SEI model was first proposed by Peled in 1979<sup>80</sup>, and since has been the subject of significant research effort<sup>81,82</sup>. By convention, the term SEI typically refers to the interphase layer on the graphite electrode. Electrolyte decomposition products do exist on the surface of positive electrode particles<sup>83-85</sup>, and this layer may be referred to as the cathode SEI or CEI. The nature and function of the cathode SEI is less well understood than the graphite SEI, although details of both cathode and anode SEI layers are still the subject of significant debate in the literature.

In a typical alkyl carbonate electrolyte (e.g. EC:DMC 3:7 + LiPF<sub>6</sub>) the main component that reacts to form the SEI is EC, though the LiPF<sub>6</sub> and DMC components may also react<sup>86-88</sup>. In this specific electrolyte, the primary SEI components are thought to be lithium ethylene dicarbonate (LEDC) and LiF<sup>89-94</sup>. The LEDC conducts lithium ions through the SEI to the active material particle, while the highly resistive LiF limits electron transfer. Recent work, however, has questioned the presence of LEDC as the primary SEI component, instead suggesting that lithium ethylene mono-carbonate (LEMC) is the primary decomposition product of EC<sup>95</sup>. The identification and characterization of SEI components is still a very active area of research.

#### 1.5.4 Electrolyte Additives



The properties of the SEI are key to increasing the lifetime of Li-ion cells. A well passivating SEI layer will prevent further parasitic reactions between the electrode and the electrolyte, and prevent the irreversible consumption of lithium as the cell cycles. Therefore, improving the passivating properties of the SEI should be a priority. The simplest and most effective way to modify the properties of the SEI is to add a small amount (usually <5% by weight) of sacrificial additive to the electrolyte. When the cell is charged for the first time, the additives are reduced at the graphite surface, yielding products that have favourable properties for the SEI. The development and screening of electrolyte additives for Li-ion batteries is a very active research area<sup>96,97</sup>, as is the effort to understand the mechanisms for electrolyte additive function<sup>90,98-101</sup>. The various electrolyte additives that were used in this thesis are given in Table 1.3 along with their chemical structures. Electrolyte additives can also be combined in binary, ternary, or even quaternary blends. This may be done in an effort to combine the favorable properties of different electrolyte additives.

One of the most frequently used electrolyte additives is vinylene carbonate (VC). Note the similarity in chemical structures between EC and VC (Table 1.1 and Table 1.3). When VC is added to the electrolyte, it is preferentially reduced on the graphite surface instead of EC, thus changing the properties of the SEI. The resulting SEI layer is rich in  $\text{Li}_2\text{CO}_3$ , and contains a passivating polymeric film known as poly(VC)<sup>89</sup>. Adding just <5% VC to an electrolyte can increase the lifetime of a Li-ion cell by nearly an order of magnitude compared to the case without any electrolyte additives<sup>102</sup>.

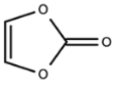
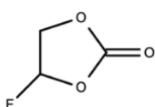
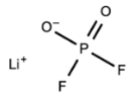
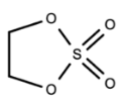
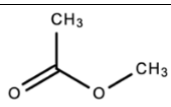
Fluoroethylene carbonate (FEC) is a similar molecule to both VC and EC. Poly(VC) is also a reaction product of FEC<sup>89</sup>. The fluorine on FEC leads to an SEI layer that is rich in LiF<sup>103</sup>.

Lithium difluorophosphate (LiPO<sub>2</sub>F<sub>2</sub>, or LFO) is another common additive in Li-ion batteries<sup>104</sup>. The use of LFO has been shown to lead to an SEI rich in fluorophosphate species that reduce the rate of parasitic reactions<sup>105,106</sup>. LFO has been used in combination with other electrolyte additives to make Li-ion cells with exceptional lifetimes as well as rate capability<sup>107,108</sup>.

The use of ethylene sulfate (DTD) has been shown to increase the cycle lifetimes of cells compared to an electrolyte without any additives<sup>109</sup>. However, DTD increases the volume of gas produced in the cell during formation<sup>110</sup>. DTD was shown to lead to a highly organic film on the graphite electrode with a high sulfur content<sup>111</sup>. Like LFO, DTD is often blended with other electrolyte additives like VC or FEC<sup>108,112</sup>.

Methyl acetate (MA) is a common co-solvent for fast charging applications<sup>113–115</sup>. The addition of MA to the electrolyte in moderate amounts (20-40% by weight) has shown significant improvement to the ionic conductivity of the solution<sup>116,117</sup>. However, the addition of MA typically results in a lifetime penalty due to the increased reactivity of MA compared to carbonate solvents such as DMC, as well as its poor SEI-forming properties<sup>115,118</sup>.

Table 1.3: Names and structures of some common electrolyte additives used in Li-ion batteries.

Additive name	Chemical formula	Chemical structure
vinylene carbonate (VC)	$C_3H_2O_3$	
Fluoroethylene carbonate (FEC)	$C_3H_3FO_3$	
Lithium difluorophosphate (LFO)	$LiPO_2F_2$	
Ethylene sulfone (DTD)	$C_2H_4O_4S$	
Methyl acetate (MA)	$C_3H_6O_2$	

The basic action of electrolyte additives can be seen from a very simple measurement. Figure 1.10 shows the derivative of cell capacity versus cell voltage for Li-ion pouch cells during their first charge cycle, known as the “formation” cycle. This refers to the initial formation of the SEI when electrolyte components are reduced at the graphite negative electrode. Cells containing different electrolyte additives are shown. The feature in the differential capacity plots 2.8 V (full cell voltage) that can be seen is typically associated with the reduction of SEI components. In a cell without additional electrolyte additives, this feature corresponds to the reduction of EC to form SEI. The impact of different electrolyte additives can be clearly seen. Cells with VC and FEC additives suppress the reduction of EC, being preferentially reduced at the graphite themselves.

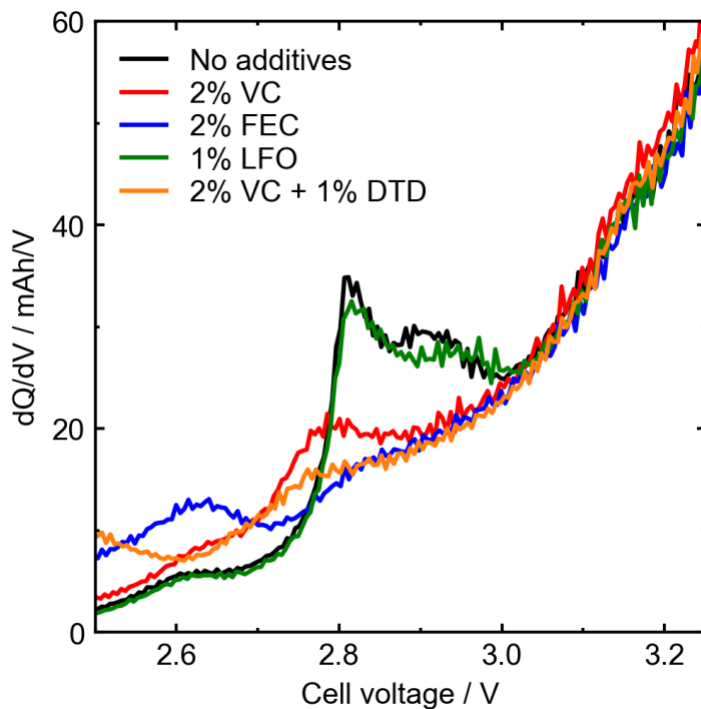


Figure 1.10: Differential capacity ( $dQ/dV$ ) versus cell voltage during the first charge of a  $\text{LiFePO}_4$ /graphite pouch cell, zoomed in on the SEI formation region. Cells with different electrolyte additives are shown.

## 1.6 SCOPE OF THIS THESIS

To extend the lifetimes of Li-ion cells, the mechanisms by which cyclable lithium is lost during the operation of a cell must be understood. A Li-ion battery is a complex system with many interrelated components, which means identifying degradation mechanism is a non-trivial task. This thesis will study the performance of the  $\text{LiFePO}_4$  (LFP)/graphite cell chemistry, attempt to identify the primary degradation mechanisms for this system, and use this knowledge to develop cells with improved lifetime. In addition to common techniques such as electrochemical cycling, storage, and destructive analyses of aged cell components, one of the principal techniques used in this thesis is isothermal microcalorimetry (IMC). Li-ion IMC techniques have previously been used to study parasitic reactions in Li-ion

batteries with great success<sup>119-122</sup>, and these techniques will be further applied and developed here.

CHAPTER 2 will discuss in detail the different types of parasitic reactions and how they affect capacity loss in Li-ion cells. Other failure mechanisms will also be discussed. CHAPTER 2 will also introduce the Li-ion isothermal microcalorimetry technique.

In CHAPTER 3, specifications for the various Li-ion pouch cells used in this thesis will be given. Descriptions for all experimental techniques will also be given in CHAPTER 3.

In CHAPTER 4, initial studies of the performance and degradation of LiFePO<sub>4</sub> (LFP)/graphite pouch cells will be presented. The impact of water contamination on the performance of LFP cells will be studied. Different systems of electrolyte additives will be screened. In addition to cycling, high temperature OCV storage experiments will be presented. Scanning  $\mu$ XRF experiments will be done on graphite negative electrodes extracted from cells aged at different temperatures with different electrolyte additives to study how these parameters impact the degree of Fe dissolution in LFP cells. Isothermal microcalorimetry techniques will be developed to measure the heat flow from parasitic reactions in LFP/graphite cells, and applied to cells with different electrolyte additives and water contents. At the end of CHAPTER 4, the best performing LFP/graphite cell up to that point will be compared to several commercial LFP cells as well as NMC532/graphite pouch cells.

In CHAPTER 5, several approaches will be taken to improve the high-temperature performance of LFP/graphite cells. The impact of LFP surface area and particle size, the impact of different Li salts in the electrolyte, and the effect of different graphite negative electrodes on the lifetime of LFP/graphite cells will be considered. Improved LFP/graphite cells resulting from these studies will again be compared to commercial LFP and lab-made NMC532 cells at the end of the Chapter.

CHAPTER 6 will attempt to further understand the dependence of different positive and negative electrodes on parasitic reactions in Li-ion cells. Long-term high temperature OCV storage experiments will be done for LFP/graphite and NMC811/graphite cells with different artificial graphite negative electrodes and different electrolytes. As well as full cell experiments, storage experiments will be done with separated electrodes to monitor gas evolution and parasitic heat flow originating at a single electrode only. At the end of CHAPTER 6, experiments that monitor parasitic reactions at the negative electrode will be correlated to capacity loss in full LFP/graphite cells at elevated temperatures.

In CHAPTER 7, the thesis will be concluded. The results from the previous chapters will be summarized, and future directions for this research will be discussed. In particular, further approaches to improve the lifetimes of LFP/graphite cells will be proposed, and further experiments to gain a better understanding of degradation in these cells will be discussed. Future directions for the Li-ion isothermal microcalorimetry technique will be discussed. Finally, there will be a short discussion on “advanced” Li-ion cells using

blended NMC/LFP positive electrodes and Mn-rich olivine materials (i.e. LMFP), and their respective benefits and drawbacks.

## CHAPTER 2 LI-ION CELL DEGRADATION AND ISOTHERMAL MICROCALORIMETRY

### 2.1 COULOMBIC EFFICIENCY AND CHARGE ENDPOINT SLIPPAGE

In an ideal Li-ion cell, all the lithium contained in the positive electrode in the discharged state can be used to store energy. It is deintercalated from the positive electrode during charge and stored in the negative electrode. In the ideal case, all this lithium can be recovered from the negative electrode during discharge, stored back in the positive electrode until the next charge, etc. Of course, this does not occur in practice. In a real Li-ion cell, cyclable lithium is irreversibly consumed in side-reactions that are often called “parasitic” reactions. These parasitic reactions reduce the amount of lithium available in the cell and reduce the coulombic efficiency (CE). CE is used to quantify this loss of lithium to parasitic reactions, and is defined as the ratio of the capacity of a discharge half-cycle ( $Q_D$ ) to the capacity of the immediately preceding charge half-cycle ( $Q_C$ ):

$$CE = \frac{Q_D}{Q_C} \quad 2.1$$

In crude terms, the CE compares how much useful charge can be “taken out” of a cell compared to how much is “put in” when it is charged. In the hypothetical cell where no lithium is irreversibly consumed, the CE as the cell cycles is exactly 1.000... In a realistic cell where some degree of parasitic reactions always occur, the CE is always less than 1. However, a state-of-the-art Li-ion cell can have a CE that is very close to 1 (i.e. > 0.99). Figure 2.1a shows the voltage curve for an LFP/graphite cell cycled at low rate ( $\sim C/20$ ).



The charge and discharge half-cycles that are used to calculate the CE for a given cycle are highlighted. Figure 2.1b plots CE as a function of cycle number for cells with two slightly different electrolyte compositions. Note that for both cell types, the CE is extremely high ( $> 0.998$  by cycle 10). However, Cell 1 has a slightly higher CE than Cell 2. Notice as well that two identical cells were cycled for each cell type, which can be seen by closely inspecting the open red points (cell 2), illustrating very good reproducibility between nominally identical pouch cells. Using appropriate experimental equipment (see CHAPTER 3) these minute differences between CEs can be resolved. The slightly lower CE value for Cell 2 suggests that more parasitic reactions occur in this type of cell. This *potentially* could mean that more Li is irreversibly consumed in these cells compared to Cell 1, leading to more capacity loss and a shorter lifetime. The contributing factors to CE are discussed further below.

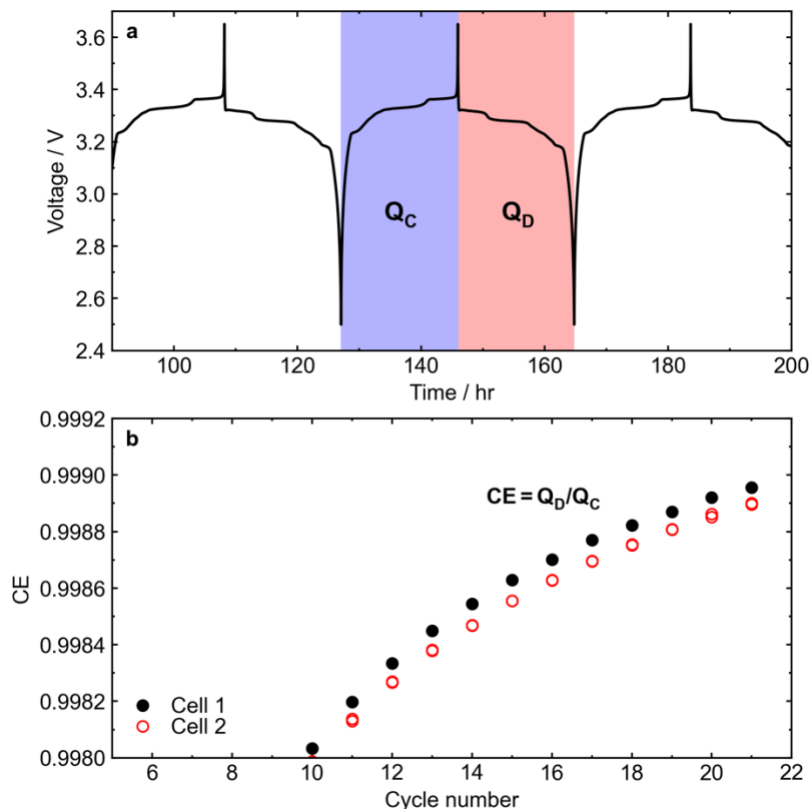


Figure 2.1: Illustrating the concept of coulombic efficiency (CE). (a) Voltage versus time for an arbitrary Li-ion cell as it cycles, highlighting the pairs of half-cycles used to calculate the CE. (b) CE versus cycle number for cells with different electrolytes, showing how CE can vary from one cell to another.

Due to the nature of a Li-ion battery as a closed system (in general), the amount of lithium in the cell can be thought of as a finite lithium “inventory”<sup>123,124</sup>. A cell begins its life with a predetermined lithium inventory in the positive electrode and in the electrolyte. As the cell is cycled, and parasitic side reactions occur and lithium is consumed, this lithium can no longer be cycled. By tracking the movement of the lithium inventory as a cell cycles, key information about its degradation and failure can be elucidated. By analyzing the movement of lithium in a cell between charge and discharge cycles in a process dubbed a lithium “accounting” model, Smith et al. showed that the coulombic efficiency of a cell as

it is cycled is related primarily to the processes of SEI formation at the negative electrode, and electrolyte oxidation at the positive electrode (both of these processes will be discussed in more detail below) in the following (approximate) relation<sup>123</sup>:

$$CE = 1 - \frac{2q_{Li}}{Q_0} + \frac{q_{ox}^a}{Q_0}, \quad 2.2$$

where  $q_{Li}$  is the lithium capacity lost due to SEI formation,  $q_{ox}^a$  is the charge passed due to parasitic oxidation reactions, and  $Q_0$  is the original capacity of the cell. Therefore, CE values less than 1.000... denote lithium loss due to SEI formation (or more generally the irreversible consumption of Li). The oxidation parasitic reactions can increase the measured CE because they (in general) do not irreversibly remove lithium from the inventory, and instead add lithium to the positive electrode from the electrolyte.

The extra charge that is counted as a result of parasitic reactions leads to a relative “shift” of the voltage curve of a cell as it cycles. Oxidation reactions at the positive electrode can lead to a higher measured capacity, and SEI formation reactions at the negative electrode lead to a lower measured capacity because cyclable lithium is removed from the inventory. These relative capacity shifts, defined as charge endpoint capacity slippage ( $\Delta_C$ ) and discharge endpoint capacity slippage ( $\Delta_D$ ), respectively, can be seen in the voltage curves as a cell cycles. Figure 2.2 shows voltage versus capacity for an LFP/graphite cell as it was cycled at a low rate (C/20). Insets in the figure zoom in to the endpoints of charge and discharge. From here it can be seen that in each cycle both the charge endpoint and the discharge endpoint shift relative to the previous cycle. As mentioned above, the charge endpoint capacity slippage is related to parasitic oxidation reactions at the positive

electrode, and the discharge endpoint capacity slippage is related (primarily) to SEI formation reactions. Therefore, these metrics can be used in addition to CE to quantify the performance of Li-ion cells. Additionally, the difference between the charge endpoint and discharge endpoint capacity movements per cycle gives the amount of capacity loss (fade) per cycle:

$$\text{Fade} = \Delta_D - \Delta_C \quad 2.3$$

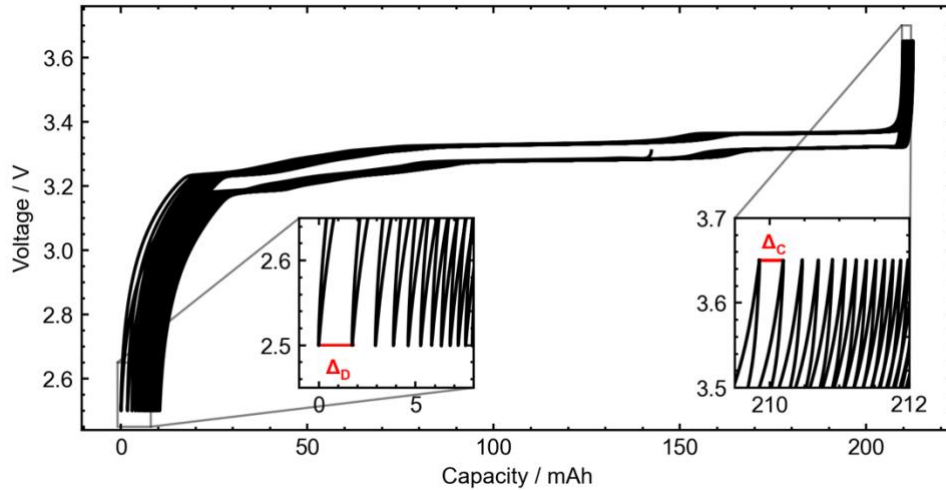


Figure 2.2: Voltage curves over several cycles for an LiFePO<sub>4</sub>/Graphite pouch cell. Charge- and discharge- endpoint capacity movement ( $\Delta Q_C$  and  $\Delta Q_D$ , respectively) are illustrated by zooming in at the endpoints of each cycle.

While this lithium inventory model simplifies the complex parasitic reactions that occur in a Li-ion cell, it is still very useful for broadly identifying different degradation modes in Li-ion cells. In the following sections, different types of parasitic reactions in Li-ion cells will be discussed in more detail. Additionally, not all capacity loss in a Li-ion cell is directly a result of parasitic chemical or electrochemical reactions. Cyclable lithium can also be lost by the fracturing and disconnection of active material particles from the electrode, commonly referred to as “active material loss”. As well, the growth of impedance in the

cell can lead to large polarizations which can reduce the amount of cyclable lithium under a given testing condition (temperature, voltage limits, cycle rate, etc.). These other modes of capacity loss will also be discussed briefly in the following sections.

## **2.2 PARASITIC REACTIONS**

### **2.2.1 Electrolyte reduction and SEI formation**

The solid electrolyte interphase (SEI) was introduced in CHAPTER 1. The existence of the SEI layer (primarily on the graphite electrode) passivates the electrode and hinders further electrolyte-electrode reactions, enabling Li-ion cells with long lifetimes. While the exact mechanisms for the formation of SEI components are complex and interrelated with various cell components<sup>81,86,87,89,100,125,126</sup>, the process of SEI formation can be simplified considerably in order to discuss this process in the context of Li inventory loss. Figure 2.3 shows a cartoon schematic of an exemplary SEI formation process. Electrolyte components, denoted S, are reduced at the negative electrode, which further react with lithium in the negative electrode to form SEI on the surface of the electrode. In this picture, S would primarily be film-forming solvents or additives such as EC, VC, or FEC, but these reactions can also involve linear carbonate EMC or DMC as well as salt anions. New SEI products are deposited on top of existing SEI.

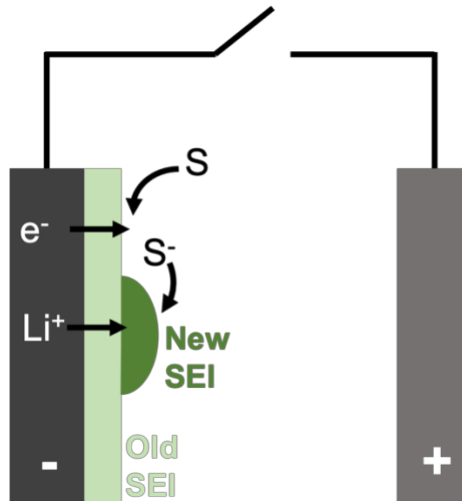


Figure 2.3: Schematic depicting the formation of SEI products on the negative electrode of a cell, reducing electrolyte components (S) and irreversibly consuming lithium. In this case the cell is in open circuit.

Most of the SEI is formed in the first cycle of a Li-ion cell. Figure 2.4 shows the first cycle of an LFP/graphite pouch cell, illustrating the capacity loss in this cycle, sometimes called the first cycle irreversible capacity. In this case, LFP has very little irreversible capacity on the first cycle, so all of the irreversible capacity in the full cell can be assumed to be due to SEI formation. The amount of lithium consumed in the first cycle SEI formation can vary depending on the choice of graphite and electrolyte additives<sup>53,127</sup>. In the case of the cell in Figure 2.4, close to 10% of initial Li in the cell was consumed in the formation cycle.

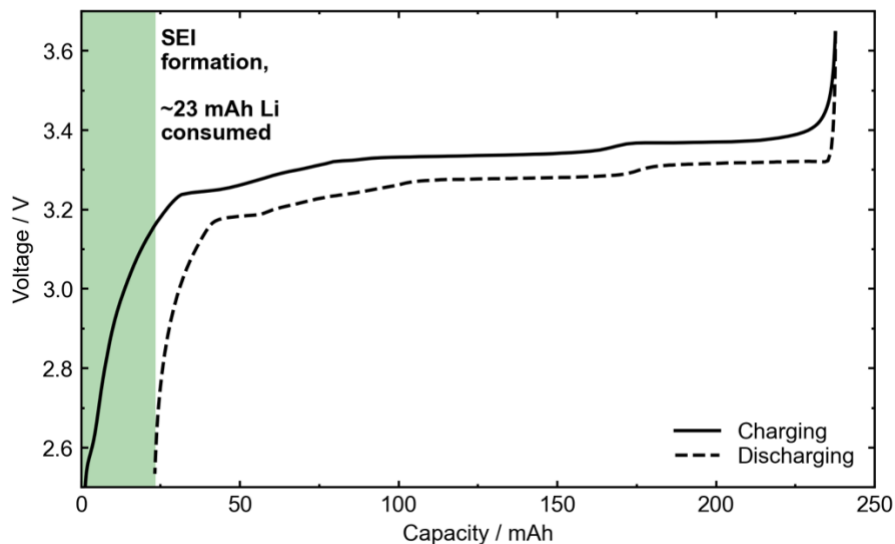


Figure 2.4: Voltage curve for the first full cycle of an LFP/graphite pouch cell, illustrating how much lithium is consumed in the initial formation of the graphite SEI layer.

While the largest fraction of SEI formation reactions are in the first cycle, SEI formation occurs continuously throughout the lifetime of a Li-ion cell at diminishing rates as the passivation of the graphite electrode improves, thus continuously removing cyclable lithium from the cell. One of the oldest and most popular models for SEI growth describes the diminishing SEI formation reactions at a  $t^{1/2}$  rate, where  $t$  is the operation time of a cell<sup>128–131</sup>. While maybe not strictly true for the growth of SEI<sup>132</sup>, this simple model serves as a good approximation for SEI growth and Li inventory loss. When electrolyte components are reduced at the negative electrode to form SEI, this lithium consumption causes the graphite voltage curve to “shift” along the capacity axis relative to the positive electrode voltage curve, lowering the accessible capacity. For this reason, capacity loss due to SEI formation is sometimes called “shift loss” in the literature.

The concepts of  $t^{1/2}$  SEI growth and shift loss is explored using a basic model in Figure 2.5. To simplify matters, the positive electrode (LFP in this case) is assumed to have zero irreversible capacity, and zero slippage during cycling (i.e. no parasitic reactions occurring at the electrode). The negative electrode is made to shift with a rate of

$$\frac{d \text{ shift}}{dt} = \frac{K}{t^{1/2}}, \quad 2.4$$

where  $t$  is the cycle time, and  $K$  is an arbitrary constant. The “cell” is cycled 25 times, with the negative electrode shift (due to SEI formation) adjusted each cycle. Figure 2.5a, b, c show the alignments of the voltage curves for key cycles: cycle 1, cycle 10, and cycle 25, respectively. The cycle number here is proportional to the cycle time, as long as every cycle is assumed to take the same amount of time. Notice the shift of the negative electrode along the capacity axis, and the corresponding “shrinking” of the full cell curve. When the negative electrode shifts, the positive electrode is pushed to a higher average state of charge, and can no longer be completely filled with lithium on discharge. Figure 2.5d shows the corresponding discharge capacity over the 25 cycles, with the key cycles where detailed voltage curves were shown highlighted in red. As cycling proceeds, the capacity loss per cycle diminishes as the rate of SEI growth on the negative electrode slows.



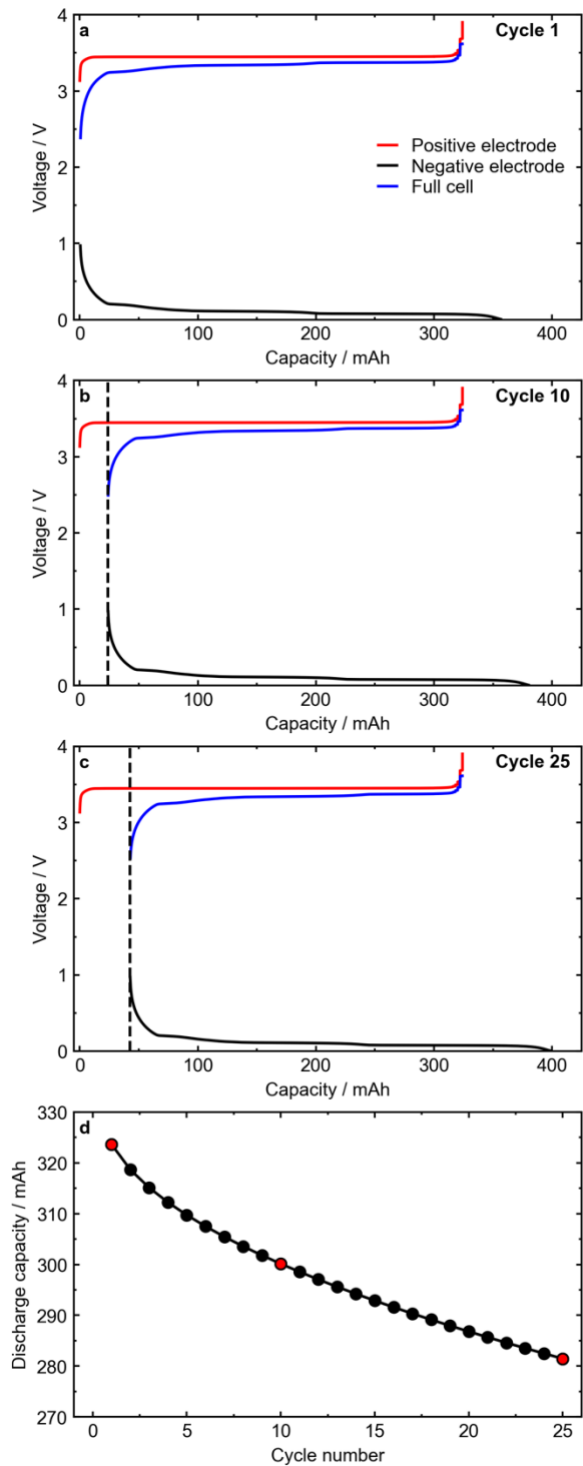


Figure 2.5: Example of a simple model of  $t^{1/2}$  SEI growth. Movement of the graphite voltage curve and corresponding full cell curve is shown for (a) cycle 1, (b) cycle 10, and (c) cycle 25. No shift of the positive electrode was assumed here. (d) Discharge capacity versus cycle number, with red points highlighting the cycles at which the voltage curves were detailed. Voltage and capacity units are arbitrary in this example.

This is obviously a significant simplification of a realistic Li-ion cell. It does not take into account any other modes of capacity fade in Li-ion cells. However, it serves as a good exercise to understand the implications of SEI growth on capacity loss and the relative alignment of the voltage curves. In cells where Li inventory loss is the dominant mode of capacity loss in a cell, the capacity versus cycle number (or cycle time) curve should look similar to what is presented in Figure 2.5d. Additionally, alignment of the voltage curves to determine shift loss can be done in real Li-ion cells, where the voltage curve of a full cell is compared to voltage curves of the individual materials measured in half-cells. This process is known as  $dV/dQ$  analysis, and is widely used in analyzing degradation in Li-ion batteries<sup>108,133–135</sup>.

It should also be noted that electrolyte reduction at the negative electrode does not exclusively form solid SEI products. In addition to SEI formed at the negative electrode from electrolyte reduction, soluble or gaseous species may also be generated<sup>88,90,136,137</sup>. These products may react further with other components of the electrolyte, SEI, or even migrate to the positive electrode and react, as will be discussed below.

### 2.2.2 Electrolyte Oxidation

As noted in CHAPTER 1, the various components of the electrolyte are typically not electrochemically stable in the voltage windows that Li-ion cells operate within. The major consequence of the reduction of electrolyte components on the negative electrode is the formation of the passivating SEI, as discussed above. Similarly, electrolyte species in the vicinity of the charged positive electrode may be oxidized. Figure 2.6 shows a schematic

of such an oxidation process, where species S could represent any component of the electrolyte. The schematic is shown with the cell in open circuit. In this case, a Li ion is intercalated into the positive electrode when species S is oxidized to maintain charge balance in the electrode. The oxidation product shown here is assumed to be soluble, but solid and gaseous products may also be formed via electrolyte oxidation<sup>64,85,126,138</sup>. Note that if the oxidation product in Figure 2.6 is neutral, and the cell is in open circuit, then a reduction reaction and corresponding deintercalation of Li is required at the negative electrode in order to maintain charge balance in the electrolyte. As may be expected, the rate of electrolyte oxidation reactions depends strongly on the operating voltage of the positive electrode material used<sup>138,139</sup>. This is in contrast to lithiated graphite, which maintains a fairly stable potential close to 0.1 V vs  $\text{Li}^0$ .

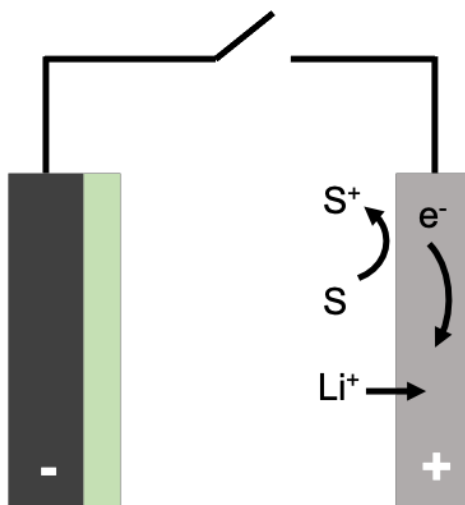


Figure 2.6: Schematic of electrolyte oxidation in a Li-ion cell. In open circuit, lithium is intercalated into the positive electrode to maintain charge balance.

In addition to the electrochemical oxidation of electrolyte components mentioned here, the electrolyte can also be oxidized by lattice oxygen released from charged positive electrode materials<sup>138,140</sup>. This *chemical* oxidation of electrolyte (primarily EC) primarily occurs in

layered NMC and NCA materials. The lattice oxygen in olivine LFP and related materials are strongly bound to the phosphorus atoms in the structure, and therefore oxygen release is less of a concern<sup>141</sup>, unless the material reaches very high temperatures well outside normal operating conditions ( $>200^{\circ}\text{C}$ )<sup>142,143</sup>.

### 2.2.3 Cross-talk and shuttle reactions

As mentioned above, not all products of electrolyte oxidation and reduction are solid precipitates on the electrode surfaces. Electrolyte reaction products can be gaseous or soluble in the electrolyte, and often can be highly reactive. This leads to the phenomenon known as “cross-talk”: species produced at one electrode that diffuse or migrate to the other electrode and react further. A schematic picture of a cross-talk reaction is given in Figure 2.7a. In this picture, an electrolyte species is reduced at the negative electrode, travels to the positive electrode and is oxidized, forming a solid product “P” (though again cross-talk products may not necessarily be solid). In this example, the cell is in open circuit mode, which forces lithium to deintercalate from the negative electrode and intercalate into the positive electrode, effectively self-discharging the cell. Note as well that in this example, the cross-talk species was initially generated at the negative electrode. The cross-talk species can also be generated at the positive electrode and react further at the negative electrode<sup>144-146</sup>.

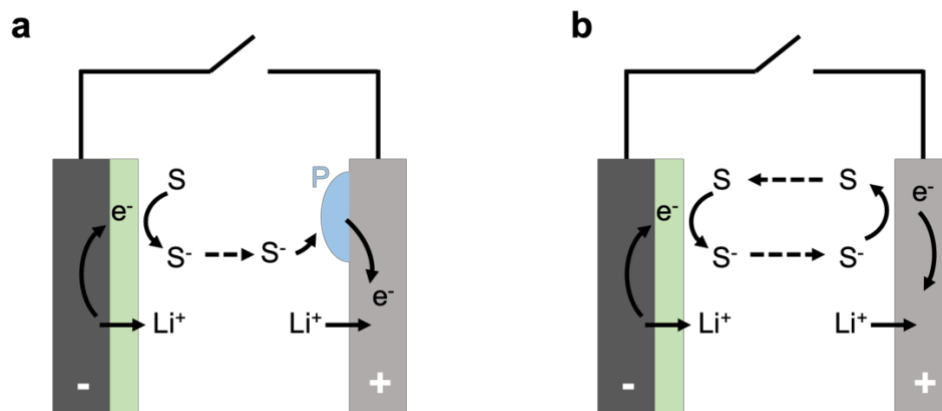


Figure 2.7: Schematics of related reaction mechanisms: (a) non-reversible cross-talk, and (b) reversible shuttle reactions. Both examples are shown in an open circuit configuration, but can also occur during charge and discharge. Note that the reaction products in these cartoons need not be charged for the schematics to still be valid.

A special case of a cross-talk reaction is what is known as a “shuttle” reaction. A schematic of a shuttle reaction is shown in Figure 2.7b. In this reaction, electrolyte species  $S$  is reduced at the negative electrode, moves to the positive electrode where it is oxidized, and the original molecule  $S$  is recovered. In a reversible shuttle process, the shuttle molecule can be oxidized and reduced indefinitely. Of course, like in the more general cross-talk reaction this process discharges the cell in open circuit conditions. However, a reversible shuttle would be much more detrimental since the reaction can continue in theory until the cell is fully discharged. In practice, redox shuttles are not fully reversible, and have finite “lifetimes” before they react to form irreversible products.

While in general the existence of redox shuttles are detrimental to Li-ion batteries, redox shuttles can sometimes be used intentionally in certain applications. Redox shuttles can be added to the electrolyte to prevent catastrophic cell failure in the case of cell

overcharge<sup>147,148</sup>. Additionally, the development of highly reversible redox shuttle molecules is a very active area of research in the field of redox flow batteries<sup>149,150</sup>. Cross-talk and shuttle reactions are particularly difficult to study because they involve and depend on all components of the cell: positive and negative electrodes, SEI composition, and electrolyte composition.

#### 2.2.4 Transition Metal Dissolution

The discussion of parasitic reactions has so far been mostly generic. One specific cross-talk mechanism that deserves special mention is transition metal dissolution and deposition. Under certain conditions, transition metals in layered oxide, olivine, and spinel materials can be dissolved from the surface of active particles into the electrolyte. Dissolved transition metals (TMs) can then diffuse to the negative electrode and react further. Figure 2.8 shows a simple schematic of the transition metal dissolution and deposition process (assuming an LFP positive electrode) in open circuit. While the total quantity of transition metals dissolved from the positive electrode is very small under practical conditions (typically representing < 1% of total positive electrode capacity), deposition of transition metals on the negative electrode is said to catalyze SEI formation reactions and consume lithium inventory<sup>151–153</sup>.

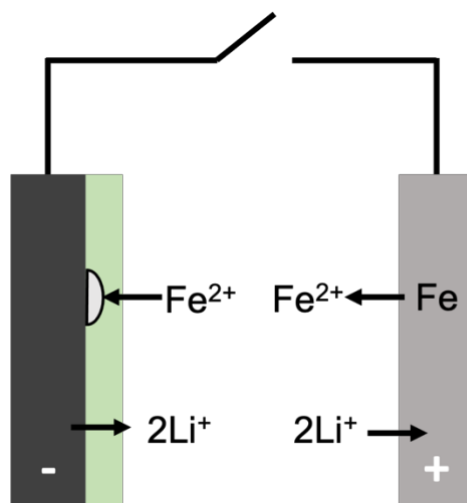


Figure 2.8: Schematic illustrating a cell in open circuit experiencing transition metal dissolution. Li is deintercalated from the negative electrode and intercalated into the positive electrode (self-discharge) to maintain charge neutrality.

There are a number of different proposed mechanisms for the dissolution of TMs from the positive electrode<sup>151</sup>. One of the commonly stated mechanisms for TM dissolution is via reaction of the positive electrode with acidic products that form in the electrolyte, specifically HF coming from  $\text{LiPF}_6$  decomposition<sup>151,154,155</sup>, though other mechanisms are proposed for the dissolution of TMs<sup>156</sup>. It has been shown that removing acidic contaminants from the electrolyte reduces TM dissolution in positive electrode materials<sup>157-159</sup>.

There is still debate about the nature of transition metals that have deposited on the negative electrode. It is generally accepted that TMs do not deposit on the graphite electrode in metallic form, but rather in higher oxidation states. It was shown convincingly by Jung et al. that in the case of NMC, Ni and Co are both incorporated into the SEI in the +2 oxidation state<sup>160</sup>. Sahore et al. showed similar results, also showing conclusively that dissolved Mn is also in the +2 oxidation state in solution<sup>156</sup>. Additionally, Jung et al. showed that

deposited TMs do not get further reduced to metallic form when deposited on a graphite electrode with an SEI layer<sup>160</sup>. Li et al showed that Fe dissolved from LFP was not deposited on either the surface of the SEI layer or the surface of the graphite itself, but rather was incorporated within the SEI layer<sup>161</sup>. Once incorporated into the SEI, deposited TMs facilitate the decomposition of the SEI, and further reactions with the electrolyte. It has been proposed that Mn deposited on a graphite electrode can undergo a catalytic cycle where it can be continuously oxidized and reduced, causing serious SEI decomposition<sup>162,163</sup>. Solchenbach et al. found that deposited Mn was more reactive than deposited Ni<sup>162</sup>.

The composition of the SEI also determines the impact of TMs in the electrolyte and the extent of TM deposition on the negative electrode. Several publications have shown reduced TM deposition when additives such as VC were used<sup>164</sup>. Previous studies from our group on transition metal dissolution in NMC/graphite cells have shown that when appropriate electrolyte additives are used, TM deposition can be virtually eliminated, even under strenuous cycling conditions such as high voltage and high temperature<sup>165,166</sup>.

### **2.3 IMPEDANCE GROWTH**

When a current is applied to a cell, the measured cell voltage deviates from the thermodynamic potential at a given state of charge. This is due to various contributions to impedance in a cell. All components of the cell contribute to the cell impedance: adhesion of active particles to the current collector, positive and negative SEI films and any other surface layers, electrolyte conductivity and lithium concentration gradients, surface area of



active materials, etc. When impedance is large, the associated voltage polarization can be large, causing the cell to reach its voltage limits much sooner than would be expected for the nominal capacity of the cell. While this does not necessarily mean Li is irreversibly consumed in the cell, it does affect the accessible Li at a given charge/discharge rate when the voltage limits of cycling are fixed. Figure 2.9 shows voltage versus capacity curves for LFP/Graphite cells with otherwise identical cell construction and electrolyte additives. The only differences are the cycling temperatures and charge/discharge rates. One cell (black) was cycled at 40°C and a rate of C/3 for charge and discharge (3 hours to charge the cell), and the other (red) was cycled at a rate of 20°C and a rate of 1C (1 hour to charge the cell). Notice that the measured cell voltage of the 20°C cycled cell is considerably higher on charge and lower on discharge than the 40°C cell. Notice as well that the 20°C cycled cell reached the upper voltage cutoff at a lower capacity than the cell cycled at 40°C. Some of this capacity can be recovered by doing a constant voltage (CV) step, showing that not all of this capacity loss is irreversible. If the 20°C cell did a full cycle at lower rate the majority of this capacity could be recovered.

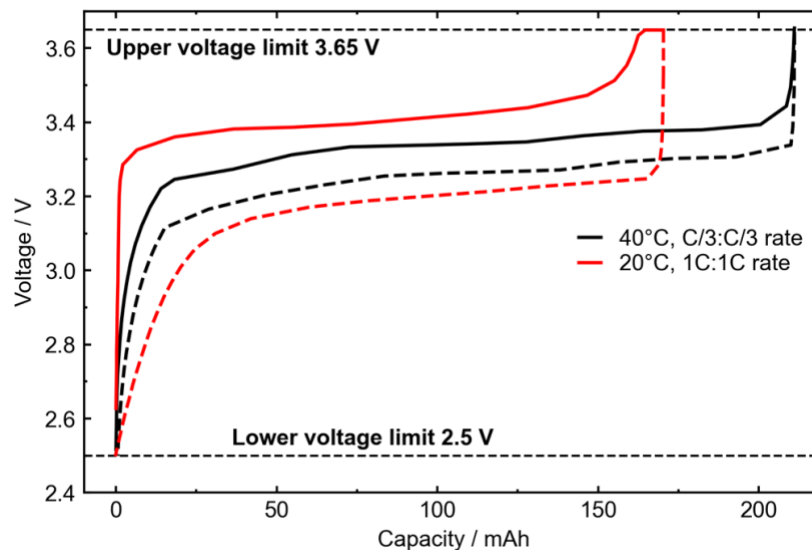


Figure 2.9: Demonstrating voltage polarization in an LFP/graphite pouch cell. Voltage versus capacity curves are shown for cells cycled at different temperature and rate conditions. These cells were nominally identical at the beginning of life.

Cycling temperature and rate play a significant role in the impedance and voltage polarization in the cell as it is cycled. Additionally, as the cell ages, continuous but diminishing reactions with the electrolyte thicken the SEI layer, which may increase the impedance contribution from Li migration through this layer<sup>167,168</sup>. This can lead to larger voltage polarization, decreasing the amount of accessible lithium for a constant voltage window. Other surface effects can also increase the interfacial resistance in a Li-ion cell; of particular note is a voltage-dependent surface reconstruction in layered transition metal oxides to form a rock-salt phase with low Li-ion diffusivity<sup>169–171</sup>. In electrochemical cycling experiments, the increase in cell impedance is monitored via the voltage polarization as described above and is quantified by taking the difference of the average charge voltage and the average discharge voltage in a given cycle,  $\Delta V$ . In a cell where capacity loss is dominated by impedance contributions, the loss of discharge capacity often mirrors the increase in  $\Delta V$ <sup>107,112</sup>.

## 2.4 ACTIVE MATERIAL LOSS

In order for lithium to cycle between the positive and negative electrode, active material must remain electrically connected to the current collector and/or to other active particle. The binder and conductive additives that are included as inactive materials in an electrode promote adhesion of active material particles, and promote electrical conductivity, respectively. However, the structure of an electrode evolves as a cell is cycled. This is primarily due to expansion/contraction of active materials as lithium is intercalated/deintercalated. However, other factors can influence the structural evolution of Li-ion battery electrodes, including degradation of the binder or conductive additive<sup>172-175</sup>, phase separation of active materials<sup>176,177</sup>, transition metal dissolution (mentioned above), or growth of SEI layers due to deposition of reaction products on particle surfaces<sup>178,179</sup>. As a result, active material can lose electrical contact with the electrode, becoming isolated from the electrode and removing Li storage capacity from the cell. Figure 2.10 shows a cartoon depicting how active material can be isolated from a positive active material primary particle (e.g. NMC). The volume of a particle goes down when lithium is removed. As the cell is cycled, this strain between regions with different states of charge can lead to the formation of fractures in the particles. Over time, these fractures can grow and spread, and eventually disconnect fractions of the particle entirely. Additionally when these microcracks form, electrolyte can permeate the new surface area, further reacting with the active material, amplifying the issues from parasitic reactions described above.

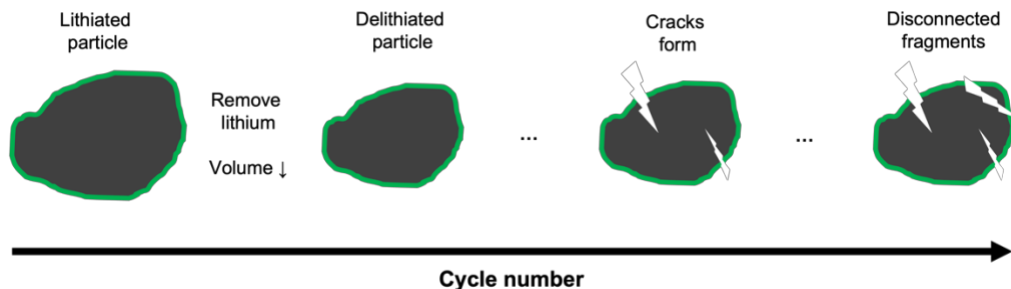


Figure 2.10: Cartoon schematic of active material loss in a positive active material particle. Structural evolution of the particle is depicted as a function of cycle number as a cell is cycled.

## 2.5 LITHIUM PLATING

One particularly unwelcome mode of lithium loss in a cell is metallic lithium deposition onto graphite electrodes during charge. Under normal conditions (reasonable rates, reasonable temperatures, cell is early in its life), when the cell is charged lithium is intercalated into the graphite host as has been described earlier (CHAPTER 1), where it is stored until the cell is discharged. However, in some circumstances lithium can be reduced onto the *surface* of the graphite particle instead of being intercalated. While the deposited Li metal can be stripped from the surface when the cell is discharged and reintercalated into the positive electrode, reversibly plating and stripping Li metal with high coulombic efficiency is notoriously difficult<sup>180</sup>, and frequently Li dendrites<sup>181</sup> and electrically disconnected Li metal can develop<sup>182</sup>. Additionally, Li metal is very reactive to typical alkyl carbonate electrodes, leading to a large amount of Li consumption to form SEI on the Li metal<sup>183</sup>.

Recall from CHAPTER 1 that as lithium is intercalated into graphite, the voltage of the graphite electrode versus  $\text{Li}^0$  goes down, and gets closer to 0 V. Particularly, the stage 2  $\rightarrow$  stage 1 plateau in the Li-graphite system is only at about  $\sim 80$  mV vs  $\text{Li}^0$ . If the voltage of

the graphite electrode drops below 0 V, it will become favorable to deposit Li metal on the graphite surface rather than intercalate into the graphite host. Under normal conditions and reasonable charge rates, the graphite can be fully lithiated to stage 1  $\text{LiC}_6$  without worry of Li plating occurring. However, in cases where cells are charged at low temperature or high rate<sup>60,184</sup>, or if the graphite SEI layer has high impedance<sup>185</sup>, or a combination of all these conditions, the graphite electrode will be polarized and the voltage will drop below 0 V, initiating Li plating.

Li plating during extremely fast charge or low temperature operation can cause catastrophic failure in the cell as the entire electrode may exhibit Li plating. However, Li plating effects in Li-ion cells can also be much more subtle. Localized effects such as current density variations, electrolyte dry-out, or even differences in cell stack pressure may cause Li plating to occur on a much smaller scale. This minor Li plating will not be as noticeable as the more catastrophic Li plating described above, but will still remove cyclable Lithium from the cell via uneven plating/stripping, and reactions with the electrolyte. Figure 2.11 shows two examples of Li plating on a graphite electrode ranging from minor (Figure 2.11a) to severe (Figure 2.11b).

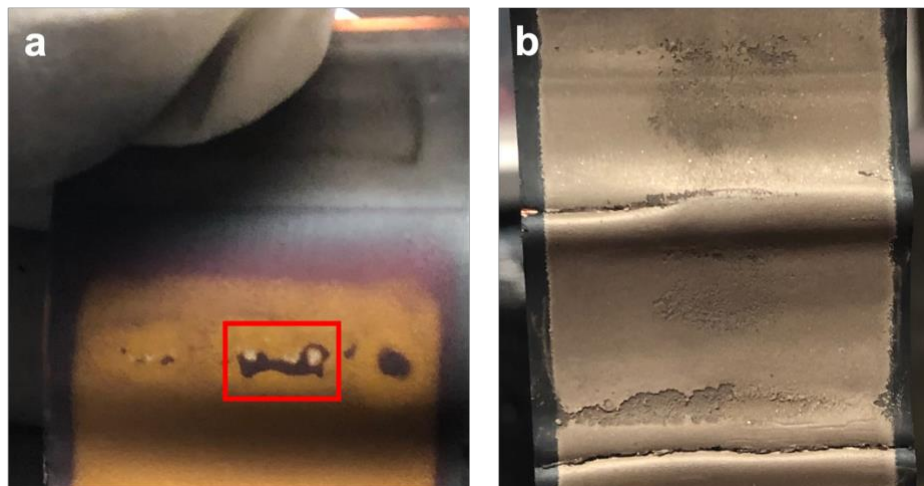


Figure 2.11: Examples of different degrees of severity of lithium metal deposition in Li-ion batteries. Images of disassembled charged graphite electrodes are shown for the case of minor Li plating (a) where specific spots along the electrode exhibit Li plating, and severe Li plating (b) where the entire surface of the electrode is covered by metallic lithium.

## 2.6 ISOTHERMAL MICROCALORIMETRY

In principle, the heat generated (or absorbed) from the various parasitic reactions in the cell can be measured with calorimetric techniques, and the lifetimes of cells can be ranked based on the magnitude of parasitic reactions that occur. However, in lab-scale Li-ion cells, the heat signatures from these reactions will be miniscule compared to other contributions to the heat flow as a cell is cycled. Therefore, high precision and highly stable calorimeters are required, and techniques are needed to remove other heat flow contributions and isolate the heat flow from parasitic reactions.

Isothermal calorimetry techniques were first applied to Li batteries in 1985, when Dahn et al. experimentally measured the entropy of a  $\text{Li}_x\text{Mo}_6\text{Se}_8$  compound as a function of Li occupation  $x$  (for  $x < 1$ ) in a calorimeter, finding good agreement with mean field theory

(MFT) calculations<sup>186</sup>. These measurements were later expanded to the same material for  $0 < x < 4$ <sup>187</sup>.

Later, other groups studied the calorimetry of different materials for Li-ion battery materials. Saito et al. measured the heat flow during charge and discharge for a commercial LiCoO<sub>2</sub> (LCO)/hard carbon commercial cell, broadly identifying the contributions from electrochemical polarization, (de)intercalation of the materials, and non-intercalation (parasitic) reactions<sup>188</sup>. Later work from the same group was able to identify staging transitions in lithiated graphite and structural changes in LCO in commercial LCO/graphite cells<sup>189</sup>. Similarly, Kobayashi et al. measured the heat flow during charge and discharge for commercial LiMn<sub>2</sub>O<sub>4</sub>/hard carbon and LCO/hard carbon cells, observing large irreversible heat flow in the LiMn<sub>2</sub>O<sub>4</sub> cell at elevated temperature (40°C) and high voltage (>3.9 V)<sup>190</sup>, indicating a large degree of unwanted parasitic reactions. Another work by Kobayashi et al. measured the separate heat flow contributions from LCO and graphite by measuring the heat flow of LCO/Li and graphite/Li coin cells<sup>191</sup>, in one of the first efforts to properly correlate full cell degradation to measurements of parasitic heat flow with calorimetry techniques.

Krause et al. successfully measured the parasitic energy in graphite/Li<sub>4</sub>Ti<sub>5</sub>O<sub>12</sub> (LTO) and graphite/Li coin cells, and were able to separate the different contributions to the heat flow (parasitic, polarization, entropic)<sup>192</sup>. Chevrier et al. used similar techniques to measure the parasitic energy in different Si-containing materials, finding high rates of parasitic reactions in Si materials with high surface areas<sup>193</sup>. Chevrier recently studied parasitic

reactions in metallurgical Si negative electrodes, finding the parasitic reaction rate in these materials depended on the charge/discharge rate<sup>194</sup>.

The methods of Krause and Chevrier were successful in detecting parasitic reactions during electrochemical cycling and ranking the performance of different materials, however these methods were not able to measure parasitic heat flows as a function of voltage. Downie developed methods to measure voltage-dependent parasitic heat flows in full Li-ion pouch cells and separate the different components of the heat flow. The heat flow from a Li-ion cell with an applied current can be derived from the first law of thermodynamics, making appropriate assumptions<sup>120,195</sup>. Downie and Dahn used the following equation for the heat flow from a cell<sup>196</sup>:

$$\dot{q} = |I\eta| + \frac{TI}{e} \left[ \left( \frac{ds_+}{dx} \right)_T - \left( \frac{ds_-}{dx} \right)_T \right] + \dot{q}_p, \quad 2.5$$

where  $\dot{q}$  is the measured heat flow (exothermic is positive  $\dot{q}$ ),  $I$  is the current,  $\eta$  is the overpotential (difference between measured cell voltage and equilibrium voltage),  $T$  is the temperature,  $e$  is the elementary charge,  $ds_{\pm}/dx$  is the derivative of entropy (per site) with respect to the Li occupancy  $x$  for the positive and negative electrodes, respectively, at constant temperature, and  $\dot{q}_p$  is the heat flow attributed to parasitic reactions. This equation captures the three main sources of heat in a cell: overpotential (polarization), entropy changes, and parasitic reactions. Downie represented the heat flow as a polynomial function of the state of charge of the cell<sup>196</sup>. The heat flow was measured at different currents, and the data was fit to the simplified model, extracting the parasitic heat flow as a function of voltage. Further work by Downie et al. added a time-dependent factor to the model, allowing the authors to study the time-evolution of the parasitic heat flow<sup>197</sup>. With



these methods, Downie was able to probe the impacts of electrolyte additives on parasitic heat flow in full Li-ion cells, and correlate those measurements to cell lifetimes, demonstrating the power of isothermal microcalorimetry to rank the performance of Li-ion cells over relatively short time-scales<sup>198</sup>.

Representing the heat flow as a polynomial function of the state of charge was effective, but not ideal. A more desirable method of extracting the parasitic heat flow would not require fitting to free parameters. Glazier et al. realized that the entropic heat flow from the (de)intercalation of the electrodes during charge and discharge should be fully reversible, assuming negligible structural changes in the materials over cycling<sup>195</sup>. Averaging the measured heat flow over a cycle between some voltage range eliminated the entropic heat flow contribution entirely:

$$\dot{q}_{\text{av}} = \frac{\dot{q}_{\text{chg}} + \dot{q}_{\text{dis}}}{2} = |I\eta| + \dot{q}_{p,\text{av}} \quad 2.6$$

The overpotential  $\eta$  was taken to be the deviation from the average voltage on a charge and discharge cycle. Subtracting the overpotential heat flow leaves only the parasitic heat flow, with no polynomial fitting required. The one drawback of this method was that low currents were required ( $\sim 1$  mA) to minimize the heat flow contributions from polarization and entropy. This “charge-discharge” method has been used successfully by Glazier et al. to study parasitic reactions in Li-ion cells with various positive electrode materials<sup>199</sup>, electrolyte additives<sup>200,201</sup>, solvents<sup>201</sup>, and different types of graphite in the negative electrode<sup>127</sup>.

These previously developed isothermal microcalorimetry techniques, especially the methods developed by Glazier<sup>195</sup>, will serve at the starting point for the calorimetry experiments used throughout this thesis. The charge-discharge technique will be used throughout CHAPTER 4 and CHAPTER 5 to investigate LFP/graphite cells with different electrolyte compositions and positive/negative electrode materials. CHAPTER 5 and CHAPTER 6 will investigate parasitic reactions occurring at one electrode only, which will be done for the first time with lab-scale pouch cells.

## CHAPTER 3 EXPERIMENTAL

### 3.1 POUCH CELLS

All pouch cells used in this thesis were 204035-sized pouch cells with nominal first charge capacities of approx. 240 mAh. Cells were constructed by LiFUN technologies (Zhuzhou, Hunan province, China). Specifications for all cells used in this thesis are given in Table 3.1 and Table 3.2. Figure 3.1 shows photographs of the type of wound pouch cells used in this work, including a tear-down of a cell to show the individual electrodes. All cells had either  $\text{LiFePO}_4$  (LFP) or NMC811 positive electrodes. Only one type of NMC811 was used: a so-called “bimodal” material consisting of large secondary particles composed of small primary particles (usually called “polycrystalline” in the battery field) as well as “single crystal” particles dispersed in the voids of the polycrystalline particles<sup>202</sup>. Four different types of LFP materials were used in this thesis: the differences between these samples will be considered in CHAPTER 5. All cells had artificial graphite (AG) negative electrodes. Three different types of AG were used in this thesis. The differences between the AG materials will be considered in CHAPTER 5 and CHAPTER 6. Dry pouch cells were received at Dalhousie University without electrolyte. Upon arrival, cells were opened in an Ar-filled glovebox, and heated under vacuum for 14 hours at different temperatures (100°C – 150°C depending on the experiment) to remove excess moisture.

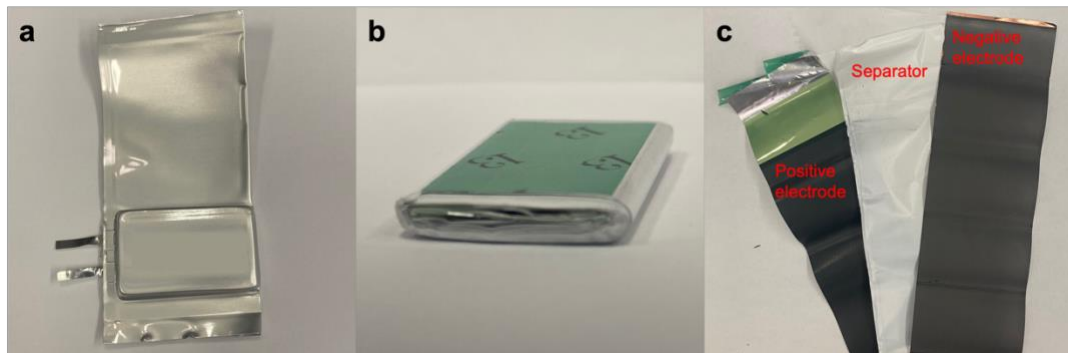


Figure 3.1: (a) Photograph of one of the the 204035-sized pouch cells used throughout this thesis. (b) Wound electrode stack known as the “jelly roll”. (c) Unwound electrodes and separator with the different components labelled.

Table 3.1: Specifications and compositions of the different Li-ion pouch cells used in this thesis.

Cell Name	LFP/AG-A	low BET LFP/AG-A	med BET LFP/AG-A	hi BET LFP/AG-A	med BET LFP/AG-B	med BET LFP/AG-C	NMC811 /AG-A	NMC811 /AG-B	NMC811 /AG-C
Balance voltage	3.65	3.65	3.65	3.65	3.65	3.65	4.4	4.4	4.4
Lower voltage	2.5	2.5	2.5	2.5	2.5	2.5	3.0	3.0	3.0
Upper voltage	3.65	3.65	3.65	3.65	3.65	3.65	4.06	4.06	4.06
positive active material	LFP	LFP	LFP	LFP	LFP	LFP	NMC 811	NMC 811	NMC 811
pos etd. coating	C	C	C	C	C	C	proprietary	proprietary	proprietary
pos etd. Conductive additive	SP:CNT (2:1)	CB	CB	CB	CB	CB	CB+KS6	CB+KS6	CB+KS6
pos etd. Binder	PVDF	PVDF	PVDF	PVDF	PVDF	PVDF	PVDF	PVDF	PVDF
pos etd. Composition	96.5:1.9:1.6	96:02:02	96:02:02	96:02:02	96:02:02	96:02:02	94:2:2:2	94:2:2:2	94:2:2:2
separator	PE	PP	PP	PP	PP	PP	PE	PE	PE
negative active material	AG-A	AG-A	AG-A	AG-A	AG-B	AG-C	AG-A	AG-B	AG-C
neg etd. Conductive additive	CB	CB	CB	CB	CB	CB	CB	CB	CB
neg etd. Binder	CMC:SBR	CMC:SBR	CMC:SBR	CMC:SBR	CMC:SBR	CMC:SBR	CMC:SBR	CMC:SBR	CMC:SBR
neg etd. Composition	96:01:03	96:01:03	96:01:03	96:01:03	96:01:03	96:01:03	96:01:03	96:01:03	96:01:03
N/P @ max V	1.15	1.15	1.15	1.15	1.15	1.1	1.1	1.1	1.1

Table 3.2: Properties of electrodes obtained from Li-ion pouch cells used in this thesis.

Cell type	electrode	Density (g/cc)	Coating thickness ( $\mu\text{m}$ )	Loading ( $\text{mg}/\text{cm}^2$ )	current collector	CC thickness ( $\mu\text{m}$ )	Etd. Area ( $\text{cm}^2$ )	total active mass (mg)
LFP/AG-A	Positive	2.45	57	12.4	C-Al	13	131.8	1633
	Negative	1.55	43	6.2	Cu	8	149.2	921
low BET LFP/AG-A	Positive	2.43	55	13.4	C-Al	18	124.8	1672
	Negative	1.42	47	6.7	Cu	8	142.2	958
med BET LFP/AG-A	Positive	2.31	54	12.5	C-Al	16	123.8	1547
	Negative	1.5	47	6.9	Cu	8	140.8	972
hi BET LFP/AG-A	Positive	2.02	59	11.9	C-Al	16	123.8	1473
	Negative	1.42	45	6.4	Cu	8	142	909
med BET LFP/AG-B	Positive	2.29	79	18	C-Al	15	85	1529
	Negative	1.45	65	9.4	Cu	8	99.4	933
med BET LFP/AG-C	Positive	2.31	79	18.2	C-Al	16	84.5	1536
	Negative	1.41	66	9.4	Cu	8	99.4	932
NMC811 /AG-A	Positive	3.26	66	21.5	Al	13	55.8	1200
	Negative	1.36	111	15.1	Cu	9	66.6	1004
NMC811 /AG-B	Positive	3.37	62	20.9	Al	21	51.5	1075
	Negative	1.42	104	14.8	Cu	8	65.5	972
NMC811 /AG-C	Positive	3.28	64	21	Al	21	52.3	1095
	Negative	1.39	106	14.7	Cu	10	64.4	949

### 3.2 ELECTROLYTE MATERIALS

All electrolyte materials were mixed and used as received. Electrolyte solutions were mixed in an Ar-filled glovebox. The solvent blend for used for all electrolytes was ethylene carbonate (EC)/dimethyl carbonate (DMC) 3/7. All electrolytes had a total Li salt concentration of 1.5 M. Throughout this thesis, references to Control (or CTRL) electrolyte refers to an electrolyte consisting solely of EC:DMC and 1.5 M Li salt (regardless of which salts used), with no additional electrolyte additives. When electrolyte additives were used, the electrolyte is typically referred to simply by the electrolyte additives used. For example, if 2% vinylene carbonate (VC) by weight is added to the base Control electrolyte, the electrolyte will be referred to as “2VC” electrolyte. This nomenclature is used throughout this thesis. A list of all electrolyte materials used in this thesis is given in Table 3.3. All electrolyte chemicals used in this thesis were high purity (>98%) with low water content (<20 ppm).

Table 3.3: List of chemicals used for electrolyte preparation in this thesis.

Name	Abbreviation	Supplier
ethylene carbonate:dimethyl carbonate 3:7 (w:w)	EC:DMC 3:7	Shenzhen Capchem
dimethyl carbonate	DMC	Shenzhen Capchem
methyl acetate	MA	Shenzhen Capchem
lithium hexafluorophosphate	LiPF <sub>6</sub>	BASF
lithium bis(fluorosulfonyl)imide	LiFSI	Shenzhen Capchem
vinylene carbonate	VC	BASF
fluoroethylene carbonate	FEC	BASF
ethylene sulfite	DTD	Shenzhen Capchem
lithium difluorophosphate	LiPO <sub>2</sub> F <sub>2</sub>	Shenzhen Capchem

### **3.3 POUCH CELL FILLING AND FORMATION**

After vacuum drying, cells were filled with electrolyte (1.0 mL, ~1.2 g for LFP cells, 0.85 mL, ~1.0 g for NMC cells), and sealed under -90 kPa gauge pressure in a vacuum sealer (MSK-115A, MTI corp.). After the pouch cells were filled, they were charged to 1.5 V and held at that voltage at room temperature for approximately 16 hours to allow electrolyte to permeate the pores of the electrodes and separator without corroding the Cu current collector. After this “wetting” step, cells were moved to a Maccor 4000 series charger to complete their first “formation” cycle. Cells underwent the following protocol: Charge at C/20 rate to upper voltage, hold at upper voltage for 1 hr, discharge at C/20 rate to lower voltage, charge at C/20 rate to ~60% state-of-charge (SOC). For LFP cell, this final charge to 60% SOC was done using a constant current charge for a set amount of time with an assumed second-cycle capacity of 220 mAh. For NMC cells, they were simply charged to 3.8V. After the formation cycle, cells were moved back to an Ar-filled glovebox, cut open to remove gases formed in the first cycle, and re-sealed. Regardless of experiment in this thesis, cells were always formed at 40°C.

### **3.4 CYCLING AND STORAGE PROTOCOLS**

#### **3.4.1 Long-term Cycling**

Long-term cycling experiments were carried out at various temperatures on Neware cyclers (Shenzhen, China). In this thesis, “long-term cycling” refers to simple electrochemical cycling experiments where cells are charged at constant current to a set upper cell voltage and the discharged at a constant current to a set lower cell voltage. In most cases, unless otherwise specified, cells were cycled at a rate of C/3 for both charge and discharge. Cells



were cycled in constant-current constant-voltage (CCCV) mode for charge, meaning a constant current ( $C/3$ ) up to the cutoff voltage followed by a constant voltage step. The current cutoff for the constant voltage step was  $C/20$ . Cells were cycled in CC mode on discharge. For cells cycled at  $C/3$ , a “checkup” cycle at  $C/20$  was done every 50 cycles to minimize cell impedance effects and monitor low-rate capacity retention. For cycling tests at  $40^{\circ}\text{C}$ , nominally identical pair cells were made for each testing condition for each electrolyte. Pair cells were not made for  $55^{\circ}\text{C}$  cycling due to limited cycler channels at  $55^{\circ}\text{C}$ .

### 3.4.2 Ultra-High Precision Coulometry (UHPC)

Some cells in this thesis were cycled on the Ultra-high precision coulometry (UHPC) system at Dalhousie University<sup>203,204</sup>. The cycler systems used for long-term cycling experiments, while relatively inexpensive per channel, do not possess the precision or accuracy required to reliably measure and compare the coulombic efficiency (CE) of cells with long lifetimes (i.e.  $\text{CE} > 0.998$ ), among other quantities discussed in CHAPTER 2. The UHPC charger system was designed to be able to detect minute differences between highly “stable” cells with high CE values, utilizing charger equipment with exceptional voltage and current precision, as well as excellent temperature control of both the cells being tested and the charger equipment<sup>204</sup>. The UHPC system has been successfully used to rank the projected lifetimes of cells subject to different cycling conditions, electrolyte additives, electrode coatings, active materials, etc. in significantly shorter times compared to conventional long-term cycling experiments. In this system, cell voltage is measured by a Keithley 2000 digital multimeter, current is supplied by a Keithley 220 current source,

and the supplied current is measured using a second Keithley 2000 multimeter across a precision resistor (Texas Components Corp.)<sup>204</sup>. This system was custom-made at Dalhousie University, and has been shown to measure CE in cells to a precision below 10 ppm and an accuracy of  $\sim 40$  ppm<sup>204</sup>. In some cases, cells in this thesis were cycled on Novonix UHPC systems. These systems are also designed to precision and accuracy levels of  $<10$  ppm and  $<50$  ppm, respectively<sup>205</sup>. Measurements on these two systems are taken to be equivalent in the results that are presented throughout this thesis.

Cells that cycled on the UHPC system first underwent the typical formation cycle described above, followed by de-gassing and EIS measurements. Cells were then cycled at  $40.0^{\circ}\text{C} \pm 0.1^{\circ}\text{C}$  at a rate of  $C/20$  for both charge and discharge between the lower and upper voltages depending on cell type. Cells were cycled for at least 14 cycles in all cases; up to 20 cycles is ideal, but in some cases unplanned power failures interrupted cycling. In these cases, cells did not resume cycling due to the highly time-dependent nature of CE measurements<sup>206</sup>. Nominally identical pair cells were made for each test condition.

### 3.4.3 OCV Storage

Sinha et al. developed a “smart” method for carrying out open circuit storage experiments, allowing reversible and irreversible capacity losses during storage to be differentiated<sup>207</sup>. Reversible capacity losses are characterized as capacity loss that does not consume lithium inventory. Examples of reactions that lead to reversible capacity loss are electrolyte oxidation reactions (See Chapter 2) and redox shuttle reactions. When these reactions occur in open circuit, lithium is forced to move between electrodes to maintain charge neutrality,

causing self-discharge of the cell. If a current is applied to the cell and it is charged, all of this lithium can be recovered. Irreversible capacity loss, on the other hand, cannot be recovered. The most common example of irreversible capacity loss is SEI formation, where Li is consumed and incorporated into the SEI layer, where it can no longer be shuttled between the electrodes to store energy. This capacity cannot be regained by recharging the cell.

An example of the smart storage protocol is given in Figure 3.2. Before storage, the initial discharge capacity of the cell is determined, defined  $D_0$ . The cell is then charged to the upper cutoff voltage and held at the top of charge to reach equilibrium. Then, the cell is put into open circuit mode for a set amount of time. During the OCV period, the cell voltage is measured periodically. At the end of the open circuit period, the cell is *immediately* discharged. This capacity is defined  $D_1$ . The difference between the initial capacity and this discharge capacity immediately after storage,  $D_0 - D_1$ , is the *total* amount of capacity loss during the storage period. The cell is then charged to the upper cutoff voltage, and discharged again. This second discharge is defined as  $D_2$ . The difference between the initial capacity and the second discharge,  $D_0 - D_2$  gives the amount of irreversible capacity loss over the storage period, since the reversible capacity loss is recovered in the previous charge half-cycle. Therefore, the reversible capacity loss over the storage period is  $D_2 - D_1$ .

In this thesis, smart storage experiments were carried out at  $60.0 \pm 0.1^\circ\text{C}$  using a custom-built high-precision charger. After formation, cells were cycled two times between 2.5 V

and 3.65 V at a rate of C/10, before being charged to 3.65 V and held at 3.65 V for 10 hr. Then, cells were put into open circuit for 500 hours, measuring the cell voltage every 6 hr. After the 500 hr OCV period, cells were discharged to 2.5 V, charged to 3.65 V, and discharged once again to 2.5 V all at C/10 rate to extract the reversible and irreversible discharge capacity.

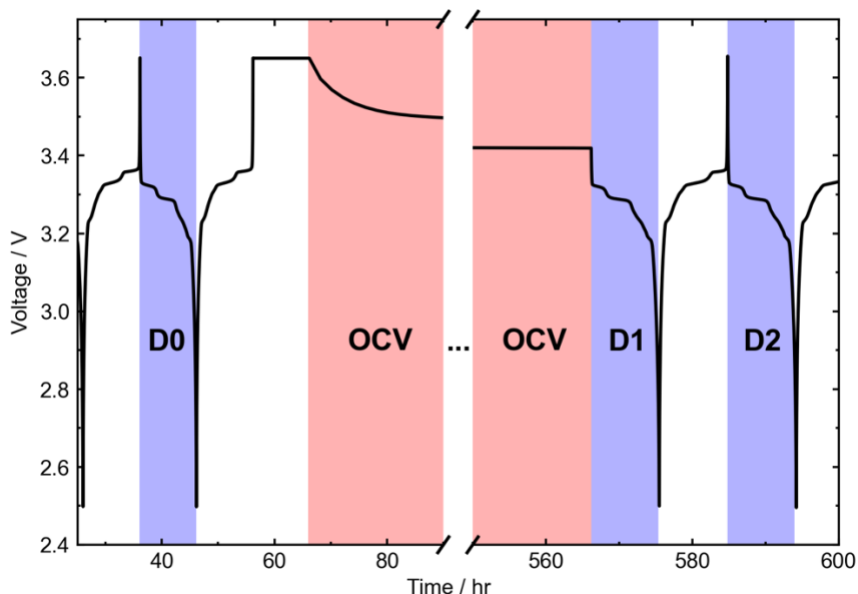


Figure 3.2: Example of the “smart” storage protocol for an LFP/graphite pouch cell. Key discharge cycles are labelled as well as the OCV storage period. These tests are typically completed at high temperature to accelerate the rate of parasitic reactions, e.g. 60°C.

### 3.5 WATER CONTENT MEASUREMENTS

Water contents in pouch cell electrodes were measured with Karl Fischer (KF) coulometric titration. The eponymous technique was first developed in 1935<sup>208</sup>, and can be done either volumetrically or coulometrically. The coulometric method will be described briefly here.

A schematic of the KF coulometric titrator is shown in Figure 3.3. The titrator consists of a beaker containing analyte solution, a “generating electrode” consisting of a cathode and anode separated by a diaphragm, and a “detector” electrode. The cathode chamber is filled with a catholyte solution. In this setup the same solution is used for both the catholyte and analyte. The detector electrodes monitor for the endpoint of the reaction between water and the iodine in the analyte.

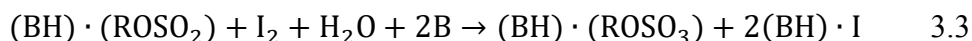
The analyte consists of several components: An alcohol (ROH), a base (typically imidazole, denoted B), iodide, and SO<sub>2</sub>. First, iodine is electrochemically generated at the generator electrode<sup>209,210</sup>:



The SO<sub>2</sub> initially reacts with the alcohol and is neutralized by the base:



Then, any water introduced to the solution reacts with the iodine and the sulfite,



reducing the iodine, oxidizing the sulfite to sulfate, and eliminating the water. The exact amount of water in the sample can be quantified by counting the number of moles of electrons liberated in the reaction of I<sup>-</sup> to I<sub>2</sub>. 2 moles of electrons are evolved in this reaction, and one mole of I<sub>2</sub> is consumed in the reaction with water. Therefore, 2 moles of electrons are evolved for every one mole of water, so by counting the total charge passed through the generator electrode circuit, the amount of water in the sample can be determined.

This thesis will be concerned with determining the water contents from electrodes extracted from Li-ion pouch cells. To do this, samples are heated in an external oven with a constant flow of dry nitrogen gas from the sample to the KF reaction beaker. As the sample heats up, the adsorbed water is evolved and carried to the beaker where it can react.

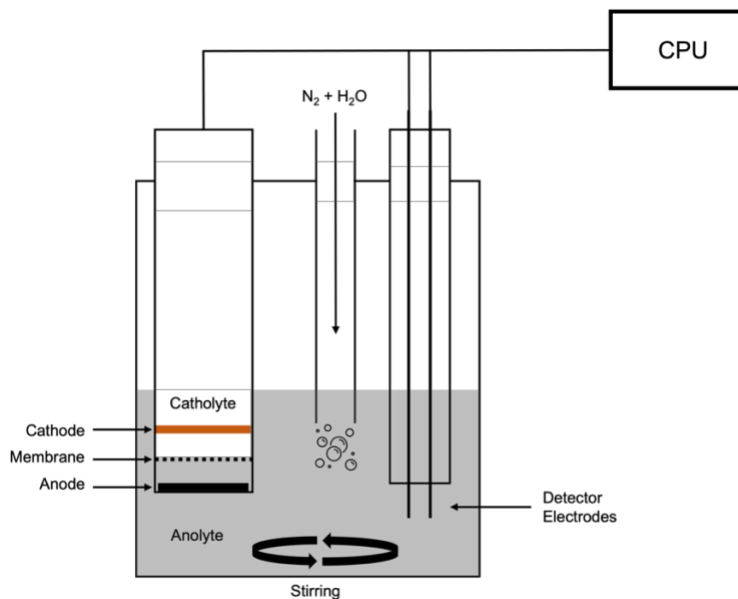


Figure 3.3: Schematic of a Karl Fischer (KF) coulometric titration setup. Evaporated water from a heated sample is bubbled through the anolyte, where it reacts with iodine produced at the generating electrode.

The KF titrator used for the measurements in this thesis was a Mettler Toledo C30 equipped with an external drying oven (Mettler Toledo DO308). Samples were extracted from pouch cells in an Ar-filled glovebox after various vacuum drying conditions. Between 0.5 g and 0.9 g of sample was used per test (active material + carbon coating + conductive additive + binder + carbon-coated current collector). The external drying oven was set to 200°C, and each sample was run for 30 minutes. A blank sample was run periodically to determine the amount of moisture in the atmosphere that was transferred during sample loading.

### 3.6 EX-SITU GAS MEASUREMENTS

The volume of gas produced in pouch cells after formation at 40°C, and in pouch bags during aging was measured using Archimedes principle. Cells or pouch bags were hung on a hook attached to the bottom of a balance (Shimadzu AUW200D) and suspended in a beaker of deionized water (~18 MΩ) at room temperature. For pouch cells, the weight of the suspended cell was measured before and after the formation cycle. The change in volume,  $\Delta v$ , of the cell due to gas evolution is related to the change in measured weight,  $\Delta w$ , by:

$$\Delta v = -\frac{\Delta w}{\rho g}, \quad 3.4$$

where  $\rho$  is the density of deionized water and  $g$  is the acceleration due to gravity.

For pouch bags, the suspended weight of the pouch bag was measured directly after they were constructed. Suspended weight was then measured periodically, and when compared to the initial weight gives the total amount of gas evolved at the time of each measurement. In some cases, the gas volume of pouch cells was measured at various stages of life. In this case, the initial suspended weight was taken after the cell was de-gassed after formation.

### 3.7 ELECTROCHEMICAL IMPEDANCE SPECTROSCOPY (EIS)

Electrochemical impedance spectroscopy (EIS) is a widely used technique to study the various contributors to internal impedance in Li-ion cells. This information is valuable for understanding how certain testing conditions impact a cell's rate capability, mechanical

integrity (e.g. catastrophic events such as current collector dissolution), SEI properties and growth, etc. EIS is a non-destructive technique, allowing for cells to be monitored at various points during their lifetimes, or even in-situ during cycling without requiring the cell to be deconstructed.

The general EIS technique involves applying a small (on the order of mV in amplitude) sinusoidal voltage to a cell, and measuring the resulting current response. This is repeated for different frequency voltage pulses, allowing the determination of the frequency dependent impedance  $Z(\omega)$ :

$$Z(\omega) = \frac{V(\omega)}{I(\omega)} \quad 3.5$$

The impedance  $Z$  is a complex number that contains information about the impedance of the cell. For a full Li-ion cell containing many different components, this resulting impedance spectrum is a complicated combination of different contributions, including contact resistances, charge-transfer resistances at the electrode/electrolyte interface, migration resistance of Li traveling through the SEI, resistance of Li-ion transport within the SEI, as well as other capacitive and inductive effects. To simplify and physically interpret impedance spectra of Li-ion cells, equivalent circuit models are employed to represent the various components of the cell that contribute to the cell impedance. Each passive component of an electrical circuit has an associated voltage-current relation. For example, for a resistor, it is simply Ohm's law, giving a real impedance independent of the frequency of voltage oscillation:



$$Z_R = \frac{V}{I} = R \quad 3.6$$

Capacitor elements have purely imaginary impedance relations that do depend on the frequency:

$$Z_C = -i \frac{1}{\omega C}, \quad 3.7$$

where  $C$  is the capacitance.

The most simple impedance model for interphases in Li-ion batteries is a parallel RC circuit. In this model, the resistor represents charge transfer through the interphase, and the capacitor represents capacitive charging at the interface with the electrolyte. A second resistor is often connected in series to represent the solution resistance in the electrolyte. The circuit diagram is shown in the inset in Figure 3.4. The impedance for this element is a complex number. When this impedance is shown in a so-called “Nyquist plot”, plotting the imaginary component of the impedance versus the real component, it forms a semi-circle, shifted along the real axis by the value of the solution resistance. An example Nyquist plot for this simple circuit is shown in Figure 3.4. The width of the semi-circle along the real axis is the resistance of the resistor in the element, and is frequently referred to as the “charge-transfer” resistance. This charge-transfer resistance is often crudely interpreted as the total resistance a lithium ion encounters as it de-solvates at the electrode surface, migrates through the SEI, and intercalates into the active material, therefore providing some information about all of these cell components. Indeed, the charge-transfer

resistance does correlate to the rate capability of Li-ion cells in many cases<sup>185,211</sup>. It should be stressed, however, that while valuable, this circuit model is very primitive, and much research effort has been spent in developing more realistic equivalent circuit models for Li-ion batteries<sup>212,213</sup>. Detailed discussion of the interpretations of EIS spectra is beyond the scope of this thesis.

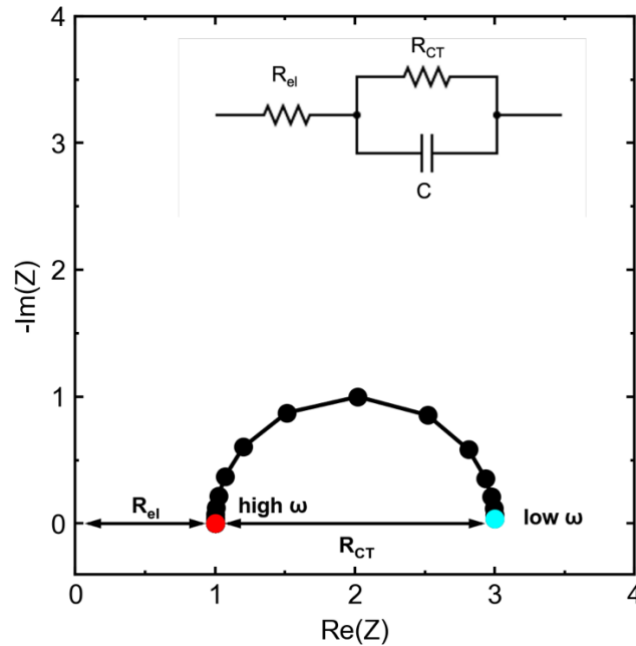


Figure 3.4: Simple model of impedance in a Li-ion cell. The equivalent circuit consists of two components, a resistor and a parallel resistor/capacitor element (arbitrary resistance and capacitance values). Corresponding Nyquist plot for this circuit model is shown, going from low frequency (blue point) to high frequency (red point) measurements.

### 3.8 MICRO X-RAY FLUORESCENCE SPECTROSCOPY ( $\mu$ -XRF)

Fluorescence refers to the process in which an atom (or molecule), which is in an excited state as the result of bombardment by high energy particles such as electrons or photons, returns to its ground state accompanied by the emission of a photon. Typically, X-rays are used to induce fluorescence in materials. The energy of the photon that is emitted is dependent on the electronic structure of the atom undergoing fluorescence. Therefore, by

analyzing the spectrum of photon energies in a fluorescence experiment, the abundance of a given element in a sample can be determined.

For each element, there are a number of characteristic emissions, depending on the specific energy transitions that occur when the atom is excited. For example, if an electron is ejected from the lowest energy level of an atom (the “K” shell,  $n = 1$ ), a number of electrons at higher energy levels may transition to take the place of the ejected electron. Depending on the energy level of these electrons, the emitted photon will have slightly different energies. Electrons that transition from the 2p energy level to the  $n=1$  energy level emit what is known as K- $\alpha$  radiation. Electrons transitioning from the 3p energy level to  $n=1$  emit K- $\beta$  radiation, and so on. These characteristic emission lines are detected in an X-ray fluorescence experiment.

In this thesis, XRF was used to detect deposited transition metals (specifically Fe) on the graphite negative electrode after cells were aged under various conditions. The XRF machine used for this work had a very small spot size (25 $\mu\text{m}$ ), allowing for graphite electrodes to be scanned, and localized features to be resolved. Scanning  $\mu\text{XRF}$  measurements presented in this study were completed by Ahmed Eldesoky (Dalhousie University) either at the University of New Brunswick in Fredericton, New Brunswick, Canada or at Saint Mary’s University in Halifax, Canada. The  $\mu\text{XRF}$  systems used in both locations were functionally identical. The experimental details are outlined in Eldesoky et al. and Thompson et al.<sup>165,166,214</sup> and will be summarized here.

The XRF system used for these experiments was a Bruker M4 Tornado  $\mu$ XRF. The X-ray source was a Rh X-ray tube, using a 200  $\mu$ A current up to 50 keV. Scanning was done with a 25  $\mu$ m spot size at a rate of 4.00 mm/s. Background Fe was determined by scanning a fresh (no electrolyte) graphite electrode extracted from a pouch cell, and subtracted from subsequent measurements.

The XRF system was calibrated to correlate Fe X-ray counts to Fe loading ( $\text{g}/\text{cm}^2$ ) on the electrode. This was done by sputtering a linear gradient of Fe onto a fresh graphite electrode (Corona Vacuum Coaters V-3T sputtering system). Concurrently, Al disks of known area and mass were placed on the sputtering table across from the graphite electrode. After sputtering, the Al disks were weighed to determine the mass of sputtered Fe at a given position. Then, this was used to correlate to the Fe counts measured on the graphite electrode at the same positions.

### **3.9 SCANNING ELECTRON MICROSCOPY (SEM)**

Cross-sectional SEM micrographs were taken on LFP electrodes extracted from pouch cells. All cells were disassembled in an Ar-filled glovebox. Small pieces of the electrode were extracted (~1 cm width) and washed with DMC. The electrode pieces were then ion-milled with a JEOL IB-19530CP cross-section polisher, using an Ar-ion beam for a 50 min, 6 kV coarse step followed by a 5 min, 6 kV fine step. SEM images were recorded with a Hitachi S-4700 field emission electron microscope equipped with a secondary electron detector. Images were recorded at an accelerating voltage of 5 kV and a current of 15  $\mu$ A. Ion milling and SEM microscopy measurements were completed by Yulong Liu at

Dalhousie University. Fresh electrodes (before filling with electrolyte) were extracted in the discharged state, while aged electrodes were in the fully charged state (3.65 V).

### **3.10 POUCH BAG CONSTRUCTION**

Construction of separated electrode “pouch bags” followed the procedure outlined in previous publications by Ellis et al. and Xiong et al.<sup>144,145,215</sup> Briefly, the process will be described here. After the formation cycle above, instead of the de-gassing procedure, cells were charged to top-of-charge (3.65 V), and held at that voltage for approximately 36 hr. Then, cells were transferred to an Ar-filled glovebox, opened, and disassembled to separate the positive and negative electrodes. The separate electrodes were then manually wound, and then inserted into laminate foil bags. 0.1 mL of DMC was added to each pouch bag to account for solvent evaporation during this process. It is assumed that minimal Li salt or EC is lost in this process, and only the volatile DMC is evaporated during pouch bag assembly. Pouch bags were then sealed under vacuum (-90 kPa). This process is detailed pictorially in Figure 3.5. After sealing, pouch bags were stored at various temperatures. Volumes of gas evolved were measured periodically using the ex-situ volume measurement technique, described above. In some cases, isothermal microcalorimetry experiments were done on pouch bags, which are explained in detail below.

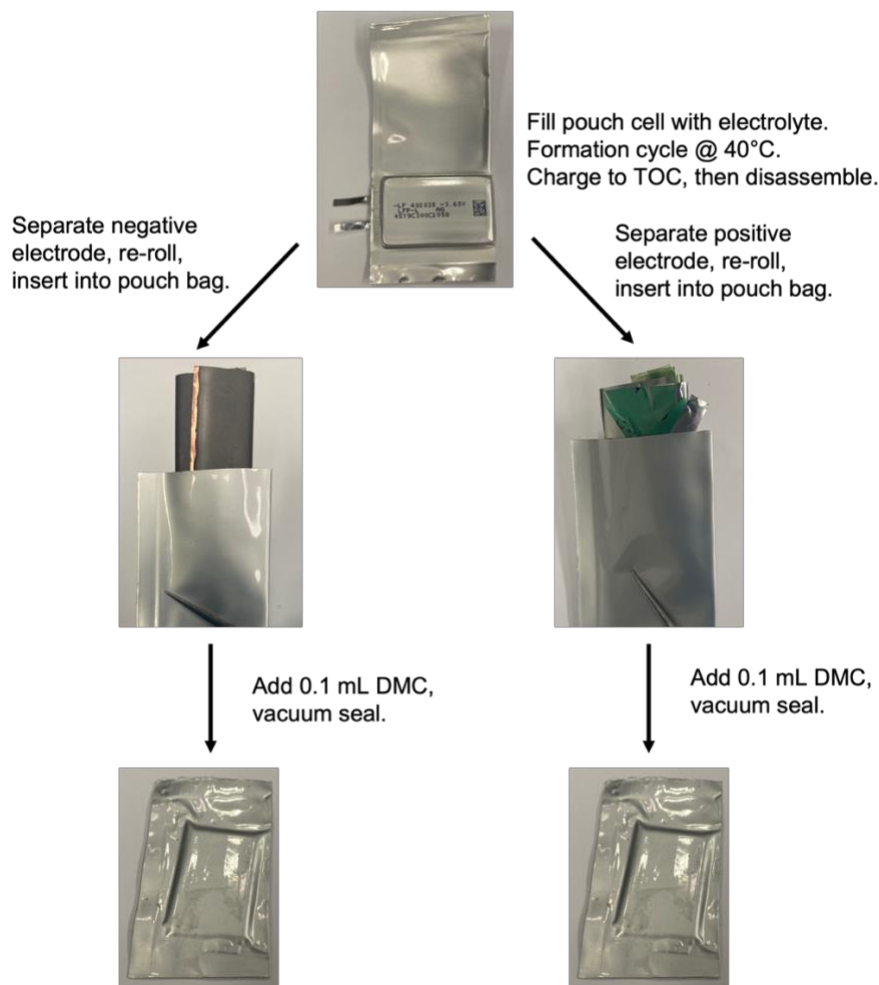


Figure 3.5: Flow chart outlining how separated electrode pouch bags are constructed from full pouch cells.

### 3.11 ISOTHERMAL MICROCALORIMETRY

Isothermal microcalorimetry (IMC) measurements in this thesis were completed using a TAM III microcalorimeter (TA instruments, temperature stability  $\pm 0.0001^\circ\text{C}$ , accuracy  $\pm 1 \mu\text{W}$ , precision  $\pm 1 \text{ nW}$ ), modified to allow for in-situ cycling of electrochemical cells<sup>121</sup>. All experiments were completed at  $40.0000^\circ\text{C}$ . Extensive background for the measurements and setup of Li-ion IMC experiments have been reported in the doctoral theses of Stephen Glazier and Laura Downie<sup>119,120</sup>, as well as in the peer-reviewed literature<sup>121</sup>. Here, these extensive reports will be summarized.

### 3.11.1 Measurement principles

A simple schematic of a single calorimeter channel is shown in Figure 3.6. The TAM III microcalorimeter operates on a twin system, meaning each channel has both a sample chamber and reference chamber. The existence of a reference allows for the subtraction of contributions to the heat flow from the surrounding environment<sup>216</sup>. Both the sample chamber (or “ampoule”) and the reference ampoule are connected to thermopiles. A heat sink separates the sample and reference ampoules. When heat is either added or removed from the system (in the case of Li-ion batteries, the various contributors to the heat flow are given in CHAPTER 2), the resulting small temperature gradient generates a voltage at the thermopile, which is then used to measure the heat flow into or out of the system. Under steady-state conditions the rate of heat generation by the sample should be equal to the rate of heat exchange by the heat sink. The measured heat flow can then be derived from the heat balance equation in terms of the voltages at the sample and reference ampoules (not including a time constant correction)<sup>119,217</sup>:

$$\frac{dq}{dt} = \dot{q} = \epsilon(V_s - V_r) \quad 3.8$$

where  $\epsilon$  is a calibration constant that depends on the Seebeck coefficients of the sample and reference thermopiles (assumed to be equal), the heat capacities of the sample and reference ampoules (assumed to be equal), and the time constant  $\tau$ ;  $V_s$  and  $V_r$  are the thermopile voltages for the sample and reference ampoules, respectively.

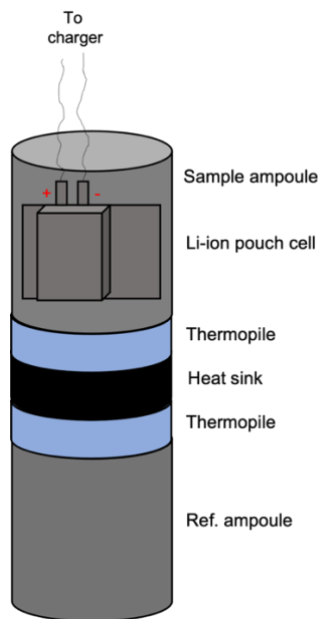


Figure 3.6: Cartoon of the reference and sample ampoules in a single calorimeter channel. Each ampoule is connected to a thermopile, and the two ampoules are separated by a heat sink. A Li-ion cell is inserted into the sample ampoule and connected to a charger outside of the calorimeter.

The TAM III has 12 identical calorimeter channels, allowing for 12 independent experiments at one time. Each channel has a ~20 cm long “lifter” that lowers the ampoule into calorimeter. A photograph of one of the lifters is shown in Figure 3.7. The lifter has several thermal barriers to thermally isolate the ampoule from the outside environment, a spring to ensure good contact with the thermopile, and a magnetic stop. The magnetic stop holds the lifter about half-way into the calorimeter channel so that the ampoule can equilibrate to the temperature of the calorimeter (40°C) before being fully installed. This is done to avoid overloading the heat flow signal when the sample is inserted. In order to charge and discharge Li-ion cells *in-situ* in the calorimeter, small holes were drilled through the thermal barriers (in the Dalhousie system this was completed by Laura Downie<sup>120</sup>), and 32 gauge polyimide-coated phosphor bronze wires (LakeShore Cryotronics Inc., thermal conductivity 48 W/m.K at 300K) were threaded into the sample



ampoule<sup>121</sup>. These wires were then soldered to connectors that allowed cells to be connected to a charger. The holes in the thermal barriers were then re-sealed with TorrSeal epoxy after the wires were inserted.

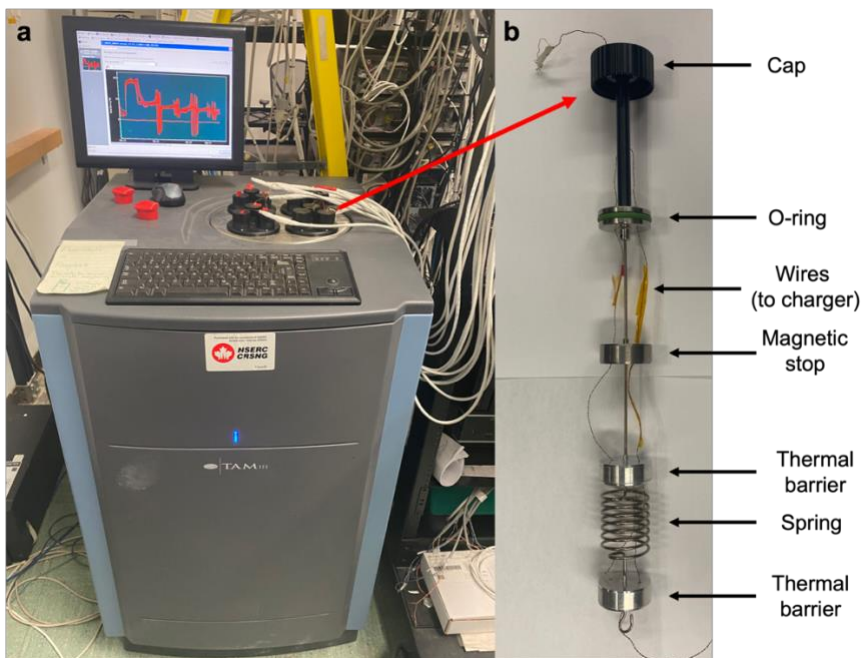


Figure 3.7: (a) Picture of the TAM III at Dalhousie University. (b) Picture of the lifter from one of the 12 calorimeter channels, with components labelled.

The temperature stability of the TAM III is exceptionally high; the specification for temperature stability is 0.1 mK/24 hr. Figure 3.8 shows the measured temperature of the thermostat fluid over an experimental period of ~85 hr. The calorimeter was set to a temperature of 40°C. The temperature spike at the beginning of the experiment was due to temperature fluctuations when cells were loaded into the calorimeter from room temperature. The points plotted below are averaged over the data reporting frequency of the calorimeter (30 s per point). After the initial temperature spike, fluctuations around the setpoint did not exceed 0.5  $\mu^{\circ}\text{C}$ . There are two different temperature measurements that are taken: the temperature of the inflowing thermostat fluid which is shown in Figure 3.8,

and the estimated temperature of the thermal bath, measured by at Pt probe. This Pt probe temperature may have higher fluctuations, but do not exceed the specification of the TAM III.

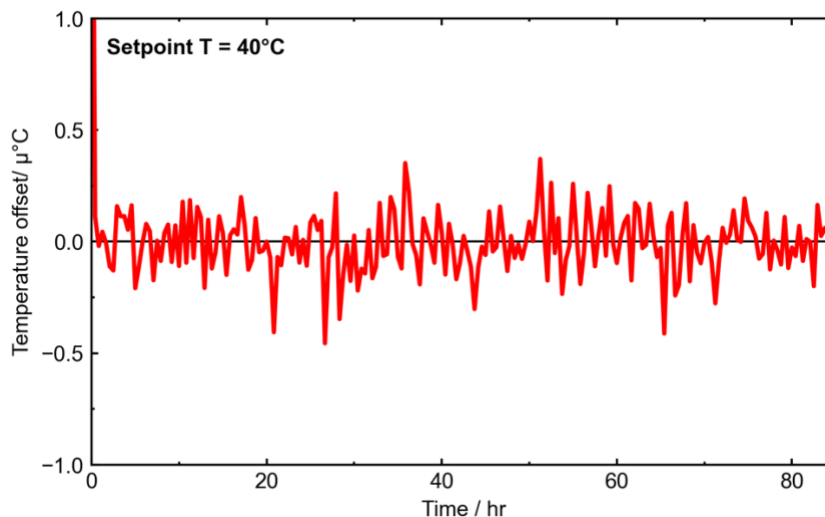


Figure 3.8: Temperature stability of the TAM III microcalorimeter over time. The calorimeter was set to a constant temperature of 40°C. The y-axis plots the offset from the setpoint (40.0000°C) in units of  $\mu\text{C}$ .

A two-point calibration was done to determine the calibration factor in Equation 3.8 above. To simulate a “real” scenario with a Li-ion pouch cell in the calorimeter, a precision resistor ( $10.00 \Omega \pm 0.01 \Omega$ , TE Connectivity, Part # YR1B10RCC) was inserted into the jelly-roll of a dry Li-ion pouch cell. The resistor was soldered to the wires and connected to a Maccor 4000 series cycler. Before applying a known heat flow, the channel was allowed to rest for at least 24 hr in the calorimeter to establish a baseline heat flow. Then, a constant current of 15 mA was applied to each channel for 3 hours generating a known heat flow of 2.25 mW. Each channel was corrected accordingly based on these known heat flow values.

Before starting any IMC experiment, cells or pouch bags that were installed in the ampoules were allowed to rest inside the calorimeter for at least 24 hr.

### 3.11.2 Cycling protocols

IMC cycling experiments were only done on LFP/graphite cells in this thesis. Cells first underwent the first formation cycle as described above. After the formation cycle, cells were degassed and cycled 4 times at 40°C between their lower and upper voltages (see Table 3.1) at a rate of C/20 (~160 hours) on a Maccor 4000 series charger to ensure a well-formed SEI layer. After the “conditioning” cycles were completed, cells were loaded into the calorimeter set to a temperature of 40.0000°C. To cycle cells inside the calorimeter, cells were connected to a Maccor 4000 series charger. Inside the calorimeter, cells were cycled at a constant current of either 1.0 mA (~C/220) or 1.5 mA (~C/150) over the 2L→2 and 2→1 graphite staging plateaus under the following protocol (see CHAPTER 1): 3 times between 3.275 V and 3.350 V, and 3 times between 3.305 V and 3.400 V. Voltage limits were modified slightly depending on the graphite used (see CHAPTER 5). Nominally identical pair cells were constructed when possible to ensure reproducibility of the results.

### 3.11.3 OCV experimental protocols

In addition to cycling tests in the microcalorimeter, open circuit tests were done on both full cells and pouch bags (described above). For full cells, they underwent the same formation and pre-cycle protocol as the cells above that did cycling tests. After the conditioning cycles, cells were charged to top of charge and held at constant voltage for ~36 hours. Full cells were then inserted into the calorimeter without connecting to a charger. For the pouch bags, full pouch cells were made, and underwent the same formation and pre-cycle protocol. After the conditioning cycles, cells were charged to 3.65 V and

held for ~ 36 hours. After cells were equilibrated at top of charge, they were immediately transferred to an Ar-filled glovebox, disassembled, and made into individual pouch bags as described above. Pouch bags were then inserted into the calorimeter at the same time as the full cells. To ensure that all cells in a given experiment were inserted into the calorimeter at the same time, cells or pouch bags were stored in a freezer for a short amount of time (~1 day) if necessary. The heat flow measurements for full cells at open circuit and pouch bags were measured at 40.0000°C for approx. 135 hours in most cases.

## CHAPTER 4 INITIAL SURVEY OF THE PERFORMANCE OF LIFEPO<sub>4</sub>/GRAPHITE CELLS

Some of the results in this Chapter have appeared in peer-reviewed articles *J. Electrochem. Soc.* **167**, 130543 (2020) and *J. Electrochem. Soc.* **168**, 120526 (2021). The author of this Thesis conceived of and planned all experiments presented in this Chapter and completed the data analysis, with the supervision and assistance of Jeff Dahn. Helena Hebecker and Aidan Luscombe assisted with making some of the cells used in this Chapter. Ahmed Eldesoky completed  $\mu$ XRF measurements on aged cells.

### 4.1 INTRODUCTION

Olivine LiFePO<sub>4</sub> (LFP) has been pursued as a cathode material for Li-ion batteries since 1997<sup>30</sup>. Its relatively high specific capacity around 170 mAh/g and high redox potential (~3.5 V vs Li<sup>+</sup>/Li) has made LFP a desirable material. While it cannot achieve the same energy density as more state-of-the-art materials such as Ni-rich layered oxides, its superior safety<sup>31,32</sup> and inexpensive precursor materials has resulted in continuing interest in LFP. As of 2018, LFP made up 34% of cathode material production in the Li-ion battery industry<sup>33</sup>. LFP is attractive for grid energy storage systems, where energy density is less of a priority than in EV applications, where maximizing the volumetric and specific energy of the pack is vital.

Despite the many advantages of using LFP in Li-ion batteries, capacity fade issues in LFP/Graphite cells operated at high temperature has been well-documented<sup>218</sup>. Many publications attribute capacity loss in LFP/graphite cells to the loss of cyclable Li via SEI forming reactions at the graphite negative electrode<sup>219–227</sup>. In some cases this loss of Li inventory at the negative electrode is proposed to be catalyzed by the dissolution of Fe from LFP and subsequent deposition on the negative electrode<sup>227–230</sup>. The Fe dissolution issue in LFP has long been established. Koltypin et al. showed that storing LFP in electrolyte containing 100 ppm of intentionally added water significantly increased Fe dissolution after 20 days of storage<sup>231</sup>. Additionally, some authors have argued that electrolyte decomposition products exist on the surface of LFP as well, despite the low redox potential of the active material<sup>232,233</sup>. Some works have considered the effect of electrolyte additives on capacity fade in LFP/graphite cells, including vinylene carbonate (VC)<sup>234</sup>, lithium difluoro(oxalate)borate (LiDFOB)<sup>235</sup>, fluoroethylene carbonate (FEC)<sup>236</sup>, trimethyl borate (TMB)<sup>237</sup>, and tris(pentafluorophenyl) borane (TPFPB)<sup>238</sup>, with varying degrees of success.

This Chapter is concerned with understanding the modes of degradation of LFP/Graphite pouch cells and mitigating identified issues to achieve long lifetimes. Issues of water contamination stemming from high surface area LFP material are considered. Various electrolyte additives that have had success in NMC/Graphite chemistries<sup>118,239,240</sup> are surveyed. The issue of Fe dissolution and deposition is investigated using scanning micro X-ray fluorescence ( $\mu$ XRF) spectroscopy to study Fe deposited on aged graphite electrodes extracted from Li-ion pouch cells. Existing isothermal microcalorimetry techniques are

applied to the LFP/graphite chemistry, allowing the measurement of parasitic heat flow during cycling and ranking lifetimes for cells with different additives and levels of water contamination. Finally, the performance of an “optimized” LFP cell from these studies is compared to a well-known NMC532/graphite cell with an identical graphite negative electrode.

## **4.2 WATER CONTAMINATION AND MECHANICAL INTEGRITY AFTER DRYING**

The high surface area of LFP materials ( $\sim 10 \text{ m}^2/\text{g}$ ) can lead to a large amount of water being retained in a prepared LFP electrode after assembly of a cell. Räsänen et al. showed that over 400 ppm of water can be adsorbed to LFP after only 1 min of exposure to 35% humidity environments<sup>241</sup>. Therefore, processing steps are important to control the amount of water contamination in the cell. The standard procedure in this laboratory for processing dry pouch cells before filling with electrolyte is to open them in an Ar-filled glovebox and heat under vacuum overnight. The temperature of the vacuum drying can be controlled. Water content in LFP electrodes was studied after different vacuum drying temperatures.

Figure 4.1 shows results from Karl Fischer (KF) titrations of LFP positive electrodes. Points at 25°C refer to LFP electrodes as received with no additional vacuum drying. The as-received electrodes had a high water content, nearing 1000 ppm. As vacuum drying temperatures were increased, the amount of water detected in the electrodes went down as expected. However, when heated at 100°C for 14 hr, the water content in the electrode was still around 500 ppm. Drying at higher temperatures of 120°C or 140°C brought this value

down even further to around 100 ppm. As it did not appear that heating to 140°C brought a significant advantage over drying at 120°C, drying temperatures up to a maximum of 120°C were used. The KF apparatus was set up in air, and while LFP samples were prepared in an Ar glovebox, the samples would have spent a small amount of time (approximately 20-30 seconds) in air before being loaded into the furnace for measurement. As mentioned above, even short exposure times in humid environments can lead to significant water adsorption onto LFP<sup>241</sup>. It is likely that some water was introduced from the environment as the samples were loaded, possibly leading to the relatively large spread in repeat samples (Figure 4.1), especially at the higher drying temperatures where most of the adsorbed water was removed.

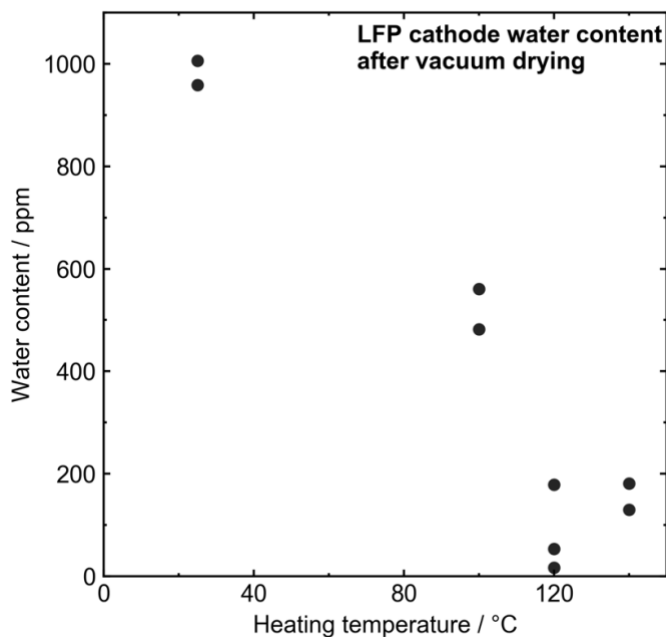


Figure 4.1: Water content in LFP electrodes as a function of vacuum drying temperature as measured by Karl Fischer (KF) titration. Repeat measurements are shown by individual points.



There was initially some concern that higher vacuum drying temperatures could possibly impact the integrity of the the separator. However, it turned out that this is not an issue. DSC thermograms shown in Figure A.1 show roughly the same melting onset for separator samples (coated polyethylene) that were not heated, and samples heated to 130°C and 140°C. Further, rate capability and voltage polarization when cycling at 1C rate at 20°C was unaffected after elevated heating temperatures, as can be seen in Figure A.2, indicating that electrolyte transport in the separator was unaffected by the elevated heating temperatures, and suggesting that the pore network in the separator was not degraded.

The mechanical integrity of both the LFP and graphite electrodes should also be considered when studying the effect of drying protocols on cell performance. Huttner et al. studied the effects of different post-drying procedures in NMC622/graphite cells, and found lower mechanical integrity of both the cathode and anode after various vacuum drying at 120°C<sup>242</sup>. It should be noted that Huttner et al. dried for 18 or 96 hr, while here cells were dried for only 14 hr. This reduction in mechanical integrity was attributed to decomposition of CMC/SBR and PVDF binders in the anode and cathode, respectively. The LFP and graphite electrodes used in this work were tested for their mechanical integrity using a “bend tester” (see Fig. 4 in Ref. <sup>243</sup>). Electrodes were bent around rods ranging in diameter from 6.3 mm to 1.5 mm. The test was considered “failed” for a given rod if there was any indication of electrode cracking or loss of adhesion from the current collector. LFP and graphite electrodes extracted from as-received, 100°C dried, and 120°C dried cells **passed** the bend test for all diameters of rods, indicating good mechanical integrity of electrodes at least in the dry state before the addition of electrolyte. However, the impact of binder

degradation on the long-term performance of cells dried at elevated temperature should not be neglected. Figure A.2 shows that while the voltage polarization was not impacted when cells were heated up to 140°C, the capacity retention was significantly lower after 1000 cycles. The impact of binder degradation may be especially visible in high-rate cycling (as was done in Figure A.2), where the electrode volumes change rapidly during charge and discharge. However, only high temperature, relatively low-rate cycling is considered here.

Further along this line, the thermal degradation of the CMC binder was tested using thermogravimetric analysis (TGA). Figure A.3 shows the thermograms for CMC material (Daicel) heated in Ar atmosphere at 10°C/min and 0.5°C/min. At both heating rates, no features were seen in the temperature range used for vacuum drying in this work (100°C – 120°C), suggesting no thermal decomposition occurred at these temperatures. Small weight loss features at low temperature were likely due to the evaporation of adsorbed water on the sample. Therefore, going forward, impacts of mechanical integrity and/or binder degradation should be considered negligible when considering cell lifetime results presented throughout.

To initially study the electrochemical performance of LFP/graphite cells as a function of vacuum drying temperature, cells were cycled at a rate of C/20 at 40°C for ~16 cycles on the Ultra High Precision cycler at Dalhousie University<sup>203</sup>. Cells were either vacuum dried at 100°C (previously the standard lab procedure, ~500 ppm water remaining, see Figure 4.1) or 120°C (<100 ppm water remaining) for 14 hr. Cells with both Control electrolyte

(CTRL, no additional electrolyte additives) and electrolyte containing 2% VC (referred to as 2VC) were cycled.

Figure 4.2 shows UHPC cycling results for LFP cells with CTRL and 2VC electrolytes. Figure 4.2a shows voltage-capacity curves for cells with Control electrolyte heated at 100°C (black line) and 120°C (red line). The reference point for zero capacity is simply the capacity at the beginning of the experiment; charge capacity counts as positive capacity and discharge capacity counts as negative capacity in these plots. The cell with Control electrolyte showed massive charge endpoint capacity slippage from cycle to cycle (movement of the voltage curve along the capacity axis). A large amount of slippage suggests either an excessive amount of electrolyte oxidation at the positive electrode, or a significant amount of dissolution of Fe from the cathode<sup>244</sup>. The question of transition metal dissolution will be considered later. It seems unlikely that electrolyte would react readily at the positive electrode since the operating potential of LFP is low. Alternatively, the result of this large slippage could be the reaction products from the negative electrode – possibly lithium alkoxides - migrating to the positive electrode and reacting, suggesting complex crosstalk reactions. Drying the cells at 120°C and thus removing most of the residual water dramatically lowered the charge endpoint capacity slippage in the Control electrolyte. In the case where electrolyte additives were used (2% VC, Figure 4.2b), charge endpoint slippage remained low in the cell dried at 100°C, with no noticeable difference when dried at 120°C. It has been shown that the incorporation of VC in the electrolyte of Li-ion cells eliminates production of lithium alkoxides<sup>245</sup>. The UHPC results were investigated further in Figure 4.2c, which shows the coulombic efficiency (CE) as a

function of cycle number for CTRL and 2VC cells vacuum dried at 100°C and 120°C. For cells with CTRL electrolyte dried at 100°C, CE decreased over the first several cycles, while the cell dried at 120°C reached a stable CE just above 0.99 after 16 cycles. The cells with 2VC both reached a CE around 0.999 after 16 cycles regardless of drying temperature.

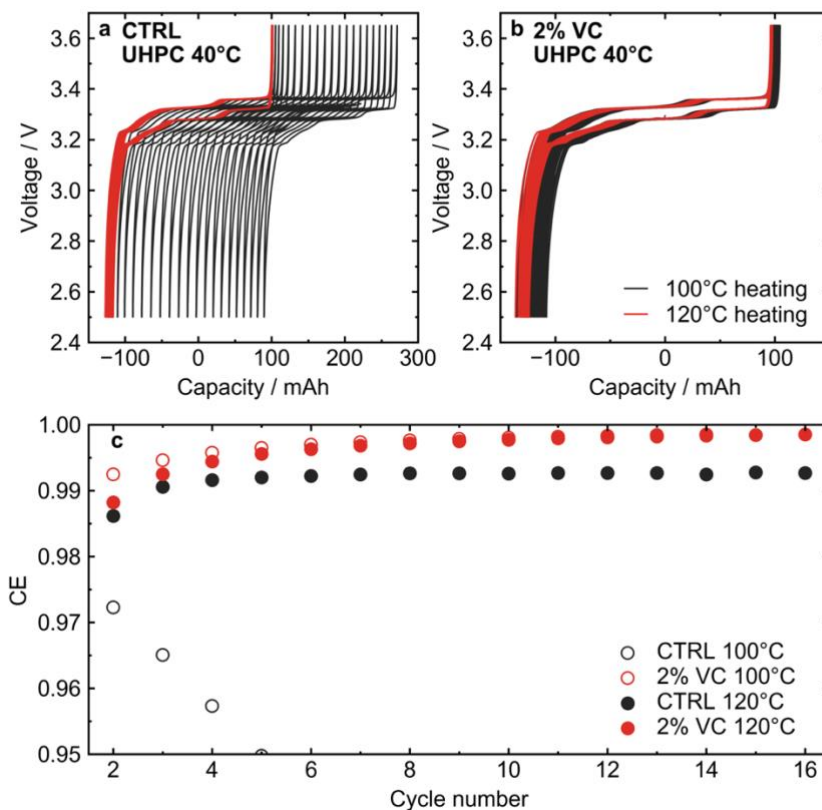


Figure 4.2: Ultra-high Precision Coulometry (UHPC) cycling measurements for LFP cells with different electrolytes and different levels of water contamination. (a) Voltage-capacity curves for LFP cells with Control electrolyte cycled at a rate of  $C/20$  at 40°C. Cells vacuum dried at 100°C vs 120°C are shown. (b) Voltage-capacity curves for LFP cells with 2VC electrolyte vacuum dried at 100°C or 120°C. (c) Coulombic efficiency (CE) vs cycle number for the cycles shown in panels (a) and (b).

### 4.3 SURVEY OF ELECTROLYTE ADDITIVES

From Figure 4.2, it could be seen that the use of electrolyte additives can significantly impact the effect of water contamination in LFP/Graphite cells. In the case of Control electrolyte, only 500 ppm of water contamination severely impacted the CE with cycling, indicating extremely poor performance. With 2VC added to the electrolyte, however, almost no difference in CE could be seen between the two drying temperatures. This highlights the essential role that electrolyte additives play in Li-ion batteries. In this group, a number of systems of electrolyte additives have been developed that are effective in NMC/Graphite chemistries<sup>118,239,240</sup>. A number of these additive systems were tested in LFP/Graphite cells.

Figure 4.3 shows CE as a function of cycle number for UHPC tests for LFP cells vacuum dried at 100°C and 120°C with various additive systems: (a) CTRL, (b) 2VC, (c) 2FEC, (d) 1LFO, (e) 2VC+1DTD, (f) 2FEC+1LFO, (g) 2VC+1DTD+20MA, and (h) 2FEC+1LFO+20MA. Figure 4.3i summarizes these results, showing the CE of the cells with the different electrolytes tested at different drying temperatures after cycle 14. It would have been ideal to compare cells after more than 16 cycles when the SEI was more mature, but unfortunately an unplanned power outage cut short the cycling of the 100°C dried cells. Due to the time-sensitive nature of CE measurements<sup>206</sup>, the cells did not resume cycling after this outage. The CE for the control cell vacuum dried at 100°C was so low that it is off scale in Figure 4.3a (~0.95 after 5 cycles and decreasing, see Figure 4.2c). While vacuum drying at 120°C greatly improved the CE of cells with control electrolyte, it was not competitive compared to cells with electrolyte additives. Looking broadly at all electrolyte additives studied, there were only small differences between the

CEs of cells dried at the different temperatures, if any. VC-containing cells (2VC, 2VC + 1DTD) had the best CE values after ~15 cycles. Some cells had 20% methyl acetate (MA), a common co-solvent for fast charging applications, added to the electrolyte<sup>113–115</sup>. Typically, the addition of MA results in a lifetime penalty due to the increased reactivity of MA compared to carbonate solvents such as DMC, as well as its poor SEI-forming properties<sup>115,118</sup>. However, in the UHPC tests, the CE of cells containing MA did not seem to be severely affected at 40°C. This was likely in part due to the lower operating voltage of LFP/Graphite cells compared to NMC chemistries, which reduces the propensity for parasitic reactions between solvent molecules in the electrolyte and the positive electrode.

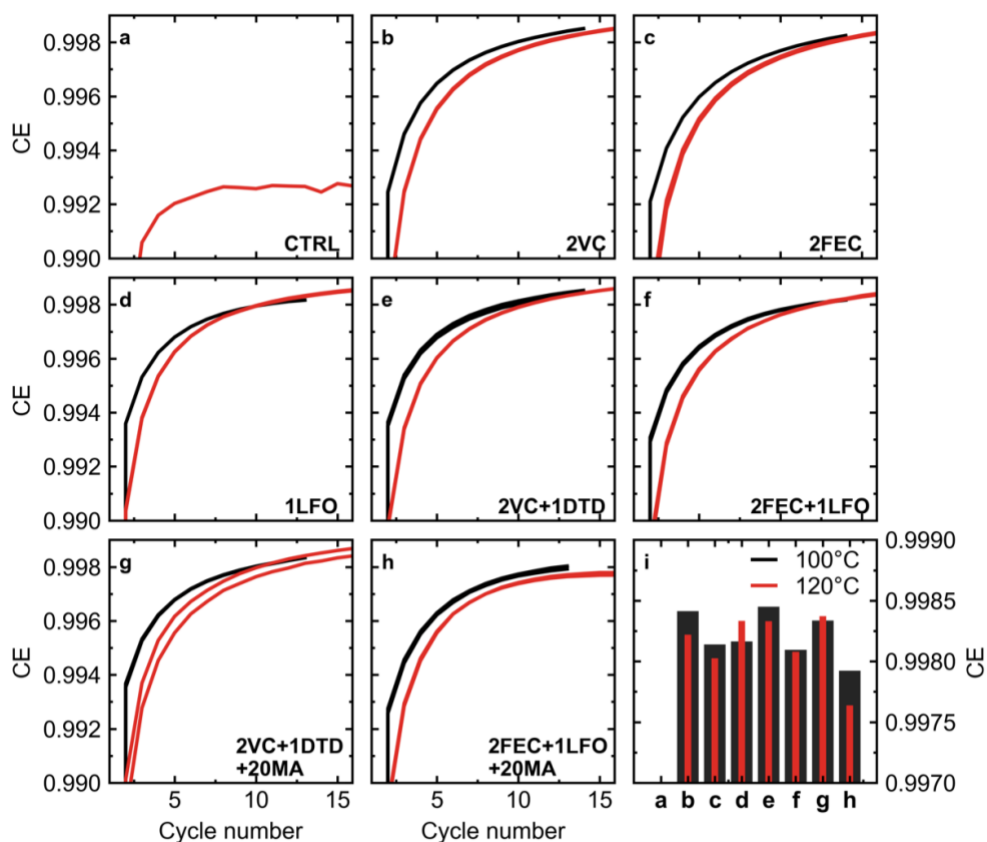


Figure 4.3: CE versus cycle number for LFP cells vacuum dried at different temperatures cycled using the UHPC cycler at 40°C and a rate of C/20. Different additive systems are shown: (a) CTRL, (b) 2% VC, (c) 2% FEC, (d) 1% LFO, (e) 2% VC + 1% DTD, (f) 2% FEC + 1% LFO, (g) 2% VC + 1% DTD + 20% MA, and (h) 2% FEC + 1% LFO + 20% MA. (i) Summary of CE

values under the conditions in the previous panels after 14 cycles Both CTRL cells are off scale in this panel.

Figure 4.2a and Figure 4.2b showed the charge endpoint motion for cells with different vacuum drying temperatures and control electrolyte vs 2VC by examining the shift in voltage curves along the capacity axis. Figure 4.4 considers charge endpoint slippage more quantitatively, showing the zeroed (at cycle 2) charge endpoint capacity versus cycle number for more electrolyte additives. Figure 4.4i shows the zeroed charge endpoint capacity at cycle 14 for all electrolytes studied. Again, the improved performance of the control electrolyte upon increased vacuum drying temperature can be seen. Looking at the various electrolyte additives, some differences could be seen between cells heated at 100°C and 120°C. Nearly all electrolytes showed higher charge endpoint capacity slippage after heating at 120°C compared to 100°C heating, with the exception of 2FEC+1LFO, where the slippage was roughly the same within error between the two heating temperatures. This suggests, interestingly, that there are in fact *more* oxidation reactions when there is less water present in the cells initially, again likely from crosstalk originating at the negative electrode.

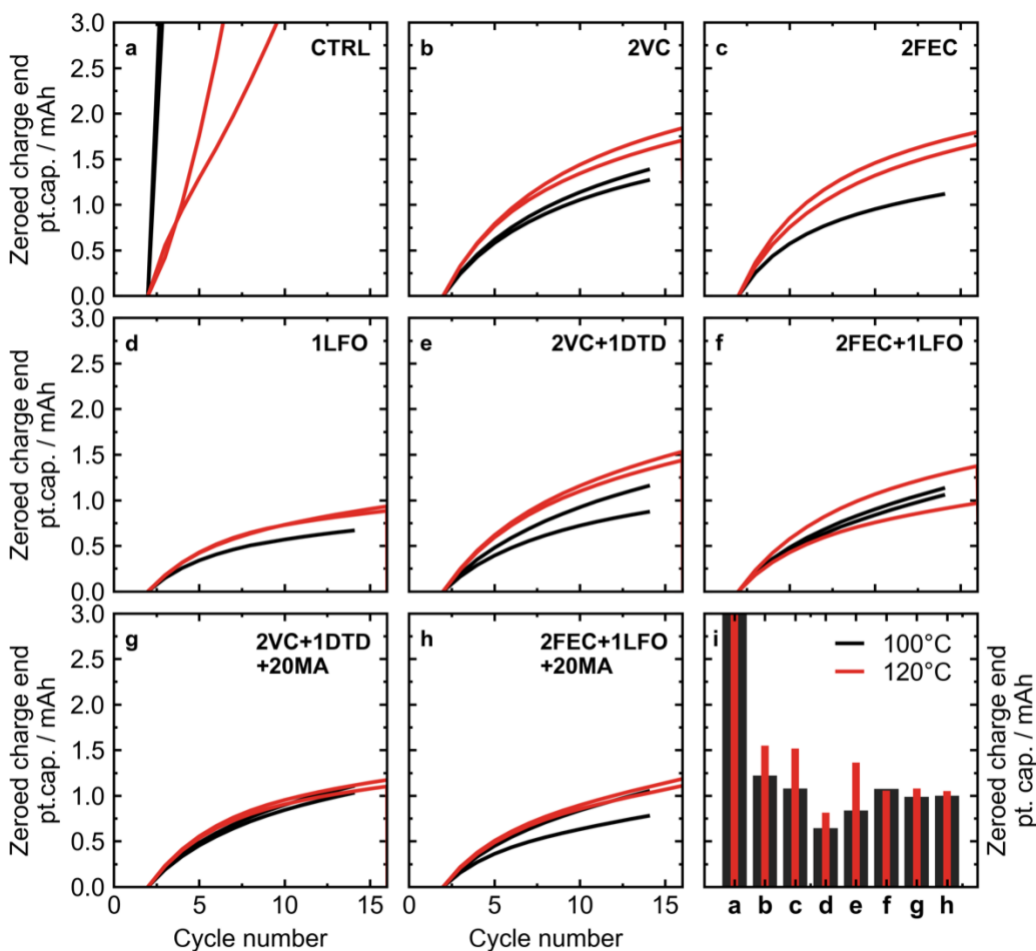


Figure 4.4: Zeroed (at cycle 2) charge endpoint capacity as a function of cycle number for LFP cells vacuum dried at different temperatures cycled using the UHPC system at 40°C and a rate of C/20. (a) CTRL, (b) 2% VC, (c) 2% FEC, (d) 1% LFO, (e) 2%VC + 1% DTD, (f) 2% FEC + 1% LFO, (g) 2% VC + 1% DTD + 20% MA, and (h) 2% FEC + 1% LFO + 20% MA. (i) Summary of zeroed charge endpoint capacity values after 14 cycles.

Figure 4.5 shows discharge capacity (normalized to cycle 2) versus cycle number for cells that underwent UHPC cycling at 40°C. Normalized discharge capacities at cycle 14 are summarized in Figure 4.5i. Once again, the cells with Control electrolyte were poor regardless of vacuum drying temperature; the 120°C dried Control cells did have better capacity retention than the 120°C cells, however. In most cases, normalized capacity retention was slightly worse for cells dried at 120°C (most water removed) compared to



cells only dried at 100°C. This result agrees with Figure 4.4 showing higher charge endpoint capacity slippage for cells dried at 120°C. While the origin of this slightly worse cycle performance is not known at this time, this observation will be discussed in more detail in Section 4.5 where isothermal microcalorimetry measurements will be presented.

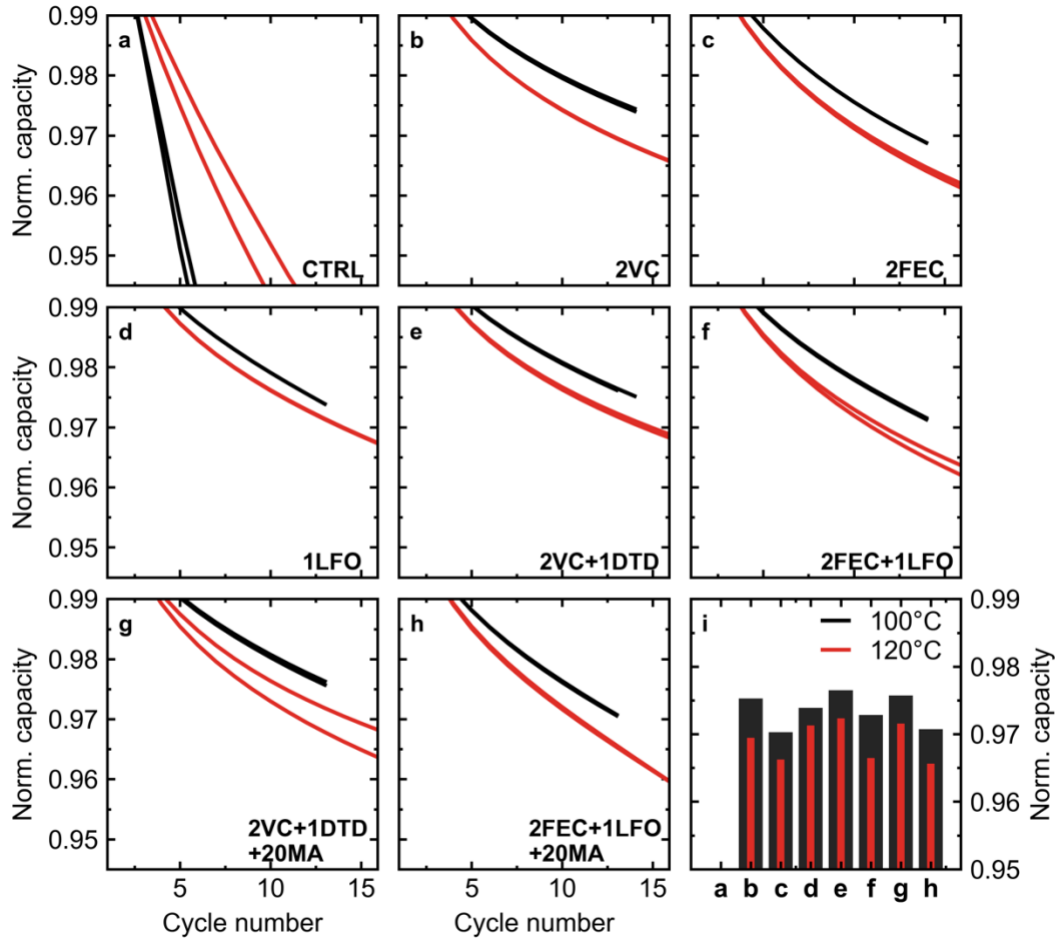


Figure 4.5: Normalized (cycle 2) discharge capacity versus cycle number for LFP cells vacuum dried at different temperatures cycled using the UHPC system at 40°C and a rate of C/20. (a) CTRL, (b) 2% VC, (c) 2% FEC, (d) 1% LFO, (e) 2%VC + 1% DTD, (f) 2% FEC + 1% LFO, (g) 2% VC + 1% DTD + 20% MA, and (h) 2% FEC + 1% LFO + 20% MA. (i) Summary of normalized capacity values after 14 cycles.

In addition to UHPC cycling at C/20 rate, cells underwent long-term cycle testing at higher charge/discharge rates. Figure 4.6 shows normalized discharge capacity (normalized to cycle 5) versus cycle number for cells cycled at 40°C. All cells were cycled at a rate of C/3

for charge and discharge. Figure 4.6i shows percent capacity loss for the different cells after 600 cycles. As was seen for cells with Control electrolyte in the UHPC cycles, an improvement in capacity retention for cells with Control electrolyte was seen when the cells were dried at 120°C. Cells containing VC (2VC, 2VC+1DTD, and 2VC+1DTD+20MA) only showed marginal, if any, improved capacity retention with increased drying temperature. On the other hand, cells with electrolytes containing FEC and/or LFO showed improved capacity retention when excess water was removed at 120°C. The biggest difference was seen in cells with 1LFO, which performed poorly when dried at 100°C, but was almost competitive with the other additive systems when dried at 120°C.

40°C, C/3:C/3

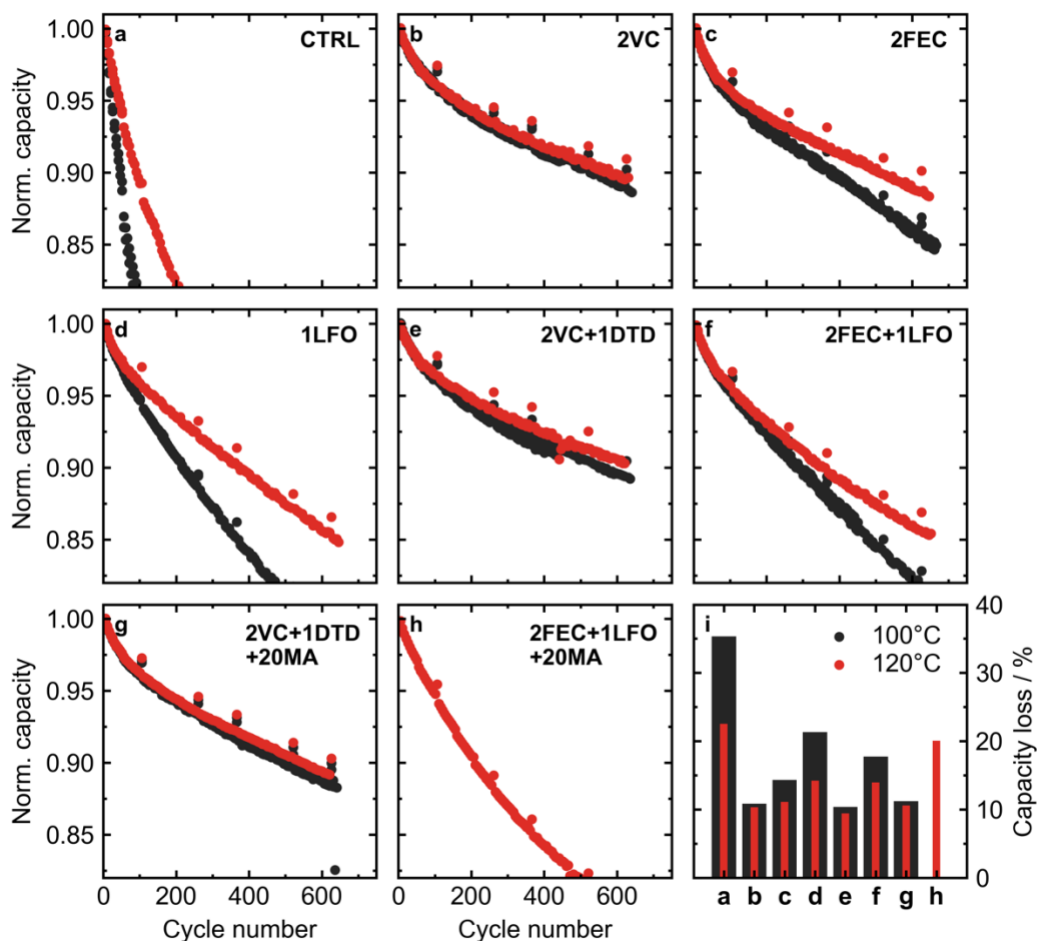


Figure 4.6: Long-term cycling results for LFP cells at 40°C and a rate of C/3:C/3. Normalized capacity versus cycle number for cells with different additive systems: (a) CTRL, (b) 2% VC, (c) 2% FEC, (d) 1% LFO, (e) 2%VC + 1% DTD, (f) 2% FEC + 1% LFO, (g) 2% VC + 1% DTD + 20% MA, and (h) 2% FEC + 1% LFO + 20% MA. (i) Summary of percent capacity lost for cells with different additives and drying temperatures after 600 cycles. Note that the capacity loss for the CTRL cells is shown after 300 cycles.

Figure 4.7 shows the corresponding voltage polarization (normalized to cycle 10) versus cycle number for the 40°C cycled cells shown in Figure 4.6. Here it can be seen that most cells show a reduction in voltage polarization when water contamination was removed (120°C drying). The biggest reductions in voltage polarization were seen in Control cells and 1LFO cells, which also showed the biggest improvement in capacity retention in Figure

4.6 when dried at 120°C. Recall in Figure 4.5, the UHPC cycles at C/20 rate showed worse capacity retention in all cells (with the exception of Control electrolyte) when dried at 120°C. At such low rate, impedance effects should not impact capacity retention, but possibly be a factor at rates as high as C/3. The reduction in voltage polarization observed in Figure 4.7 could contribute to the improvement in capacity retention in the C/3 cycling, but other factors may contribute to this as well.

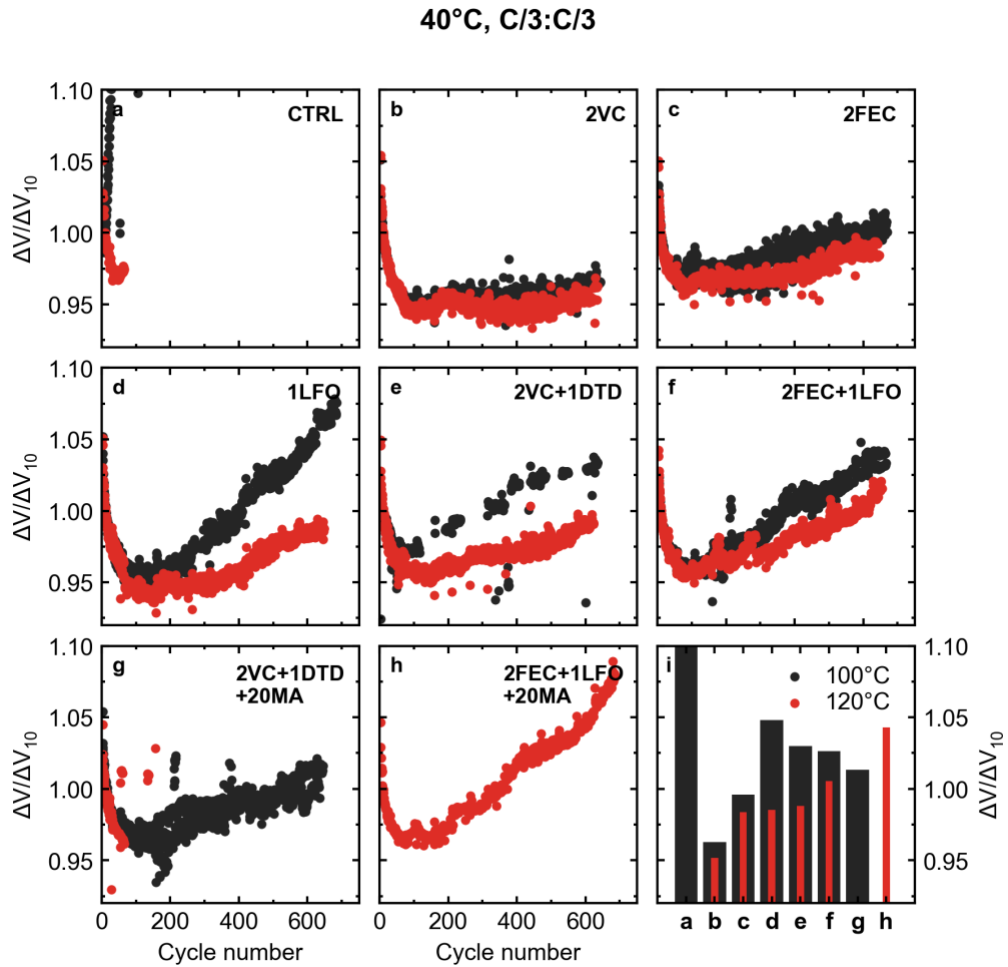


Figure 4.7: Normalized voltage polarization versus cycle number for cells cycling at 40°C, C/3:C/3 rate. Different additive systems are shown: (a) CTRL, (b) 2% VC, (c) 2% FEC, (d) 1% LFO, (e) 2%VC + 1% DTD, (f) 2% FEC + 1% LFO, (g) 2% VC + 1% DTD + 20% MA, and (h) 2% FEC + 1% LFO + 20% MA. (i) Summary of normalized voltage polarization after 600 cycles.

OCV storage tests were carried out at 60°C. Cells were charged to the top of charge (3.65 V) and let rest at OCV for two storage periods of 500 hr each, with checkup cycles at the end of each period to monitor reversible and irreversible capacity losses. Figure 4.8 shows voltage versus time for these OCV periods for cells dried at 100°C and 120°C. Voltage drop during storage can give an indication of the capacity loss during the OCV period<sup>246</sup>. For cells with a given electrolyte and drying temperature, the first storage period is shown as a solid line, and the second storage period as a dashed line. Figure 4.8i shows the total *irreversible* capacity loss over the two storage periods. This was obtained by subtracting the capacity of the discharge cycle immediately preceding the first storage period from the capacity of the *second* discharge after the second OCV period. Once again, the extremely poor performance of cells with the control electrolyte at high temperature was seen (Fig. 9a). While off scale in this Figure, the control cell dried at 100°C fully self-discharged to the lower cut-off voltage (2.5 V) before the end of the first 500 hr storage period. The second storage period was also poor, but the cell did not fully self-discharge. The 120°C heated cell with control electrolyte showed slightly better performance, but was still poor compared to cells with additives.

Cells containing electrolyte additives fared much better in this test, with all cells remaining above ~3.35 V during both storage periods. Cells that performed well in other tests showed good resistance to self-discharge in the high temperature storage tests. Here, very little differences were seen between cells with the two drying temperatures, even in the 1LFO electrolytes which showed clear improvements in 40°C cycling. For most additive systems, the voltage versus time curves matched almost exactly for the two drying temperatures.

One notable exception was 2VC, which showed more voltage drop after vacuum drying at 120°C. This once again supports the notion that the high temperature degradation of LFP is likely not due to excessive water contamination when electrolyte additives are used.

A comparison can be made between the first and second 500 hr OCV periods in the high temperature storage experiments. As the cells aged and the SEI thickened, one would expect that the SEI layers in a good additive system will become better passivating, and thus cell will be less prone to parasitic reactions and self-discharge. This should translate to less voltage drop in an OCV storage experiment. Indeed, for the electrolytes in the LFP/graphite system that had already been proven to perform well in other tests, including 2VC, 2FEC, and 2VC+1DTD, less voltage drop was seen in the second storage period. This suggests a better passivating SEI as time goes on, which is a good sign for the long-term calendar life of these cells. On the other hand, electrolytes that performed relatively poorly—like 1LFO—showed greater voltage drop in the second storage period. Comparing the first and second storage periods provided yet another metric to rank the performance of different electrolyte additives in LFP/AG cells.

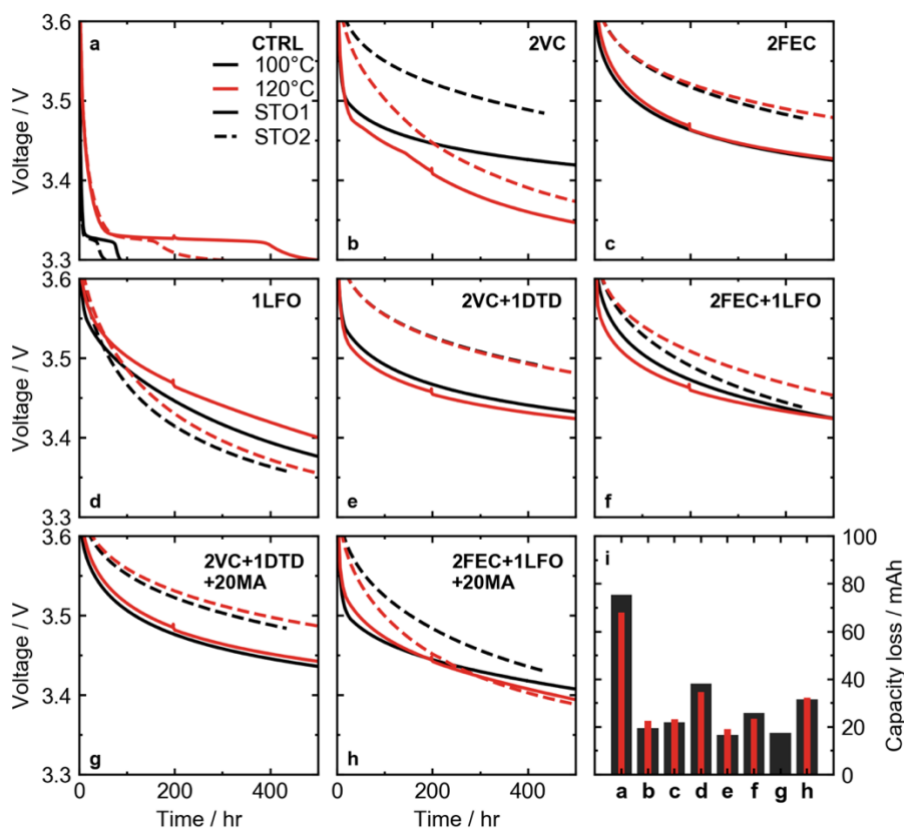


Figure 4.8: High temperature OCV storage results for LFP cells vacuum dried at different temperatures. Cell voltage versus storage time for cells with different additive systems: (a) CTRL, (b) 2% VC, (c) 2% FEC, (d) 1% LFO, (e) 2%VC + 1% DTD, (f) 2% FEC + 1% LFO, (g) 2% VC + 1% DTD + 20% MA, and (h) 2% FEC + 1% LFO + 20% MA. (i) Summary of absolute irreversible capacity loss after 1000 hr of storage at 60°C.

#### 4.4 FE DISSOLUTION AND DEPOSITION

One of the commonly stated degradation mechanisms for LFP is the dissolution of Fe from the cathode. This is believed to be a result of  $\text{LiPF}_6$  salt hydrolysis and corrosion of LFP surface by acidic products such as HF, and subsequent deposition of Fe on the graphite negative electrode. It was therefore crucial to understand the extent of Fe dissolution under various experimental conditions and water contents in LFP to interpret the results presented

above. Scanning micro X-ray fluorescence spectroscopy ( $\mu$ XRF) was performed on the disassembled graphite electrodes from cells with a selection of different electrolyte additives to measure the concentration of Fe found after various cycling tests<sup>247,248</sup>. Cells were cycled at C/3:C/3 rate between 2.5 V and 3.65 V at either 20°C, 40°C, or 55°C for different amounts of time. Figure 4.9 shows normalized capacity versus cycle number for Control electrolyte (Figure 4.9a) and 2VC electrolyte (Figure 4.9c) to illustrate how capacity fade varied with temperature. Clearly in both cases, capacity fade was more severe as the cycling temperature was increased. However, while 2VC cells had reasonable capacity retention at all temperatures, cells with Control electrolyte failed rapidly at temperatures above 20°C.

After cycling, cells were discharged to 2.5 V and disassembled. Aged graphite electrodes were extracted and measured for deposited Fe using scanning micro X-ray fluorescence ( $\mu$ XRF) spectroscopy. This technique has a very high resolution (25  $\mu$ m spot size), so localized features in the Fe distribution could be resolved. These features are examined in Figure 4.9 below.

Figure 4.9b,d shows optical images of aged graphite electrodes and corresponding Fe mapping for electrodes extracted from Control cells and 2VC cells, respectively. Cells are shown after the initial formation cycle (all done at 40°C), and after cycling at various temperatures, with cycle numbers shown in each panel. For now, the magnitudes of Fe deposition will not be compared, especially between the two electrolyte types. Instead, the purpose of this Figure is to look at the different *distributions* of deposited Fe with the



different electrolytes and cycling conditions. First considering the cells cycled with Control electrolyte (Figure 4.9b): at 20°C, most of the noticeable Fe deposits show up as “hot spots”, extremely localized regions along the electrode. These hot spots also correspond to noticeable features in the optical image which are likely regions where metallic Li has deposited. It is likely that the Li metal deposited first, providing a conductive region for Fe to be reduced. It is likely that the Li plating initially occurred because of locally high current densities, since these hot spots were found in the folds of the jelly roll where locally low N/P ratios could be encountered. The Control cells cycled at 40°C and 55°C showed more uniform Fe deposition than the 20°C case. However, especially in the case of the 40°C cell, more Fe was deposited in the centre of the electrodes than the outer edges. One possible explanation for this is that excessive gas production for cells with Control electrolyte (see Figure 4.10) could force the edges of the jelly roll to lose contact and become inactive.

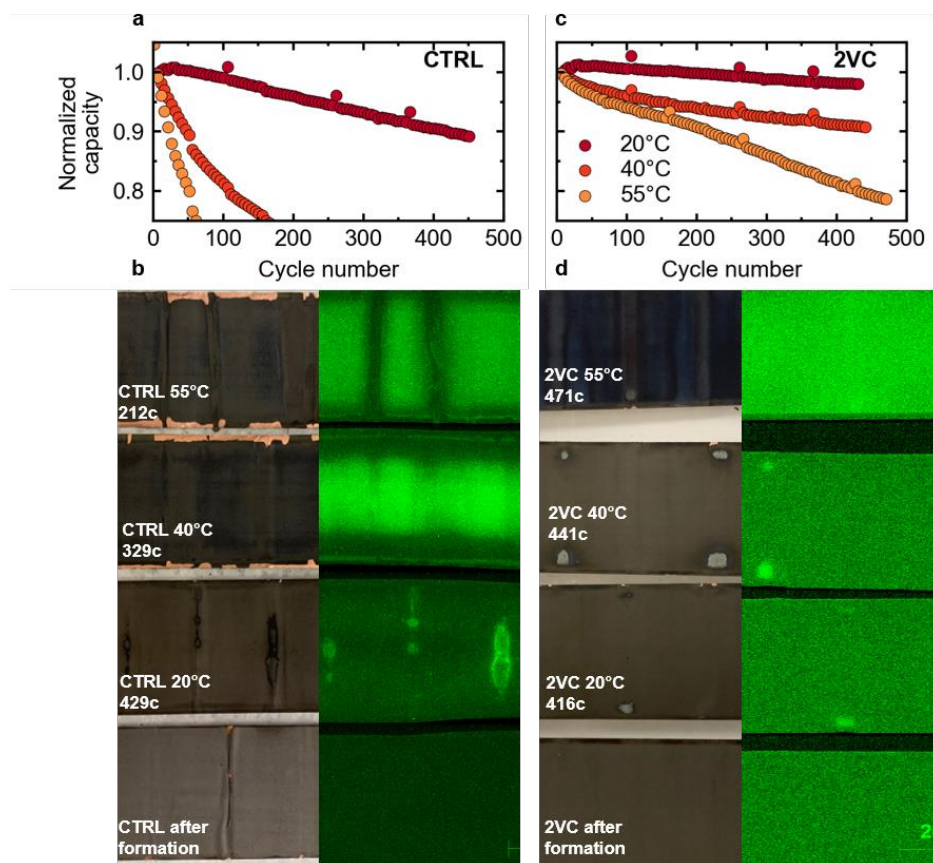


Figure 4.9: Visualizing the deposition of Fe on graphite electrodes. (a) Normalized capacity versus cycle number for LFP cells with the control electrolyte at 20°C, 40°C, and 55°C. (b) Optical images (left) and corresponding Fe mapping (right) from micro-XRF for graphite negative electrodes extracted from LFP cells in control electrolyte directly after formation, and after cycling at different temperatures. (c) Normalized capacity versus cycle number for LFP cells with the 2% VC electrolyte at 20°C, 40°C, and 55°C. (d) Optical images (left) and corresponding Fe mapping (right) for cells with the 2% VC electrolyte after formation and after cycling at different temperatures.

For cells with 2VC electrolyte, the distribution of Fe deposition was much more uniform. With the exception of a few small hotspots that clearly correspond to localized Li plating in the optical image, there are very few noticeable features in the 2VC Fe distribution.

Fe deposition could be tracked as a function of cycle number by constructing several nominally identical cells and cycling them for set amounts of time. This was done for some

of the key electrolyte additive systems discussed above (CTRL, 2VC, 1LFO, 2VC+1DTD, and 2FEC+1LFO) at 20°C, 40°C, and 55°C. Figure 4.10 shows percent capacity loss, Fe loading on the negative electrode, gas volumes and charge-transfer resistance as a function of cycle number for cells with these different electrolyte additives at different temperatures. Note that all cells were cycled at C/3 rate, and gas and EIS were measured after cycling before they were disassembled for  $\mu$ XRF measurement. All cells shown here were dried at 100°C, leaving ~500 ppm water in the electrodes. At 20°C, cells with Control electrolyte lost 20% capacity in 700 cycles or so. However cells with any of the electrolyte additives lost virtually zero capacity. Correspondingly, cells with additives show no Fe depositon, while Control had noticeable Fe deposited after cycling. Very little gas was produced in cells with additives at 20°C, with much more produced in Control cells.

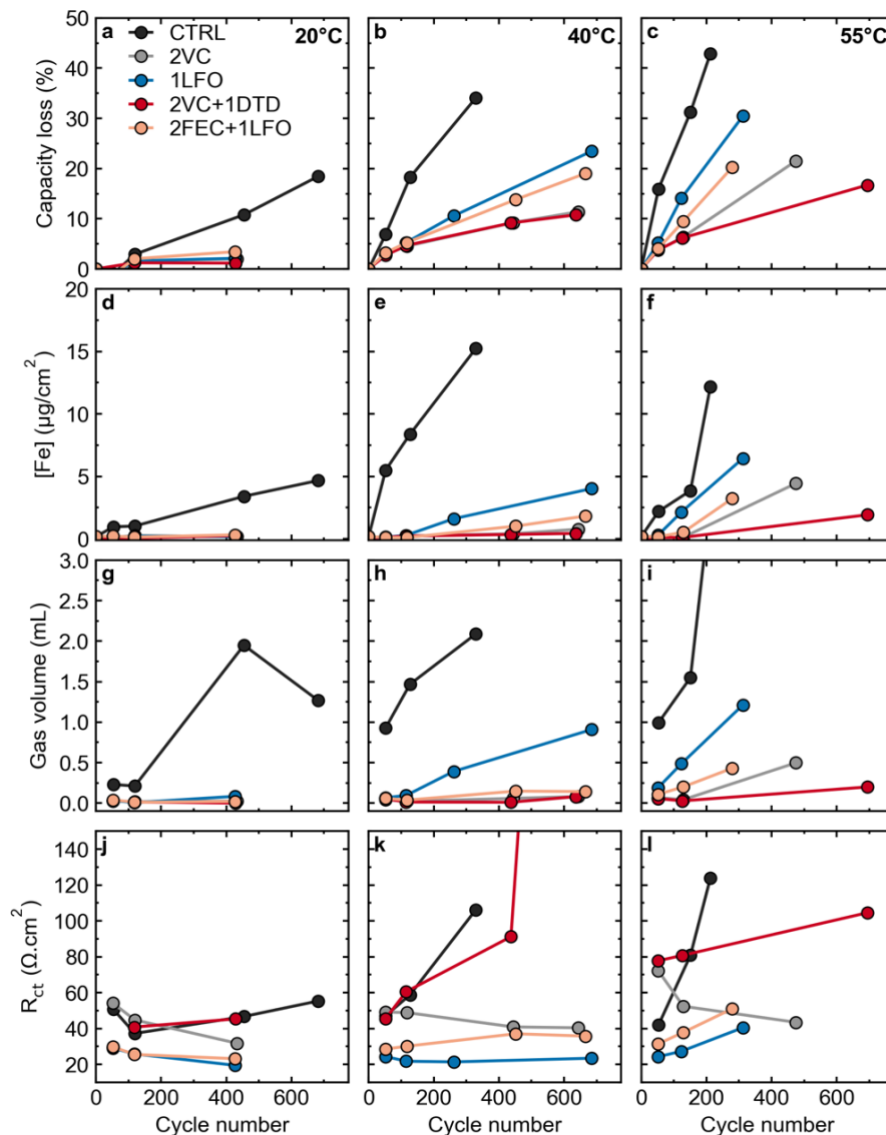


Figure 4.10: Different measurements as a function of cycle number for cells that were eventually disassembled for  $\mu$ XRF measurements. All cells were cycled at  $C/3$  rate, and vacuum dried at  $100^\circ\text{C}$  prior to filling with electrolyte. (a-c) Percent capacity loss at  $20^\circ\text{C}$ ,  $40^\circ\text{C}$ , and  $55^\circ\text{C}$ , respectively. (d-f) Fe loading detected on the graphite negative electrode at  $20^\circ\text{C}$ ,  $40^\circ\text{C}$ , and  $55^\circ\text{C}$ , respectively. (g-i) Volume of gas evolved in cells at  $20^\circ\text{C}$ ,  $40^\circ\text{C}$ , and  $55^\circ\text{C}$ , respectively. (j-l) Charge-transfer impedance at  $20^\circ\text{C}$ ,  $40^\circ\text{C}$ , and  $55^\circ\text{C}$ , respectively.

Some differences were seen in cells cycled at  $40^\circ\text{C}$ . Once again, Control electrolyte showed rapid capacity fade, with associated high levels of Fe deposition and gas production. Electrolyte additives that performed very well in the tests discussed above (2VC and 2VC+1DTD, Figure 4.6) still showed virtually no Fe deposition after  $\sim 650$  cycles at  $40^\circ\text{C}$ .

1LFO, which performed noticeably worse at 40°C than the other additives, did show more Fe deposition than either 2VC or 2VC+1DTD cells. 1LFO also showed a higher volume of gas evolved than the other additives at 40°C.

At 55°C, all cells showed some degree of Fe deposition, though at this temperature the Fe deposition was highly additive dependent. The degree of Fe deposition at 55°C was also roughly in line with the capacity loss of each of the cells: 2VC+1DTD showed the least capacity loss as well as the least amount of deposited Fe at 55°C, followed by 2VC, 2FEC+1LFO, 1LFO, and finally CTRL. Like at the lower temperatures, higher amounts of Fe corresponded to higher volumes of gas evolved during testing. No trends could be seen in the charge-transfer resistance for any of the temperatures or different electrolyte additives.

$\mu$ XRF measurements were also done on cells dried at 120°C to consider the effect of water contamination on Fe dissolution from LFP. Figure 4.11 compares the capacity loss and Fe loading detected on the graphite electrode in cells cycled at 40°C and 55°C. Black bars indicate cells dried at 100°C, and red bars indicate cells dried at 120°C. All cells in Figure 4.11 were cycled for approximately 60 cycles at C/3 rate before disassembly. At both 40°C and 55°C, removing excess water from LFP had an impact on the amount of Fe dissolution in cells with the Control electrolyte, even though the absolute capacity losses for these cells were similar. At 40°C, the Fe loading on the negative electrode in cells with control electrolyte was reduced from 5.5  $\mu\text{g}/\text{cm}^2$  when dried at 100°C to only 0.2  $\mu\text{g}/\text{cm}^2$  when

dried at 120°C. At 55°C, the amount of Fe deposition in cells with Control electrolyte was reduced by almost a factor of 2.

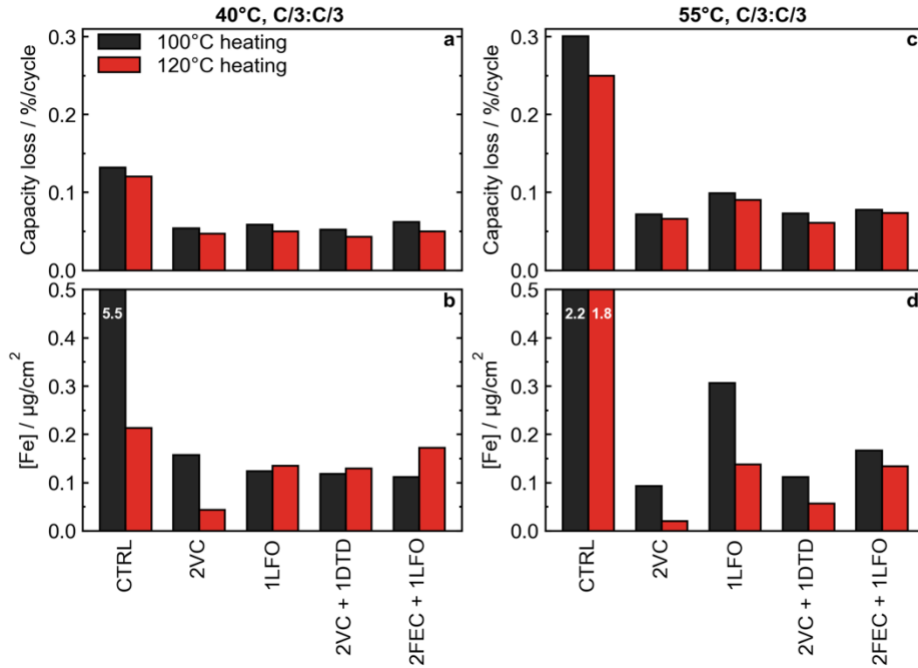


Figure 4.11: Comparison of Fe dissolution for LFP cells at different vacuum drying temperatures. (a, b) Percent capacity loss per cycle and Fe concentration on the graphite electrode, respectively, for LFP cells with different drying temperatures cycled at 40°C. (c, d) Percent capacity loss per cycle and Fe concentration on the graphite electrode, respectively, for LFP cells dried at different temperatures and cycled at 55°C.

The trends were less clear with cells that contained additives. In all cases when electrolyte additives were used, the amount of Fe detected was much lower in cells containing additives, regardless of the drying temperature of the cell. At 40°C, only cells with the 2VC electrolyte saw less Fe on the anode at the higher drying temperature. Cells with 1LFO, 2VC+1DTD, and 2FEC+1LFO all had roughly the same Fe loading detected with 100°C and 120°C drying. At 55°C there was a small reduction in Fe dissolution for the cells dried at 120°C, but again the amount of Fe dissolution was much less than in cells with the control electrolyte. One point to reiterate is that these cells were in the early stages of

cycling when they were disassembled for the  $\mu$ XRF measurement (~60 cycles). It may take more time to begin to see more significant differences in Fe dissolution between cells with and without water contamination.

While significant Fe dissolution was detected in the cells with Control electrolyte, it is still unlikely that Fe dissolution can be blamed entirely for the massive capacity fade that is observed. The performance of cells with Control electrolyte was improved with the removal of water contamination, which also corresponded to a reduction in Fe dissolution, but the performance of these cells was still very poor relative to cells with electrolyte additives. While the dissolution of Fe may contribute somewhat to capacity fade in these cells, it is likely Li inventory loss is the dominant capacity fade mechanism, as has been observed by other groups in LFP/graphite cells<sup>221,224</sup>.

To further underline this point, the correlation between Fe deposition and capacity loss was explored. Figure 4.12 shows [Fe] as a function of percent capacity loss for all cells presented earlier in Figure 4.10. Different cycling temperatures are plotted as different colours, and different electrolyte additives as different symbols. On first glance, it appears that there is some correlation between deposited Fe and capacity loss, and it can probably be broadly stated that cells with high capacity loss have high amounts of Fe deposition. However, most of the cells that show a positive correlation were Control and 1LFO cells that also had a significant amount of capacity loss. Most of the data points are concentrated in the low-Fe, low-capacity fade region. Figure 4.12b shows a zoomed-in look at cells with capacity loss up to 15%. Here, there is much less of an obvious correlation between Fe and

capacity loss. While Fe deposition seems to correlate somewhat with capacity loss, the convolution of other capacity fade mechanisms make it hard to solely blame Fe deposition for capacity loss in LFP cells. Even in the case of “bad” electrolyte additives or Control, the argument becomes a “chicken or egg” problem; do the cells lose so much capacity because of the high amount of Fe deposition, or does Fe deposition occur alongside significant capacity loss? The latter seems to be more likely since Fe deposition does not seem to significantly affect capacity retention in the other cases. It is probably more likely that in the case of Control or 1LFO cells that as the cells cycle, the already poorly passivating graphite SEI decomposes further, which allows Fe to be deposited more easily.

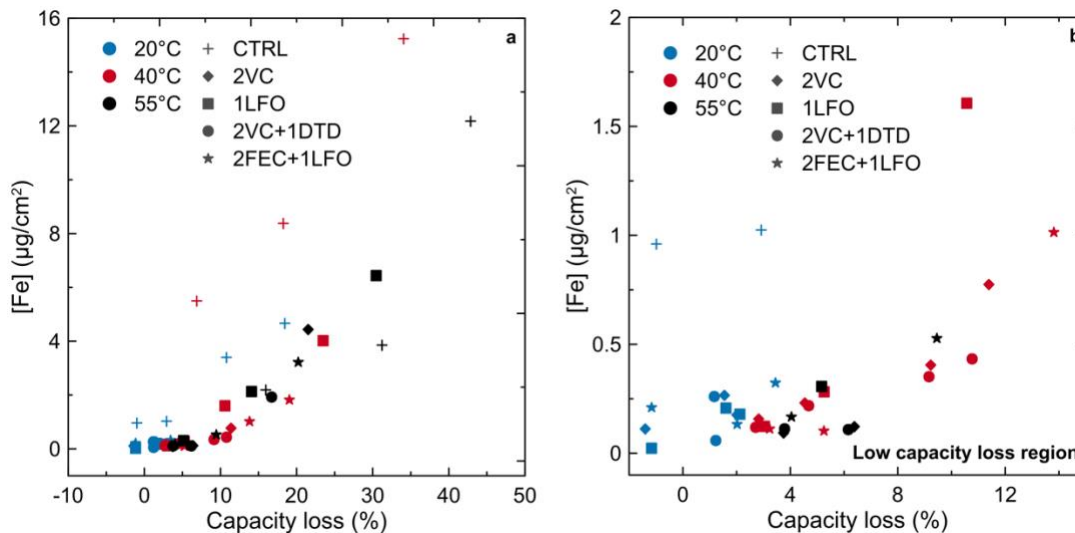


Figure 4.12: (a) Concentration of Fe detected on the negative electrode versus percent capacity loss for the various electrolyte additives and cycling temperatures considered in this work. All points are C/3:C/3 cycling rate. (b) Panel (a) magnified to show the low capacity loss region (15% capacity loss or less).



## 4.5 MEASURING PARASITIC REACTIONS WITH ISOTHERMAL MICROCALORIMETRY

Isothermal microcalorimetry has previously been employed as an effective tool to screen for promising electrolyte additives in NMC/graphite chemistries, as well as to further understand the degradation and failure of cells. In this Section, these techniques (introduced in CHAPTER 2) will be further developed and applied to the LFP/graphite chemistry.

### 4.5.1 Measuring the Entropy change of Li intercalation into Graphite and Mean Field Theory Calculations

Before applying the charge-discharge method (see CHAPTER 2) to extract parasitic heat flow in LFP/graphite cells, heat flow features originating from the lithiated graphite will be explored. Figure 4.13a shows voltage versus capacity for one cycle of an LFP cell cycled inside the calorimeter (2VC electrolyte, 1.5 mA current,  $\sim C/150$  rate), and the corresponding measured heat flow. Due to the flat voltage curve of the LFP material, features from the graphite can be seen during charge and discharge of this cell. The voltage plateaus of the graphite stage  $2L \rightarrow 2$  and stage  $2 \rightarrow 1$  transitions can clearly be seen in Figure 4.13a<sup>249</sup>, and are indicated in the Figure. The relatively large heat flow measured over the stage  $2L \rightarrow 2$  transition is primarily due to entropy changes. This change in entropy can be estimated using a simple lattice-gas model argument, detailed below.

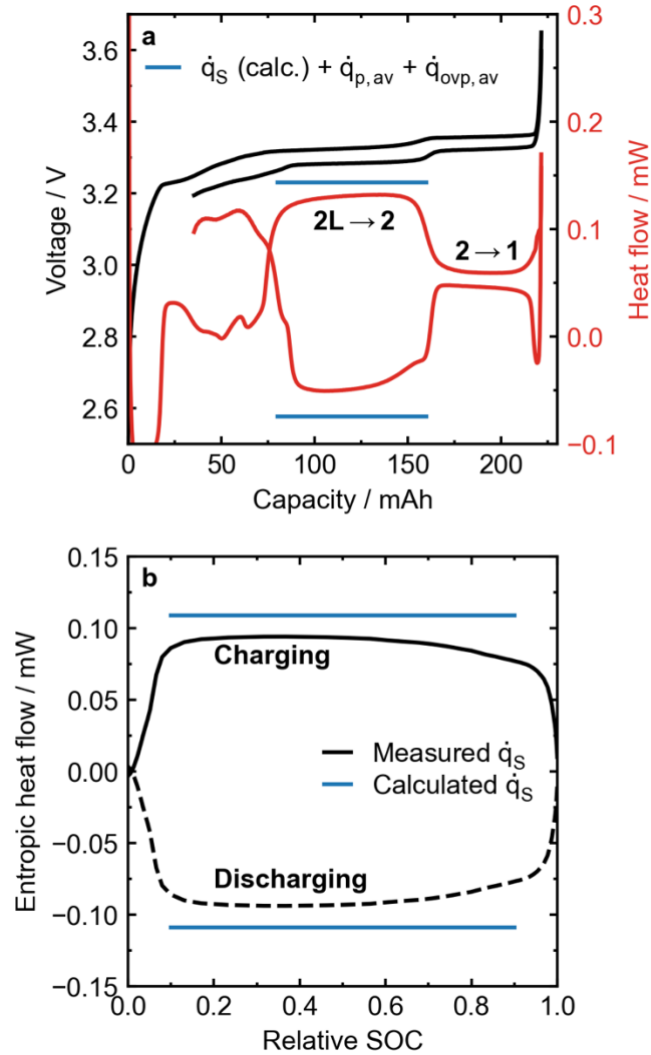


Figure 4.13: (a) Voltage versus capacity for an LFP/graphite cell with 2% VC in the electrolyte over a full cycle between 2.5 V and 3.65 V at  $\sim C/150$  rate, and the corresponding measured heat flow as a function of capacity. Calculations of the expected heat flow due to entropy changes for the graphite 2L  $\rightarrow$  2 transition on both charge and discharge are shown (blue lines). (b) Entropic heat flow contribution versus relative state of charge over the stage 2L  $\rightarrow$  2 graphite plateau as extracted using the charge-discharge method (black, described in the text) compared to the lattice-gas mean field theory calculation (blue).

Stage 2L and stage 2 occur at  $x=0.25$  and  $x=0.5$  in the  $\text{Li}_x\text{C}_6$  system, respectively. In the stage 2 phase, Li *completely* fills every third layer of the graphite host in an ordered arrangement avoiding near-neighbour interactions with each other. In the 2L phase, Li is only half-filled on every third layer of the graphite and is randomly distributed on the lattice

while still avoiding near-neighbour interactions. The phase diagram for the  $\text{Li}_x\text{C}_6$  system is shown in Figure 4.14. In the 2L phase, the random distribution of Li on the lattice leads to a configurational entropy:

$$S = k \ln \Omega, \quad 4.1$$

where  $k$  is Boltzmann's constant and  $\Omega$  is the multiplicity of the state. There exist three identical lattice sites in a gallery between graphene layers for Li to be intercalated, denoted A, B, and C sites<sup>250,251</sup>. In a completely full layer, Li will fill all of one type of site, i.e. all A sites. In the 2L stage, however, Li can occupy each of the A, B, and C sites, still avoiding near-neighbour interactions as long as each of the three sublattices are 1/6 full. **Error! Reference source not found.** Figure 4.15 illustrates the A, B, and C intercalation sites for Li on the graphite lattice. In Figure 4.15b**Error! Reference source not found.**, a completely full Li layer is shown, where Li occupies the A sites. An identical configuration could be achieved with Li occupying B sites or C sites. Figure 4.15c**Error! Reference source not found.** shows a lithium layer in stage 2L, where Li is randomly distributed across A, B, and C sites. Here, each of the A, B, and C sites are 1/6 filled, and the layer as a whole is 1/2 filled.

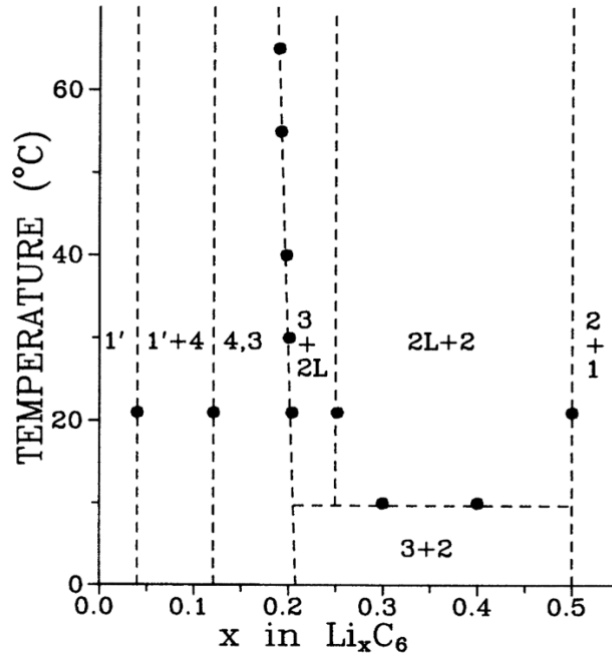


Figure 4.14: Phase diagram for  $\text{Li}_x\text{C}_6$  at different temperatures. Regions with either one stage or coexisting stages are labelled. Reproduced with permission from Reference <sup>51</sup>.

The random configuration of Li in the stage 2L phase leads to an approximate configurational entropy

$$S_{2L} = \frac{3}{2} Nk \left[ \frac{1}{6} \ln \frac{1}{6} + \frac{5}{6} \ln \frac{5}{6} \right], \quad 4.2$$

where  $N$  is the total number of available sites, and  $k$  is Boltzmann's constant. The factor of  $3/2$  accounts for the fact that there are three sub-lattices on each layer, and only half of the available layers are filled with lithium. Since the stage 2 phase is ordered, it will have a configurational entropy of zero. The change in entropy over the stage  $2L \rightarrow 2$  transition is therefore

$$\frac{dS}{dx} \approx \frac{\Delta S}{\Delta x} = -\frac{S_{2L}}{0.25} \quad 4.3$$

This change in entropy can be converted into a heat flow that we would expect to see on charge and discharge in the calorimeter:

$$\dot{q}_s = \frac{IT}{e} \frac{ds}{dx} = \pm 0.109 \text{mW}, \quad 4.4$$

where  $I$  is the current ( $\pm 1.5$  mA),  $T$  is the temperature (313.1500 K), and  $e$  is the electron charge. This calculation ignores any contribution to the entropy from the LFP positive electrode, because the  $\text{LiFePO}_4$  and  $\text{FePO}_4$  phases<sup>252</sup> have either virtually full or virtually empty sites for lithium so each will have zero configurational entropy. Hence there will be no change in entropy of the LFP electrode over any change in state of charge of the cell. Lines are added to Figure 4.13a over the graphite  $2L \rightarrow 2$  transition region showing the expected heat flow based on the simple lattice gas calculation, also accounting for average heat flow contributions from parasitic reactions and voltage polarization, to be detailed below. While this calculation slightly over-estimates the measured heat flow in this LFP/graphite cell, it comes rather close given the assumptions that were made in this calculation.

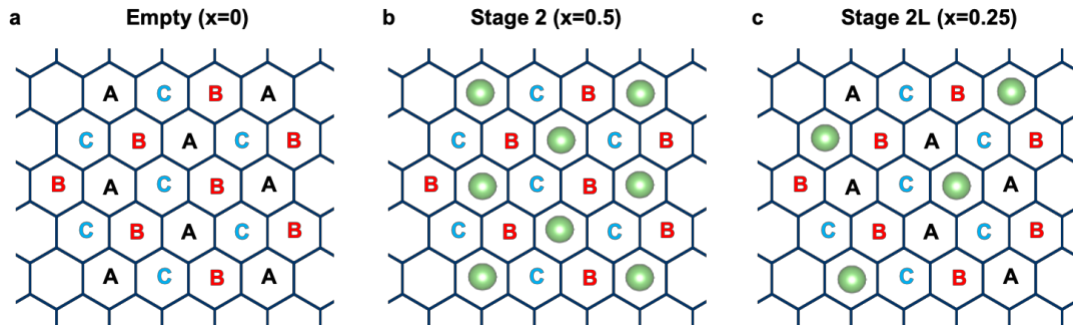


Figure 4.15: Demonstrating the lattice sites A, B, and C for the intercalation of lithium into graphite. (a) Empty lattice showing all available intercalation sites. (b) Stage 2 phase, demonstrating a full Li layer occupying A sites (equivalent configurations can be achieved by

filling only B sites or only C sites). (c) Stage 2L phase demonstrating the random distribution of Li across A, B, and C sites. Each of these sites are (approximately) 1/6 full.

Figure 4.13b again shows the lattice gas entropy calculation over the  $2L \rightarrow 2$  transition, this time as a function of relative state of charge over this plateau, compared to the extracted entropic heat flow using the charge-discharge method (detailed below). This shows the lattice gas calculation deviates from the measured entropic heat flow by only a small amount, on the order of  $\sim 10 \mu\text{W}$ . While this is already a very good agreement, a more rigorous treatment of the entropy changes in graphite as Li is intercalated and deintercalated, for example considering the details of short range ordering<sup>253</sup>, would give an even better agreement with the measured entropic heat flow.

There is no configurational entropy change between stage 2  $\text{LiC}_{12}$  and stage 1  $\text{LiC}_6$  as both have zero configurational entropy. Similarly, there is no configurational entropy change between  $\text{LiFePO}_4$  and  $\text{FePO}_4$ . This means that the second term on the right-hand side of Equation 2.5 should be zero when the LFP/graphite cell is in the stage 2 to stage 1 coexistence region and therefore the measured heat flow should be the same during charge and discharge. Figure 4.13a shows that the difference between the measured heat flow during charge and discharge in the stage 2 to stage 1 coexistence region is only about  $20 \mu\text{W}$  (approximately zero, as predicted), **much** smaller than the difference between charge and discharge heat flows in the stage 2L to stage 2 coexistence region which is about  $190 \mu\text{W}$ . In fact, in Figure 4.13, the difference between the charge and discharge heat flows in the stage 2-stage 1 coexistence region is close to zero for a cell cycled repeatedly only over that portion of the V-Q curve. This gives further support for the lattice gas evaluation of

the entropy changes provided above to explain the measured heat flow signals in Figure 4.13.

#### 4.5.2 Measuring parasitic heat flow for LFP/graphite cells with different electrolyte additives and different levels of water contamination

The charge-discharge method of extracting the average parasitic heat flow over a cycle (described in detail in CHAPTER 2) works particularly well for NMC/graphite chemistries where the voltage curve is relatively linear as a function of capacity at high voltage, allowing for the design of protocols that probe parasitic reactions at successively higher upper cut-off voltages. This method is not possible for LFP/graphite given the flat voltage curve of LFP. Here, a modified charge-discharge method was adopted where the voltage cut-offs for the cycling protocol were determined by the graphite features visible in the LFP/graphite voltage curve. Figure 4.16 shows the full protocol that was used to determine parasitic heat flow. Voltage versus capacity is shown in black while measured heat flow versus capacity is shown in red. Cells were cycled three times over the graphite stage 2L  $\rightarrow$  2 voltage plateau, followed by three cycles over the stage 2  $\rightarrow$  1 voltage plateau. This corresponds to voltage limits of 3.275 V – 3.350 V for the 2L  $\rightarrow$  2 plateau, and 3.305 V – 3.400 V for the 2  $\rightarrow$  1 plateau. Cells were cycled at a constant current of 1.5 mA or approximately C/150 to limit contributions to the heat flow from overpotential and entropy changes. Figure 4.16 demonstrates the stability of the measured heat flow over the different graphite plateaus.

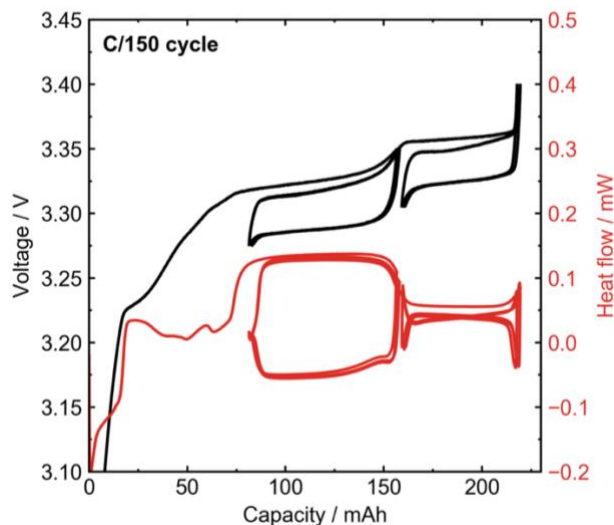


Figure 4.16: Full cycling protocol to determine parasitic heat flow in LFP/graphite cells. Voltage versus capacity is shown as well as the corresponding heat flow versus capacity. Cycling test was completed at 40°C and a current of 1.5 mA (~C/150) for both charge and discharge.

Typically, experiments measuring parasitic heat flow using the charge-discharge method show the heat flow as a function of voltage to demonstrate the effect of high voltage on parasitic reactions. However, in the case of LFP/graphite, high cell voltage was not a concern. It is more convenient to present the heat flow in LFP/graphite cells as a function of capacity, or the relative state of charge (SOC) over a narrow voltage range. Figure 4.17 shows the various heat flow components extracted using the charge-discharge method as a function of relative SOC for the lower graphite plateau (Figure 4.17a, 3.275 V – 3.350 V) and the upper graphite plateau (Figure 4.17b, 3.305 V – 3.400 V) for an LFP/graphite cell containing 2% VC in the electrolyte. In both panels, measured heat flow is shown in black, entropic heat flow is shown in yellow, overpotential heat flow is shown in blue, and the average parasitic heat flow is shown in red. The most noticeable difference in heat flow between the two voltage ranges is the difference between the entropic heat flow components. The large entropic heat flow in Figure 4.17a is due to the large difference in



entropy in the graphite stage  $2L \rightarrow 2$  transition as discussed above. The entropic heat flow in the 3.305 V – 3.400 V range averages around zero. Again, this is expected because this voltage range corresponds to the graphite stage  $2 \rightarrow 1$  transition, which are both ordered phases and have zero configurational entropy.

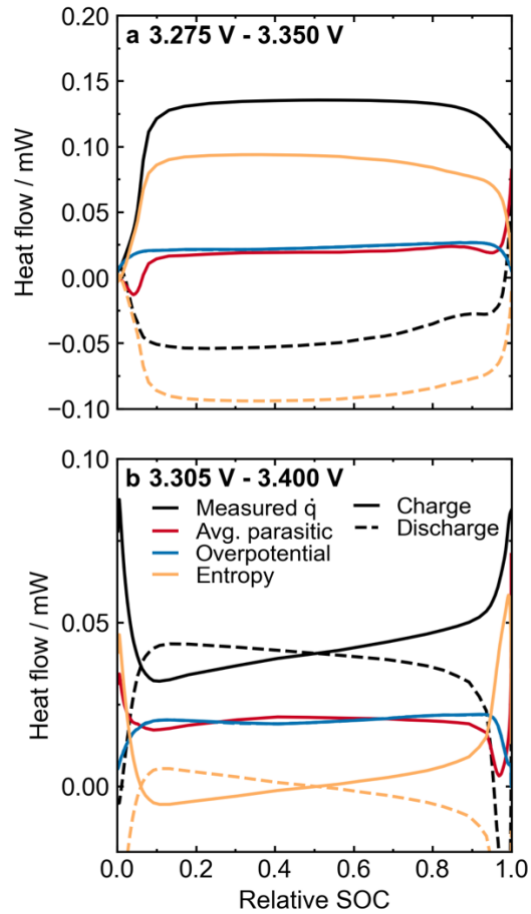


Figure 4.17: Extracted components of the heat flow for (a) the lower graphite plateau 3.275 V – 3.350 V, and (b) the upper graphite plateau 3.305 V – 3.400 V for an LFP/graphite cell cycled at 40°C with a current of 1.5 mA ( $\sim C/150$ ). Entropy and overpotential contributions are shown for both charge and discharge, while the average parasitic heat flow for the full cycle is shown. Note the differences in the vertical scale between panels a) and b).

The overpotential heat flow measured over both graphite plateaus is relatively large in the LFP/graphite system. Glazier et al. found that the overpotential heat flow for NMC 532/graphite cells cycled above 4.0 V was typically  $< 10 \mu\text{W}$ <sup>127,201</sup>, while the overpotential

heat flow in the LFP cells shown here is on the order of  $\sim 20 \mu\text{W}$ , approximately the same as the average parasitic heat flow. It would be desirable to lower the overpotential heat flow contribution such that it is well below the magnitude of the parasitic heat flow. However the relatively large voltage hysteresis seen in the LFP/graphite cells (see Figure 4.16) would mean very low currents would have to be used ( $< 1.0 \text{ mA}$ ), making these experiments prohibitively long. The currents used in this experiment present a compromise between experimental time and reduction of noise in determining the parasitic heat flow.

Figure 4.18 shows parasitic heat flow as a function of relative SOC for all cycles for cells with Control electrolyte (CTRL). Cycles on the different graphite plateaus are specified by different colours. For all cycles in the control electrolyte, a massive parasitic heat flow is seen ( $> 0.7 \text{ mW}$  for all cycles). Parasitic heat flow decreases slightly over the first cycles as SEI layer matures further<sup>254</sup>. Parasitic heat flow increases during the first cycle to the upper graphite plateau (3.305 V – 3.400 V) after cycling on the lower plateau (3.275 V – 3.350 V). This increase could in part be due to the more strongly reducing environment of the negative electrode (lower voltage versus  $\text{Li}^0$ ) at this slightly higher full cell voltage (see Figure 1.8).

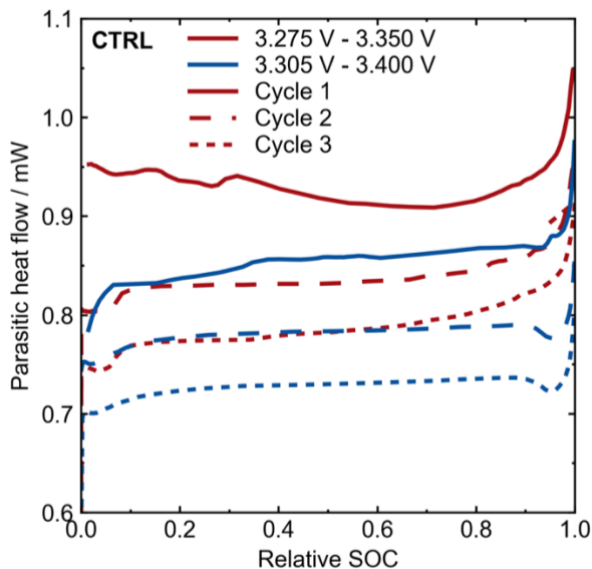


Figure 4.18: Parasitic heat flow versus relative state of charge for all cycles with the control electrolyte. Cells were cycled at 40°C with a current of 1.5 mA (~C/150). Three cycles over each graphite plateau (specified by the full cell voltage range) are shown.

The massive parasitic heat flow with Control electrolyte in LFP/graphite cells at 40°C reflects what was seen in the long-term cycling results. Recall in Figure 4.6, Control cells cycling at 40°C, C/3:C/3 lost 10% of their initial capacity in only 50 cycles, while cells containing most additives took almost 600 cycles to reach 90% capacity. Additionally, in 60°C storage, cells with Control electrolyte showed complete self-discharge in <500 hours (Figure 4.8). This suggests the existence of some high-rate parasitic reaction in LFP/graphite cells with control electrolyte at elevated temperature that leads to extremely rapid capacity fade. The dependence on the choice of positive electrode suggests a complex cross-talk reaction that occurs specifically in LFP/graphite cells.

Measured parasitic heat flow was dramatically lower in LFP cells containing electrolyte additives. Figure 4.19 shows parasitic heat flow versus relative SOC for cells containing 2VC, 1LFO and 2VC + 1DTD additives. Figure 4.19a-c show the cycles over the lower

graphite plateau (3.275 V – 3.350 V), while Figure 4.19d-f show the cycles over the upper graphite plateau (3.305 V – 3.400 V). The first feature to note in these cycles is that the parasitic heat flow for all cells was much lower than for cells with the control electrolyte (Figure 4.18); the parasitic heat flow for all cells is in the neighbourhood of 20  $\mu\text{W}$ , in contrast to 700  $\mu\text{W}$  – 1000  $\mu\text{W}$  in the Control electrolyte. In the cycles on the lower graphite plateau, all cells show approximately the same parasitic heat flow. However, as cycling progresses, some differences start to emerge. By the final cycles in the upper voltage range, the 1LFO electrolyte had the highest parasitic heat flow, followed by 2VC, and finally 2VC + 1DTD with the lowest parasitic heat flow by the end of cycling. The differences were small, on the order of just a few  $\mu\text{W}$ , but the good agreement of the pair cells adds confidence in discussing the differences in parasitic heat flow between different additives.

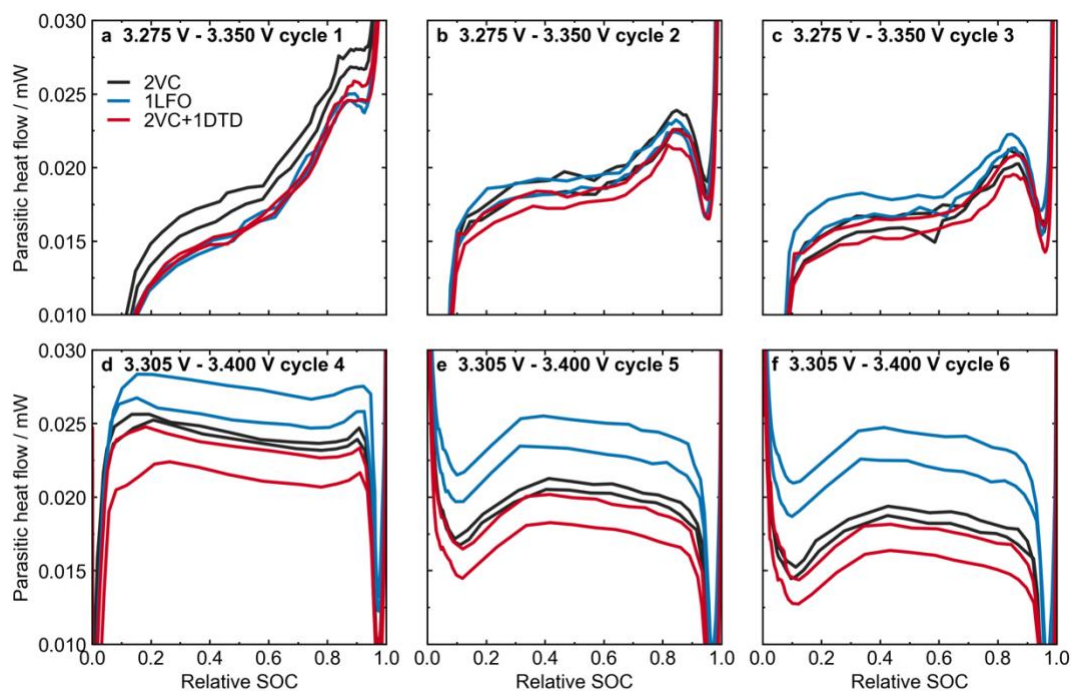


Figure 4.19: Parasitic heat flow versus relative state of charge for LFP cells with different electrolyte additives. Cells were cycled at 40°C with a current of 1.5 mA ( $\sim C/150$ ). (a-c) Cycles between 3.275 V and 3.350 V. (d-f) Cycles between 3.305 V and 3.400 V.

Comparing the parasitic heat flow observed for different additives to the long-term cycling results in Figure 4.6, good correlation is found. Of the different additives studied in this Chapter, 2VC and 2VC+1DTD showed the best capacity retention in long-term cycling corresponding to the lowest measured parasitic heat flow. Cells with 1LFO had worse capacity retention compared to the VC-containing cells, and an associated higher parasitic heat flow in the calorimetry experiments. However, while the ranking of long-term cycle performance of these cells was correctly mirrored in the calorimetry experiments, the relatively poor long-term performance of the 1LFO cells are somewhat surprising given the calorimetry result. While 1LFO had a higher parasitic heat flow, it was only higher by a few  $\mu\text{W}$  compared to the VC-containing cells which should in principle correspond to a smaller difference in long-term capacity retention.

Looking closer at the cycling results in Figure 4.6, the capacity retention for 1LFO is very similar to that of 2VC and 2VC + 1DTD in the first 100 cycles or so. Beyond this point, the capacity fade started to diverge from the other additives. By a rough calculation, 100 cycles at C/3 rate corresponds to about 600 hours of testing time, which is similar to the total time of the calorimetry experiment (~770 hr). It is possible, then, that if the calorimetry cycling were to have continued, the difference in parasitic heat flow between 1LFO and the VC-containing cells would have increased further, corresponding to the diverging capacity fade curves. To rank the long-term performance of additive systems that perform very well, i.e. to better differentiate between 2VC and 2VC+1DTD, it may be necessary to increase the number of cycles in the calorimetry experiment for future experiments.

This presents a challenge for techniques that aim to rank or predict lifetimes of Li-ion cells in a shorter time than conventional charge-discharge cycling. One possible approach could be to carry out the microcalorimetry experiments after a considerably longer conditioning period, possibly on the order of 1000 hr. This would give time for the SEI to mature, and possible differences between different electrolytes in the parasitic heat flow measurement would be more obvious. As a comparison, a typical cycling protocol for a UHPC experiment is 20 cycles at C/20 rate operating at 40°C. This corresponds to a test time of ~800 hours, which is on the same order of time as the calorimetry experiments presented here. Now, referring back to the UHPC measurements from earlier, the CE values measured in LFP cells with 1LFO were very similar to 2VC and 2VC+1DTD cells after

~15 cycles, and in fact the charge endpoint capacity slippage values were lower (Figure 4.3 and Figure 4.4). This is again surprising given the significant difference in long-term cycling. This again may suggest that longer cycling times are required for these “rapid screening” techniques to properly reflect and anticipate the long-term cycle life of LFP cells.

The exact origin of the poor performance of LFP/graphite cells with 1LFO is not entirely clear. It is possible that LFO does not passivate the graphite electrode as effectively as VC or DTD, and over time Fe is able to deposit on the graphite and catalyze excessive SEI formation. One argument in favour of this explanation is that more Fe was detected on negative electrodes from 1LFO cells after cycling compared to VC-containing cells (Figure 4.10). It is possible that the capacity fade mechanism in 1LFO is similar in origin to Control electrolyte, but more subdued compared to what is seen in cells with Control. Further experiments, including electrolyte analysis of aged cells, would be required to make a more definitive statement about the origin of capacity fade in LFP/graphite cells with 1LFO electrolyte, which is outside the scope of this work. For now it suffices to say that the parasitic heat flow correctly ranks the long-term performance of these cells.

Earlier in this Chapter it was shown that removing excess water led to a significant improvement in capacity retention for cells with Control electrolyte and 1LFO electrolyte, but less obvious improvements were seen in cells containing other electrolyte additives such as VC (see Figure 4.6, for example). However, in the case of cells with Control electrolyte, capacity retention was still extremely poor even after water was removed,

suggesting that a high rate of parasitic reactions still occur. Therefore, for this discussion only cells containing electrolyte additives will be considered going forward.

Isothermal microcalorimetry measurements were carried out to investigate the effect of excess water content on parasitic heat flow. Figure 4.20 shows parasitic heat flow versus relative SOC in selected cycles for cells containing 2% VC after different drying conditions. On the lower graphite plateau (3.275 V – 3.350 V, Figure 4.20a-c), the difference in parasitic heat flow between the cells with and without excess water is very small, essentially negligible within pair cells. However, on the upper graphite plateau cycles (3.305 V – 3.400 V, Figure 4.20d-f), the parasitic heat flow for the cells dried at 120°C was higher than the cells dried at lower temperature with excess water. While the difference in parasitic heat flow was small, it was consistent between the pair cells in the higher voltage range.



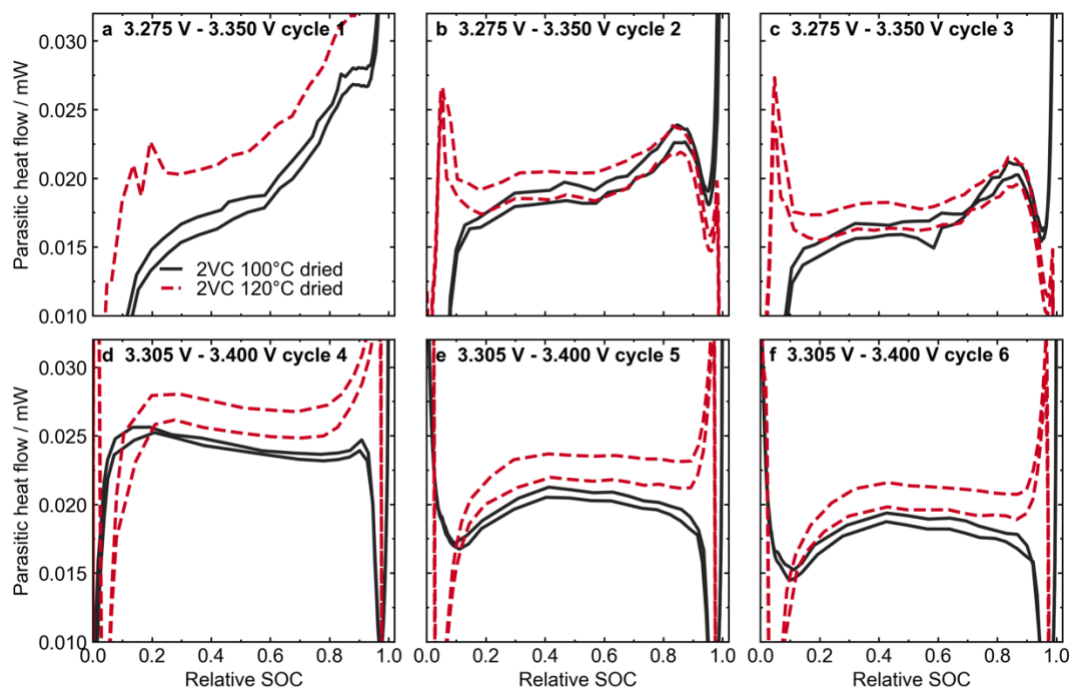


Figure 4.20: Comparing parasitic heat flow at different vacuum drying temperatures for LFP cells with 2VC in the electrolyte. Pair cells are shown here for both drying conditions. Cells were cycled at 40°C with a current of 1.5 mA (~C/150). (a-c) Parasitic heat flow versus relative state of charge for the cycles between 3.275 V and 3.350 V. (d-f) Parasitic heat flow versus relative state of charge for the cycles between 3.305 V and 3.400 V.

Similar trends between drying temperatures were seen in the cells with other additives that were investigated. Figure 4.21 shows the average parasitic heat flow over each full cycle for cells with 2VC, 2VC+1DTD, and 1LFO additives in cells dried at 100°C and 120°C. Error bars in Figure 4.21 indicate the absolute difference in average parasitic heat flow between pair cells for each condition, when available. For cells with 2VC electrolyte, higher parasitic heat flow was seen on the upper voltage plateau in cells where excess water was removed, as was also seen in the complete cycle data in Figure 4.20. There may also be slightly higher parasitic heat flow in the 1LFO cells dried at 120°C, but the variation in 1LFO pair cells was relatively large, meaning this difference cannot be stated with certainty. In the 2VC case at least, this suggests that slightly fewer parasitic reactions occur

in cells with these electrolyte systems when a relatively large amount of water (~500 ppm) is present in the cell, seemingly contradicting the long-term cycling results. In cells with the 2VC+1DTD system, however, roughly the same parasitic heat flow is seen between the two drying temperatures, suggesting that this electrolyte system is less sensitive to water contamination. It should be noted in this case that the differences in parasitic heat flow are very small here, close to the limits of the microcalorimeter.

While the parasitic heat flow values in Figure 4.21 appeared to contradict the long-term cycling results in Figure 4.6, complementary results to the calorimetry studies were seen in the UHPC experiments presented earlier. Differences in CE (Figure 4.3) were very small between cells with and without water, though the CE was slightly lower (worse) in 2VC and 2VC+1DTD cells after drying at the higher temperature. Cells with 1LFO dried at 120°C appeared to have a slightly higher CE than 1LFO with water contamination, agreeing with long-term cycling results at 40°C. Additionally, the higher drying temperature increased the charge endpoint capacity slippage compared to cells dried at 100°C (refer to Figure 4.4). A higher charge endpoint capacity slippage suggests more parasitic reactions occurring at the positive electrode<sup>244</sup>, which agrees with the parasitic heat flow observed in Figure 4.20 and Figure 4.21, at least in the 2VC case. It is likely that more reactions occur at the negative electrode, the products migrate to the positive electrode and react further in a “cross-talk” reaction or redox shuttle reaction which is reflected in the higher charge endpoint capacity slippage that was observed.

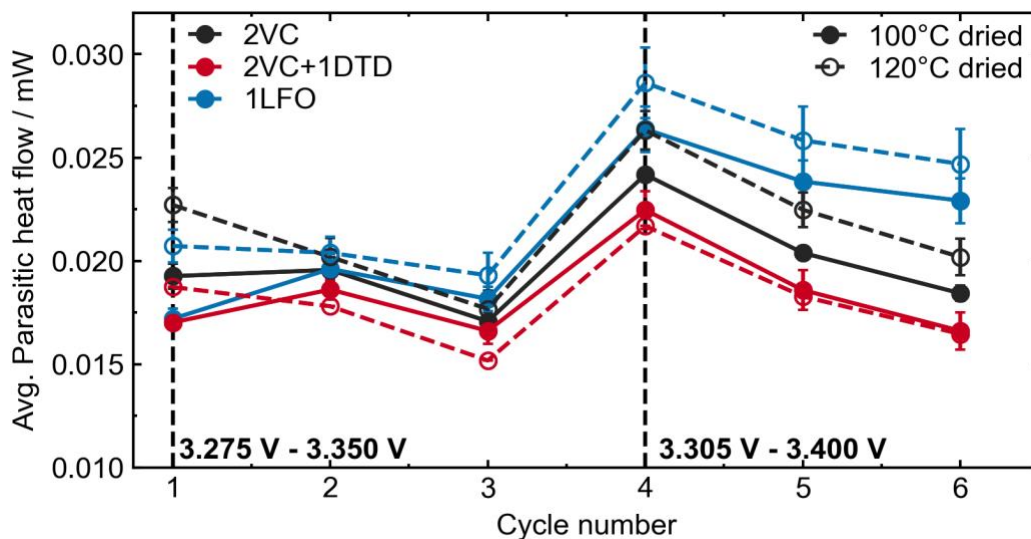


Figure 4.21: Summary of average parasitic heat flow versus cycle number for LFP/graphite cells vacuum dried at different temperatures with different electrolyte additives as indicated in the Figure. All cells were cycled at 40°C with a current of 1.5 mA (~C/150).

In the UHPC cycles at 40°C, most cells dried at 120°C showed worse capacity retention than cells dried at 100°C (Figure 4.5), which agrees with the slightly higher parasitic heat flow that was observed in Figure 4.20 and Figure 4.21. This suggests that when comparing cells with and without water contamination the capacity fade at low rate (C/20 and below, i.e. UHPC and calorimetry experiments) may be of a different origin than at higher rates (~C/3).

## 4.6 DISCUSSION

Figure 4.22 summarizes the cycling, storage, and calorimetry results for cells with the selected electrolyte systems CTRL, 2VC, 1LFO, and 2VC+1DTD. As shown throughout this Chapter, the biggest improvement in performance as a result of higher drying temperature was in cells with control electrolyte. Cells with no electrolyte additives showed much better cycle performance at 40°C, higher CE, lower slippage, and better storage

performance when water was removed from the cell. Parasitic heat flow, interestingly, was higher in control cells dried at 120°C. This likely stems from the fact that cycle performance was still extremely poor in cells with control electrolyte, even with excess water removed. Therefore, the high parasitic heat flow observed in these cells does not come directly from water-related effects, but from other degradation modes that exist in this system. In cells with VC-containing electrolytes (2VC, 2VC+1DTD), water had less of an impact on performance. Performance in 40°C cycling and 60°C storage was virtually identical between cells at the two drying temperatures, and parasitic heat flow was marginally higher in cells dried at 120°C. For all cells with electrolyte additives, charge endpoint capacity slippage in UHPC cycling was higher when cells were dried at 120°C.

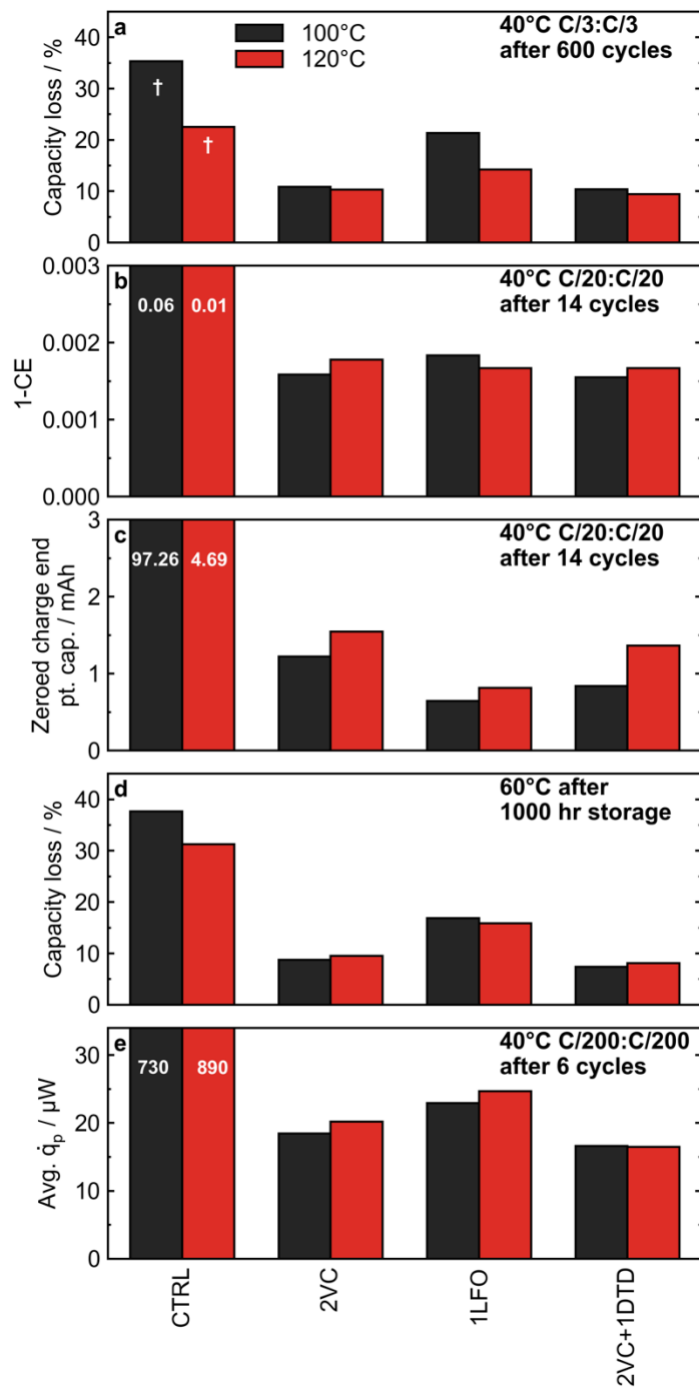


Figure 4.22: Summary of cycling and storage tests for key additives in cells with different vacuum drying temperatures. (a) Percent capacity loss after cycling at 40°C at C/3:C/3 rate for 600 cycles. The bars marked by † indicates only 300 cycles were completed. (b) Coulombic inefficiency (1-CE) at cycle 14 from UHPC cycles at 40°C, C/20 rate. (c) Charge endpoint capacity (zeroed at cycle 2) at cycle 14 from UHPC cycles at 40°C, C/20 rate. (d) Percent irreversible capacity loss after 1000 hr of OCV storage a 60 °C. (e) Average parasitic heat flow on the last cycle at 1 mA current in the calorimeter at 40°C.

There appears to be two distinct regimes for the influence of water in LFP/graphite cells: one where the electrodes are poorly passivated (CTRL and 1LFO electrolytes), and another when the electrodes are sufficiently passivated (VC and FEC-containing electrolytes). In the case where the electrodes were not effectively passivated, excess water contamination led to Fe dissolution from LFP, and poor cycling performance was observed. On the other hand, when the electrodes were effectively passivated, the presence of water (up to 500 ppm) had no little effect, and in some cases led to slightly improved performance under certain test conditions.

There has been some evidence in the literature that small amounts of intentionally added water could improve long-term performance of Li-ion cells, primarily with NMC-based chemistries. For example, Burns et al. found that intentionally adding 100 ppm of water to an NMC/graphite cell containing VC as an additive reduced coulombic inefficiency ( $CIE = 1 - CE$ ) and charge endpoint slippage compared to a VC-containing cell without added water, although the effects were minor<sup>255</sup>. Recall in Figure 5 that charge endpoint capacity slippage was lower in cells dried at 100°C, with the exception of the control electrolyte. Bernhard et al. showed that the addition of water to an alkyl carbonate electrolyte lead to an excess of H<sub>2</sub> production on the initial formation cycle of a graphite electrode, which further lead to the production of CO<sub>2</sub><sup>256</sup>. This CO<sub>2</sub> can then react to form lithium formate and lithium carbonate which can help passivate the graphite electrode against further electrolyte reduction<sup>257</sup>.

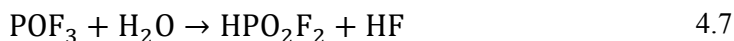
Some of the benefit of adding water, intentional or otherwise, could come from the decomposition of the LiPF<sub>6</sub> salt with water. LiPF<sub>6</sub> is known to decompose in an equilibrium reaction



The decomposition product PF<sub>5</sub> then can react with water



The POF<sub>3</sub> can then further react with water to form PO<sub>2</sub>F<sub>2</sub><sup>-</sup> anions



It was shown by Stich et al. that the reaction between PF<sub>5</sub> and water producing POF<sub>3</sub> is a fast step, and that significant concentrations of HPO<sub>2</sub>F<sub>2</sub> were detected in a carbonate electrolyte contaminated with 70 mmol/L of water<sup>258</sup> after only a few hours of storage. The addition of LiPO<sub>2</sub>F<sub>2</sub> (LFO) has been shown in previous work to improve cell performance in NMC chemistries<sup>259,260</sup>, and in this work, LFO improved capacity retention in LFP/graphite cells compared to the control electrolyte. It is therefore possible that cells dried at 100°C with excess water contamination would have some concentration of PO<sub>2</sub>F<sub>2</sub><sup>-</sup> anions in the electrolyte after the wetting step and before the first formation cycle. The small amount of PO<sub>2</sub>F<sub>2</sub><sup>-</sup> anions could have a synergistic effect with other additives and help explain the slightly better performance of some cells dried at 100°C. Further, the presence of higher concentrations of HF in the water-contaminated cells may lead to the formation of LiF on the graphite anode, which may further passivate against parasitic reactions<sup>261</sup>.

Addressing the results of the calorimetry experiments, there are a few possible explanations for increased parasitic heat flow in “dry” (120°C dried, <100 ppm H<sub>2</sub>O) compared to “wet”

(100°C dried, 500 ppm H<sub>2</sub>O) LFP/graphite cells in the case of the 2VC electrolyte. It is possible that there are indeed more parasitic reactions that occur at the LFP cathode when water is removed. This may not be due to the water itself, but instead some other reaction induced by the high temperature heating, such as slight degradation of the PVDF binder as suggested by Huttner et al.<sup>242</sup> As well, water can modify the graphite SEI via reaction with the LiPF<sub>6</sub> salt, becoming rich in LiF and phospho-fluorides<sup>261–265</sup>, as described in more detail above. An SEI layer rich in LiF may be more passivating - reducing the amount of parasitic reactions - but also highly resistive to Li ion transport<sup>266</sup>, possibly leading to impedance growth. This explanation falls in line with the experimental results in this chapter combining high-rate long-term cycling, low-rate UHPC cycling, and low-rate microcalorimetry measurements.

The use of isothermal microcalorimetry measurements to probe parasitic reactions has been consistently correct in ranking the long-term cycle life of Li-ion cells<sup>127,198,200,201,267,268</sup>. Typically, higher parasitic heat flow in a given voltage range corresponds to shorter cycle life, all other conditions being equal. One notable exception, and possibly the only currently known exception to this rule of thumb in the literature, can be found in Glazier et al.<sup>199</sup>. That study compared the parasitic heat flow in various compositions of NMC materials with different coatings on the positive electrode active material. In particular, Al<sub>2</sub>O<sub>3</sub>-coated LiNi<sub>0.6</sub>Mn<sub>0.2</sub>Co<sub>0.2</sub>O<sub>2</sub> (NMC622)/graphite cells showed the highest parasitic heat flow, but had the best long-term cycle life. Like that seen in the LFP cells in this study, those cells also had higher charge endpoint capacity slippage as measured in UHPC experiments. Glazier et al. suggested that a reversible “shuttle”-like mechanism in this



particular cell chemistry could explain the higher observed parasitic heat flow, while not negatively impacting reversible capacity loss. A shuttle reaction has already been hypothesized for Control electrolyte in LFP/Graphite cells here as the cause of the massive parasitic heat flow that was observed (Figure 4.18), and its existence has been confirmed in a recent publication by Boulanger et al.<sup>269</sup> It is therefore possible that shuttle reactions are present at smaller rates in cells with electrolyte additives, and that the initial water content in these cells could impact the degree of shuttle activity.

Another explanation for the behaviour observed in the microcalorimetry experiments is that the initial structure of the SEI and subsequent measured parasitic heat flow may not determine the long-term cycle life of LFP/graphite cells, but rather the evolution of the SEI that determines the lifetime of the cell. Both UHPC and microcalorimetry experiments probe parasitic reactions at the beginning of life of the LFP/graphite cells studied here, capturing the initial characteristics of the SEI layer with the expectation that these initial observations will reflect the long-term cycle life. However, as the cells age, the structure of the SEI evolves<sup>270</sup>. While the initial state of the cells is important for determining cycle life (take for example the Control electrolyte in LFP compared to cells with electrolyte additives), more subtle changes as the cells age should also be taken into account. In the case of water content in LFP/graphite cells, it is possible that the effects of water contamination on the structure and passivating quality of the SEI take longer to emerge than the first ~500 hours of the cell's life. Previous studies by Joshi et al. have shown that transition metal deposition on a graphite electrode affects the long-term evolution of the SEI layer<sup>271</sup>, and Fe deposition has been seen at least to some extent in all of the electrolyte

systems studied here<sup>272,273</sup>. This longer-term evolution was also seen to an extent when looking at different electrolyte additives (Figure 4.19). The 1LFO electrolyte initially had very similar parasitic heat flow compared to the 2VC and 2VC+1DTD systems, and only after several cycles (at  $\sim C/100$ ) did noticeable differences in the parasitic heat flow emerge. While techniques such as isothermal microcalorimetry are not typically used for long-term cycling experiments, in the future they may need to be modified to capture more subtle effects in LFP/graphite cells. For example, the temperature of the calorimeter could be increased to accelerate cell aging and the evolution of the SEI to a more “steady-state” composition. Further, the number of conditioning cycles used before calorimetry experiments could be increased, and parasitic heat flow would then be probed after this “burn-in” period. The existing techniques for ranking cell lifetime with isothermal microcalorimetry were effective for comparing different electrolyte additives in LFP/graphite cells, but more subtle effects such as water content require more careful investigation and tuning of existing protocols.

#### **4.7 COMPARING THE PERFORMANCE OF LFP TO NMC**

Recently, Harlow et al. demonstrated that exceptionally long lifetimes could be achieved in NMC532/graphite Li-ion cells if single crystal particle morphologies were used for the positive electrode and an appropriate additive system was chosen<sup>239</sup>. It was estimated that in an electric vehicle application, these cells would last a total driven distance of 1,200,000 km before reaching 70% capacity when cycled at 40°C in a worst-case scenario where every drive was of maximum range. The LFP/graphite cells used in this Chapter (and throughout this Thesis) had the same artificial graphite material as the NMC cells in

Harlow et al., so the performance of these cells could be compared. Note that the cell designs differed appreciably with a positive electrode loading of 21.1 mg/cm<sup>2</sup> (4.2 mAh/cm<sup>2</sup>) for the NMC532 cells in Harlow et al., while the positive electrode loading was 12.4 mg/cm<sup>2</sup> (2.1 mAh/cm<sup>2</sup>) for the LFP cells studied here. This difference should favor the LFP cells.

Figure 4.23 compares the cycling performance of the LFP cells presented in this work (dried at 100°C) with the NMC cells in Harlow et al.<sup>239</sup> Figure 4.23a shows normalized capacity (cycle 5) versus cycle time for cycling at 40°C, and Figure 4.23b shows normalized capacity versus cycle time for cycling at 55°C. Charge and discharge rates are indicated in the Figure legend. Additionally, cycling results for commercial LFP from 3 vendors are shown. The additive system shown for the LFP/AG cells in this work and the NMC532/AG cells was 2VC + 1DTD (wt.%), although the solvent blend was slightly different for the LFP and NMC cells (see Ref. <sup>239</sup>). The electrolytes used in the commercial LFP cells were not specified. 2VC+1DTD was arguably the best additive system for LFP/Graphite of the candidates studied in this Chapter.

At both 40°C and 55°C, the NMC cells had much better capacity retention than all the LFP cells shown. Differences in removing residual water from LFP, if any, were insignificant compared to the difference in capacity retention with NMC. It was shown above in Figure 4.10 that Fe dissolution was virtually eliminated in LFP when the 2VC+1DTD electrolyte was used, so degradation resulting from Fe dissolution cannot be blamed for the relatively poor performance of LFP. Figure 4.23 shows that the commercial LFP cells, being charged

to 3.65 V, also perform worse than the NMC/graphite cells being charged to 4.3 V, indicating that even in cells optimized for commercial production, the high-temperature degradation of LFP is still a significant issue for this chemistry.

At this point, likely culprits for the increased capacity loss in LFP compared to NMC cells are parasitic reactions leading to Li inventory loss or possibly active material loss at the positive electrode. Alternatively, unique crosstalk reactions between NMC/graphite and LFP/graphite could contribute to the difference in capacity fade between the two chemistries. Even though the average operating voltage of the LFP/graphite cells was considerably lower than in the NMC/graphite cells, the surface area of the LFP cathodes are very high ( $\sim 15 \text{ m}^2/\text{g}$  vs  $\sim 0.4 \text{ m}^2/\text{g}$  for the NMC used in Ref. <sup>239</sup>) which could increase the rate of parasitic reactions in LFP. The question of LFP surface area will be considered in the next Chapter.

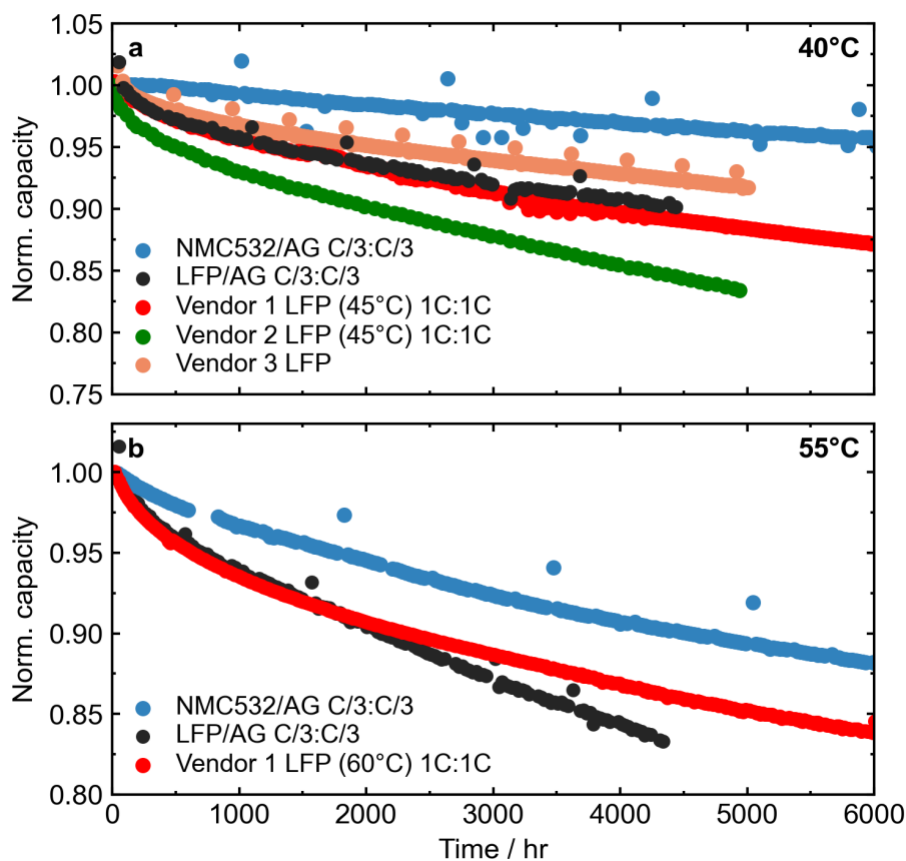


Figure 4.23: Comparing LFP/Graphite pouch cells to commercial LFP cells and NMC/Graphite pouch cells. Normalized capacity versus cycle time for cycling at (a) 40°C (unless specified otherwise in the legend) and (b) 55°C (unless specified otherwise in the legend) for the best LFP/AG cells studied in this work (dried at 100°C), commercial LFP cells, and single crystal NMC532/AG cells (see Ref. <sup>239</sup> for more details). Charge and discharge rates for each cell are indicated in the legend of each panel.

## 4.8 CONCLUSIONS

This Chapter surveyed the performance of LFP/graphite pouch cells under various conditions, including water contamination, different electrolyte additives, cycling conditions, and cycling temperatures. It was found that cells containing no electrolyte additives (control electrolyte) showed very poor performance, which could be improved if excess water was removed from the cell by vacuum drying at higher temperatures.

However, the performance cells with control electrolyte was still poor even after removing water, indicating poorly passivating SEI layers and Li inventory loss. On the other hand, cells containing electrolyte additives generally were not affected by ~500 ppm of water in the cell. All cells containing additives greatly outperformed the control electrolyte in all tests, regardless of water contamination level. In some tests, including UHPC and isothermal microcalorimetry cells containing water showed favorable metrics such as lower charge endpoint capacity slippage and slightly lower parasitic heat flow.

$\mu$ XRF measurements on aged graphite negative electrodes revealed significant Fe dissolution in cells containing control electrolyte at all cycling temperatures (20°C, 40°C, and 55°C). Removing water contamination virtually eliminated Fe dissolution in the control electrolyte at 40°C, and was reduced somewhat at 55°C. Most electrolyte additives tested successfully suppressed Fe dissolution regardless of water content in the cell. These results suggested that parasitic reactions other than Fe dissolution are responsible for capacity fade in LFP cells containing electrolyte additives or when water contamination is removed.

Isothermal microcalorimetry techniques were extended to the LFP/graphite chemistry. Existing charge-discharge methods of extracting the parasitic heat flow have been adopted to the LFP/graphite system using the distinct graphite staging plateaus for voltage limits in the cycling protocol. Entropy contributions due to 2L  $\rightarrow$  2 and 2  $\rightarrow$  1 graphite staging transitions have been estimated using simple lattice-gas mean field theory arguments, finding good agreement with measurement. Parasitic heat flow was then measured in

LFP/graphite cells with different electrolyte additives. Extracted parasitic heat flows for these cells agreed well with long-term cycling results at 40°C, confirming that isothermal microcalorimetry techniques can successfully be used to rank long-term performance between different electrolyte additive systems in the LFP/graphite system. Parasitic heat flow measurements for cells with different water contents did not correctly rank cells according to long-term cycling results, but did agree with charge endpoint slippage values observed in UHPC cycles.

Comparing cycling results with NMC/graphite cells with an identical graphite negative electrode showed that capacity fade is more severe in LFP at elevated temperature, despite a much lower operating voltage. While at this point the exact origin of the inferior performance of LFP cannot be elucidated, the various results presented in this Chapter have laid the groundwork for understanding this discrepancy and further improving the lifetime of LFP/graphite cells. The impacts of water contamination and Fe dissolution have been discounted as significant failure modes when effective electrolyte additives are employed. Further, several well-performing additive systems have been identified, and techniques such as isothermal microcalorimetry have been developed to screen these systems. The next Chapter will consider other approaches to further improve the lifetime of LFP/graphite cells.

## **CHAPTER 5 STRATEGIES FOR IMPROVING THE PERFORMANCE OF LFP/GRAPHITE CELLS**

This chapter contains material that has been published in peer-reviewed journals (J. Electrochem. Soc. **169** 050524 (2022), J. Electrochem. Soc. **169** 040560 (2022)), as well as material that is being prepared for submission to peer-reviewed journals, all primarily written by the author of this thesis. The author of this thesis conceived of, planned, and completed all data analysis for the experiments presented in this chapter under the supervision of Jeff Dahn. Helena Hebecker, Aidan Luscombe, and Ethan Eastwood assisted with making some of the Li-ion cells used in this Chapter. Aidan Luscombe and Michel Johnson assisted with Karl Fischer measurements. Ahmed Eldesoky completed  $\mu$ XRF measurements on aged cells. The author of this thesis prepared samples for cross-sectional SEM, and Yulong Liu completed the measurements. Marc Cormier wrote software that assisted in constructing plots in Figure 5.7. Discussions with Connor Aiken and Michael Metzger were valuable in shaping the interpretation of some results in Section 5.3.

### **5.1 INTRODUCTION**

The previous chapter presented initial studies of LFP/graphite pouch cells, mainly focusing on the impact of water contamination and different electrolyte additives on cell lifetimes at high temperature. The studies in Chapter 5 represented more of a broad survey,



establishing a baseline of understanding of degradation in the LFP/graphite chemistry, setting up for the more targeted studies that are described in this chapter. The impact of water contamination was found to be only noticeable when electrolyte additives were not used. Additionally, Fe dissolution and deposition was significantly suppressed by most electrolyte additives. Isothermal microcalorimetry (IMC), already successful in studying NMC/graphite cells, was found to be a valuable screening technique for the LFP/graphite chemistry as well, at least for different electrolyte additives. However, even with optimal drying conditions and electrolyte additives, the best LFP/graphite cells made in the previous chapter could not compete with optimized NMC532 cells operating to much higher voltages.

In this chapter, several different components of the cell are scrutinized to further understand degradation in the LFP/graphite system, and further improve high temperature lifetimes of these cells. The impact of LFP particle size and surface area, Li salts used in the electrolyte, and different graphite materials are all investigated in the following sections. In this chapter, all cells containing electrolyte additives used either 2VC or 2VC+1DTD additive systems. At the end of this chapter, the lessons learned from these studies will be combined to again compare a further optimized LFP/graphite cell to an NMC532 cell.

## **5.2 STUDYING THE EFFECT OF LFP PARTICLE SIZE ON LIFETIME**

It was postulated at the end of CHAPTER 4 that the high surface area LFP could contribute to parasitic reactions leading to capacity fade in LFP/graphite cells. Even if the electrolyte

itself was not particularly reactive to LFP due to its low voltage, parasitic reaction products produced at the negative electrode could migrate to the positive electrode and further react more readily at the positive electrode in a cross-talk type reaction. To study the impact of LFP particle size on lifetime, pouch cells composed of LFP material with different surface areas and particle sizes were tested. These materials were dubbed “low BET”, “medium BET”, and “high BET” LFP, referring to their specific surface area as measured from a Brunauer-Emmett-Teller (BET) experiment . In addition to long-term cycling, additional experiments were carried out to understand capacity fade in these cells as was done in the previous chapter, including IMC cycling experiments to measure parasitic heat flow,  $\mu$ XRF measurements of Fe deposition, and cross-sectional SEM measurements to probe microcracking in the LFP particles.

### 5.2.1 Water content and cycling results

Table 5.1: Physical properties of the different LFP materials studied in this work. Measurements were provided by the manufacturer of the materials (Pulead).

<b>Sample</b>	<b>BET surface area (m<sup>2</sup>/g)</b>	<b>D<sub>50</sub> (μm)</b>	<b>Carbon content (%)</b>	<b>Half-cell spec. capacity at RT (mAh/g)</b>
Low	6.4	1.8	0.4	151
Medium	11.2	1.4	1.3	155
High	15	1.0	2.0	157

Table 5.1 shows the physical properties of the low, medium, and high BET LFP materials studied here. The surface areas ranged from 6.4 m<sup>2</sup>/g for the low BET LFP to 15 m<sup>2</sup>/g for

the high BET LFP, and correspondingly the average particle size varied ( $D_{50} = 1.8 \mu\text{m}$  for low BET,  $D_{50} = 1.0 \mu\text{m}$  for high BET). The considerable variation in surface area of the LFP materials here should impact the amount of water retained on the prepared electrodes. Water content in electrodes extracted from pouch cells was measured using Karl Fischer (KF) coulometric titration, as was done on LFP electrodes in CHAPTER 4. Figure 5.1 shows measured water content in low, medium, and high BET LFP electrodes after various vacuum drying procedures. The points at  $25^\circ\text{C}$  were measured “as received” and did not undergo any additional vacuum drying. The remaining points are from cells that were vacuum dried at the specified temperature for 14 hr. Multiple repeat measurements were completed for all temperatures and LFP types. These results show a clear trend in water content as a function of LFP surface area. The high BET LFP had the highest water content in the as-received measurements, and consistently showed higher water content than low and medium BET LFP samples at drying temperatures up to  $155^\circ\text{C}$ . Additionally, in the case of low and medium BET LFP, most of the water could be removed by adequate drying procedures (down to  $\sim 250$  ppm level). In the case of the high BET samples, the water content in the electrodes seems to plateau around 750 ppm, even when dried at  $155^\circ\text{C}$ . Note that in the time between preparing the samples in Ar atmosphere and starting the measurement in air, the prepared LFP electrode would have been briefly exposed to air, which could be the reason at least  $\sim 100$  ppm of water is detected in all cases.

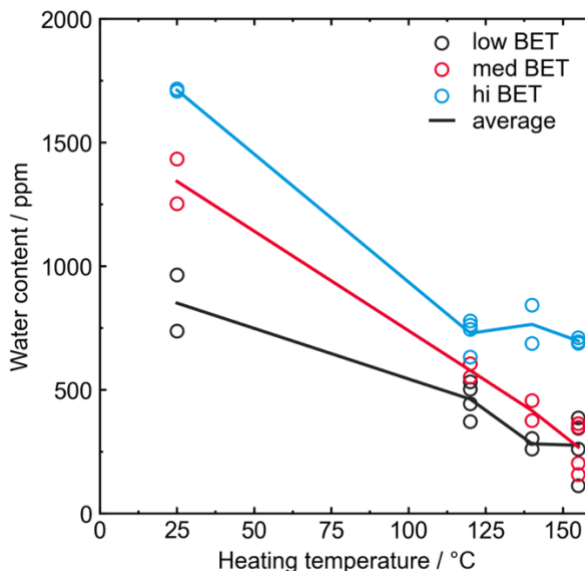


Figure 5.1: Water content detected in different LFP electrodes by Karl Fischer (KF) titration after vacuum drying at different temperatures. Individual datapoints represent repeat trials, and the lines show the average of all trials done at each temperature.

In CHAPTER 4, it was shown that there were minimal differences in cell performance between water contents of 500 ppm and <100 ppm when effectively passivating electrolyte additives were used, such as 2% VC. However, water contents above 500 ppm have not been tested, and both the medium BET and high BET LFP materials heated to 120°C have water contents >500 ppm. While most results presented in this chapter consider cells dried at 120°C, the effect of increased vacuum drying temperatures will be considered later on.

Figure 5.2 shows cycling results for cells tested at 55°C and a rate of C/3 for both charge and discharge. While medium and high BET cells had approximately the same capacity retention, the low BET LFP cells showed worse capacity retention in both 2VC and 2VC+1DTD electrolytes. The normalized voltage polarization was approximately constant as a function of cycle number for low, medium, and high BET cells, suggesting that impedance growth was not the origin of the increased capacity fade in low BET cells. The

medium and high BET LFP cells had similar capacity retention in 2VC and 2VC + 1DTD electrolytes, while low BET performed noticeably worse in 2VC electrolyte. Next, attempts were made to understand the inferior cycle performance of low surface area LFP.

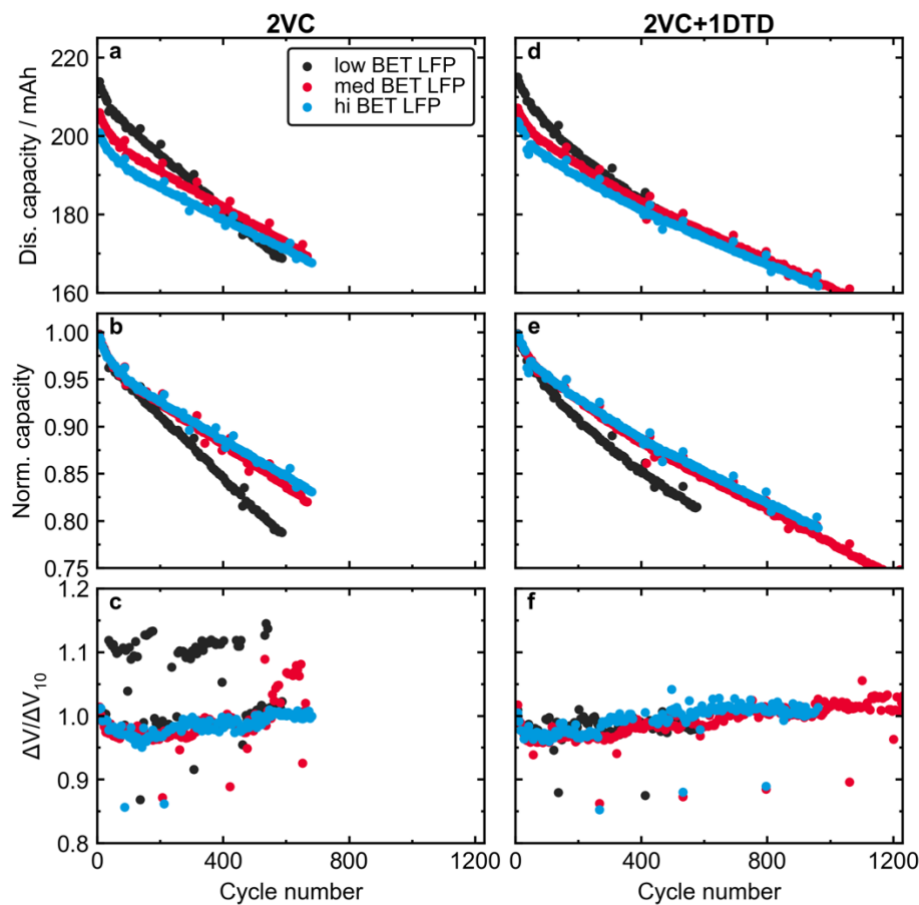


Figure 5.2: Capacity retention and voltage polarization results for cells cycled at 55°C, C/3 rate, between 2.5 V and 3.65 V. (a,d) Absolute discharge capacity versus cycle number for cells with 2VC and 2VC+1DTD electrolyte, respectively. (b,e) Normalized discharge capacity versus cycle number (normalized to the 5<sup>th</sup> cycle) for cells with 2VC and 2VC+1DTD electrolyte, respectively. (c,f) Normalized voltage polarization (normalized to the 10<sup>th</sup> cycle) versus cycle number for cells with 2VC and 2VC+1DTD electrolyte, respectively.

### 5.2.2 Understanding the differences between low, medium, and high BET LFP

Cells with different surface area LFP aged at different temperatures were disassembled and scanned for deposited Fe on the negative electrode with  $\mu$ XRF spectroscopy. Figure 5.3

shows detected Fe loadings for cells with Control electrolyte and 2VC electrolyte aged at 20°C, 40°C, or 55°C. All cells were cycled at a rate of C/3 for both charge and discharge. The cells shown in this Figure were not all cycled for the same amount of time. To compare cells cycled at different times on the same scale,  $\mu$ XRF measurements are presented as [Fe] per cycle time, giving an average Fe deposition rate. Absolute [Fe] measurements along with cycle numbers and cycle times for cells shown in Figure 5.3 are shown in the Appendix (Table A.1). Cells cycled at 20°C and 40°C were all on test for approximately 1400 hours. Cells at 55°C with CTRL electrolyte had between 720-740 hours of cycle time, and 55°C cells with 2VC electrolyte had between 3500-4100 hours of cycle time. The different times that cells were cycled for should be kept in mind in the discussion of the results below.

The cells with Control electrolyte (Figure 5.3a,c,e) had much higher Fe deposited on the negative. This is not surprising given the dependence of electrolyte additives on Fe deposition that was shown in CHAPTER 4. While cells with Control electrolyte were not competitive in terms of lifetime, measuring Fe deposition for cells with Control electrolyte may still be valuable as it can potentially amplify differences between cell types. Indeed, Figure 5.3 shows that in Control electrolyte at 40°C and 55°C, low BET LFP cells consistently show the highest amount of Fe deposition at all temperatures tested, followed by medium BET cells, and finally high BET cells with the lowest amount of Fe deposited. At 20°C, medium BET cells with Control electrolyte had slightly higher Fe deposition per hour than the low and high BET LFP cells, but at that temperature the amount of Fe

deposition was much lower. While the medium BET cell at 20°C appears to be an outlier, the high BET cell still had the lowest Fe deposition rate at this temperature.

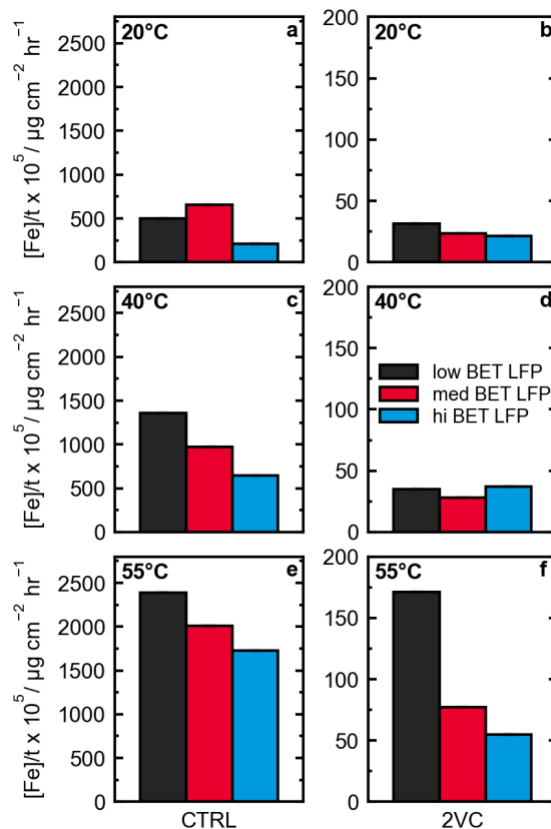


Figure 5.3: Fe deposition per hour for LFP/graphite cells cycled at different temperature with different electrolytes used. **Note the different y-scales used in the first and second columns.** (a,b) Fe deposition for cells cycled at 20°C with CTRL and 2VC electrolyte, respectively. (c,d) Fe deposition for cells cycled at 40°C with CTRL and 2VC electrolyte, respectively. (e,f) Fe deposition for cells cycled at 55°C with CTRL and 2VC electrolyte, respectively.

Figure 5.3b, Figure 5.3d, and Figure 5.3f show the average Fe deposition rate for cells with 2VC electrolyte cycled at 20°C, 40°C, and 55°C, respectively. While the Fe deposition rate was similar for the different LFP types in cells cycled at 20°C and 40°C (recall only ~1400 hr of cycling was completed for these cells), there was a clear trend with LFP type in the 55°C cells, with the low BET cell showing the most deposited Fe, followed by medium BET and high BET LFP cells. Note the difference in scales between the Control and 2VC

cells. To put these numbers into perspective, an Fe deposition rate of  $0.01 \mu\text{g cm}^{-2} \text{hr}^{-1}$  (roughly what is seen in  $40^\circ\text{C}$  Control cells) corresponds to  $10 \mu\text{g cm}^{-2}$  of Fe on the negative in 1000 hr of cycling, while a rate of  $0.0005 \mu\text{g cm}^{-2} \text{hr}^{-1}$  (approximately the rate for  $40^\circ\text{C}$  2VC cells) corresponds to only  $0.5 \mu\text{g cm}^{-2}$  of Fe after 1000 hr of cycling.

Except for the outliers discussed above, the low BET LFP cells showed the most Fe deposition and high BET LFP cells showed the least. This correlates with the long-term cycling results in Figure 5.2 where low BET LFP cells had higher rates of capacity fade at  $40^\circ\text{C}$  and  $55^\circ\text{C}$ . However, naively it may be expected that an LFP material with lower surface area and larger average particle size like the low BET material should have *less* Fe dissolution than a higher surface area material simply because there should be less sites for Fe to be etched from the material. Therefore, this suggests that there is some other form of material degradation that occurs in the low BET case that causes those cells to exhibit more Fe deposition. One possibility is that the larger LFP particles may fracture when the cells are cycled. This is certainly possible in the case of LFP because of mismatch strains that would be established between the lithiated and delithiated phases as the material is charged and discharged. The delithiated phase ( $\text{FePO}_4$ ) is  $\sim 7\%$  smaller in volume than the lithiated phase ( $\text{LiFePO}_4$ ). In this case, fresh, LFP surface (that is not carbon-coated) would be exposed to electrolyte which could lead to higher rates of Fe dissolution. The increased rate of parasitic reactions (Fe dissolution and subsequent catalysis of SEI forming reactions) as well as possible electrical disconnect of cracked particles could be to blame for the higher rate of capacity fade of the low BET LFP cells.



To test if fracturing of large LFP particles was to blame for the increased capacity fade and Fe deposition observed in low BET LFP cells, aged cells were disassembled, and cross-sectional SEM images were taken. Figure 5.4 shows SEM images of fresh low BET and high BET electrodes in the discharged state (Figure 5.4a,b), and low and high BET electrodes after cycling at 55°C in 2VC+1DTD electrolyte in the fully charged state (3.65 V, Figure 5.4c,d). The low BET cell had 580 C/3 cycles at 55°C while the high BET LFP cell had 964 C/3 cycles at 55°C. The images of the fresh electrodes demonstrate the difference in particle size between the low and high BET samples. While the  $D_{50}$  of the high BET material is considerably lower than the low BET sample, there are still some large particles (several  $\mu\text{m}$  in diameter) in the material. Looking at the images of the aged low BET electrode (Figure 5.4c), multiple cracks are visible in many of the larger particles. In contrast, in Figure 5.4d there are not many visible fractures in the high BET electrode, though some cracks could be found in the few large particles in the image. However, in general much less particle cracking seems to have occurred in the high BET LFP, even after many more cycles than the low BET LFP.

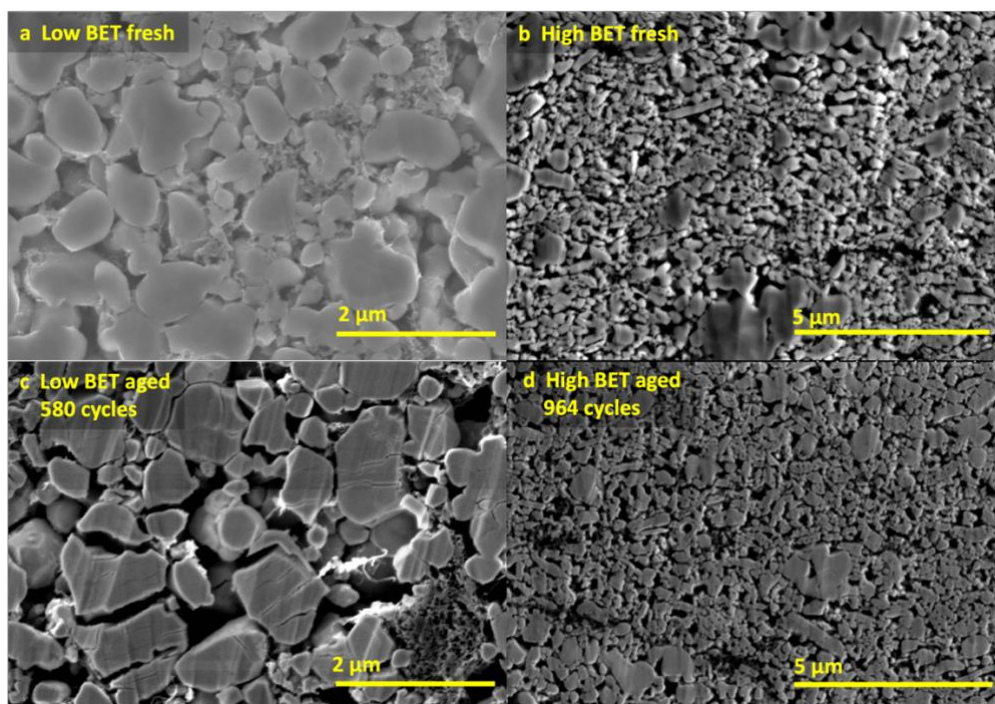


Figure 5.4: SEM images of low and high BET LFP electrodes before and after cycling at 55°C, C/3 rate. Scale bars are indicated on each panel. (a) Fresh low BET LFP electrode. (b) Fresh high BET LFP electrode. (c) low BET LFP electrode at top of charge after 580 cycles at 55°C. (d) high BET LFP electrode at top of charge after 964 cycles at 55°C.

Isothermal microcalorimetry methods were applied in CHAPTER 4 to measure parasitic heat flow in LFP/graphite cells. This same technique was applied here to study parasitic reactions in the different surface area LFP cells. If the higher capacity loss in the low BET cells was due to particle cracking and increased Fe dissolution, this should translate to a higher parasitic heat flow. Cells with the different surface area LFP materials were cycled using the same protocol that was used in CHAPTER 4: 3 cycles between 3.275 V and 3.350 V (graphite 2L  $\rightarrow$  2 staging transition) followed by 3 cycles between 3.305 V and 3.400 V (graphite 2  $\rightarrow$  1 staging transition). A slightly lower current was used here (1.0 mA instead of 1.5 mA) to minimize the polarization heat flow term, especially in the low BET case with relatively large LFP particles. The parasitic heat flow versus relative SOC is omitted here, but can be found in the Appendix (Figure A.4). Low, medium, and high BET LFP

cells were tested with both 2VC electrolyte and 2VC+1DTD electrolyte. Some cells were interrupted due to an unplanned power failure in cycle 2, leading to noise in the data in one cycle. Figure 5.5 shows the averaged parasitic heat flow for each cycle. Error bars indicate the range for nominally identical pair cells, when available. An asterisk over cycle 2 indicates the cycle where an unplanned power outage occurred. As was observed in CHAPTER 4 for LFP cells with most electrolyte additives, the parasitic heat flow in cells was very small, on the order of 10-20  $\mu\text{W}$ . Differences between LFP cell types were small here, but for most cycles the low BET cells showed higher parasitic heat flow in both 2VC and 2VC+1DTD electrolyte. Medium and high BET cells showed virtually identical parasitic heat flow in 2VC electrolyte, while high BET cells had slightly higher parasitic heat flow than medium BET cells in 2VC+1DTD electrolyte. The marginally higher parasitic heat flow in low BET cells agrees with what was seen earlier in long-term cycling experiments (Figure 5.2), and correlates with the observations made in the  $\mu\text{XRF}$  studies (Figure 5.3) and cross-sectional SEM experiments (Figure 5.4). The higher parasitic heat flow in low BET cells could originate from either a higher rate of parasitic reactions on the negative electrode from the higher amount of Fe that is deposited, or from the increased Fe dissolution on the positive side that occurs when microcracks are formed in the LFP particles. Indeed, microcracking was also observed in the low BET LFP cells that were cycled at C/220 in the calorimeter (See Figure A.5).

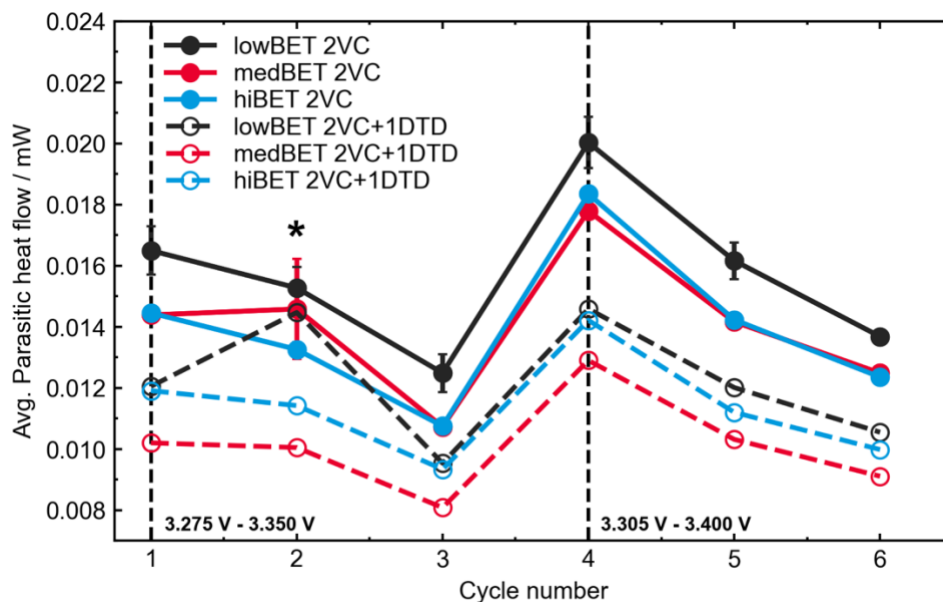


Figure 5.5: Average parasitic heat flow as a function of cycle number for low, medium, and high BET LFP/AG cells. Voltage limits of the cycles are indicated on the plot and separated by the dashed lines.

### 5.2.3 Further considerations on the effects of residual water in LFP cells

The results presented in CHAPTER 4 showed that the impact of water contamination on LFP/graphite cell lifetime is highly dependent on electrolyte additive choice and cycling temperature. The cells used here were constructed with polypropylene separators (PP, MP = 160°C) so that higher vacuum drying temperatures could be used to remove as much residual water as possible (see Figure 5.1). In these cells, vacuum drying temperatures as high as 150°C were used, and cycling performance compared to the “standard” drying temperature of 120°C. Referring to Figure 5.1, this higher drying temperature reduced the amount of water in low and medium BET cells, but less so for high BET cells.

Figure 5.6b and Figure 5.6d show normalized capacity versus cycle number for cells cycled at 40°C and 55°C, respectively, after vacuum drying at either 120°C or 150°C.

Additionally,  $\mu$ XRF measurements of Fe deposition are shown for these cells as a function of cycle time (Figure 5.6a and Figure 5.6c). All cells shown in Figure 5.6 had 2VC electrolyte. For the  $\mu$ XRF results, a straight line is drawn between the origin (0,0) and the points that were measured for each cell type. This is simply meant to be a guide to the eye to help compare cells that cycled for different times, and is not meant to make the assumption that the rate of Fe deposition is constant over time. Cells vacuum dried at 120°C are shown as solid circles, while cells cycled at 150°C are shown as open circles. First looking at the cycling data, the increased vacuum drying temperature did not impact cycle life significantly for any of the LFP types at either 40°C or 55°C. Normalized capacity retention was virtually identical for the cells tested here regardless of whether the cells were dried at 120°C or 150°C, even though Figure 5.1 shows the water content in the LFP electrode was significantly reduced by drying at the higher temperature.

While capacity retention was unaffected by vacuum drying temperature, differences were found in the magnitude of Fe deposition. Figure 5.6a shows [Fe] versus cycle time for the various cells cycled at 40°C. Here, a clear reduction in Fe deposition can be seen in all three cell types (low, medium, high BET LFP) when the drying temperature was increased to 150°C. Similarly, for cells cycled at 55°C (Figure 5.6c), less Fe was detected for all cell types after vacuum drying at higher temperature, although the 150°C dried cells had roughly half as much cycling time as the 120°C dried cells. The results of this drying study suggest that Fe deposition, at least in the magnitude observed here, does not severely affect the capacity retention of LFP/graphite cells, even at cycling temperatures as high as 55°C. It is more likely, then, that in the case of the LFP materials studied here, Fe deposition is

more of an “indicator” for degradation of the positive electrode, as will be discussed below. Note as well that even in the case of drying at 150°C that the low BET cells showed the highest degree of Fe deposition.

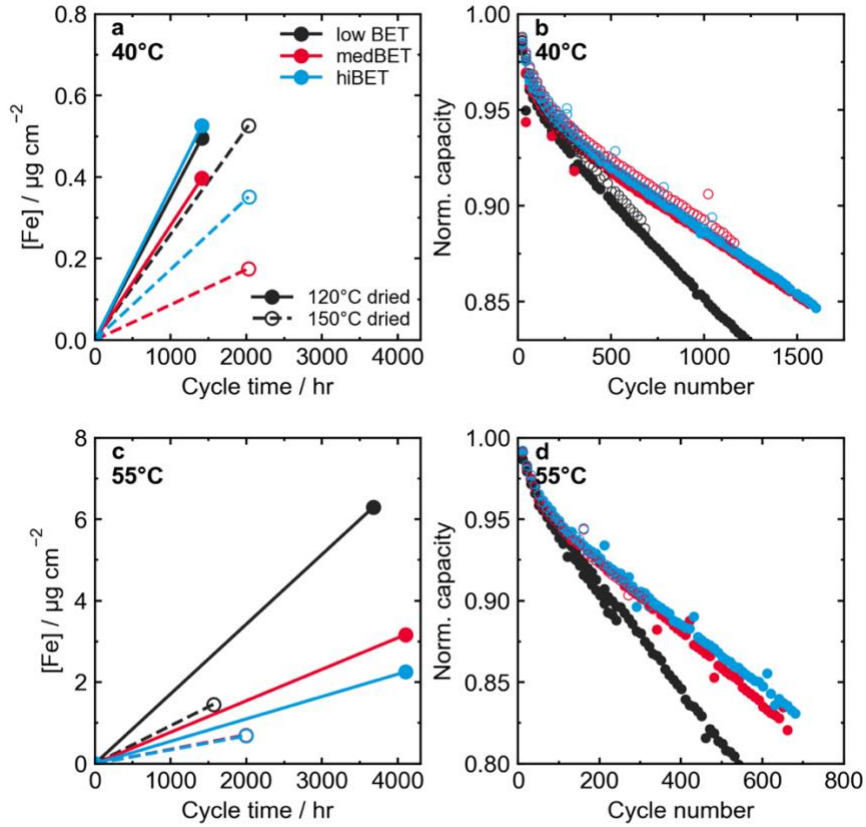


Figure 5.6: XRF results and capacity retention for LFP cells vacuum dried at different temperatures. All cells shown here were cycled with 2VC electrolyte. (a) Fe loading detected on the negative electrode versus cycle time for cells that were cycled at 40°C, C/3 rate. (b) Associated normalized capacity retention (cycle 5) versus cycle number for cells cycled at 40°C after vacuum drying at 120°C or 150°C. (c) Fe loading versus cycle time for cells cycled at 55°C. (d) Normalized capacity (cycle 5) versus cycle number for cells cycled at 55°C after vacuum drying at different temperatures.

#### 5.2.4 Discussion and conclusions

Putting together the results of the different experiments that have been presented in this section, an explanation for the different performance of the low, medium, and high BET LFP cells studied here can be developed. Recall that in all long-term cycling tests the low BET LFP cells had either the worst capacity retention of the three materials for both 2VC and 2VC+1DTD electrolyte (Figure 5.2).  $\mu$ XRF measurements of Fe deposition showed that the low BET cells typically had more Fe on the negative electrode after cycling. Cross-sectional SEM images showed more micro-cracking in the low BET material compared to the high BET material, and isothermal microcalorimetry experiments showed that low BET cells had slightly higher parasitic heat flow than the other cell types. At this point, the question is which of the various degradation modes identified here was the primary cause of the larger capacity fade in the low BET cells. The results from Figure 5.6 for different vacuum drying temperatures showed that while Fe deposition after cycling was reduced considerably when the drying temperature was increased from 120°C to 150°C, no obvious differences in long-term capacity retention could be detected in cells cycled at either 40°C or 55°C based on differences in drying temperature. This suggests that the larger amount of Fe detected on the negative electrode in the low BET cells may not be the cause of capacity fade in these cells. The higher Fe deposition in low BET cells may just be a side-effect of the particle cracking, where fresh, non carbon-coated LFP surface is exposed to the electrolyte, allowing for more Fe to be dissolved, and subsequently deposited on the graphite.

Figure 5.7 compares the differential voltage,  $dV/dQ$ , at beginning of life and end of life for low, medium, and high BET LFP cells that were cycled at 40°C, C/3 rate. The cycles shown

in this Figure are from the C/20 “check-up” cycles at the cycle number indicated in the legend. All cells shown in Figure 5.7 had 2VC+1DTD electrolyte. Looking at the  $dV/dQ$  curves for the low BET LFP cell, the graphite intercalation and deintercalation features were clearly visible during charge and discharge and change very little from cycle 52 to cycle 1174. In every case, the graphite could be fully delithiated, meaning that there was always enough positive electrode active mass to accept all the lithium coming from the graphite during discharge. The main difference in these voltage curves is the endpoint on the capacity axis. This difference can be attributed to negative electrode shift loss due to SEI growth, a conclusion made similarly by Li et al. by examining the  $dV/dQ$  profile of LFP/graphite cells after aging<sup>228</sup>. If significant active material loss was to blame for capacity loss in these cells, the graphite features at the end of discharge would be affected because there would be less sites available at the positive electrode when discharging the cell. It is possible that when LFP particles fracture that fully lithiated  $\text{LiFePO}_4$  particles could become disconnected from the electrode, which could also cause the effect seen in the  $dV/dQ$  curve in Figure 5.7c. However, if this were the case similar features would likely be seen at the end of discharge due to disconnected  $\text{FePO}_4$ , which was not observed in these cells. Further, there is evidence in the literature that positive active material loss in LFP/graphite cells is not an issue. Guo and Chen showed this convincingly with LFP/Li half cells extracted from aged LFP/graphite cells<sup>221</sup>. The full cells showed capacity fade after 500 cycles at various temperatures, and the half cells delivered considerably less than the theoretical capacity for LFP on the first charge. However, on the subsequent discharge, almost all theoretical capacity was recovered, proving that it was Li inventory loss rather than positive active material loss that caused capacity fade in the full cells. Similar results



were also found by Kim et al. and Kassem and Delacourt<sup>274,275</sup>. Combining these literature reports with the previous results discussed above, it is likely that Li inventory loss is the main cause of capacity fade in the cells studied here. The medium BET cell (Figure 5.7b,e) cycled for longer than the other cells, so more C/20 cycles could be plotted later in life. The graphite intercalation/deintercalation features at the beginning of charge/end of discharge in the dV/dQ curve at cycle 1925 (~11,500 hr of test) were virtually unchanged from the beginning of life. The only difference visible in the dV/dQ plots is the movement of the capacity endpoint described above and a slight shift in the peak corresponding to the transition between the graphite stage 2L→ 2 plateau and the stage 2→1 plateau. Additionally, the high BET LFP cell also showed very little change in dV/dQ features over 1000 cycles at 40°C. These results show it is unlikely that positive active material loss can be attributed to the differences seen in the different LFP types and that graphite electrochemical performance is virtually unchanged over the life of these cells. Regardless of LFP particle size, the main cause of capacity loss is through Li inventory loss.

The overall impact of LFP particle size on cell lifetime was minor compared to the impact of electrolyte additives as seen in CHAPTER 4. However, some lessons could be learned from this study. LFP cells designed for long lifetimes should utilize LFP materials with small, uniform particle size, and high surface area.

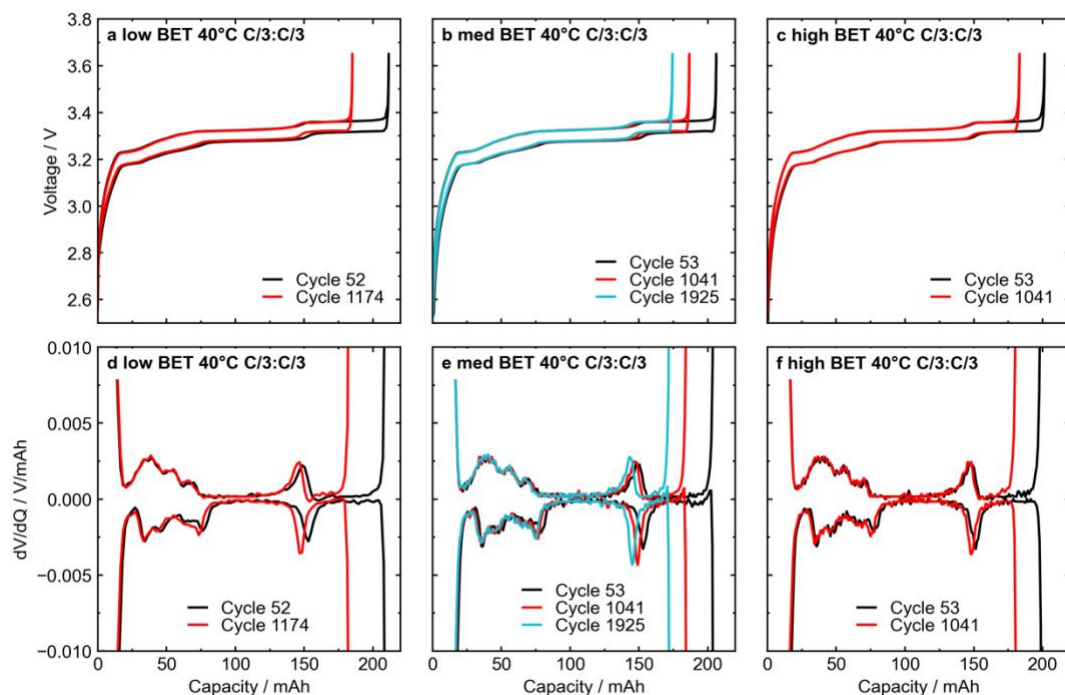


Figure 5.7: Examining differential voltage for C/20 check-up cycles at beginning of life and end of life for LFP/graphite cells with 2VC+1DTD electrolyte cycled at 40°C, C/3 rate. (a,d) Voltage versus capacity and corresponding dV/dQ versus capacity, respectively for cycle 52 and cycles 1174 of a low BET/graphite cell. (b,e) Voltage and dV/dQ, respectively, versus capacity for cycles 53, 1041, and 1925 of a medium BET/graphite cell. (c,f) Voltage and dV/dQ, respectively, versus capacity for cycles 53 and 1041 of a high BET/graphite cell.

### 5.3 IMPACT OF DIFFERENT LI SALTS AND ELECTROLYTE ADDITIVES

#### 5.3.1 Introduction

The previous section found little differences in lifetime in the medium and high BET LFP cells, and slightly higher capacity fade with the low BET material. In the following sections, the medium BET material will be used exclusively.

LiPF<sub>6</sub> has long been the salt of choice for Li-ion batteries due to its balance of low cost, high ionic conductivity in alkyl carbonate solutions, relative stability against electrochemical reactions, moderate thermal stability, and relatively high degree of

dissociation in polar solution<sup>61</sup> (see CHAPTER 1). Despite this, LiPF<sub>6</sub> can thermally decompose at relatively low temperatures<sup>63</sup>, and is prone to hydrolysis, forming acidic species which can interact with various components of the cell<sup>64-67</sup>, which may contribute to the leaching of transition metals from the positive electrode<sup>152,157,161,276,277</sup>. Many groups have studied alternative salts to LiPF<sub>6</sub>, to varying degrees of success. Two examples that have stood out are the related imide salts: lithium bis(trifluoromethanesulfonyl)imide (LiTFSI) and lithium bis(fluorosulfonyl)imide (LiFSI). These salts demonstrate high ionic conductivity and excellent dissociation in carbonate solvents<sup>61,68,69</sup>, as well as high thermal stability<sup>70</sup>. However, nagging issues exist with these salts as well, notably corrosion of the Al current collector when used in high-voltage chemistries<sup>69,71-73</sup>.

While CHAPTER 4 found that Fe dissolution and deposition could be minimized by the use of electrolyte additives in an LiPF<sub>6</sub>-based electrolyte, previous studies have shown that the use of alternative Li salts can also inhibit Fe dissolution and improve high temperature cycle life in LFP cells<sup>157,158</sup>. Other groups have also demonstrated improved cyclability of LFP cells when conducting salts other than LiPF<sub>6</sub> were used<sup>278-281</sup>. LiFSI and LiTFSI salts should be a good match for the LFP/Graphite chemistry, as the low operating potential of LFP should limit the amount of corrosion of the Al current collector, which is one of the main issues with lithium imide salts<sup>282</sup>.

This section considers the use of LiFSI in LFP/graphite cells, both with and without additional electrolyte additives. Conventional long-term cycling was done, as well as the advanced characterization techniques that have been used throughout this thesis (UHPC,

IMC, OCV storage, etc.). Additionally, the existing technique of isolating parasitic reactions to the individual electrodes (and electrolyte) in “pouch bags” is carried out in the calorimeter for the first time to detect *all* parasitic reactions that occur at a given electrode, and compared with full cell experiments to estimate the degree of cross-talk reactions in a given cell.

### 5.3.2 Results

Figure 5.8 shows long term cycling results for LFP/AG cells at 40°C for cells with Control and 2VC electrolytes. All cells were cycled at C/3 rate for both charge and discharge. Figure 5.8a,b,c show discharge capacity, normalized capacity, and normalized voltage polarization, respectively, as a function of cycle number for cells with Control electrolyte, while Figure 5.8d,e,f show these quantities for cells with 2VC electrolyte. Only marginal improvement was seen in capacity retention when the LiPF<sub>6</sub>/LiFSI salt mixture was used. However, a significant improvement was seen with the 1.5 M LiFSI electrolyte, extending the number of cycles to reach 85% capacity to ~700 cycles from only ~100 cycles with the LiPF<sub>6</sub>-based electrolyte.

When 2VC was used in the electrolyte, the differences in performance between the Li salts were less dramatic. However, an improvement in capacity retention could still be seen going from LiPF<sub>6</sub> to LiFSI. Additionally, the mixed LiPF<sub>6</sub>/LiFSI electrolyte showed improved capacity retention compared to the pure 1.5 M LiPF<sub>6</sub> electrolyte at 40°C. Notice as well that the voltage polarization versus cycle number for LFP cells with 2VC was

virtually unchanged over almost 1200 cycles at C/3 rate, indicating that impedance growth could not be blamed for capacity loss.

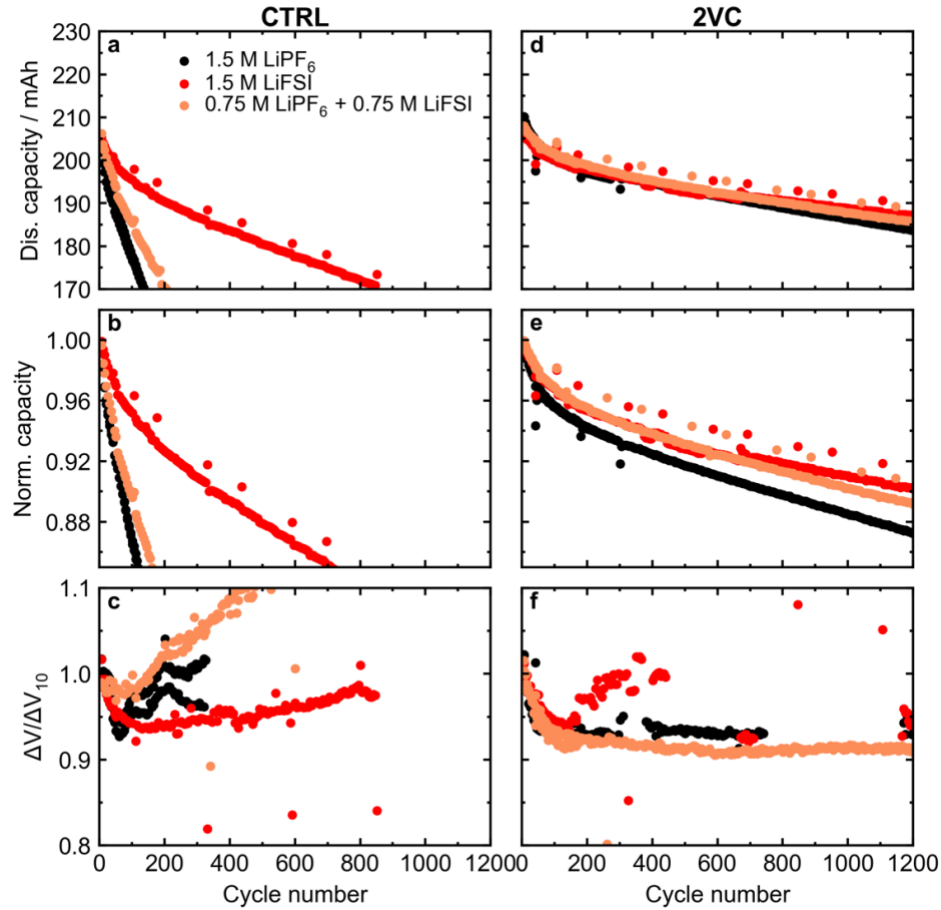


Figure 5.8: Long-term cycling for LFP/AG cells cycled at 40°C and a rate of C/3. (a-c) Absolute discharge capacity, normalized discharge capacity (normalized to cycle 5), and normalized voltage polarization (cycle 10) versus cycle number, respectively, for cells with CTRL electrolyte. (d-f) Absolute discharge capacity, normalized discharge capacity (cycle 5), and normalized voltage polarization (cycle 10) versus cycle number, respectively, for cells with 2VC electrolyte.

Figure 5.9 shows cycling results for LFP/Graphite cells at 55°C. Similar to the results at 40°C, cycling is shown for cells with Control electrolyte (Figure 5.9a-c) and 2VC electrolyte (Figure 5.9d-f). Once again, in cells with Control electrolyte, LiFSI improved capacity retention compared to the LiPF<sub>6</sub> based electrolyte. However, at this higher cycling temperature all cells with Control electrolyte cycled very poorly.

In cells with 2VC, clear improvements in capacity retention were seen with the use of LiFSI salt. Additionally, the magnitude of capacity retention improvement depended strongly on the fraction of LiFSI in the electrolyte (or the amount of LiPF<sub>6</sub> removed), as the capacity retention for the 50/50 LiPF<sub>6</sub>/LiFSI blend was near the midpoint of the pure 1.5 M LiPF<sub>6</sub> and 1.5 M LiFSI cells. Like what was seen at 40°C, very little increase in voltage polarization was seen in all cells with 2% VC cycled at 55°C. Overall, the long-term cycling experiments at 40°C and 55°C showed a marked improvement in capacity retention in LFP/Graphite cells when LiFSI salt was used over LiPF<sub>6</sub>.

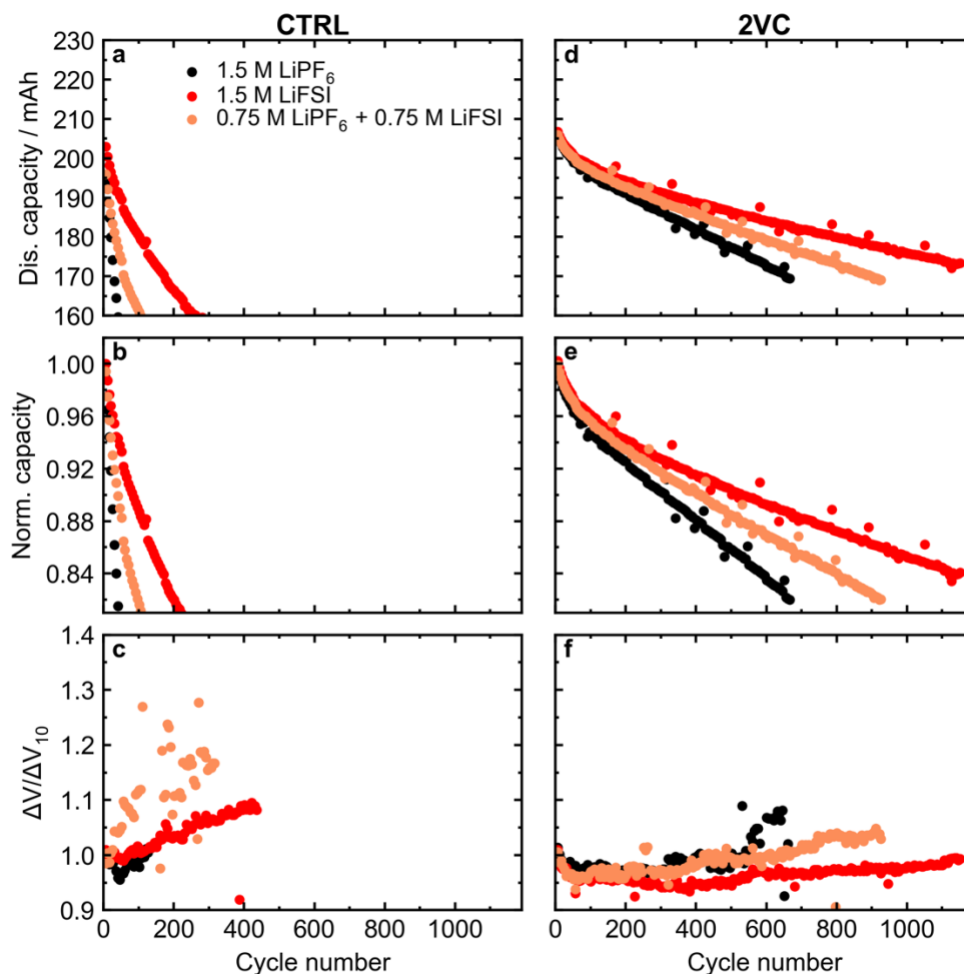


Figure 5.9: Long-term cycling for LFP/AG cells cycled at 55°C and a rate of C/3. (a-c) Absolute discharge capacity, normalized discharge capacity (normalized to cycle 5), and normalized voltage polarization (cycle 10) versus cycle number, respectively, for cells with CTRL electrolyte. (d-f) Absolute discharge capacity, normalized discharge capacity (cycle 5), and normalized voltage polarization (cycle 10) versus cycle number, respectively, for cells with 2VC electrolyte.

$\mu$ XRF spectroscopy was carried out on graphite electrodes from aged cells to study the impact of Li salt choice on Fe deposition. Figure 5.10 shows Fe deposition results for cells cycled at 20°C, 40°C (Figure 5.10a), and 55°C (Figure 5.10b). Fe deposition was measured in 20°C and 40°C cycled cells with both Control and 2VC electrolytes, while only 2VC electrolytes were tested at 55°C. Cells tested at 20°C and 40°C were cycled at C/3 rate for ~1400 hours, corresponding to approximately 250 cycles. At both 20°C and 40°C, a

significant reduction in Fe deposition was seen going from 1.5 M LiPF<sub>6</sub> electrolyte to 1.5 M LiFSI in cells with Control electrolyte. Cells with 2VC cycled at 20°C or 40°C had very low deposited Fe after 250 cycles for both LiPF<sub>6</sub> and LiFSI electrolytes. However, the LiFSI-containing cells with 2VC had slightly lower Fe deposited than the LiPF<sub>6</sub>-based cells.

Since very little Fe deposition was seen in cells with 2VC electrolyte after 250 cycles at 40°C, cells cycled at 55°C for longer times were studied. The points shown in Figure 5.10b come from the same cells that were shown in Figure 5.9d-f. These cells were cycled for different times so [Fe] detected on the graphite is plotted versus cycle number to give a better indication of the time dependence of these measurements. Of these cells, the 1.5 M LiPF<sub>6</sub> electrolyte showed the highest amount of Fe deposition, despite having completed almost half as many cycles as the 1.5 M LiFSI cell. The mixed LiPF<sub>6</sub>/LiFSI cell showed less deposited Fe than the pure LiFSI cell, which could simply be due to less time cycled at 55°C. This result, combined with the  $\mu$ XRF measurements from 20°C and 40°C cycled cells, confirms that the use of LiFSI does reduce the amount of Fe deposited on the negative electrode even in the presence of electrolyte additives. The use of LiFSI combined with appropriate electrolyte additives gives an LFP/Graphite cell that exhibits very low amounts of Fe dissolution and deposition, which therefore should have very little impact on lifetime.



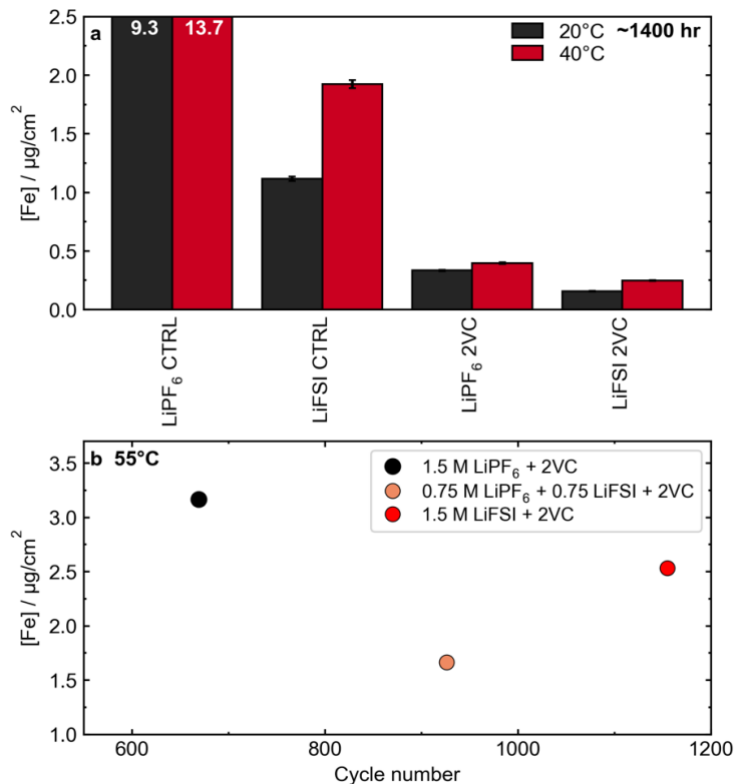


Figure 5.10:  $\mu$ XRF measurements of deposited Fe on the negative electrode extracted from LFP/graphite cells with different electrolytes aged under different conditions. (a) [Fe] detected on the negative electrode from cells with either Control (CTRL, no additives) electrolyte, or 2VC electrolyte, cycled at either 20°C or 40°C for  $\sim$ 1400 hours at C/3 rate ( $\sim$ 250 cycles). (b) [Fe] detected on the negative electrode from cells cycled at 55°C for different numbers of cycles. Cells were cycled at C/3 rate for both charge and discharge.

UHPC cycling experiments were completed for LFP/Graphite cells with different salts in the electrolyte. Cells with both Control electrolyte and 2VC electrolyte were tested. Cells were cycled at 40°C and C/20 rate for charge and discharge. Figure 5.11 shows results for coulombic efficiency (CE), zeroed charge endpoint capacity movement, discharge capacity, and voltage polarization as a function of cycle number. Note the different axis scales used for these quantities between Control electrolyte and 2VC electrolyte.

As was seen in the long-term cycling experiments with Control electrolyte, using LiFSI greatly improved capacity retention over LiPF<sub>6</sub>-based electrolytes. In the UHPC experiments, cells with LiPF<sub>6</sub> Control electrolyte had extremely low CE, settling at just over 0.92 after 20 cycles, agreeing with the previous results in CHAPTER 4. LiFSI-containing cells with Control electrolyte showed much higher CE, reaching around 0.99 after 20 cycles. While a CE of 0.99 is not nearly competitive for a state-of-the-art Li-ion cell, it was a big improvement over the LiPF<sub>6</sub> electrolyte, and may be considered “high” for a cell with no additional electrolyte additives.

Recall in CHAPTER 4 that massive charge-endpoint capacity slippage was observed in LFP cells with LiPF<sub>6</sub> Control electrolyte. That was again seen here, and Figure 5.11b shows that the use of LiFSI electrolyte greatly reduced slippage in Control electrolyte. This suggests that much of the slippage observed in Control electrolyte involves the LiPF<sub>6</sub> salt either directly or indirectly. Along with the higher CE and lower slippage in Control electrolyte, LiFSI cells had improved capacity retention in the UHPC cycles (Figure 5.11c) with no increase in voltage polarization (Figure 5.11d).

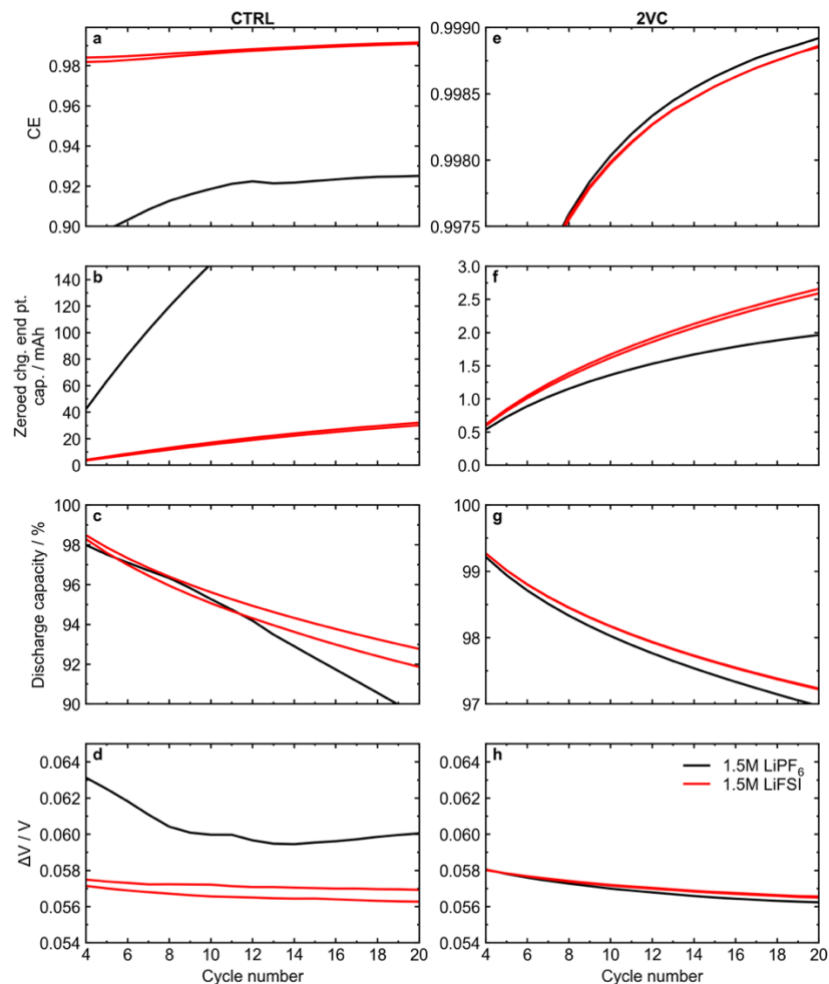


Figure 5.11: Ultra high-precision coulometry cycles for LFP/AG cells with different Li salts in the electrolyte. Cells were cycled at 40°C at a rate of C/20 for both charge and discharge. (a-d) Coulombic efficiency (CE), zeroed charge endpoint capacity movement, discharge capacity (%), and absolute voltage polarization versus cycle number, respectively, for cells with CTRL electrolyte. (e-h) CE, charge endpoint capacity movement, percent discharge capacity, and voltage polarization versus cycle number, respectively, for cells with 2VC electrolyte.

The trends in UHPC cycling were much different when VC was added to the electrolyte. In this case, all cells had very high CE values (>0.998) after 20 cycles. However, LiFSI cells with 2VC electrolyte had *lower* CE than LiPF<sub>6</sub> cells. As well, charge endpoint slippage, while extremely low for all cells, was slightly *higher* for LiFSI cells. While these metrics are usually indicative of worse long-term performance of Li-ion cells<sup>123,283,284</sup>, LiFSI-containing cells had much better capacity retention compared to LiPF<sub>6</sub> at high

temperature, and even showed better capacity retention in these same UHPC cycles (Figure 5.11g). One possible explanation for these results is the existence of a shuttle reaction that does not consume lithium inventory.

The isothermal microcalorimetry (IMC) methods that have been developed in this thesis are used to further study the impact of LiFSI salt on parasitic reactions. Figure 5.12 shows parasitic heat flow versus relative state of charge (SOC) for each cycle for LFP/graphite cells with Control electrolyte. The voltage ranges for each cycle are shown in each of the panels. The extremely high parasitic heat flow observed in LiPF<sub>6</sub> Control electrolyte in CHAPTER 4 was again seen here. As LiFSI was added to the electrolyte, the parasitic heat flow decreased dramatically, going from ~0.7 mW with 1.5 M LiPF<sub>6</sub> to ~0.45 mW with 0.75 M LiPF<sub>6</sub> + 0.75 M LiFSI, and finally down to around 0.2 mW for pure 1.5 M LiFSI electrolyte (cycle 1, Figure 5.12a). This substantial reduction in the parasitic heat flow suggests a reduction of parasitic reactions in the Control electrolyte when LiPF<sub>6</sub> was replaced with LiFSI. Indeed, recall that in long-term cycling tests at 40°C (Figure 5.8), a large improvement in capacity retention was seen going from LiPF<sub>6</sub> to LiFSI Control electrolytes.

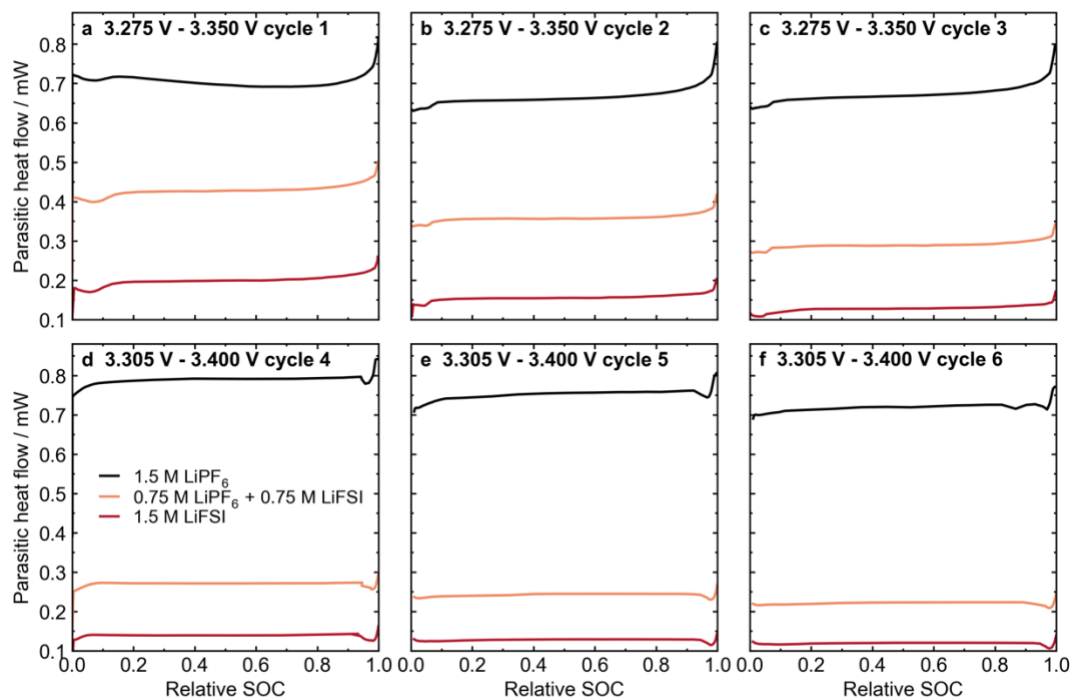


Figure 5.12: Parasitic heat flow results extracted from cycles in the isothermal microcalorimeter at 40.0000°C and a rate of  $\sim C/220$ . Cells had different Li salts in the electrolyte, as indicated, and no additional electrolyte additives (Control electrolyte). (a-c) Parasitic heat flow versus relative state of charge (SOC) for cycles between 3.275 V and 3.350 V. (d-f) Parasitic heat flow versus relative SOC for cycles between 3.305 V and 3.400 V.

Figure 5.13 shows parasitic heat flow versus relative SOC for all cycles for cells with 2VC electrolyte and different fractions of LiFSI. One of the 1.5 M LiPF<sub>6</sub> cells experienced an unplanned power failure in cycle 2 leading to poor quality data, so it was omitted in panel Figure 5.13b. However, for the remainder of the cycles and despite the power failure for one of the pairs, notice the exceptional agreement in parasitic heat flow between LiPF<sub>6</sub> pair cells. For all cells with 2VC, regardless of Li salt, the measured parasitic heat flow was very small, on the order of 10-20  $\mu$ W, as has been seen throughout this thesis so far when electrolyte additives are used. In all cycles, however, the 1.5 M LiFSI cells had slightly *higher* parasitic heat flow than the 1.5 M LiPF<sub>6</sub> cells. While the higher parasitic heat flow does not agree with the superior capacity retention of LiFSI-containing LFP cells at 40°C

and 55°C, it does agree with the higher charge endpoint capacity slippage and slightly lower CE measured in the UHPC cycles when LiFSI was used in 2VC electrolyte, indicating the prevalence of more parasitic reactions in the LiFSI case.

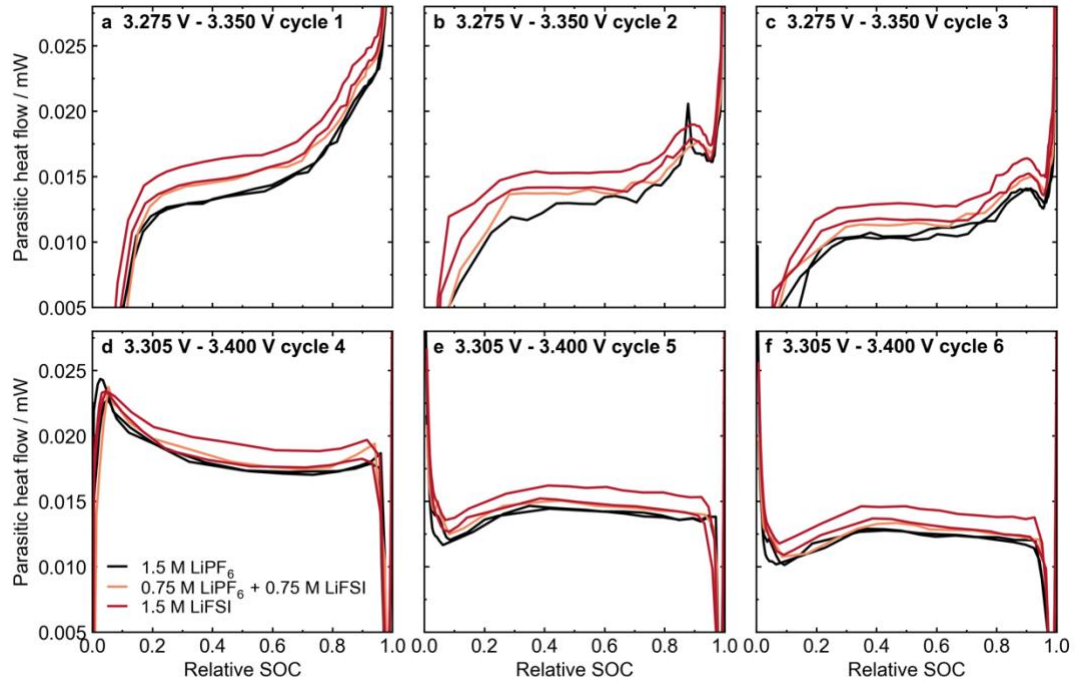


Figure 5.13: Parasitic heat flow results for LFP/AG cells with 2VC electrolyte. Cells were cycled at 40.0000°C and a rate of  $\sim C/200$ . (a-c) Parasitic heat flow versus relative SOC for cycles between 3.275 V and 3.350 V. (d-f) Parasitic heat flow versus relative SOC for cycles between 3.305 V and 3.400 V.

Figure 5.14 gives a summary of the IMC experiments discussed above. Figure 5.14a shows the average parasitic heat flow for each cycle for cells with Control electrolyte, while Figure 5.14b shows averaged parasitic heat flow versus cycle number for cells with 2VC in the electrolyte. In this Figure, cycle dependent trends can be seen more clearly. In particular, the decrease in parasitic heat flow for the mixed  $\text{LiPF}_6/\text{LiFSI}$  Control electrolyte cell from above 0.4 mW to just above 0.2 mW can be seen as the cell was cycled. As well, the marginally higher parasitic heat flows of cells with LiFSI + 2VC electrolyte compared to  $\text{LiPF}_6$  + 2VC electrolyte was seen consistently over all the IMC cycles. To summarize,

the measured parasitic heat flow strongly depends on the fraction of LiFSI in LiFSI/LiPF<sub>6</sub> electrolytes in Control electrolyte, with much lower parasitic heat flow seen in a 1.5 M LiFSI electrolyte than a 1.5 M LiPF<sub>6</sub> electrolyte. This massive parasitic heat flow in the LiPF<sub>6</sub>-based cell is likely due to some shuttling species that is produced in relatively large quantities and causes rapid self-discharge and irreversible capacity fade. The reduction in parasitic heat flow that was seen when LiFSI is used in Control electrolyte suggests that the LiPF<sub>6</sub> salt participates in the formation of the species that causes self-discharge and lithium loss in these cells one way or another.

When VC was added to the electrolyte, cells with 1.5 M LiFSI electrolyte had slightly *higher* parasitic heat flow compared to 1.5 M LiPF<sub>6</sub> electrolyte. While a higher parasitic heat flow can typically be correlated to shorter cycle life, that does not appear to be the case with these LFP/graphite cells when 2VC is used. In an attempt to reconcile the discrepancy between the long-term cycle life and IMC measurements (and UHPC measurements), it is possible that this marginally higher parasitic heat flow in LiFSI-containing cells is due to a small self-discharge current, likely due to the formation of a shuttle species that may not affect reversible capacity in long-term cycling. It is possible that this shuttling molecule involves the LiFSI salt, and is different than the more severe shuttle in the LiPF<sub>6</sub> Control electrolyte. This idea is investigated further below with open-circuit storage experiments.

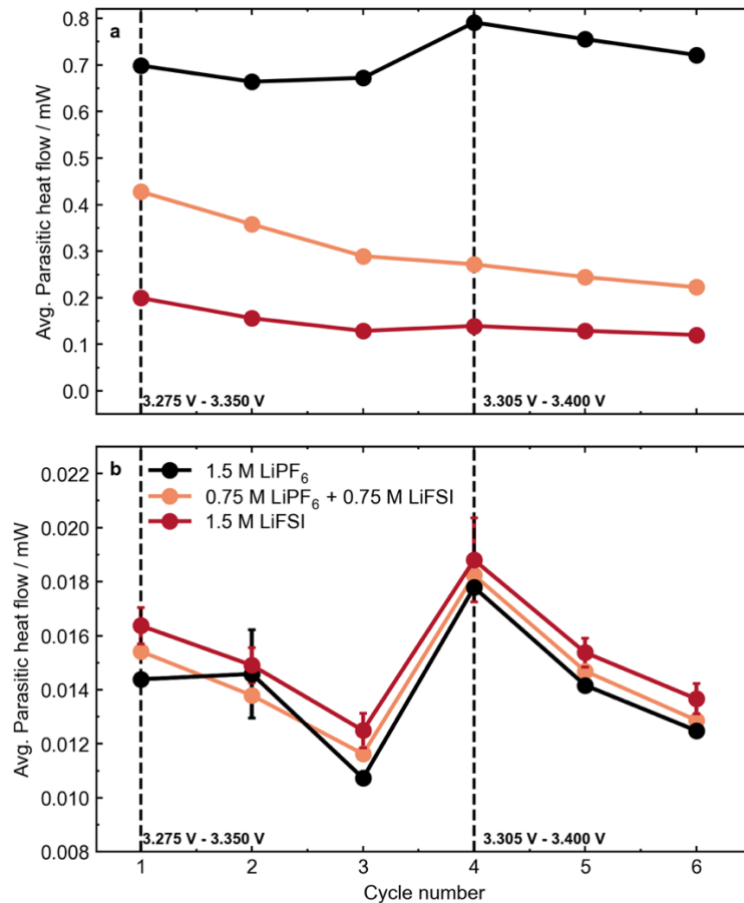


Figure 5.14: Summary of isothermal microcalorimetry results. The averaged parasitic heat flow in each cycle (between 20% and 80% relative SOC) is plotted versus cycle number for (a) CTRL electrolyte, and (b) 2VC electrolyte.

Figure 5.15a shows open-circuit voltage versus time for LFP cells stored initially at top of charge (3.65 V) at 60°C for 500 hours. Figure 5.15b shows reversible and irreversible capacity losses determined from check-up cycles at the end of the 500 hr storage period (see ref. <sup>207</sup>). The poor performance of LiPF<sub>6</sub> Control electrolyte cells was previously seen in CHAPTER 4, and does not need to be reiterated. Cells with LiFSI-based Control electrolyte fared much better than LiPF<sub>6</sub> cells, with much less voltage drop and less capacity losses seen in the check-up cycles.



Following what was seen in the UHPC and IMC experiments, the storage results were reversed when 2VC was used in the electrolyte. In this case, the  $\text{LiPF}_6 + 2\text{VC}$  electrolyte showed lower voltage drop, and lower total capacity loss compared to  $\text{LiFSI} + 2\text{VC}$ . Notice that the irreversible capacity losses were similar between the  $\text{LiPF}_6$  and  $\text{LiFSI}$  cells (red bars in Figure 5.15b), and the main difference was a slightly higher reversible capacity loss for the  $\text{LiFSI} + 2\text{VC}$  cell. This implies that the larger self-discharge observed in the  $\text{LiFSI} + 2\text{VC}$  cell is reversible, and can be recovered on the subsequent charge half-cycle, which adds more evidence to support the shuttle argument for  $\text{LiFSI} + 2\text{VC}$ . The total amount of lithium consumed irreversibly in the storage experiment was virtually the same for  $\text{LiFSI} + 2\text{VC}$  and  $\text{LiPF}_6 + 2\text{VC}$ .

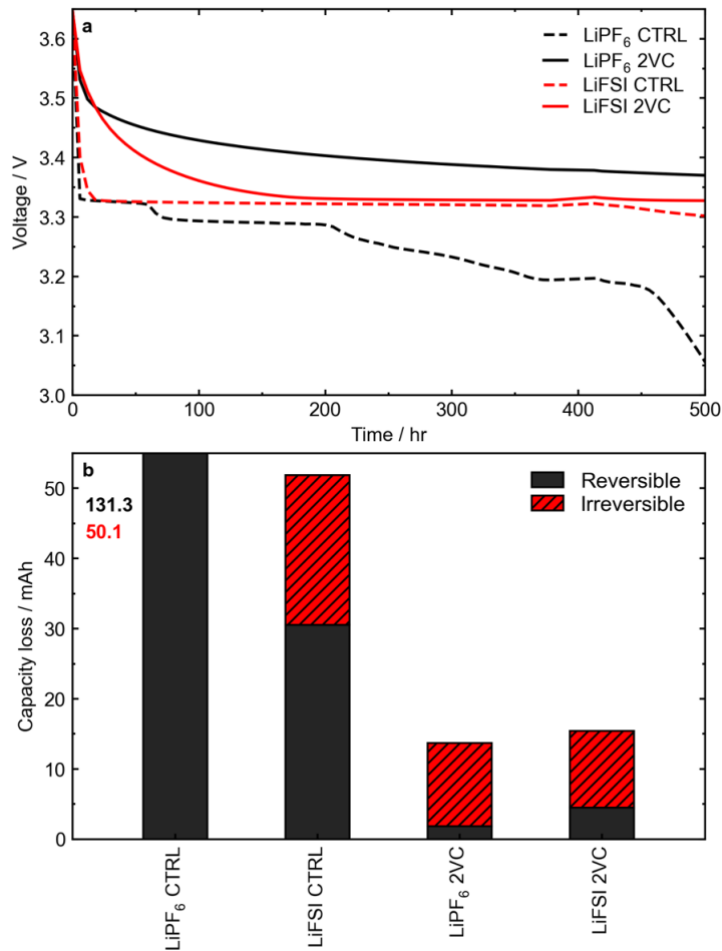


Figure 5.15: OCV storage experiments at 60°C for LFP cells with different electrolytes. (a) Voltage versus time for LFP/graphite cells measured during the 500 hr storage experiment. (b) Irreversible ( $D_0 - D_2$ ) and reversible ( $D_2 - D_1$ ) capacity losses for cells after 500 hr at 60°C. The sum of the two bars gives the total capacity loss during this storage period. The values for LiPF<sub>6</sub> CTRL electrolyte are off scale, and are indicated to the left of the bar chart.

To better understand the origin of parasitic reactions in LFP/graphite cells as functions of Li salt and electrolyte additives, so-called “pouch bag” experiments were carried out to observe gas production in separated electrodes wetted with electrolyte. This method was pioneered by Xiong et al. and Ellis et al.<sup>144,145,215</sup> to better understand gas-producing parasitic reactions in high voltage NMC/Graphite cells as well as complex crosstalk reactions. To properly interpret the pouch bag experiment result, the experimental procedure will be summarized (see CHAPTER 3 for full details). LFP/graphite cells were

filled with electrolyte and underwent the typical first cycle. Then, cells were charged to top of charge (3.65 V) and held at that voltage for approximately 36 hr. Next, cells were brought into a glovebox and disassembled. Positive and negative electrodes were separated and placed into separate laminate foil bags. Extra DMC was added to the bags to account for evaporation during the disassembly process, and the bags were vacuum sealed. At this point, the pouch bags could be monitored for gas production originating from one electrode alone using the ex-situ gas volume measurement. To accelerate the rate of parasitic reactions, the pouch bags were stored at 60°C.

Figure 5.16 shows evolved gas volumes versus storage time for (a) LFP positive electrodes, and (b) graphite negative electrodes. Both Control electrolytes and 2VC electrolytes were tested with LiPF<sub>6</sub> and LiFSI salts. The volume of gas produced in charged LFP pouch bags was very small, regardless of electrolyte used. The two Control electrolytes (LiPF<sub>6</sub>-based and LiFSI-based, respectively) had the highest absolute volume of gas produced by a small margin, but the average gas production rate estimated by the slope of the volume vs time plot was essentially zero for all electrolytes. This result suggests that the charged LFP cathode is essentially inert to reactions with the electrolyte, even in electrolyte solutions that perform extremely poorly in full cell cycling experiments. Of course, this may be expected given the low redox potential of LFP and tightly bound oxygen that is not prone to release from the lattice at high states of charge<sup>141</sup>, unlike that seen in layered oxide materials<sup>138</sup>. This also suggests that the majority of gas-producing parasitic reactions in LFP/graphite cells originate at the charged graphite negative electrode.

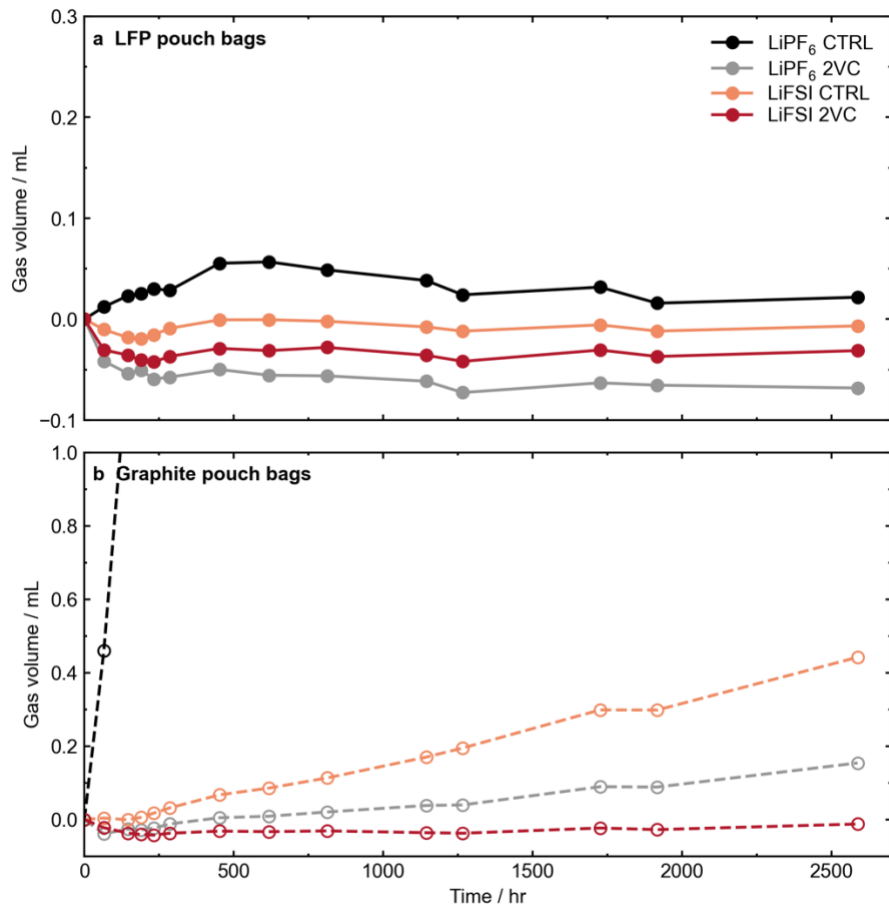


Figure 5.16: Volumes of gas formation versus time for pouch bags constructed from disassembled LFP/AG pouch cells stored at 60°C. (a) Pouch bags from LFP positive electrodes. (b) Pouch bags from graphite negative electrodes.

Figure 5.16b shows volumes of gas evolved versus time for pouch bags with charged negative electrodes and different electrolytes. Immediately, significant differences between the electrolytes can be seen. A large volume of gas was produced in the LiPF<sub>6</sub> Control pouch bag, with 1 mL of gas evolved in less than 200 hours. In contrast, the remaining pouch bags with the other electrolytes each produced less than 0.5 mL of gas in over 2500 hr of storage at 60°C. The pouch bag with the next highest gas volume had LiFSI Control electrolyte. A small amount of gas (0.2 mL) was produced with LiPF<sub>6</sub> + 2VC electrolyte, while the pouch bag with LiFSI + 2VC electrolyte produced virtually zero gas over 2500

hr at 60°C. Note as well that the ordering of gas production in the negative electrode pouch bags matches the ordering of long-term cycling performance at high temperature: LiPF<sub>6</sub> CTRL <<< LiFSI CTRL < LiPF<sub>6</sub> 2VC < LiFSI 2VC, where LiPF<sub>6</sub> CTRL has the worst cycle life (by a wide margin) and LiFSI 2VC has the best cycle life at high temperature. This also suggests that the reversible capacity retention in LFP/Graphite cells should be primarily dictated by the reactivity of the charged negative electrode. These results do not preclude the existence of a reversible shuttle in the case of LiFSI + 2VC, since reaction products at the negative electrode were not able to interact with the positive electrode in this experiment.

Measuring gas produced in pouch bags is valuable to understand at which electrode gas-producing parasitic reactions originate in LFP/graphite cells. However, not all parasitic reactions will have gaseous products, so therefore not all parasitic reactions occurring in the pouch bags may be captured by measuring the gas volume. Similar experiments were carried out in the microcalorimeter to capture parasitic reactions that do not have gaseous products, and as well to rank the parasitic reactions of separated pouch bags on a shorter timescale, taking advantage of the extremely high sensitivity of the calorimeter. In this experiment only electrolytes containing 2% VC were considered. Additionally, to further understand the dependence of choice of Li salt on “cross-talk” parasitic reactions, full cells were constructed alongside separated electrodes in pouch bags so that the full cell parasitic heat flow (in open circuit at top of charge) could be compared to the parasitic heat flows occurring separately at the positive and negative electrodes. To develop this idea, consider the model equation of heat flow from a Li-ion cell introduced in CHAPTER 2<sup>285-287</sup>:

$$\dot{q} = |I\eta| + \frac{IT}{e} \left[ \frac{ds_+}{dx} - \frac{ds_-}{dx} \right] + q_p \quad 5.1$$

If the cell is fully charged, i.e. the cell is in equilibrium with no internal Li concentration gradients, and the cell is in open circuit ( $I = 0$ ), the measured heat flow is simply equal to the parasitic heat flow:

$$\dot{q} = q_p \quad 5.2$$

Since in the pouch bag experiments the parasitic reactions occurring at the positive and negative electrode occur separately without any cross talk, they will be labelled separately as  $q_P$  and  $q_N$ , respectively (note the subtle difference between  $q_p$  and  $q_P$ ). Now, imagine a full cell with no cross-talk between the positive and negative electrodes, meaning parasitic reactions occurring at the positive electrode do not further react at the negative electrode and vice versa. In this case, the total parasitic heat flow of the full cell should equal the sum of the heat flows of the separated pouch bags:

$$q_p \equiv q_F = q_P + q_N, \quad 5.3$$

where  $q_F$  is defined for simplicity to be the parasitic heat flow of the full cell to avoid confusion with nomenclature. However, such cross-talk reactions are very common in Li-ion batteries<sup>136,146,151,215</sup>, so it would be expected that these values would not match exactly. Therefore, Equation 3 will be modified slightly to account for excess heat flow from cross-talk reactions  $\Delta\dot{q}$ :

$$q_F = q_P + q_N + \Delta\dot{q} \quad 5.4$$

Comparing full cell heat flow to the heat flows from the pouch bags will allow for a better understanding of where parasitic reactions occur in LFP/graphite cells and the degree of cross talk that occurs as a function of different Li salts used in the electrolyte.

Figure 5.17a shows measured heat flow versus time for pouch bags and full cells (OCV mode) in the calorimeter. Note that  $t = 0$  refers to the moment the cells were inserted into the calorimeter, so a small equilibration period was expected for the measured heat flow. The experiment ran for approximately 135 hours. First, notice the large difference in measured heat flow for the positive pouch bags compared to the negative pouch bags. Both the LFP pouch bags with  $\text{LiPF}_6 + 2\text{VC}$  electrolyte and  $\text{LiFSI} + 2\text{VC}$  electrolyte had heat flows of  $\sim 2.5 \mu\text{W}$  and were identical by the end of the experiment. The heat flows of the LFP pouch bags were only slightly larger than that of electrolyte alone, shown in Figure A.6. The graphite pouch bags showed much higher heat flow than the LFP pouch bags, much closer to the values of parasitic heat flow that were seen in the full cell cycling experiments in Figure 5.8 ( $\sim 10 - 15 \mu\text{W}$ ). In the full cell cycling experiments, the  $\text{LiFSI}$ -containing cells with 2VC showed slightly higher parasitic heat flow in all cycles. Here, the  $\text{LiFSI}$ -containing graphite pouch bags had slightly *lower* heat flow than the  $\text{LiPF}_6$ -containing counterpart by the end of the experiment. Interestingly, the charged full cells had similar heat flow, where the  $\text{LiFSI}$ -containing full cell was marginally higher by the end. This suggests that full cell effects such as cross talk or shuttle reactions, contributed to the higher parasitic heat flow that was seen in  $\text{LiFSI} + 2\text{VC}$  cells in the cycling experiments, and when isolated from the positive electrode, the graphite SEI formed from the  $\text{LiFSI}$  electrolyte may be less reactive than with  $\text{LiPF}_6$ -based electrolyte.

Once the cells equilibrated in the calorimeter, the measured heat flow was equal to the parasitic heat flow as discussed above. Here, the parasitic heat flow was taken to be the average heat flow over the last 5 hours of the experiment. Figure 5.17b shows the parasitic

heat flow for each of the pouch bags (blue bars) and full cells (black bars) such that the sum of the pouch bag heat flows can be compared to full cell heat flow for each electrolyte. As discussed above, the difference between the full cell heat flow and the individual pouch bag heat flows,  $\Delta\dot{q}$ , is a measure of the parasitic heat flow from cross talk or shuttle reactions that interact with both electrodes. The full cell parasitic heat flow values for both the LiPF<sub>6</sub> and LiFSI cells were similar, but  $\Delta\dot{q}$  was higher for the LiFSI-containing cell. This suggests that more crosstalk or shuttle reactions occur in full LFP/Graphite cells when LiFSI electrolyte is used, agreeing with the earlier IMC cycling experiments. The higher  $\Delta\dot{q}$  observed in LiFSI + 2VC electrolyte agrees with earlier UHPC and storage results that showed higher slippage and self-discharge, respectively, all pointing to the existence of a shuttle reaction in this electrolyte. So, while the parasitic heat flow measurements for graphite pouch bags suggest a better passivating SEI layer when using LiFSI electrolyte, additional parasitic reactions arise with the use of this salt in full cells that are not seen in LiPF<sub>6</sub>-containing electrolytes. The nature of these reactions will be discussed in more detail below.



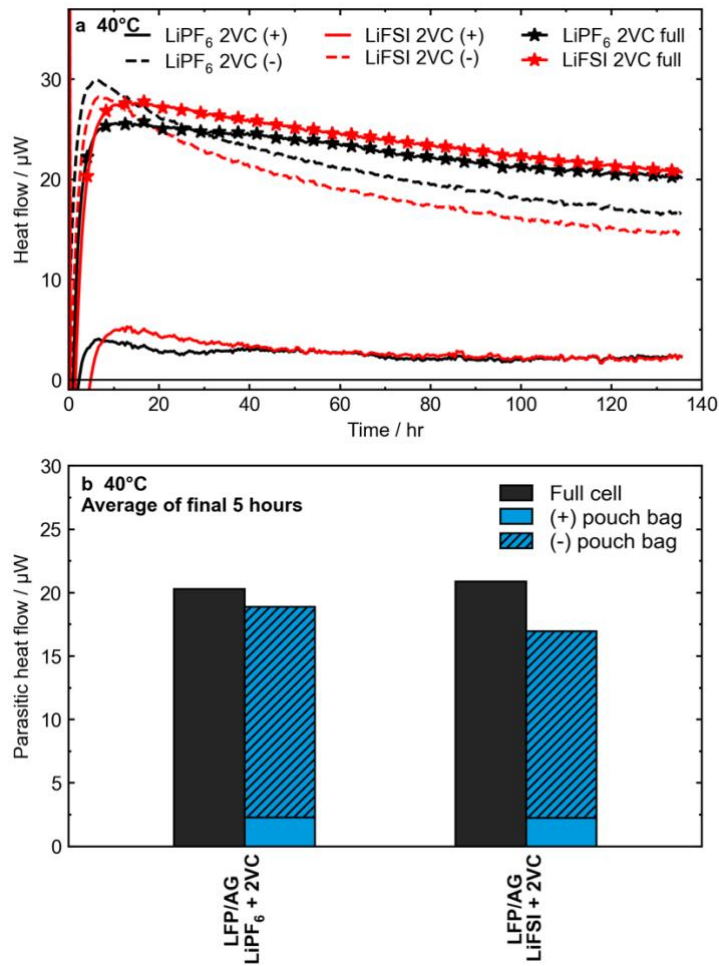


Figure 5.17: (a) Heat flow in open circuit versus time as measured using isothermal microcalorimetry for LFP/AG pouch bags and pouch cells. Full pouch cells were charged to top of charge (3.65 V), and held at that voltage for ~36 hr before being inserted into the calorimeter. Pouch bags made from full pouch cells (+ or – electrodes as indicated in the legend) were held at top of charge for ~36 hr before being disassembled into pouch bags. (b) Parasitic heat flow as defined as the average heat flow over the last 5 hours of the experiment. The sum of heat flows from the individual positive/negative pouch bags are compared to the heat flow from a full cell in open circuit.

While the results of the pouch bag calorimetry experiments agree with the results of other studies including UHPC, storage, and calorimetry cycling experiments, some limitations of this method must be noted. When pouch cells are disassembled in the glovebox, it may take up to 10 minutes to unroll the jelly roll and reassemble the electrodes into pouch bags. The key assumption that is made in this process is that only the most volatile component

of the electrolyte, DMC, is lost. Extra DMC is added to the pouch bag to account for this loss. While this is likely a good assumption, the resulting electrolyte compositions of the pouch bags will not be identical to the full cell that they are compared to in the calorimeter, which may cause small differences in the measured heat flow. This point should be kept in mind by the reader going forward.

### 5.3.3 Discussion

Many results for the Li salt/electrolyte additive parameter space (LiPF<sub>6</sub> CTRL, LiPF<sub>6</sub> 2VC, LiFSI CTRL, LiFSI 2VC) have been shown here. Now, these results will be discussed in an attempt to synthesize the results of the various experiments and present a coherent narrative for the impact of both different salts and electrolyte additives in LFP/Graphite cells.

The behaviour and cycle performance of LFP/Graphite cells with different Li salts was highly dependent on whether additional electrolyte additives were used. First consider the case of Control electrolyte (no additives). In this case, the extremely poor capacity retention of cells with LiPF<sub>6</sub>-based electrolyte could be mitigated with the use of LiFSI. Better capacity retention was seen with LiFSI-based Control electrolytes at 40°C and 55°C (Figure 5.8, Figure 5.9). Consequently, UHPC cycling revealed replacing LiPF<sub>6</sub> with LiFSI in Control electrolyte led to a large increase in coulombic efficiency (CE) and dramatically lowered charge endpoint capacity slippage (Figure 5.11), and isothermal microcalorimetry (IMC) measurements of parasitic heat flow showed much lower parasitic heat flow with LiFSI-based electrolyte compared to LiPF<sub>6</sub> (Figure 5.12, Figure 5.14), all issues that were

identified with the LiPF<sub>6</sub> Control electrolyte in CHAPTER 4. In high temperature OCV storage (Figure 5.15), severe self-discharge in Control electrolyte was prevented by using LiFSI. Approximately 7 times less deposited Fe was detected in a cell with LiFSI Control electrolyte (1.9 μg/cm<sup>2</sup>) compared to LiPF<sub>6</sub> Control after the same cycling conditions at 40°C. Finally, pouch bag storage experiments at 60°C (Figure 5.16) revealed minimal gas originating from the LFP electrode in Control electrolyte regardless of salt used, and substantial volumes of gas produced at the graphite electrode in LiPF<sub>6</sub> Control electrolyte only.

All these results indicate the presence of rapid and severe degradation in the LFP/graphite chemistry that are enabled by the presence of the LiPF<sub>6</sub> salt. The complete self-discharge of the LiPF<sub>6</sub> Control cells in high temperature storage and extremely high parasitic heat flow in IMC experiments suggests the existence of a molecular shuttle that can be oxidized at the positive electrode, and subsequently be reduced at the negative electrode to its original form. This process would be accompanied by a continual rapid self-discharge as Li ions are removed from the negative electrode and intercalated into the positive electrode to balance the charge as this shuttle reaction occurs<sup>123</sup>. Shuttling behaviour has been observed in LiPF<sub>6</sub> Control electrolyte extracted from LFP cells, and is discussed in much more depth in a recent publication by Boulanger et al.<sup>269</sup>

In addition to the shuttling molecule that arises in LiPF<sub>6</sub> Control electrolyte, a substantial amount of Fe dissolution and deposition occurs when this electrolyte was used. This is likely a combination of Fe dissolution arising from the acidic decomposition products of

LiPF<sub>6</sub>, and facile deposition of Fe at the negative electrode by a poorly passivating SEI layer.

The initial structure of an EC-based SEI on a graphite electrode has been shown to primarily consist of LiF and lithium ethylene decarbonate (LEDC)<sup>89-94</sup>. Some recent work has called this interpretation into question, instead proposing lithium ethylene monocarbonate (LEMC) is primary component of the SEI<sup>95</sup>. However, given the similar structures of these two compounds, they will likely decompose similarly in a full cell environment, so the below discussion should not be affected by the LEDC/LEMC debate. LEDC is quite reactive, and can be hydrolyzed easily to form Li<sub>2</sub>CO<sub>3</sub>, CO<sub>2</sub>, and lithium alkoxides<sup>88</sup>. Additionally, LEDC can thermally decompose (again forming Li<sub>2</sub>CO<sub>3</sub> and CO<sub>2</sub>, among other products), and can react in the presence of LiPF<sub>6</sub> salt to form LiF and CO<sub>2</sub>, among other products<sup>86</sup>. Once Li<sub>2</sub>CO<sub>3</sub> is formed, it can further react with the LiPF<sub>6</sub> salt, forming more CO<sub>2</sub> and LiF. Note that CO<sub>2</sub> is a product in all of these decomposition reactions. The decomposition of LEDC and Li<sub>2</sub>CO<sub>3</sub> could explain the large amount of gas detected in the graphite pouch bag experiment. These reactions would also contribute to the parasitic heat flow detected in IMC experiments. As noted by Heiskanen et al.<sup>89</sup>, this severe decomposition of the SEI in Control electrolyte (especially in the presence of LiPF<sub>6</sub>) will result in a film that is porous, leading to further EC reduction and SEI formation. Additionally, a porous, poorly passivating SEI film would likely allow for dissolved Fe ions to deposit easily.

When LiFSI replaces LiPF<sub>6</sub> in the electrolyte, the initial structure of the SEI in Control electrolyte should be similar, primarily consisting of LEDC and LiF (LiPF<sub>6</sub> is the primary source of LiF in the initial SEI structure, but LiFSI has also been shown to decompose into LiF<sup>288</sup>). However, the decomposition of LEDC catalyzed by LiPF<sub>6</sub> would no longer occur in the case of LiFSI. Since that reaction is said to occur rapidly at high temperature<sup>86</sup>, LEDC may decompose much more slowly in LiFSI electrolyte, which could explain the much lower gas volumes detected (Figure 5.16b), lower parasitic heat flow (Figure 5.12), and much improved long-term cycle life (Figure 5.8). Therefore, LFP/Graphite cells with LiPF<sub>6</sub>-based Control electrolyte suffer from the concomitant issues of rapid SEI decomposition, facile Fe dissolution, and continuous reduction of EC, all of which can be remedied by replacing LiPF<sub>6</sub> with LiFSI.

VC-containing electrolyte presents a different situation. The initial structure of the graphite SEI is different, now likely consisting primarily of poly(VC), LiF, and Li<sub>2</sub>CO<sub>3</sub><sup>89,90</sup>. Again, the choice of salt should not significantly impact the SEI composition after the first cycle. The poly(VC) in the SEI will be more robust than LEDC, and decomposition should not occur quickly. Li<sub>2</sub>CO<sub>3</sub> will react via the reactions outlined above, producing some CO<sub>2</sub>.

The mysteries that remain are the unexpected results for LiFSI + 2VC electrolyte in calorimetry, UHPC, and storage experiments, which all showed metrics that would *typically* point to worse long-term performance compared to the LiPF<sub>6</sub> + 2VC electrolyte, despite the significantly *better* cycling of LiFSI-containing cells. The most logical explanation for these seemingly contradictory results is that the lower CE, higher slippage,

higher parasitic heat flow, and higher storage losses in LiFSI cells correspond to some parasitic reaction, likely a shuttle or some other type of crosstalk reaction, that does not affect the cyclable Li inventory. One hint that leads to this explanation is that only the *reversible* capacity loss (i.e. capacity that can be recovered on the next charge) was higher in LiFSI-containing cells in OCV storage, and irreversible capacity loss (e.g. from SEI formation) was very similar for LiPF<sub>6</sub> and LiFSI cells with 2VC electrolyte. Further, experiments that considered the LFP and graphite electrodes *separately* saw benefits to using LiFSI over LiPF<sub>6</sub>; less gas was produced in LiFSI + 2VC graphite pouch bags, and similarly the parasitic heat flow was lower for graphite pouch bags containing LiFSI. Therefore, it seems that the lifetime benefit brought on by the use of LiFSI has to do with a better passivating SEI on the negative electrode. In the literature, Kang et al. have reported a thinner SEI layer rich in inorganic species was achieved in an LiFSI-based electrolyte compared to an LiPF<sub>6</sub>-based electrolyte<sup>289</sup>, which may be reflected in the positive results of the pouch bag experiments here. This additional cross-talk reaction, whatever it may be, “muddies the water” for typical advanced characterization techniques such as UHPC and IMC, but does not seem to affect cycle lifetime.

This section highlighted the significant impact that the choice of Li salt in the electrolyte can make to the high temperature lifetime of LFP/graphite cells. Using LiFSI as the primary salt in the electrolyte significantly improved high temperature lifetime. Despite some unexpected results in the LiFSI + 2VC electrolyte that suggested a redox shuttle, the use of LiFSI is promising in LFP cells. The LFP/Graphite cells with 1.5 M LiFSI + 2VC electrolyte cycled exceptionally well at high temperature despite the slight shuttling

behaviour observed **in the early cycles** in more sensitive experiments. This self-discharge was clearly not an issue in the CCCV cycling protocols considered here, but it may be worth considering for more commercially-relevant applications, such as grid-storage. In cases where cells are required to remain at high states of charge for long periods of time at extremely high temperatures before the stored energy is needed, a self-discharge process like that seen in LiFSI + 2VC may reduce the storage efficiency, as a small amount of charge is continually lost during storage. Given the clear benefits that LiFSI provides in cycling in LFP/graphite cells, other solutions could be considered to mitigate this self-discharge process.

#### **5.4 IMPACT OF DIFFERENT GRAPHITE MATERIALS**

In the previous section, it was shown that using LiFSI instead of LiPF<sub>6</sub> in the electrolyte improved the high temperature cycling of LFP cells. Pouch bag experiments measuring both gas volumes (Figure 5.16) and parasitic heat flow (Figure 5.17) suggested that most parasitic reactions and thus most Li inventory loss was occurring at the negative electrode. Therefore, attention is now placed on the graphite material itself as an avenue to further improve high temperature lifetime in LFP/graphite cells.

Eldesoky et al. recently published a series of papers looking at the impact of different graphite materials on the performance of NMC811/graphite cells<sup>53,290</sup>. In these works, important differences in the physical properties of several natural graphites (NGs) and artificial graphites (AGs) were found, which were correlated to significant differences in electrochemical performance. In particular, AGs with low electrochemically active surface

area greatly improved the high temperature capacity retention of NMC811/graphite cells operating at relatively low voltage. Previously, Glazier et al. correlated parasitic heat flow from IMC measurements to cycle life in NMC532/Graphite and NMC622/Graphite cells<sup>54</sup>. Huang et al. studied the impact of graphite pyrolysis temperature on cycle life in NMC532/Graphite cells<sup>291</sup>.

This section will consider the performance of LFP cells with three different artificial graphite (AG) negative electrodes. These are the same AG materials that were studied in Eldesoky et al.<sup>53,290</sup> Table 5.2 shows some of the relevant physical properties of these different materials. Note that AG-A is the same graphite material that has been used in all cells throughout this thesis up to this point. AG-B has the largest average particle size as well as the largest tap density. Both AG-B and AG-C have lower surface areas compared to AG-A. Cells were tested with both LiPF<sub>6</sub> and LiFSI-based electrolytes. LiPF<sub>6</sub> Control electrolyte was excluded from this study.

Table 5.2: Physical properties of the different artificial graphites (AG) studied. These values were previously reported in Eldesoky et al.<sup>53</sup>

Artificial Graphite type	D50 (μm)	SSA (m <sup>2</sup> /g)	Tap density (g/cm <sup>3</sup> )
AG-A	16.02	1.29	1.08
AG-B	17.94	1.08	1.40
AG-C	15.64	1.00	1.12

Figure 5.18a shows the gas volume evolved in the formation cycle versus first cycle efficiency (FCE) of LFP/AG cells with different AGs, and Figure 5.18b shows charge-transfer resistance versus FCE. First note how the FCE varies as a function of graphite



type. AG-A had the lowest FCE (around 0.90) followed by AG-B, and AG-C with the highest FCE, averaging around 0.95. This means that for AG-B and AG-C, less Li was consumed in the first cycle compared to AG-A. Accordingly, less gas was produced in this first cycle for AG-B and AG-C cells. For all cells, there was little difference between the gas produced in LiPF<sub>6</sub> and LiFSI-containing cells.

The opposite correlation with FCE was seen for the charge-transfer resistance,  $R_{CT}$  (Figure 5.18b). Here, the  $R_{CT}$  measured after formation increased as FCE increased in a linear fashion. As well, the use of LiFSI electrolyte appeared to decrease  $R_{CT}$  after formation by a near constant amount, regardless of the AG type used. The high  $R_{CT}$  values seen in AG-B and AG-C cells may cause worries about impedance growth issues as these cells cycle, so LiFSI may be an option to limit this impedance growth. The issue of impedance growth will be considered in more detail in the next chapter.

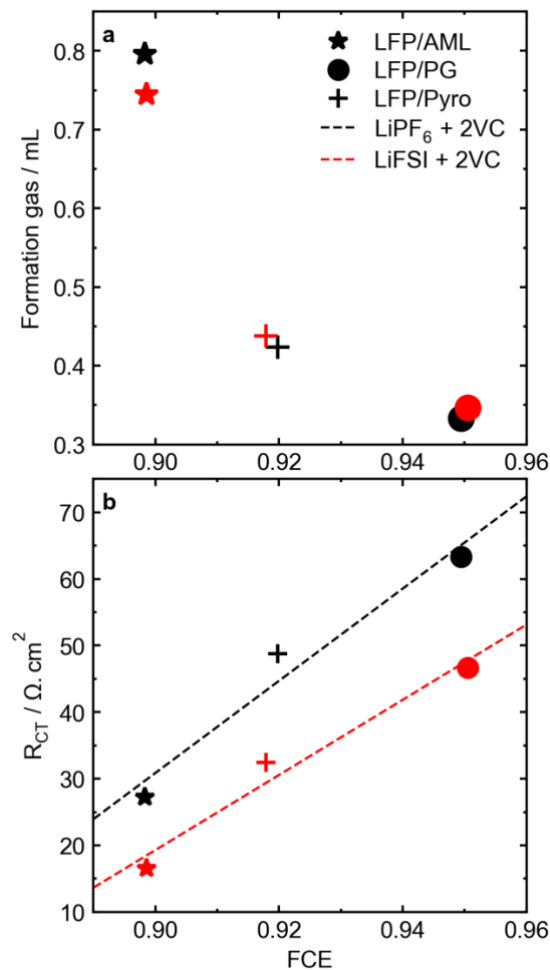


Figure 5.18: Correlation of formation quantities to the first cycle efficiency. (a) Gas volume as a function of FCE. (b) Charge-transfer resistance as a function of FCE.

Figure 5.19 shows long-term cycling results for LFP/AG cells at 55°C. Cells were cycled at C/3 rate for both charge and discharge. The type of AG used is specified by different colours in the plot, and different electrolyte types are shown by different symbols. It is not surprising that LiFSI Control electrolyte performed the worst here, as this was seen already in the previous section (Figure 5.9). However, this electrolyte was still valuable as it amplified the differences between the different AGs. While the AG-A cell with LiFSI Control electrolyte lost 10% of its initial capacity after only 50 cycles at 55°C, the AG-C cell took closer to 300 cycles at 55°C to reach 90% capacity. Similarly, the AG-B cell

reached 90% capacity at around 225 cycles. In cells with 2VC electrolyte, the differences between AGs were more subtle. However, after 350 cycles or so it became clear that AG-B and AG-C cells had better capacity retention than AG-A cells, both in the LiPF<sub>6</sub> and LiFSI cases. Also note that for all graphite types, cells with LiFSI + 2VC electrolyte had the best capacity retention at 55°C. Despite the high R<sub>CT</sub> of AG-B and AG-C cells after the first cycle (Figure 5.18), voltage polarization was very stable for all cells cycled at 55°C, again suggesting that impedance growth is not a significant concern in these cells.

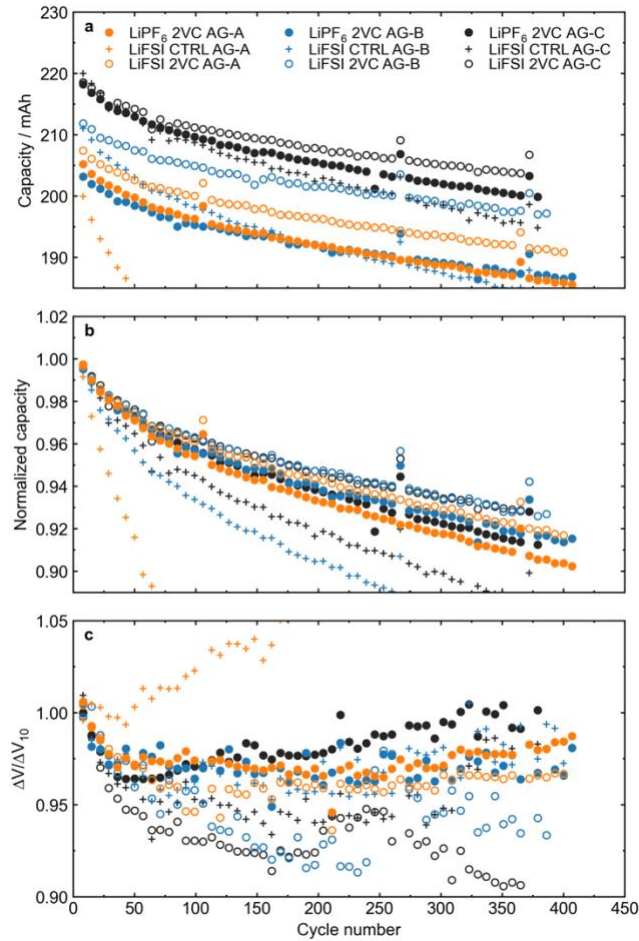


Figure 5.19: Long-term cycling results for LFP cells with different graphite negatives cycling at C/3 rate at 55°C. (a) Absolute discharge capacity versus cycle number. (b) Normalized capacity (normalized to cycle 5) versus cycle number. (c) Absolute voltage polarization versus cycle number.

OCV storage experiments were carried out at 60°C for cells with different AGs to probe the reversible and irreversible capacity loss for the different graphite types. Once again, both LiPF<sub>6</sub> + 2VC and LiFSI + 2VC electrolytes were used. Figure 5.20 shows the reversible and irreversible capacity losses after 500 hr of storage for the different cells. The sum of the two bars for each cell type gives the total capacity lost over this period (i.e. D<sub>0</sub> – D<sub>1</sub>, see CHAPTER 3). A dashed line in Figure 5.20 represents the total capacity loss for LFP/AG-A with LiPF<sub>6</sub> + 2VC electrolyte and is meant to be a guide to the eye for comparison with the other cell types. Both LFP/AG-B and LFP/AG-C cells had less total capacity loss during storage than LFP/AG-A cells, and this was true for both LiPF<sub>6</sub> + 2VC and LiFSI + 2VC electrolytes. As well, notice the ratio between reversible and irreversible capacity losses. Like that seen in the previous section (Figure 5.15), more *reversible* capacity loss was seen in LiFSI + 2VC electrolytes compared to LiPF<sub>6</sub> + 2VC electrolytes regardless of AG choice, meaning that the shuttle proposed for LiFSI + 2VC electrolytes may still potentially be an issue in AG-B and AG-C cells. However, notice the magnitude of reversible capacity loss was lower for AG-B and AG-C cells with LiFSI electrolyte, suggesting that the use of these AGs could at least reduce the impact from this shuttle. Notice as well that the reversible capacity loss for LiPF<sub>6</sub> electrolytes was virtually identical for all AGs, suggesting that there is some inherent reversible capacity loss that occurs in all cells. The improvements in the AG-B and AG-C cells came from the reduction in irreversible capacity loss, suggesting that SEI-forming reactions or other reactions that consume Li inventory were less prevalent in these cells.

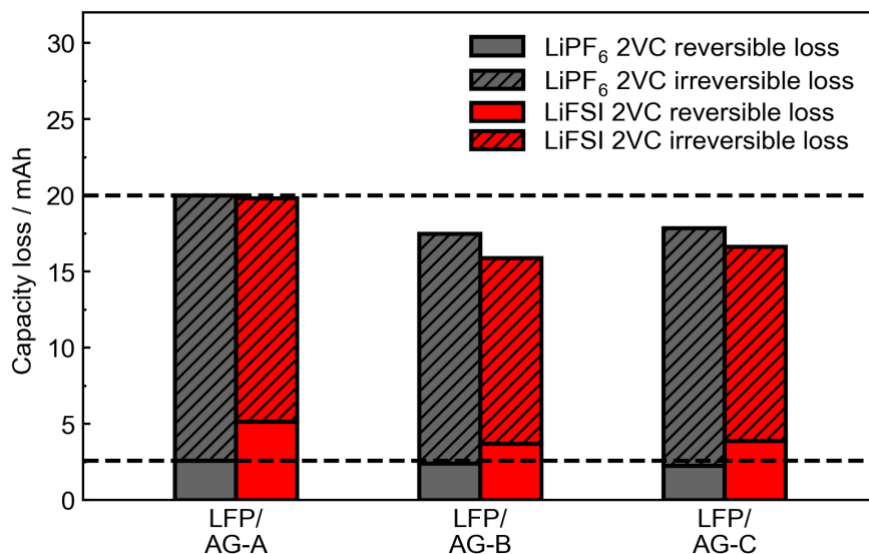


Figure 5.20: Reversible and irreversible capacity losses in 60°C storage experiments. The dashed line shows total capacity loss for LFP/AG-A with LiPF<sub>6</sub> + 2VC electrolyte as a guide to the eye.

IMC cycling experiments were done on LFP cells with the different AG negative electrodes. Both the LiPF<sub>6</sub> + 2VC and LiFSI + 2VC electrolytes were tested. These cells used the same cycling protocol that was introduced in CHAPTER 4. A slight modification was needed for the LFP/AG-B cells, as the voltage limits for the graphite plateaus were slightly different than the LFP/AG-A and LFP/AG-C cells (see Figure A.7). The voltage limits for the LFP/AG-B cells were 3.250 V – 3.335 V for the 2L → 2 plateau and 3.290 V – 3.400 V for the 2 → 1 plateau. This slight difference should not affect the interpretation of the results. Graphs of parasitic heat flow versus relative SOC are shown in the appendix (Figure A.8). It should also be noted that the explanation for the different voltage curves between AG-A/AG-C and AG-B cells is not known at this time.

Figure 5.21 shows the average parasitic heat flow versus cycle number for the IMC cycles at 40°C. Here, a clear decrease in parasitic heat flow was seen in the LFP/AG-B and

LFP/AG-C cells compared to the LFP/AG-A cells with both electrolyte types. The average parasitic heat flow for LFP/AC-C cells in the last cycle was almost half that of the LFP/AG-A cells at the same cycle. This suggests much fewer parasitic reactions occur in the LFP/AG-B and LFP/AG-C cells compared to AG-A, supporting the long-term cycling and OCV storage experiments. As well, notice the differences in parasitic heat flow between LiPF<sub>6</sub> and LiFSI electrolytes in the different LFP/AG cells. In the LFP/AG-A cells, cells with LiFSI + 2VC electrolyte had slightly higher parasitic heat flow, as was discussed in the previous section. Here, both LFP/AG-B and LFP/AG-C cells with LiFSI electrolyte had essentially the same parasitic heat flow as their corresponding LiPF<sub>6</sub>-based cells. This higher parasitic heat flow that was observed in LiFSI + 2VC cells was attributed to a cross-talk or shuttle reaction. This means that AG-B and AG-C cells could inhibit this reaction. This result is also consistent with the storage results above (Figure 5.20) that showed lower reversible capacity loss in AG-B and AG-C cells with LiFSI compared to AG-A. This being said, the differences in parasitic heat flows between electrolytes were small to begin with, so it is difficult to say with certainty that AG-B and AG-C inhibits the shuttle in LiFSI + 2VC electrolyte.

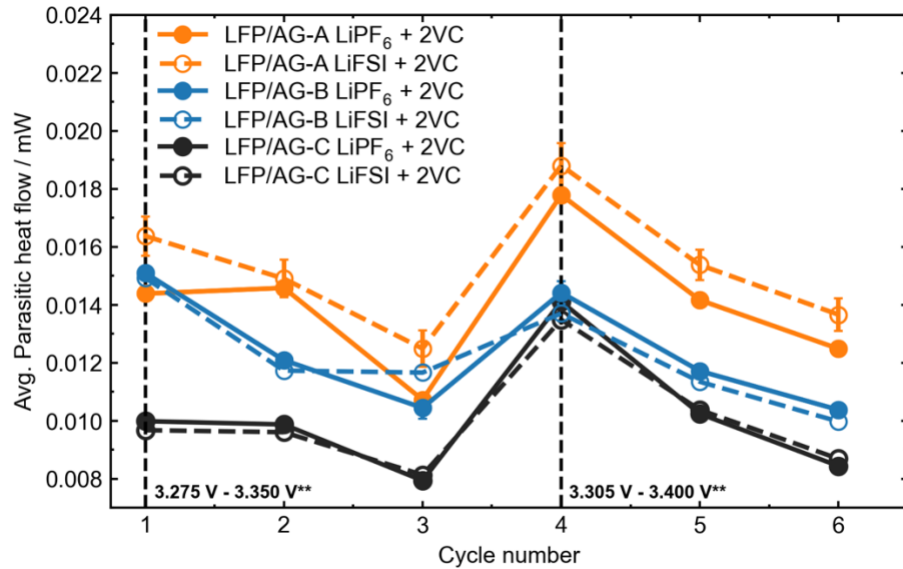


Figure 5.21: Average parasitic heat flow versus cycle number for LFP/AG cells with different graphites. Note that the voltage limits for the LFP/AG-B cells was slightly different than that indicated in the graph legend (3.250 V – 3.335 V and 3.290 V – 3.400 V, respectively).

Pouch bag experiments were carried out in the microcalorimeter as was done in the previous section. Due to limited channels, only LFP/AG-A and LFP/AG-C cells were tested. Both LiPF<sub>6</sub> + 2VC and LiFSI + 2VC electrolytes were tested. Like in the previous section, both fully charged electrodes in pouch bags and full cells in open circuit were tested in the microcalorimeter. Figure 5.22 shows the average parasitic heat flow at 40°C for these cells and pouch bags, which again was taken to be the average heat flow over the final 5 hours of the experiment. Full cell heat flow is compared to the sum of pouch bag heat flows. First notice that the parasitic heat flows for the LFP pouch bags extracted from LFP/AG-C cells were again very low. The parasitic heat flow may have been marginally lower than the LFP pouch bags from LFP/AG-A cells, which could be due to less cross-talk products being formed in the first cycle before the pouch bags were constructed, but this cannot be said with certainty. The graphite pouch bags from AG-C cells also showed lower parasitic heat flow than corresponding AG-A pouch bags. This was true for both

LiPF<sub>6</sub> and LiFSI electrolytes. As well, the LFP/AG-C full cells in open circuit showed lower parasitic heat flow than the LFP/AG-A cells, agreeing with the full cell cycling experiments (Figure 5.21). Finally, consider the quantity  $\Delta\dot{q}$ , which was defined to be the difference between full cell parasitic heat flow, and the sum of positive and negative pouch bag parasitic heat flow, attributable to cross-talk and shuttle reactions that require both electrodes. This quantity is smaller in the LFP/AG-C case, especially in LiFSI electrolyte. This result again suggests that the use of the AG-C graphite reduces shuttle reactions arising from the LiFSI + 2VC electrolyte.

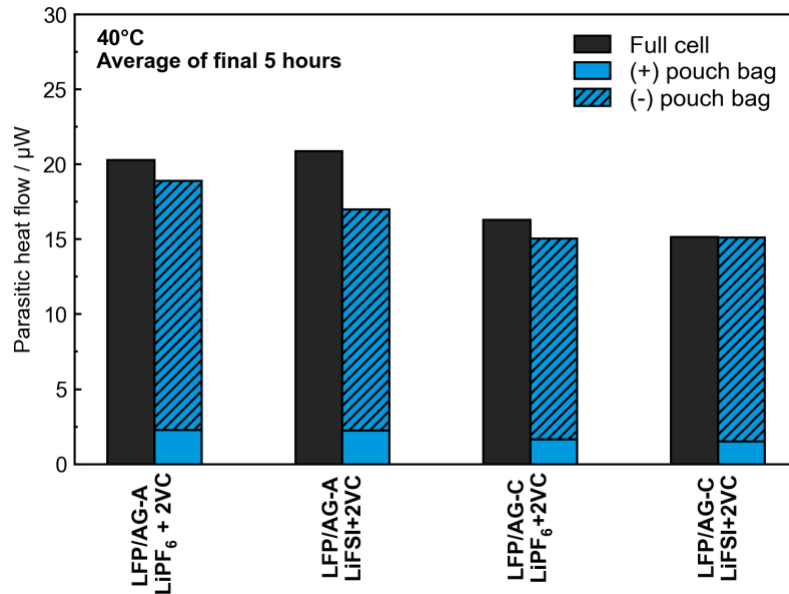


Figure 5.22: Average parasitic heat flow (averaged over final five hours of experiment) for LFP/AG-A and LFP/AG-C cells, comparing full cells in OCV mode and the sum of separate pouch bags.

The results of the previous two sections (Sections 5.2 and 5.3) indicated that the most significant mechanism of capacity loss in LFP/graphite cells was Li inventory loss at the negative electrode. This section considered the impact of artificial graphite materials with



low surface area as a potential solution to further improve capacity retention in LFP cells. Indeed, cells with AG-B or AG-C showed better cycle performance at 55°C in all electrolytes. Storage experiments at 60°C showed less capacity loss in AG-B and AG-C cells, including less reversible capacity loss with LiFSI + 2VC electrolyte, which was found to be an issue in the previous section (5.3). IMC cycling experiments in full cells showed lower parasitic heat flow in AG-B and AG-C cells. IMC experiments in pouch bags found lower parasitic heat flow in AG-C pouch bags compared to AG-A, and less “cross-talk” parasitic heat flow,  $\Delta\dot{q}$ , in the case of LiFSI + 2VC electrolyte paired with AG-C. These experiments have shown that the improved cycle performance of LFP/AG-B and LFP/AG-C cells was a result of less Li inventory loss in these cells compared to LFP/AG-A.

## **5.5 SUMMARY AND OUTLOOK**

In this chapter, several studies were done to better understand degradation of LFP/graphite cells and improve high temperature lifetime. These studies targeted the positive electrode, the electrolyte, and the graphite negative electrode. Studies on the impact of LFP particle size and surface area found that cells with low surface area LFP had more capacity loss. This was found to be due to fracturing of the LFP particles, leading to exposed, non-carbon coated LFP surface reacting with electrolyte. When LiPF<sub>6</sub> in the electrolyte was replaced with LiFSI, an improvement in high temperature capacity retention was seen in cells both with and without electrolyte additives. While several tests such as UHPC, IMC, and OCV storage indicated the existence of a self-discharging shuttle mechanism in LiFSI + 2VC electrolyte, it did not impact cycle life in long-term cycling experiments. Additionally, pouch bag experiments indicated the graphite SEI in LiFSI + 2VC electrolyte was better

passivating than in  $\text{LiPF}_6 + 2\text{VC}$  electrolyte. Finally, LFP/Graphite cells with three different artificial graphites (AGs) were tested. AGs with lower surface area showed improved high temperature cycle performance, as well as lower parasitic heat flow and better storage performance. As well, the use of improved AG materials may have reduced the shuttle activity in  $\text{LiFSI} + 2\text{VC}$  electrolyte.

At this point, the net improvement to high temperature cycle life of LFP/graphite cells can be gauged. Figure 5.23 shows normalized capacity versus cycling time at (a)  $40^\circ\text{C}$  and (b)  $55^\circ\text{C}$  for a number of cells that have been presented in this thesis up to this point. All cells were cycled at C/3:C/3 rate, with the exception of the “famous” commercial LFP at  $40^\circ\text{C}$ . The previous “best effort” cell from CHAPTER 4 was LFP/AG-A with 1.5 M  $\text{LiPF}_6 + 2\text{VC} + 1\text{DTD}$  electrolyte (orange points). This cell reached 90% capacity after approximately 4000 hr and 2000 hr at  $40^\circ\text{C}$  and  $55^\circ\text{C}$ , respectively. The next improvement was using medium BET LFP/AG-A cells with 1.5 M  $\text{LiFSI} + 2\text{VC}$  electrolyte. Next, using the low surface area artificial graphite AG-C with  $\text{LiFSI}$  electrolyte showed further improvements at  $55^\circ\text{C}$ , but little improvement at  $40^\circ\text{C}$  after >8000 hr of testing. It is possible that LFP/AG-C would show improved capacity retention over LFP/AG-A after more hours of testing at  $40^\circ\text{C}$ . Finally, these improvements that have been made in this chapter are compared to the same NMC532/AG-A cells from Chapter 5, as well as a commercial (“famous”) LFP cell that represents a state-of-the art commercial LFP cell. Both LFP/AG-A and LFP/AG-C cells with  $\text{LiFSI} + 2\text{VC}$  electrolyte show very similar capacity retention to the commercial LFP cell at  $40^\circ\text{C}$ . At  $40^\circ\text{C}$ , capacity retention of the optimized LFP cells are still worse than the NMC532/AG-A cells, but note that the rate of capacity fade became

similar for these cells after many hours of cycling. At 55°C, the LFP/AG-C cell with LiFSI + 2VC electrolyte showed very similar capacity retention to the NMC532/AG-A cell. This Figure does well to highlight the improvements that have been made from CHAPTER 4 to the end of this chapter.

Of course, it must be noted that the lifetime of NMC532 cells could also be improved if the AG-C electrode material was used. On the other hand, LiFSI likely would be incompatible with NMC532/graphite cells due to their high operating voltage. To make a fairer comparison between cell chemistries, the LFP/AG-A cell with LiFSI + 2VC electrolyte had slightly worse capacity retention than the NMC532/AG-A cell with LiPF<sub>6</sub> + 2VC + 1DTD electrolyte at 55°C. It does seem then that NMC cells have inherently better capacity retention than LFP cells, even despite the large difference in operating voltages. Going forward, the differences between LFP and NMC chemistries will be scrutinized further. The next chapter will consider several one-to-one comparisons between LFP and NMC to learn more about the lifetime differences between these cells.

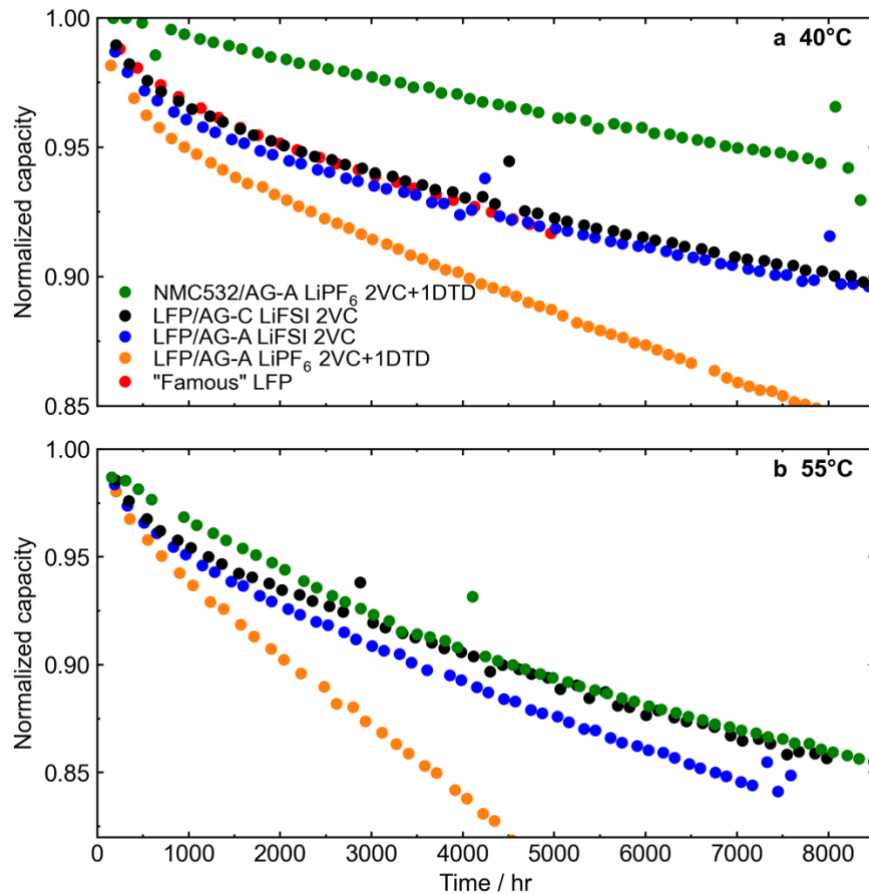


Figure 5.23: Normalized discharge capacity versus cycling time for various LFP cells presented throughout this thesis, cycling at (a) 40°C, and (b) 55°C Also shown is a commercial LFP cell (“famous” LFP), and NMC532/AG-A cells (shown previously in CHAPTER 5). All cells were cycled at C/3 rate, with the exception of the commercial LFP cell (~C/8).

## **CHAPTER 6 LONG-TERM STORAGE STUDIES OF LFP/GRAPHITE AND NMC811/GRAPHITE POUCH CELLS**

This chapter contains material that is being prepared for submission to a peer-reviewed journal, all primarily written by the author of this thesis. The author of this thesis conceived of, planned, and completed all data analysis for the experiments presented in this chapter under the supervision of Jeff Dahn. Ethan Eastwood assisted with constructing pouch cells and pouch bags, as well as measurements of gas evolution. Discussions with Connor Aiken and Michael Metzger were valuable in shaping the interpretation of some of the pouch bag results.

### **6.1 INTRODUCTION**

CHAPTER 5 presented several strategies to improve the high temperature lifetime of LFP/graphite cells. The most successful improvements were made by replacing the  $\text{LiPF}_6$  salt in the electrolyte with LiFSI and using low surface area artificial graphite (AG) negative electrodes. Throughout this thesis, the performance of LFP cells have been compared to NMC cells, typically finding that NMC cells show better capacity retention than comparable LFP cells in many cases. This chapter aims to delve deeper into this comparison, looking at the interactions of different positive electrodes, negative electrodes, and electrolytes, and the implications of these combinations on the performance and degradation of Li-ion cells. This chapter presents the culmination of the work in this thesis up to this point, directly comparing NMC811, LFP, artificial graphites AG-A,B,C, and the two different Li salts used in the electrolyte,  $\text{LiPF}_6$  and LiFSI.

In this comparison, effects such as particle cracking from volume change in the NMC case were minimized. It was shown in some recent publications that cycling NMC811/graphite cells to a cell voltage below the point in which a large lattice contraction occurs<sup>28</sup> led to excellent cycle performance<sup>53,292</sup>. Additionally, impedance growth was minor when NMC811 cells were cycled in a low voltage range, meaning nearly all capacity loss in these cells was due to Li inventory loss at the negative electrode<sup>290</sup>. Restricted voltage range cycling of NMC811 cells will provide a good comparison to LFP, where Li inventory loss will be the main degradation mode in both cases. In this Chapter, NMC811/graphite cells were operated to a maximum of 4.06 V. Table 6.1 summarizes the matrix of different parameters that are studied in this chapter.

In this chapter, high-temperature storage experiments are used in place of CCCV cycling experiments. There are some logical reasons for this choice over cycling experiments. First, the high temperature (60°C) and high state of charge the cells are kept at will accelerate parasitic reactions and Li inventory loss<sup>112</sup>, hopefully showing meaningful differences between the different cells in a shorter amount of time than CCCV cycling at lower temperatures. Second, OCV storage experiments at the top of charge will allow for comparisons between full cells and pouch bags, described below. Finally, the high temperature storage experiments allow for periodic check-ups of not just discharge capacity, but also impedance (vis EIS) and gas evolution, which should also help to better understand the differences between the cells in this matrix. Cells were stored for 5 separate periods of 500 hr each at 60°C for a total of 2500 hours. After each 500 hr storage period,

the cells were cycled and recharged according to the “smart” storage protocol described in CHAPTER 3.

In addition to the high temperature storage experiments, pouch bags were made in a similar fashion to the experiments that were done in CHAPTER 5. Here, in addition to pouch bags stored at 60°C, pouch bags were also constructed and stored at additional temperatures: 40°C, 70°C, and 80°C. The purpose for the expanded temperature range of the pouch bag experiments was to investigate the temperature dependence of parasitic reactions in the pouch bags, as well as to accelerate parasitic reactions in the graphite pouch bags specifically, since it took well over 1000 hr to see detectable gas volumes at 60°C in graphite pouch bags with 2VC electrolytes in CHAPTER 5 (see Figure 5.16). Pouch bags were also run in the microcalorimeter in the same fashion as the previous chapter. These IMC experiments were run exclusively at 40°C. Since 2VC was used in the electrolyte for all cells in this chapter, that detail may be omitted when discussing the results of these experiments.

Table 6.1: Matrix of different positive electrode/negative electrode/electrolyte combinations used in this chapter.

Positive electrode	Negative electrode	Voltage range	Electrolyte
LFP	AG-A	2.5 V - 3.65 V	1.5 M LiPF <sub>6</sub> + 2VC
LFP	AG-A	2.5 V - 3.65 V	1.5 M LiFSI + 2VC
LFP	AG-B	2.5 V - 3.65 V	1.5 M LiPF <sub>6</sub> + 2VC
LFP	AG-B	2.5 V - 3.65 V	1.5 M LiFSI + 2VC
LFP	AG-C	2.5 V - 3.65 V	1.5 M LiPF <sub>6</sub> + 2VC
LFP	AG-C	2.5 V - 3.65 V	1.5 M LiFSI + 2VC
NMC811	AG-A	3.0 V - 4.06 V	1.5 M LiPF <sub>6</sub> + 2VC
NMC811	AG-A	3.0 V - 4.06 V	1.5 M LiFSI + 2VC
NMC811	AG-B	3.0 V - 4.06 V	1.5 M LiPF <sub>6</sub> + 2VC
NMC811	AG-B	3.0 V - 4.06 V	1.5 M LiFSI + 2VC
NMC811	AG-C	3.0 V - 4.06 V	1.5 M LiPF <sub>6</sub> + 2VC
NMC811	AG-C	3.0 V - 4.06 V	1.5 M LiFSI + 2VC

## 6.2 RESULTS

### 6.2.1 Full cell storage

Figure 6.1 shows voltage versus time during OCV storage at 60°C for the different cells used in this study. As mentioned earlier in this thesis, the measure of voltage drop in a storage experiment is not a direct measure of capacity loss, but it can be correlated to capacity loss<sup>207</sup>. The NMC811/AG-A cell with LiFSI + 2VC electrolyte failed in the first storage period, and therefore is not shown here. Each subsequent storage period starts at  $t=0$  and sequential storage periods are denoted by lighter coloured points and lines. Points are plotted along the voltage curves periodically as a guide to the eye to better compare different storage periods. First, the LFP/AG results will be discussed.



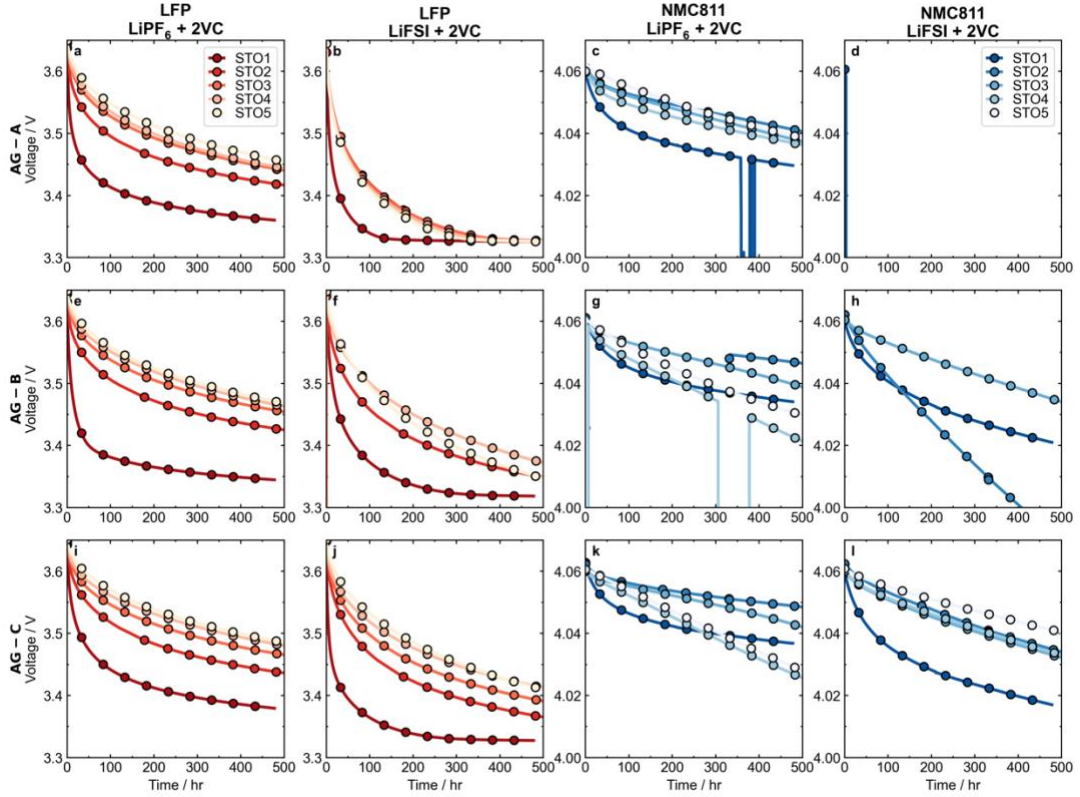


Figure 6.1: Voltage versus time over five 500 hr OCV storage periods at 60°C. (a) LFP/AG-A with  $\text{LiPF}_6 + 2\text{VC}$  electrolyte. (b) LFP/AG-A with  $\text{LiFSI} + 2\text{VC}$  electrolyte. (c) NMC811/AG-A with  $\text{LiPF}_6 + 2\text{VC}$  electrolyte. (d) NMC811/AG-A with  $\text{LiFSI} + 2\text{VC}$  electrolyte. (e) LFP/AG-B with  $\text{LiPF}_6 + 2\text{VC}$  electrolyte. (f) LFP/AG-B with  $\text{LiFSI} + 2\text{VC}$  electrolyte. (g) NMC811/AG-B with  $\text{LiPF}_6 + 2\text{VC}$ . (h) NMC811/AG-B with  $\text{LiFSI} + 2\text{VC}$  electrolyte. (i) LFP/AG-C with  $\text{LiPF}_6 + 2\text{VC}$  electrolyte. (j) LFP/AG-C with  $\text{LiFSI} + 2\text{VC}$  electrolyte. (k) NMC811/AG-C  $\text{LiPF}_6 + 2\text{VC}$  electrolyte. (l) NMC811/AG-C with  $\text{LiFSI} + 2\text{VC}$ .

Storage results have been presented for LFP/AG cells in previous chapters (CHAPTER 4 and CHAPTER 5). The biggest difference here is that the storage trends can be observed for more than one or two 500 hr storage periods. As reported earlier (CHAPTER 5), a higher voltage drop was seen in cells with  $\text{LiFSI} + 2\text{VC}$  electrolyte than cells with  $\text{LiPF}_6 + 2\text{VC}$  electrolyte, despite having better capacity retention in long-term cycling experiments. To reiterate the results of CHAPTER 5, this is likely due to a redox shuttle reaction that is unique to the  $\text{LiFSI}$  electrolyte. This trend holds for LFP cells with the three different AGs, though cells with AG-B or AG-C and  $\text{LiFSI}$  electrolyte did have less voltage

drop than LFP/AG-A cells. The voltage drop for LFP/AG-A with LiFSI electrolyte was high enough that in each storage period the cell reached the LFP voltage plateau (see the LFP half cell voltage curve in Figure 1.2), leading to the flat voltage profile by the end of each storage period. Looking at the trend with subsequent storage periods, in the majority of cases the voltage drop over the 500 hr storage period became lower as the LFP/AG cells aged. As the cells are aged, especially at high temperature, the SEI on the graphite electrode thickens, improving the passivation of the negative electrode. This should reduce the amount of products formed at the negative electrode, and reduce the amount of cross-talk causing self-discharge. In one case, LFP/AG-B with LiFSI electrolyte, the last storage period (STO5) showed slightly more voltage drop than previous runs, indicating a larger rate of self-discharge compared to previous storage periods. This could be due to the breakdown the SEI layer, leading to more cross-talk species and self-discharge. This may have happened in LFP/AG-A as well, but it is hard to tell from this data. The quantitative extent of the self-discharge will be easier to see by comparing the discharge capacities after each storage period, which will be done below.

The trends in the NMC811/AG cells were not as straightforward as the LFP matrix. In the NMC/AG-A cells with LiPF<sub>6</sub> electrolyte, the voltage drop over each 500 hr storage period expectedly became lower as the cell was aged. On the other hand, in NMC/AG-B and NMC/AG-C cells, voltage drop decreased over the first 2-3 storage periods, but then started to increase in subsequent experiments. Again, as was suggested in the case of LFP/AG-B with LiFSI electrolyte, the higher voltage drop indicates more facile self-discharge and degradation of the interphases in the cell. This result was unexpected because LFP/AG-B

and LFP/AG-C cells performed better in high temperature cycling experiments in CHAPTER 5, and in the literature NMC811 cells with AG-B and AG-C also performed better than NMC/AG-A cells in cycling experiments to 4.06 V<sup>53,290</sup>. As of now this trend of worsening storage performance for NMC/AG-B and NMC/AG-C cells cannot be explained.

Finally, long-term storage of NMC cells with LiFSI electrolyte were considered. This slice of the parameter space is interesting, primarily because of the higher upper-cutoff voltage of NMC811 compared to LFP. Since LiFSI is said to corrode the positive electrode current collector at high voltage, this becomes an extra factor to consider when analyzing these cells. It was argued in CHAPTER 5 that LFP cells with LiFSI electrolyte do not experience Al corrosion. Of the surviving NMC/AG cells with LiFSI electrolyte (AG-B and AG-C), the voltage drop went down as the cells were aged, similar to what was seen in the LFP case. Interestingly, the increasing voltage drop with increasing storage number in the NMC/AG cells with LiPF<sub>6</sub> electrolyte was not seen when LiFSI was used. It is possible, then, that the LiPF<sub>6</sub> salt is involved in whatever parasitic reaction leads to the increasing self-discharge with cell age, and the use of LiFSI prevents this from occurring.

Figure 6.2 shows full discharge capacity after storage (i.e. D<sub>2</sub> defined in CHAPTER 3) versus storage time for the matrix of cells tested. Note that the post-storage cycles were done at 40°C on a different system (Maccor 4000 series), as opposed to previous “smart” storage experiments presented in this thesis, where the entire experiment was completed in the same temperature box with the same charger. Both absolute capacity (Figure 6.2a,b)

and normalized capacity (Figure 6.2c,d) are shown. As well, note the different y-axis scales that are used for the LFP and NMC cells. A dashed line in Figure 6.2d indicates the y-axis minimum for LFP cells in Figure 6.2c to aid in making comparisons between the different cell types.

For LFP/AG-B and LFP/AG-C cells, capacity retention over many storage periods was better in LiFSI electrolyte than in LiPF<sub>6</sub> electrolyte. Both LFP/AG-B and LFP/AG-C cells had just under 90% of their original capacity remaining after 2500 hr of storage at 60°C. In CHAPTER 5 it was shown in similar high temperature storage experiments (only one 500 hr storage period) that LFP cells with AG-B and AG-C reduced the capacity loss that was observed in LiFSI electrolyte (D<sub>2</sub>-D<sub>1</sub>), possibly owing to the lower electrochemically active surface areas of these graphites. A similar effect may be occurring here for multiple storage periods; the lower surface area of AG-B and AG-C may inhibit SEI breakdown that seems to occur in AG-A in LiFSI electrolyte after many hours of storage. It is unclear if further storage would lead to an increasing rate of capacity fade in the LFP/AG-B and LFP/AG-C cells with LiFSI electrolyte.

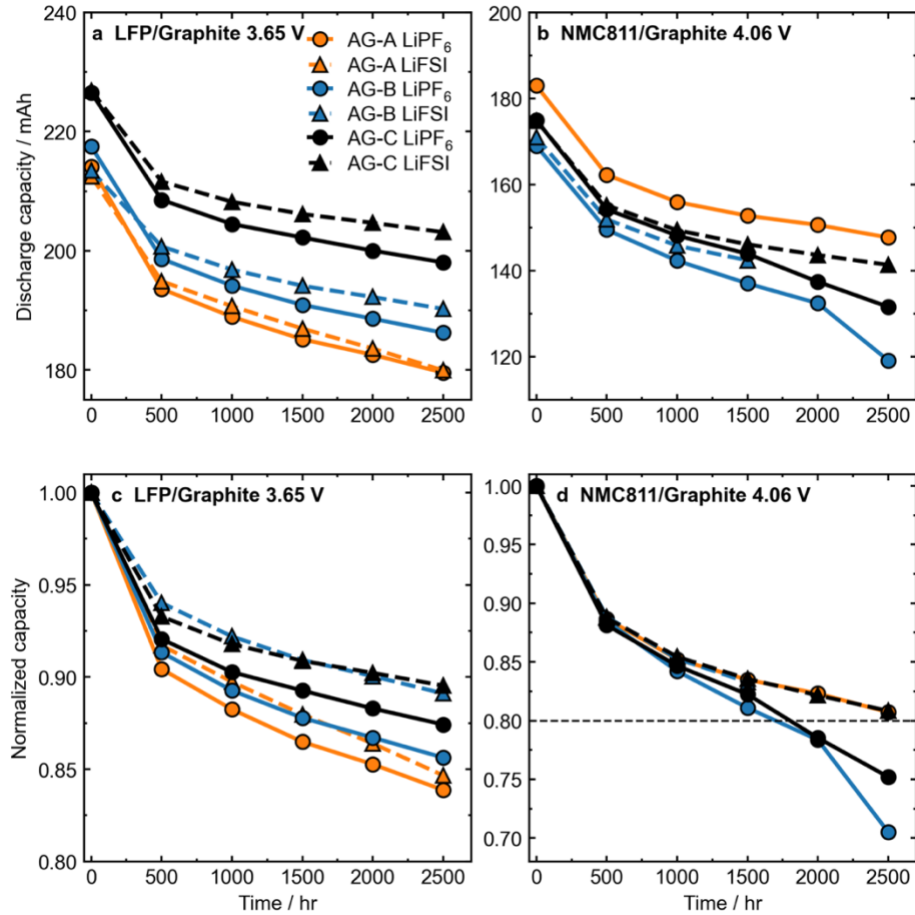


Figure 6.2: Discharge capacity and normalized capacity ( $D_2$  in the smart storage protocol) versus storage time for different cell types. Each point was measured after 500 hr of storage at  $60^\circ\text{C}$ . Check-up cycles were measured at  $40^\circ\text{C}$ . Cells with  $\text{LiPF}_6$  electrolyte are shown with circle markers and solid lines, and cells with  $\text{LiFSI}$  electrolyte are shown with triangle markers and dashed lines. (a,c) LFP/AG cells. (b,d) NMC811/AG cells. A dashed line is drawn at 80% normalized capacity in panel (d).

The increasing voltage drop that was seen in NMC/AG-B and NMC/AG-C cells with  $\text{LiPF}_6$  electrolyte in Figure 6.1 showed an associated increase in the rate of capacity loss with increasing storage time (Figure 6.2d), much more severe than what was seen in the LFP/AG cells. In the worst case, NMC/AG-B with  $\text{LiPF}_6$  electrolyte reached 70% of its initial capacity after 2500 hours of storage. This increasing rate of capacity loss was *not* seen in NMC/AG-A with  $\text{LiPF}_6$  electrolyte. As well, this increasing rate of capacity loss was not observed in NMC/AG-C cells with  $\text{LiFSI}$  electrolyte.

For the first time in this thesis, NMC cells showed worse performance than LFP cells in this set of experiments. In particular, the accelerating capacity fade in NMC/AG-B and NMC/AG-C cells was a worrying feature, especially since it was not observed in the NMC/AG-A cell. The use of LiFSI in the electrolyte appeared to remedy the accelerating capacity fade issue in NMC cells with AG-B and AG-C negative electrodes. The higher storage voltage of the NMC cells (4.06 V) compared to the LFP cells (3.65 V) must be taken into account, which could contribute to the difference in storage performance between LFP and NMC. After each storage period, gas evolution and impedance were also measured, which should help to understand the voltage drop and capacity loss results presented so far.

Figure 6.3 shows the charge-transfer resistance,  $R_{CT}$  of cells measured after each 500 hr storage period. As a reminder (see CHAPTER 3), these EIS measurements were done at 10°C. Both the LFP/AG cells and NMC/AG cells were measured at ~60% SOC. The  $R_{CT}$  was determined by taking the width of the semi-circle (i.e. the distance between the two minima) on the real impedance axis in the Nyquist plot. Nyquist plots for each of these measurements can be seen in Figure A.9.

Figure 6.3a shows the charge-transfer resistance for LFP/AG cells. Cells with  $\text{LiPF}_6$  electrolyte are shown with solid lines, and cells with LiFSI electrolyte are shown with dashed lines. Here, there is a clear dependence on Li salt on  $R_{CT}$  growth as these cells age. LFP/AG-B and LFP/AG-C cells with  $\text{LiPF}_6$  electrolyte had massive increases in  $R_{CT}$  with

storage time at 60°C, while the LFP/AG-A with LiPF<sub>6</sub> showed a modest increase. All cells with LiFSI electrolyte showed virtually no growth in R<sub>CT</sub> with storage time. This suggests that parasitic reactions involving the Li salt during storage could be responsible for the large increase in impedance. Notice as well in LFP cells with LiPF<sub>6</sub> electrolyte that the growth in R<sub>CT</sub> with storage time was the largest with AG-C, while R<sub>CT</sub> change with time was relatively stable with AG-A.

The large impedance increase in the LFP cells with LiPF<sub>6</sub> electrolyte likely did not affect the capacity retention measured in Figure 6.2 since these cycles were completed at a slow rate of C/10. However, this may affect capacity retention if the cells were cycled at a higher rate. As well, high impedance likely originating at the negative electrode could also lead to unwanted Li plating during charge at higher rates, leading to significant irreversible capacity loss<sup>185</sup>.

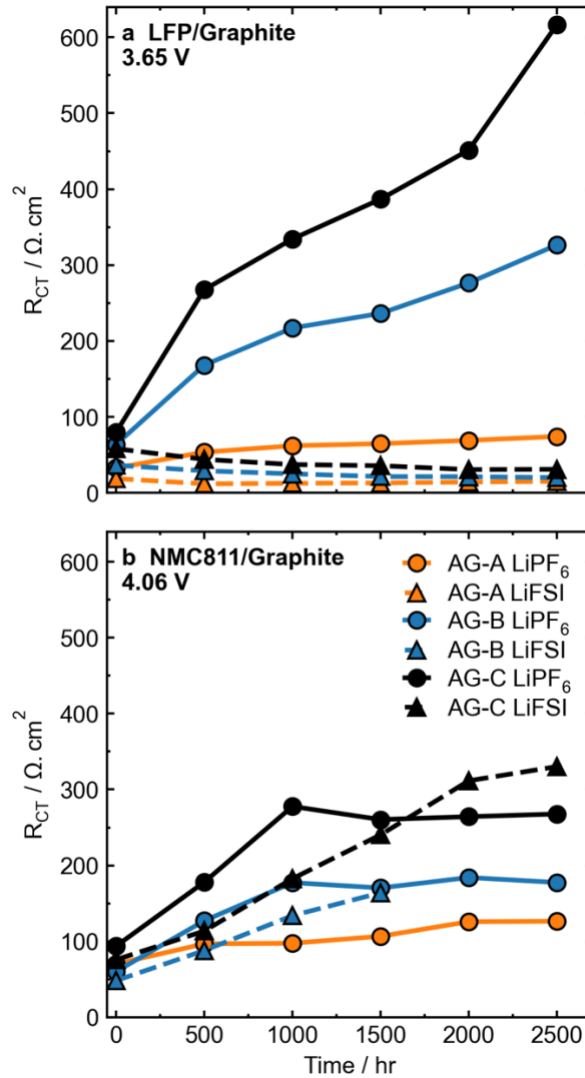


Figure 6.3: Charge-transfer resistance versus storage time for (a) LFP/AG cells at 3.65 V, and (b) NMC811/AG cells at 4.06 V. Cells were stored at 60°C. Cells with LiPF<sub>6</sub> electrolyte are shown as circle markers with solid lines and cells with LiFSI electrolyte are shown with triangle markers and dashed lines. EIS after each storage period was measured at 10°C.

Charge transfer resistance versus storage time for NMC/AG is shown in Figure 6.3b. Here, the increase in  $R_{CT}$  with storage time was not as large as in the LFP/AG cells. However, in the NMC case cells with both LiPF<sub>6</sub> electrolyte and LiFSI electrolyte showed similar magnitude of impedance growth, in contrast to the LFP cells where there were more stark



differences between the electrolytes. These impedance results do not provide any clear explanation for the capacity loss observed in NMC/AG-A and AG-B cells with  $\text{LiPF}_6$ .

Figure 6.4 shows the volume of gas evolved as a function of storage time. This was measured using Archimedes principle at the end of each storage period. LFP/AG cells are shown in Figure 6.4a and NMC811/AG cells are shown in Figure 6.4b. Note the different scales used in the two panels.

Regardless of electrolyte and AG type used, relatively little gas was evolved in the LFP cells during these high-temperature storage experiments. Of these cells, LFP cells with AG-A negative electrodes had the most gas. This is expected given the higher reactivity of AG-A compared to AG-B and AG-C found in CHAPTER 5. The higher gas volumes evolved in LFP/AG-A also correlates with the higher capacity loss in LFP/AG-A in Figure 6.2. LFP/AG-B and LFP/AG-C cells with  $\text{LiPF}_6$  electrolyte had almost a factor of three lower gas production at 2500 hours compared to the LFP/AG-A cell. Additionally, LFP/AG-B and LFP/AG-C cells with LiFSI electrolyte had more gas evolved than their  $\text{LiPF}_6$  counterparts. Recall that LFP cells with LiFSI electrolyte had the best capacity retention during storage (Figure 6.2c). This higher gas production could be related to some reaction involving the LiFSI salt that does not consume lithium inventory (related to the redox shuttle discussion in CHAPTER 5), so the higher gas production in these cells may not impact capacity retention.

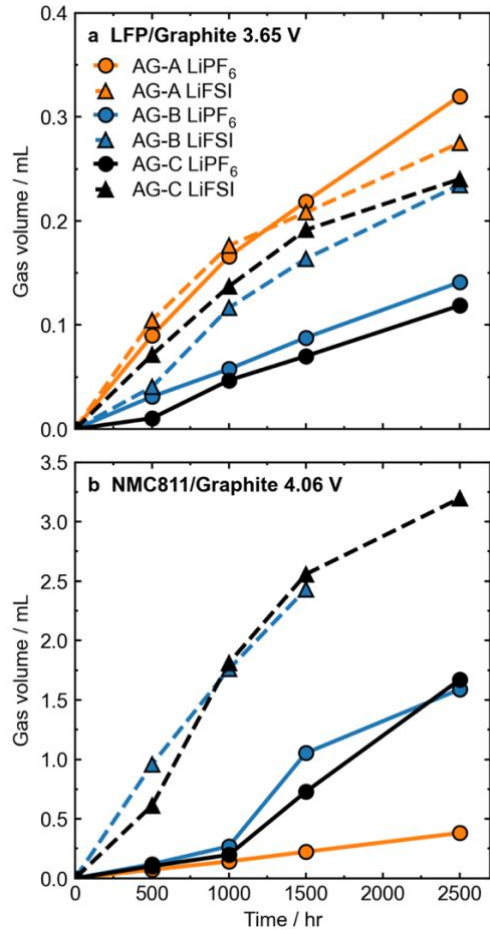


Figure 6.4: Gas volume evolved as a function of storage time for (a) LFP/AG cells at 3.65 V, and (b) NMC811/AG cells at 4.06 V with different electrolytes and negative electrodes. Cells were stored at 60°C. Cells with LiPF<sub>6</sub> electrolyte are shown as circle markers with solid lines and cells with LiFSI electrolyte are shown with triangle markers and dashed lines.

Gas evolution measurements for the NMC/AG cells are shown in Figure 6.4b. In this case, the gas volumes in NMC cells with LiFSI electrolyte were much higher than cells with LiPF<sub>6</sub> electrolyte. This may agree with the Al corrosion argument, suggesting parasitic reactions at and degradation of the positive electrode when LiFSI is used in NMC cells, even when charged to a relatively low voltage (4.06 V). However, recall that the NMC/AG-C cell with LiFSI electrolyte had better capacity retention than NMC/AG-C + LiPF<sub>6</sub> in the storage experiments. Additionally, the cell with the lowest gas volume of the NMC + LiPF<sub>6</sub>

cells was NMC/AG-A, the reverse of the LFP/AG case. A sharp increase in gas evolution for the NMC/AG-B and NMC/AG-C cells coincided with the decrease in capacity retention and increase in voltage drop in the storage experiments (Figure 6.1 and Figure 6.2).

These results so far highlight the complex interactions that exist between positive and negative electrodes, electrolyte, and even the testing protocol used. While LFP/AG-C cells performed very well in these high temperature storage experiments with both LiFSI and LiPF<sub>6</sub> electrolyte, NMC/AG-C + LiPF<sub>6</sub> saw rapid capacity fade after 1500 hours of storage. In a recent publication, NMC811/AG-C cells with LiPF<sub>6</sub> electrolyte and similar electrolyte additives performed very well in high temperature CCCV cycling experiments<sup>290</sup>, so it was expected that this cell/electrolyte combination would do equally as well here. The next section will attempt to investigate these interactions further using pouch bags.

### 6.2.2 Pouch bags

Pouch bags were constructed from pouch cells with different positive electrode, negative electrode, and electrolyte combinations (see Table 6.1) to try to better understand the impact of these components on parasitic reactions in these cells. Additionally, pouch bags were stored at different temperatures to: (1) probe the temperature dependence of these gas-producing parasitic reactions, and (2) to accelerate gas production in graphite pouch bags since over 2000 hrs were required to see any gas formation in pouch bags at 60°C with VC in the electrolyte in the previous chapter (see Figure 5.16).

Figure 6.5 shows specific gas volume (volume of gas divided by the mass of active material in the given electrode, active material mass was determined from measurements of dry cells, see Table 3.2) versus time for positive electrode pouch bags with different electrolytes. Each panel in the graph represents positive electrodes extracted from pouch cells with different positive electrode/negative electrode/electrolyte combinations. Pouch bags stored at different temperatures are plotted as different colors here. Note the different y-axis scales for the LFP and NMC pouch bags. Apparent negative gas production at early times in some cases is not considered to be physical. Rather, this could be due to small changes in the pouch bag shape at early times that could influence the volume of water displaced in the Archimedes volume measurement. It was shown in CHAPTER 5 that very little gas was formed in LFP pouch bags when stored at 60°C at top of charge, suggesting that very little gas-forming parasitic reactions occur at the LFP electrode. That again was seen here, and even at higher temperatures (70°C, 80°C) virtually no gas was detected in the LFP pouch bags after 3000 hours of testing. There appeared to be no influence of negative electrode choice or Li salt choice on the amount of gas evolved in LFP positive electrode pouch bags.

On the other hand, NMC pouch bags produced a lot of gas in a clearly temperature-dependent relation. Large amounts of gas evolution have previously been observed in pouch bags containing charged NMC<sup>144,145,215,293</sup>. The products detected in aged NMC pouch bags have been shown to be primarily CO and CO<sub>2</sub> from the oxidation of EC and DMC<sup>140,145</sup>. In some cases, pouch bags stored at very high temperatures showed sharp decreases in gas volume (Figure 6.5g, k). In these cases, it is likely that the pouch bag

leaked or burst, releasing most of the evolved gas. In these experiments there did not seem to be a strong dependence on the graphite used in the pouch cell before disassembly, as may be expected. While not clear at higher temperatures ( $\geq 70^\circ\text{C}$ ), lower temperatures (most notably  $60^\circ\text{C}$ ) indicated slightly less gas was produced in pouch bags with LiFSI electrolyte. These more subtle differences in gas production will be investigated in more detail later.

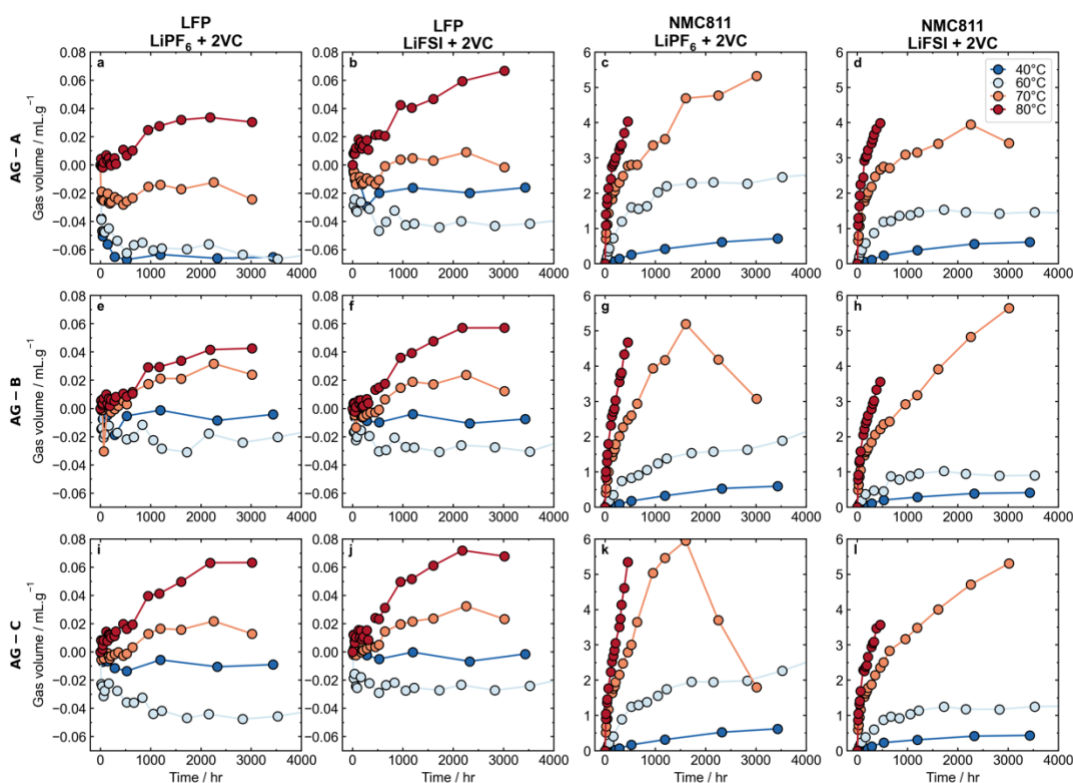


Figure 6.5: Specific gas volumes evolved in charged positive electrode pouch bags at different temperatures from cells with different positive electrode/negative electrode pairings. (a) LFP/AG-A with  $\text{LiPF}_6 + 2\text{VC}$  electrolyte. (b) LFP/AG-A with  $\text{LiFSI} + 2\text{VC}$  electrolyte. (c) NMC811/AG-A with  $\text{LiPF}_6 + 2\text{VC}$  electrolyte. (d) NMC811/AG-A with  $\text{LiFSI} + 2\text{VC}$  electrolyte. (e) LFP/AG-B with  $\text{LiPF}_6 + 2\text{VC}$  electrolyte. (f) LFP/AG-B with  $\text{LiFSI} + 2\text{VC}$  electrolyte. (g) NMC811/AG-B with  $\text{LiPF}_6 + 2\text{VC}$ . (h) NMC811/AG-B with  $\text{LiFSI} + 2\text{VC}$  electrolyte. (i) LFP/AG-C with  $\text{LiPF}_6 + 2\text{VC}$  electrolyte. (j) LFP/AG-C with  $\text{LiFSI} + 2\text{VC}$  electrolyte. (k) NMC811/AG-C  $\text{LiPF}_6 + 2\text{VC}$  electrolyte. (l) NMC811/AG-C with  $\text{LiFSI} + 2\text{VC}$ .

Figure 6.6 shows specific gas volumes evolved from graphite pouch bags stored at different temperatures. Here, a clear dependence in temperature on gas production was observed, as may be expected. First, consider the graphite pouch bags originating from LFP/AG pouch cells. In all cases, the 40°C pouch bags produced virtually no gas, and the 60°C pouch bags produced very little gas after >4000 hours of aging at the given temperature. Therefore, the main focus here will be on the 70°C and 80°C pouch bags in order to see significant differences in gas production. Initially, less gas was produced in pouch bags with LiFSI electrolyte. However, especially at 80°C, after ~1500 hours or so of testing the rate of gas production increased. The rate of gas production in AG-A with LiFSI was always high at 80°C, but in AG-B and AG-C, the rate of gas evolution started low and saw a large increase. No increase in gas production rate was seen in the graphite pouch bags at 70°C out to at least 3000 hours. This increasing rate of gas production suggests the breakdown of the SEI or some related other process that caused a large increase in parasitic reaction rate. This feature may be cause for concern for the use of LiFSI in LFP/AG cells, though it is noted that 80°C is typically not a practical operating temperature. Instead, this may have consequences for thermal safety events such as thermal runaway, where the LiFSI electrolyte may contribute to SEI breakdown if very high temperatures are reached. However, at more realistic temperatures, the use of LiFSI electrolyte seemed to reduce gas production in negative electrode pouch bags compared to LiPF<sub>6</sub> electrolyte.

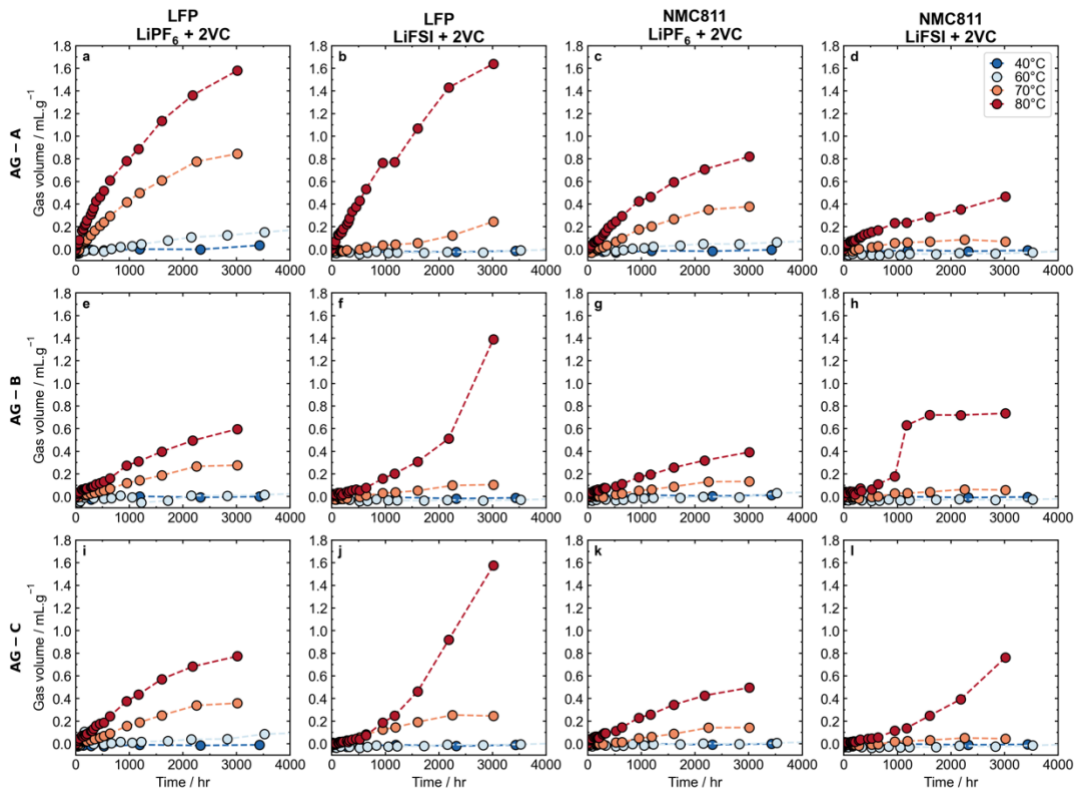


Figure 6.6: Specific gas volumes evolved in charged negative electrode pouch bags at different temperatures from cells with different positive electrode/negative electrode pairings. (a) LFP/AG-A with  $\text{LiPF}_6 + 2\text{VC}$  electrolyte. (b) LFP/AG-A with  $\text{LiFSI} + 2\text{VC}$  electrolyte. (c) NMC811/AG-A with  $\text{LiPF}_6 + 2\text{VC}$  electrolyte. (d) NMC811/AG-A with  $\text{LiFSI} + 2\text{VC}$  electrolyte. (e) LFP/AG-B with  $\text{LiPF}_6 + 2\text{VC}$  electrolyte. (f) LFP/AG-B with  $\text{LiFSI} + 2\text{VC}$  electrolyte. (g) NMC811/AG-B with  $\text{LiPF}_6 + 2\text{VC}$ . (h) NMC811/AG-B with  $\text{LiFSI} + 2\text{VC}$  electrolyte. (i) LFP/AG-C with  $\text{LiPF}_6 + 2\text{VC}$  electrolyte. (j) LFP/AG-C with  $\text{LiFSI} + 2\text{VC}$  electrolyte. (k) NMC811/AG-C  $\text{LiPF}_6 + 2\text{VC}$  electrolyte. (l) NMC811/AG-C with  $\text{LiFSI} + 2\text{VC}$ .

The low surface area artificial graphites (AG-B and AG-C) that had better cycle performance in LFP/AG cells in CHAPTER 5 showed greatly reduced gas volumes in pouch bags compared to AG-A graphite. For comparison, AG-A pouch bags from LFP cells with  $\text{LiPF}_6$  electrolyte evolved over 0.8 mL/g after 3000 hours at 70°C, while AG-B and AG-C evolved approximately 0.3 mL/g and 0.4 mL/g, respectively, in the same amount of time. Much less gas was evolved in all pouch bags at 60°C, but still a reduction could be seen in AG-B and AG-C compared to AG-A, especially with  $\text{LiPF}_6$  electrolyte.

Graphite pouch bags that originated from NMC811/AG cells appeared to show lower specific gas evolution than graphite pouch bags originating from LFP/AG cells, especially at high temperatures. As a comparison, an AG-A pouch bag with LiPF<sub>6</sub> electrolyte originating from an LFP/AG-A cell had 0.8 mL/g of gas after 3000 hours at 70°C, while an AG-A pouch bag with LiPF<sub>6</sub> electrolyte originating from an NMC811/AG-A cell had only 0.4 mL/g of gas after 3000 hours at 70°C. Similar trends could also be seen for AG-B and AG-C pouch bags, and with LiFSI electrolyte (though to a lesser extent). These results raise an interesting question: how does the positive electrode impact gas-forming parasitic reactions at the negative electrode, especially after the relatively short amount of time that the full cells were together before disassembly?

One simple explanation could be the different states-of-charge (SOCs) of the graphite electrodes. LFP/AG cells for pouch bags were charged to 3.65 V, very close to 100% SOC. In contrast, NMC811/AG cells were charged to 4.06 V, which is only approximately 75% SOC in a cell balanced to 4.4 V. The slightly different voltage of the graphite negative electrode could impact the rate of parasitic reactions that occur in the pouch bags. Alternatively, species produced at the positive electrode before pouch cells were made into pouch bags could impact the gas volume evolved over time. It must be kept in mind that cells only underwent one formation cycle at C/20 and 40°C (plus another charge at C/20), followed by a voltage hold at the upper cutoff voltage for ~36 hours. This means the positive and negative electrode could only interact for a maximum of ~95 hours before the cells were disassembled into pouch bags. Looking at the positive electrode pouch bag data in Figure 6.5, the NMC positive electrode pouch bags did not evolve very much gas after



100 hours at 40°C. However, it is still possible that cross-talk products from the positive electrode could influence the SEI structure of the negative electrode and thus the gas production of graphite pouch bags. These cross-talk reactions could also help to explain the difference in long-term cycle performance between LFP/graphite cells and NMC/graphite cells that has been reported in CHAPTER 4 and CHAPTER 5.

Pouch bags that contained only electrolyte with no electrodes or separator were also constructed. Figure 6.7 shows gas volume versus time for pouch bags with 1.0 mL of either LiPF<sub>6</sub> electrolyte or LiFSI electrolyte. Pouch bags were stored at 40°C, 60°C, 70°C, or 80°C like in Figure 6.5 and Figure 6.6. Both electrolytes did not show any gas evolution over >3000 hours at 40°C or 60°C. At 70°C, the LiPF<sub>6</sub> electrolyte started to show some gas evolution, and at 80°C there is obvious gas evolution. LiFSI electrolyte pouch bags did not show any gas evolution even up to 80°C. This suggests that the LiFSI electrolyte is exceptionally stable by itself at high temperatures. The LiPF<sub>6</sub> thermally decomposes according to the often reported reaction<sup>63</sup>:



The generation of PF<sub>5</sub> could explain the gas that is observed in the LiPF<sub>6</sub> electrolyte pouch bag at 80°C. Additionally, PF<sub>5</sub> has been shown to react further with components of the electrolyte, specifically EC<sup>294</sup>. In the presence of H<sub>2</sub>O contamination in the electrolyte, PF<sub>5</sub> also reacts further to form POF<sub>3</sub> and HF<sup>295</sup>. However, the only water that would be present in these pouch bags would be trace water from the neat solvent mixture.

It is interesting to note the the discrepancy between gas evolution data for the pure electrolyte pouch bags in Figure 6.7 and the LFP positive electrode pouch bags in Figure 6.5. These LFP pouch bags showed virtually zero gas evolution after over 3000 hours at 80°C in LiPF<sub>6</sub> electrolyte. This means that gas produced via LiPF<sub>6</sub> decomposition of the electrolyte either is adsorbed to the LFP electrode, or these gas products react further with LFP. The adsorption argument is possible, given the high surface area of the LFP material. However, it is also possible that some parasitic reactions do occur at the LFP electrode, despite the low amount of gas and low parasitic heat flow that has been observed. Some publications have observed electrolyte decomposition products on the LFP surface using surface sensitive techniques such as XPS<sup>296</sup>.

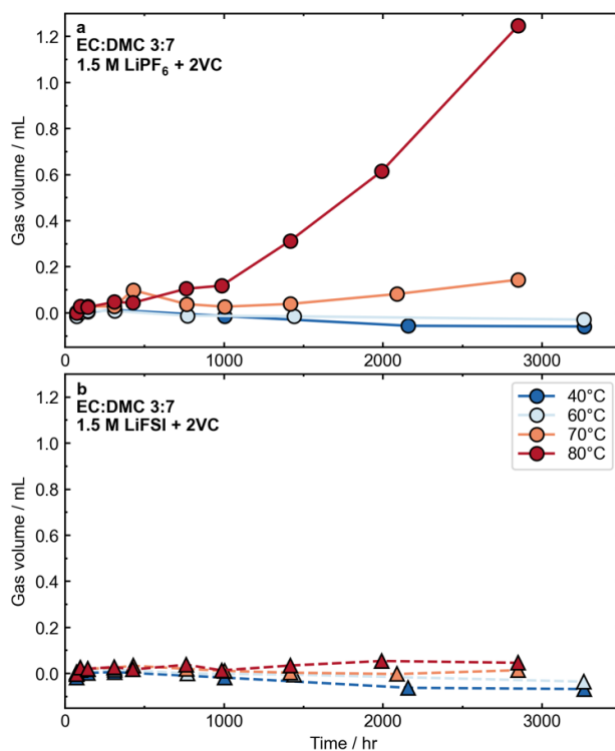


Figure 6.7: Gas produced in pouch bags containing only electrolyte stored at different temperatures. (a) 1.0 mL of EC:DMC 3:7 + 1.5 M LiPF<sub>6</sub> + 2% VC. (b) 1.0 mL of EC:DMC 3:7 + 1.5 M LiFSI + 2% VC.

If gas-producing parasitic reactions in pouch bags are primarily controlled by temperature, the gas evolution in pouch bags should follow an Arrhenius relation. These experiments are slightly complicated by the fact that the gas evolution rate is not constant as a function of time. If enough gas is produced to pressurize the pouch bag, the Archimedes method will no longer be accurate. As the electrodes become more passivated, the parasitic reaction rate will decrease (possibly at  $t^{1/2}$  rate, especially in the negative electrode). To compare the temperature dependence of gas-evolving reactions in pouch bags, linear fits were made to the data in early times where the gas evolution rate was relatively constant, and all gas produced was confidently at a pressure of 1 atm. It should be noted that this analysis is not meant to be a quantitative evaluation of these data. Instead, this analysis is meant to simplify and summarize the qualitative comparisons between the different combinations of positive electrodes, negative electrodes, and electrolytes presented in this chapter. Fits to gas production data are shown in the Appendix (Figure A.10 - Figure A.13). The slopes of the fitted lines are indicated in each of the panels of these Figures, in units of  $\text{mL}\cdot\text{g}^{-1}\cdot\text{hr}^{-1}$ . For LFP positive electrode pouch bags, all measured data were used in the fits, NMC pouch bags used only the first 5, 6, 5, and 3 measurements for 40°C, 60°C, 70°C, and 80°C, respectively. For graphite pouch bags, all measured points were used in the fit for 40°C and 60°C pouch bags, and only the first 1000 hours were used in 70°C and 80°C pouch bags.

These initial gas evolution fits were plotted against inverse temperature to study the possible Arrhenius-like behaviour of pouch bags under different conditions. Figure 6.8 shows the initial gas formation rates for NMC811 positive electrode pouch bags. NMC

pouch bags coming from various initial cell configurations show almost perfect Arrhenius behaviour, indicating the rate of parasitic reactions at the NMC positive electrode is strongly temperature controlled. Additionally, there was little variation observed between different graphite types (in the original full cell) and different electrolytes. NMC pouch bags originating from NMC/AG-A cells may have marginally higher gas formation rates at most temperatures. Gas formation rates for one LFP pouch bag (LFP/AG-A + LiPF<sub>6</sub>) is included for comparison to the NMC pouch bags. On the scale plotted (down to 5 x 10<sup>-6</sup> mL/g/hr) only the 80°C point appears on the graph, and is almost 5 orders of magnitude lower than the NMC pouch bags at 80°C. This highlights the massive difference in gas production between LFP and NMC pouch bags, again showing that the rate of parasitic reactions at the LFP surface is very low compared to NMC.

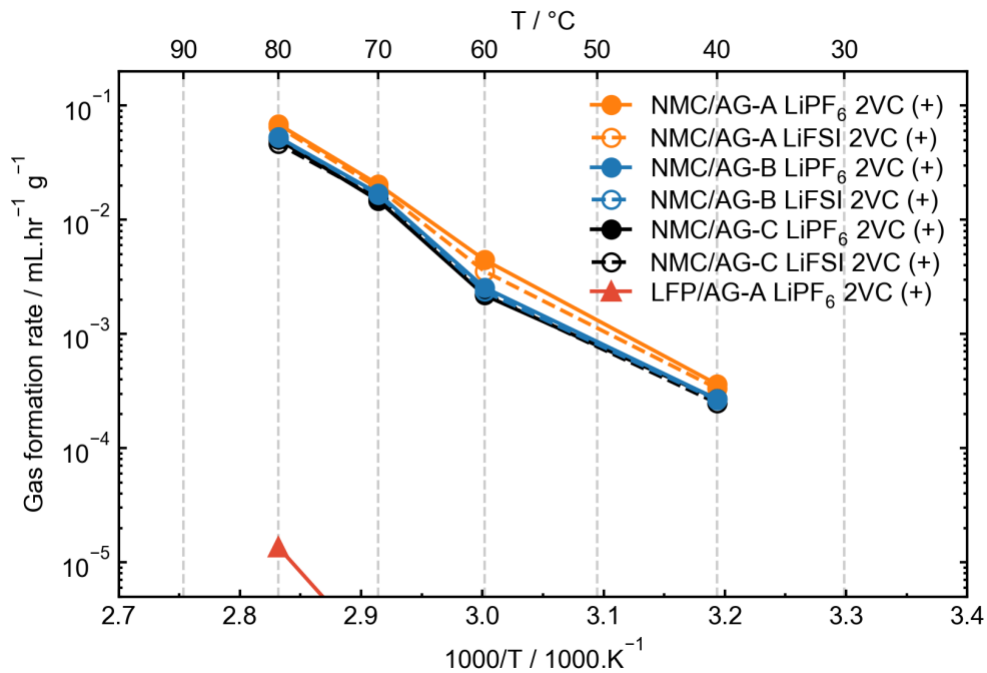


Figure 6.8: Arrhenius plot showing average initial specific gas production rate for NMC811 positive electrode pouch bags. One LFP positive electrode pouch bag (LFP/AG-A + LiPF<sub>6</sub> + 2VC) is shown for comparison.

Figure 6.9 shows the initial gas formation rate for graphite pouch bags originating from LFP/AG pouch cells. Here, some clear differences between different graphite types and electrolytes can be seen. The highest rate of gas production at all temperatures was from AG-A pouch bags with LiPF<sub>6</sub> electrolyte. Graphite pouch bags with LiFSI electrolyte had lower gas evolution rates than pouch bags with LiPF<sub>6</sub> electrolyte, with the exception of AG-A at 80°C where the rates were similar between electrolytes. Points that were not plotted in the range 40°C – 80°C indicate that the fit to the gas formation data had a negative slope, indicating very little (virtually zero) gas was formed (see Figure A.10 – Figure A.13); this is notable for the AG-C + LiFSI pouch bag at 60°C, where no significant amount of gas was evolved after >4000 hr at 60°C (see Figure A.11r). Both AG-B and AC-C pouch bags with LiPF<sub>6</sub> electrolyte showed lower gas production than AG-A pouch bags at all temperatures. The dramatic reduction in gas formation in the AG-A LiFSI pouch bags compared to AG-A with LiPF<sub>6</sub> was not seen to the same extent in AG-B and AG-C pouch bags.

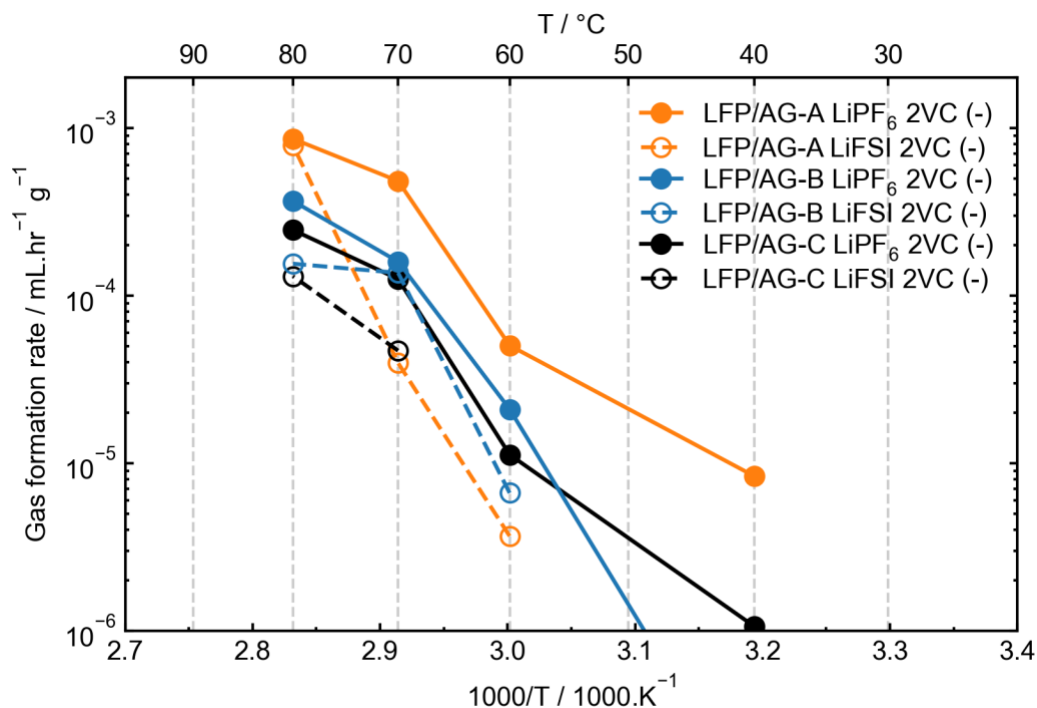


Figure 6.9: Arrhenius plot comparing the initial specific gas production rate for graphite pouch bags extracted from different LFP/AG cells with different electrolytes.

At this point it is valuable to compare graphite pouch bags that were originally in full pouch cells with different positive electrodes. Figure 6.10 shows the initial gas formation rate for AG-A pouch bags that originated from either LFP or NMC811 pouch cells. The highest rate of gas production at all temperatures came from the AG-A + LiPF<sub>6</sub> pouch bags that were originally paired with LFP positive electrodes. This is followed by AG-A + LiPF<sub>6</sub> from NMC811 cells. AG-A pouch bags from both LFP and NMC811 cells showed reduced gas production with LiFSI was used in the electrolyte instead of LiPF<sub>6</sub>. Again, the AG-A + LiFSI pouch bag at 80°C appears to be an outlier from the rest of the data.

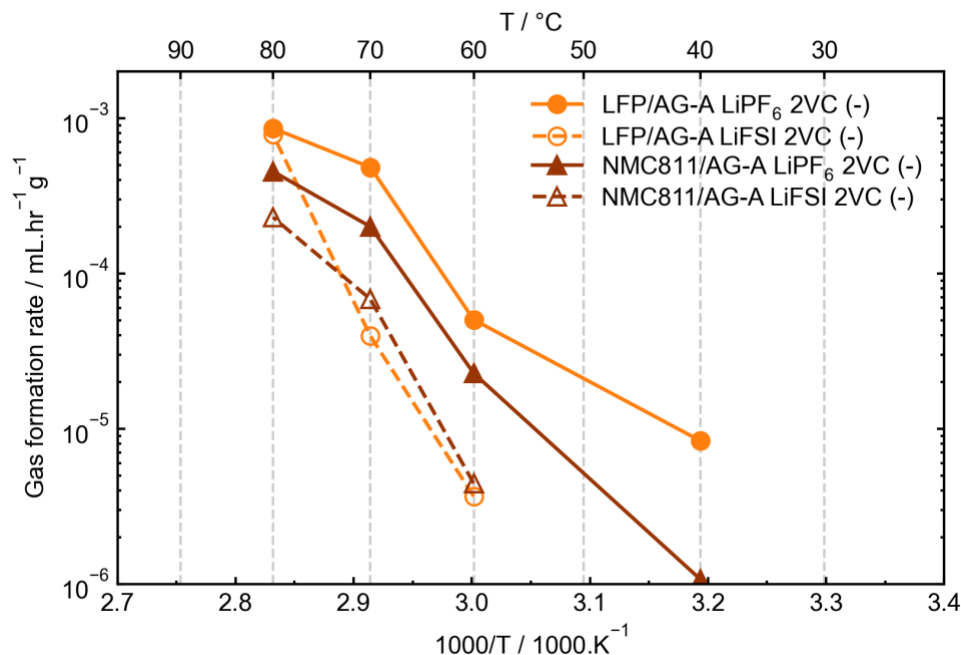


Figure 6.10: Arrhenius plot comparing initial specific gas production rate for AG-A pouch bags extracted from either LFP/AG-A or NMC811/AG-A cells. Both LiPF<sub>6</sub> and LiFSI electrolytes are shown.

At least in the case of LiPF<sub>6</sub> electrolyte, it seems that the “history” of AG-A electrodes in the pouch bag experiments matters for the resulting gas production rate. Although cells only spent a limited amount of time as full cells before they were disassembled into pouch bags, the complex cross-talk parasitic reactions that occur during this time may impact the species in the electrolyte and the structure of the graphite SEI. Interestingly, AG-A pouch bags with LiFSI electrolyte showed similar gas evolution rates when originating from LFP or NMC pouch cells. This could indicate that the LiPF<sub>6</sub> electrolyte’s interaction with NMC or LFP could influence the differences that were seen in that case.

Similar results are shown for AG-C pouch bags in Figure 6.11. In these pouch bags, an overall reduction in gas production rate was observed going from LiPF<sub>6</sub> electrolyte to LiFSI

electrolyte, as was seen in the AG-A pouch bags. AG-C + LiPF<sub>6</sub> pouch bags from LFP cells showed higher gas formation rates at high temperature (70°C and 80°C) but similar rates at lower temperatures. Additionally, AG-C + LiFSI pouch bags from NMC cells had a lower gas production rate at 70°C, but pouch bags from LFP and NMC cells converged at 80°C.

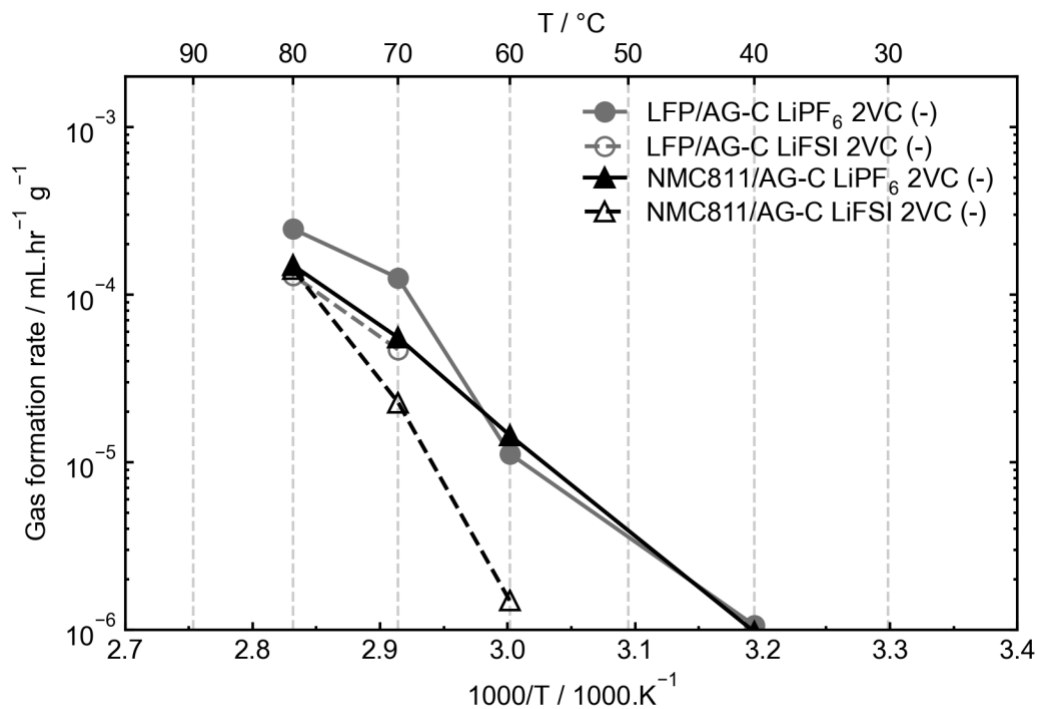


Figure 6.11: Arrhenius plot comparing initial specific gas production rate for AG-C pouch bags extracted from either LFP/AG-C or NMC811/AG-C cells. Both LiPF<sub>6</sub> and LiFSI electrolytes are shown.

### 6.2.3 Isothermal Microcalorimetry

As was noted in CHAPTER 5, not all parasitic reactions that occur in a Li-ion cell generate exclusively gaseous products. Many products of parasitic reactions will be soluble or solid. Isothermal microcalorimetry can be used to detect the heat flow originating from *all* parasitic reactions in a pouch cell or pouch bag. Additionally, the discrepancy between full



cell parasitic heat flow and the sum of pouch bag heat flows ( $\Delta\dot{q}$  as defined in Equation 5.4) can be used to infer the degree of cross-talk occurring in a given cell type.

OCV pouch cell/pouch bag IMC experiments that were done on LFP/AG cells in CHAPTER 5 were extended to include NMC811/AG cells. Only cells with AG-A and AG-C graphite negative electrodes were tested due to limited channel availability in the calorimeter. All cells underwent the same pre-cycling procedure outlined in CHAPTER 5, and spent roughly the same amount of time in the calorimeter. All experiments were done at 40°C. Figure 6.12 shows measured heat flow versus time for an example case of NMC811/AG-A and LFP/AG-A cells, both with LiPF<sub>6</sub> electrolyte. Recall from CHAPTER 5 (Figure 5.17) that LFP pouch bags alone had very little heat flow, and graphite pouch bags had parasitic heat flows on the order of ~15 – 20 μW. As may have been expected based on the pouch bag gas evolution experiments, the NMC811 positive electrode pouch bag showed considerably higher heat flow than the LFP pouch bag in Figure 6.12. However, the NMC pouch bag heat flow was still lower than the heat flow from the graphite pouch bags. Additionally, both the NMC full cell and AG-A pouch bag from NMC had higher heat flow than the corresponding LFP full cell and AG-A pouch bag from LFP. This was somewhat surprising given the superior high temperature performance that has been seen in NMC pouch cells compared to LFP pouch cells throughout this thesis (see Figure 4.23 and Figure 5.23). This may point to the possibility that some of the “parasitic” reactions specifically in NMC cells may in fact be beneficial for long-term cycle performance.

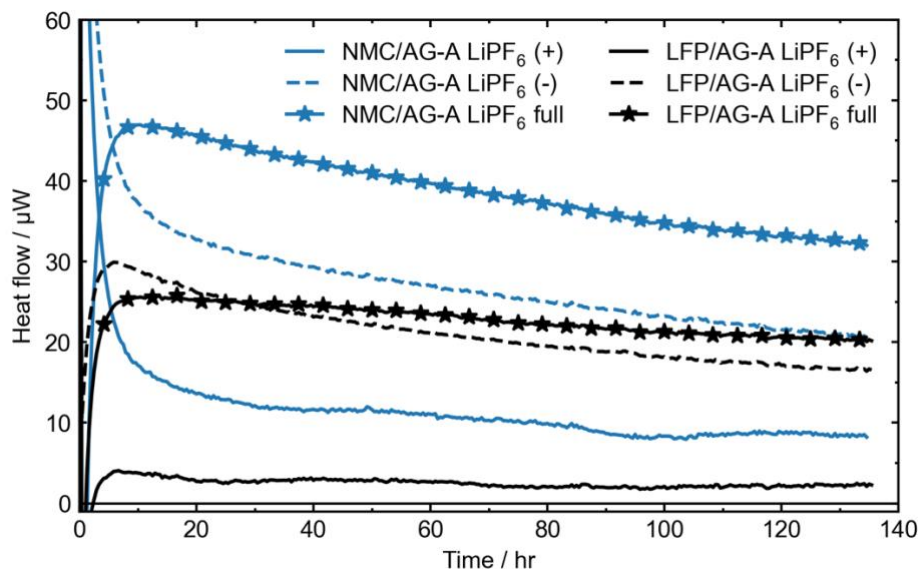


Figure 6.12: Measured heat flow versus time for pouch bags and full pouch cells (in OCV mode) in the microcalorimeter. All cells and pouch bags here had  $\text{LiPF}_6 + 2\text{VC}$  electrolyte.

Figure 6.13 shows the average parasitic heat flow for LFP/AG and NMC811/AG cells and pouch bags with different electrolytes measured at  $40^\circ\text{C}$  in the calorimeter. As was done in CHAPTER 5, the average parasitic heat flow was obtained by taking the average of the measured heat flow over the last five hours of the experiment in the calorimeter. The LFP results have been shown previously (Figure 5.22); briefly, LFP/AG-C cells showed lower overall parasitic heat flow than LFP/AG-A cells, agreeing with the improved performance that was seen.  $\Delta\dot{q}$  was higher for the LFP/AG-A chemistry with LiFSI electrolyte, indicating a larger degree of cross talk or shuttle reactions.  $\Delta\dot{q}$  was lower when AG-C negative electrodes were used, suggesting that the use of lower surface area graphite could lower the cross-talk reaction seen with LiFSI electrolyte.

Now, NMC/AG cells can be compared in a similar fashion. The higher parasitic heat flow of NMC811 positive electrode pouch bags can be seen clearly in Figure 6.13. Like what

was seen in the LFP/AG chemistry, parasitic heat flows were lower in NMC/AG-C compared to NMC/AG-A, for both LiPF<sub>6</sub> electrolyte and LiFSI electrolyte. This reduction could be seen in both full cells and negative electrode pouch bags. As well,  $\Delta\dot{q}$  was larger for the NMC/AG-A chemistry with LiFSI electrolyte compared to LiPF<sub>6</sub> electrolyte. This suggests a similar increase in cross-talk reactions in the NMC811 chemistry when LiFSI salt is used. The use of AG-C reduced  $\Delta\dot{q}$  in NMC811, as was also seen in the LFP case.

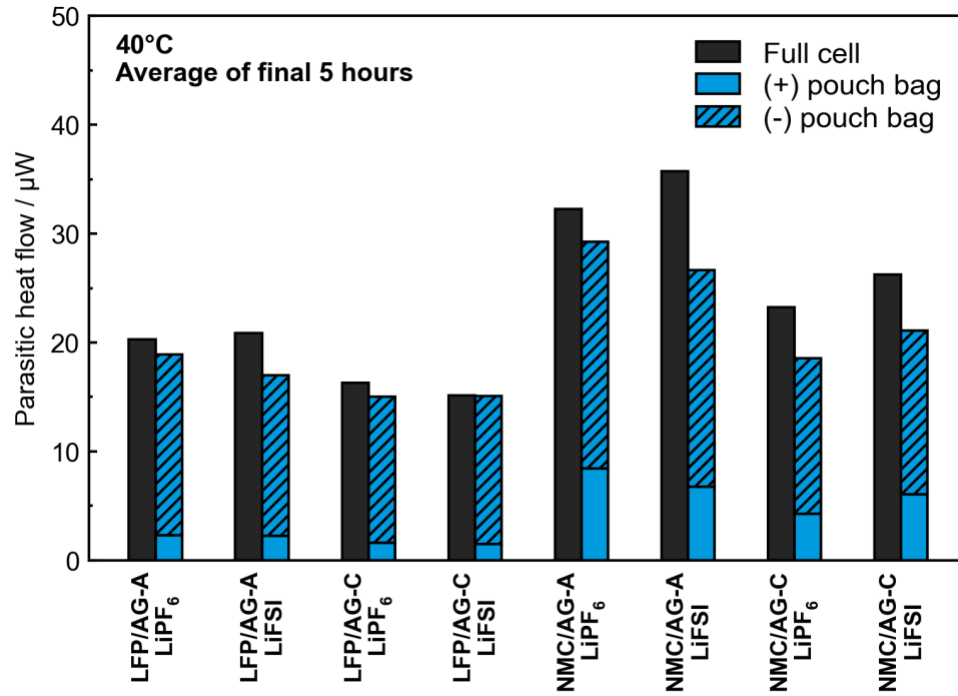


Figure 6.13: Average parasitic heat flow (averaged over the last 5 hours of the experiment) for full cells (black bars) and pouch bags (blue bars) for different positive/negative electrode/electrolyte combinations.

Finally, comparing NMC/AG and LFP/AG chemistries, higher parasitic heat flows were seen in the NMC811 cells compared to LFP. This was partly due to the higher parasitic heat flow at the positive electrode alone, which can be seen in both Figure 6.12 and Figure 6.13, as well as the larger heat flow from cross-talk,  $\Delta\dot{q}$ , as discussed above. However, the

parasitic heat flow from graphite electrodes was also marginally higher for these cells. Figure 6.14 shows the average parasitic heat flow for graphite pouch bags only, originating from pouch cells with different positive electrodes and electrolytes. Here it can be seen that the parasitic heat flows for AG-A pouch bags originating from NMC811 cells were slightly higher than in AG-A pouch bags originating from LFP cells. The difference in parasitic heat flow between AG-C pouch bags was much smaller. This is a peculiar result because the pouch bag gas evolution measurements above (Figure 6.10) showed a clear reduction in gas evolution in graphite pouch bags originating from NMC811 cells compared to LFP cells, at least with  $\text{LiPF}_6$  electrolyte.

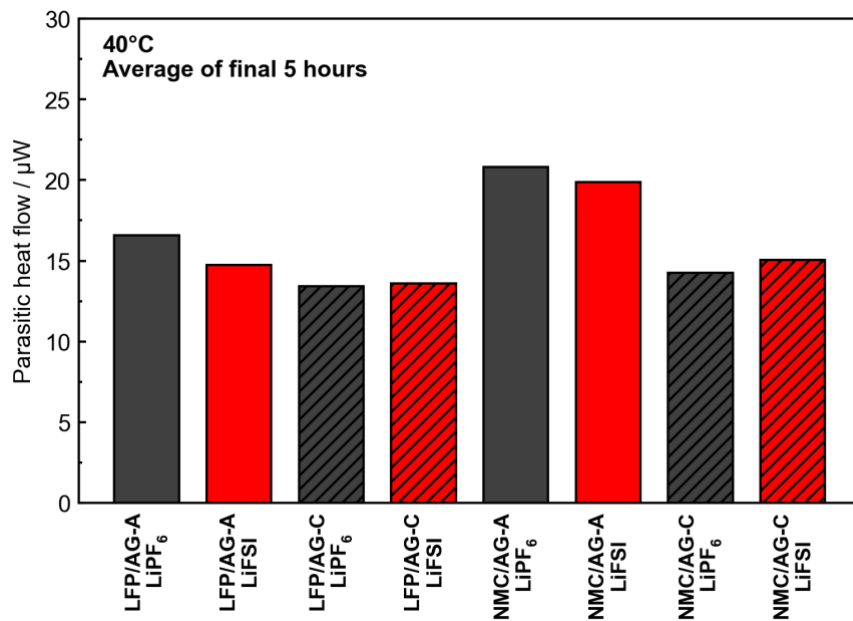


Figure 6.14: Average parasitic heat flow (averaged over the last 5 hours of the experiment) for artificial graphite pouch bags originating from pouch cells with different positive electrodes and electrolytes, indicated by the labels on the x-axis.

There are a few ways that this discrepancy can be resolved. First, the difference in parasitic heat flows between, say, AG-A +  $\text{LiPF}_6$  from NMC811/AG-A and AG-A +  $\text{LiPF}_6$  from LFP was relatively small, only on the order of a few  $\mu\text{W}$ . This difference could be attributed

to small cell-to-cell variations, or other inherent uncertainties in the measurements. Since pair cells were not used in this experiment, the uncertainty on these measurements could not be determined beyond the accuracy limitations of the calorimeter ( $\pm 1 \mu\text{W}$ ). However, it should be noted that results presented in these pouch bag experiments are in line with other experimental results (e.g. lower parasitic heat flow in AG-C pouch bags compared to AG-A pouch bags agrees with long term cycling results). Second, it could be possible that the *types* of parasitic reactions occurring in the AG pouch bags are different depending on the original positive electrode they were paired with. This simplified approach of presenting the *net* parasitic heat flow somewhat obscures the fact that a large combination of parasitic reactions likely occur in these pouch bags, all with different enthalpies of reaction that affect the amount of heat released (or absorbed) as they occur. A different “blend” of parasitic reactions will lead to a different net parasitic heat flow. So, instead of a higher parasitic heat flow in the AG pouch bags from NMC cells indicating “worse” performance or more Li consumption, it could simply indicate that different parasitic reactions were occurring compared to the LFP case. Third, as a corollary of the previous point, it is likely incorrect to assume all parasitic reactions are “bad” for cell lifetime. Obviously, some parasitic reactions in Li-ion cells are necessary, such as the initial formation of SEI on the negative electrode. It is possible that some of the cross-talk species produced in the initial conditioning cycles may actually be beneficial to the negative electrode SEI and improve passivation in the long run.

Finally, it is likely that the parasitic heat flow is dependent on the type of experiment that is done. While inferior performance was seen in long-term CCCV cycling for LFP cells

compared to NMC cells throughout this thesis, in the head-to-head comparisons of high temperature OCV storage presented in this chapter, LFP cells performed better than their NMC811 counterparts (see Figure 6.2, for example). This opens another discussion about storage versus cycling experiments, a detailed description of which is likely beyond the scope of this thesis. There are certainly significant differences in these tests, however. Long-term cycling experiments involve constant charging and discharging, leading to continuous volume expansion/contraction of the active material, with its associated problems, including SEI cracking and repair. These factors are not present in the OCV storage experiments, as cells are only periodically cycled. In OCV experiments, on the other hand, cells spend the majority of time at the top of charge, which may accelerate high-voltage parasitic reactions. Note that the NMC cells were stored at 4.06 V and the LFP cells were stored at 3.65 V.

## **6.3 DISCUSSION AND CONCLUSION**

### **6.3.1 Full cell versus pouch bag gas evolution**

This chapter has presented a systematic investigation of the interaction between different components in a Li-ion cell with the aim of achieving a better understanding of the complex cross-talk reactions that occur in these systems. As well, one-to-one comparisons were made between LFP/graphite and NMC811/graphite cells in an attempt to better understand the different lifetimes that were seen between these cell chemistries throughout this thesis.

In the full cell storage experiments, the cells were always near the top of charge (except when doing check-up cycles), so the gas produced in the full pouch cells can be compared to the pouch bag gas evolution. Figure 6.15 shows gas volumes evolved at 60°C in positive pouch bags, negative pouch bags, and full cells as a function of time. Note that absolute gas volumes are plotted here rather than values normalized to electrode active mass as was done earlier in this chapter. In the absence of any cross-talk between electrodes, it would be expected that the sum of the gas volumes observed in the pouch bags would be equal to the full cell gas evolution. Of course, this is not the case. Interestingly, though, the trends in gas evolution between pouch bags and pouch cells are different between the NMC811/AG and LFP/AG cells. In the NMC/AG cells with LiPF<sub>6</sub> electrolyte, the volume of gas evolved in the full cells was less than in the positive pouch bag. This is not a new result; Ellis et al. showed that CO<sub>2</sub> evolved at an NMC positive electrode as a result of EC oxidation can be reduced to form lithium oxalate (Li<sub>2</sub>C<sub>2</sub>O<sub>4</sub>) and lithium carbonate (Li<sub>2</sub>CO<sub>3</sub>)<sup>145</sup>. Rinkel et al. proposed the reduction of CO<sub>2</sub> at the negative electrode to form lithium formate<sup>126</sup>. In NMC811/AG-B and AG-C cells with LiPF<sub>6</sub> electrolyte, the sharp increase in gas volume in the full cells can be seen after 1000 hours, where the full cell gas volume almost matches positive electrode gas evolution. It is possible that by some mechanism the graphite electrode becomes unable to reduce CO<sub>2</sub> and other gases that are formed at the positive electrode after a certain point in the full cell storage.

In the case of NMC811/AG with LiFSI, the full cell gas volume exceeds the positive electrode pouch bag gas evolution. Recall the NMC811/AG-A cell with LiFSI electrolyte failed at the beginning of storage, so full cell data is not shown in panel Figure 6.15d. Other

than the implication that this large gas evolution likely involves the LiFSI salt, the origin of this increased gas evolution is not known. It is possible that it could be related to Al corrosion resulting from the use of LiFSI.

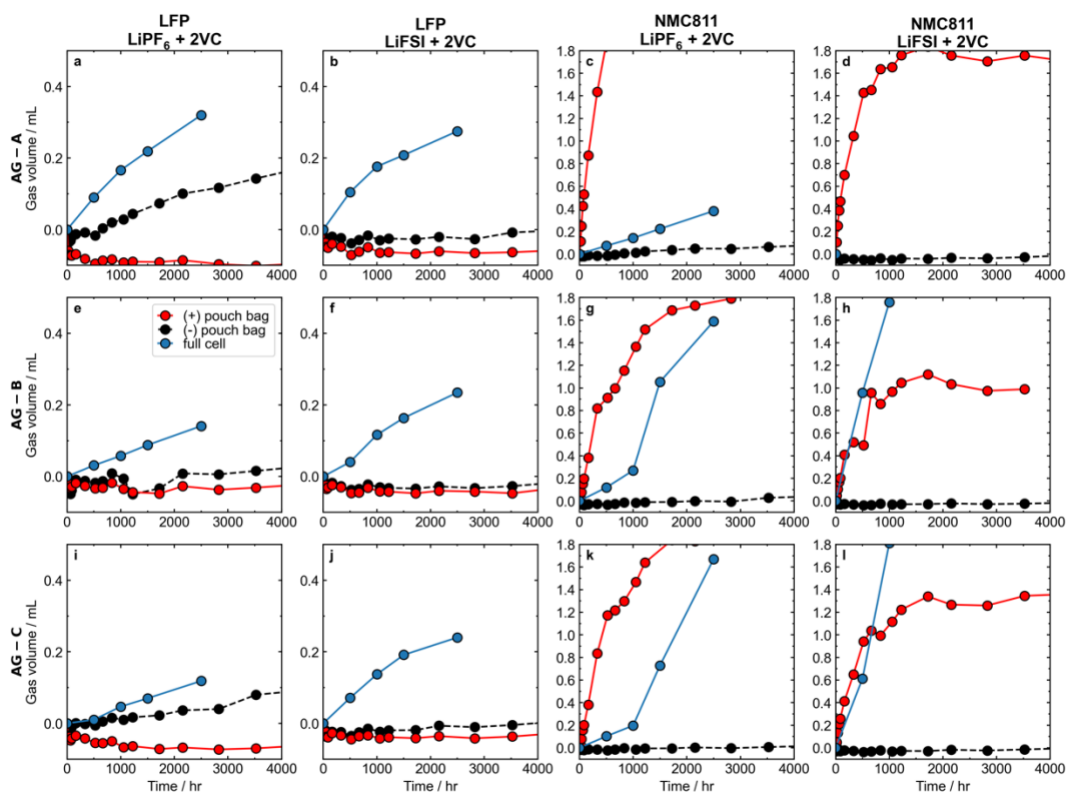


Figure 6.15: Comparing gas evolution in pouch bags and full cells. All cells and pouch bags were aged at 60°C. Different combinations of positive and negative electrodes and electrolytes are shown in the different panels.

The gas evolution trends in LFP/AG cells are somewhat different than their NMC811/AG counterparts. For LFP, more gas was always produced in the full cells than in either the positive or negative cell pouch bags. This is a surprising result given that virtually zero gas was produced in the LFP positive electrode pouch bags. This suggests that the gas produced in LFP full cells results from reactions with soluble species that are originally produced at another electrode, i.e. cross-talk reactions. This gas evolution in the full cells could also be



a result of Fe deposition on the graphite negative electrode and subsequent solvent reduction. However, Fe deposition has been shown to be very low in cells that contained 2% VC in the electrolyte (see Figure 5.10, for example). This again highlights some of the differences between LFP and NMC cells that could contribute to the observed differences in performance.

### 6.3.2 Capacity fade dominated by Li inventory loss

Throughout this thesis, it has been suggested that capacity fade in LFP/graphite cells is primarily driven by Li inventory loss at the negative electrode (i.e. SEI formation). One of the goals of testing pouch bags at temperatures as high as 80°C was to accelerate the parasitic reaction rate between lithiated graphite and the electrolyte to more quickly screen and rank graphite/electrolyte pairs. Here, the correlation between reactivity at the negative electrode and capacity fade in full LFP/graphite cells is tested. To parameterize the capacity loss of an LFP/graphite cell, the discharge capacity versus time was fitted to a simple model of  $t^{1/2}$  SEI growth and capacity loss. Ignoring contributions from SEI fracture and repair from volume changes as the cell is charged and discharged (i.e. a simplification of the equations developed by Deshpande and Bernardi<sup>297</sup>), the discharge capacity of a cell as a function of time can be modeled by:

$$Q(t) = Q_0(1 - At^{1/2}), \quad 6.2$$

where  $Q_0$  is the initial capacity of the cell,  $A$  is a parameter representing time-dependent capacity loss via SEI growth. Both  $Q_0$  and  $A$  are free parameters in the fit. These fits were done on LFP/AG cells with different AG negative electrodes and different electrolytes. The cells were cycled at 55°C at a rate of  $C/3$ , with  $C/20$  “check-up” cycles every 50 cycles

(these cells were presented in CHAPTER 5). Only the C/20 cycles were used in the fit of Equation 6.2 to minimize the impact of polarization effects at higher rates. The results of these fits can be seen in Figure A.14. The fitted value of the  $A$  parameter is indicated in each panel for each individual cell.

The parameterized capacity fade of these cells was then correlated to results from the high temperature pouch bag experiments presented earlier. Figure 6.16 shows the capacity fade parameter  $A$  for LFP/AG cells cycled at 55°C versus the initial specific gas evolution rate for graphite pouch bags extracted from LFP/AG cells stored at 80°C. Note that the fits on the y-axis were from cells that had several thousand hours of test time, and the fits to initial gas production in the pouch bags were done only for the first 1000 hours of testing. While not a perfect description of the data, there is a clear positive correlation between gas evolution at 80°C in the graphite pouch bags, and capacity loss in full LFP/AG cells at 55°C. This is somewhat an extension of the observation made in CHAPTER 5 that the ranking of full cell cycle performance between LiPF<sub>6</sub> Control, LiPF<sub>6</sub> 2VC, LiFSI Control, and LiFSI 2VC electrolytes agreed with the ranking of gas production in negative electrode pouch bags at 60°C. The main difference here is that the pouch bags at 80°C evolved noticeable volumes of gas in less time (<1000 hr) compared to the 60°C pouch bags in CHAPTER 5 (> 2000 hours for electrolytes with 2VC). This kind of experiment could potentially allow for the ranking of expected capacity loss in full cells a short amount of time.

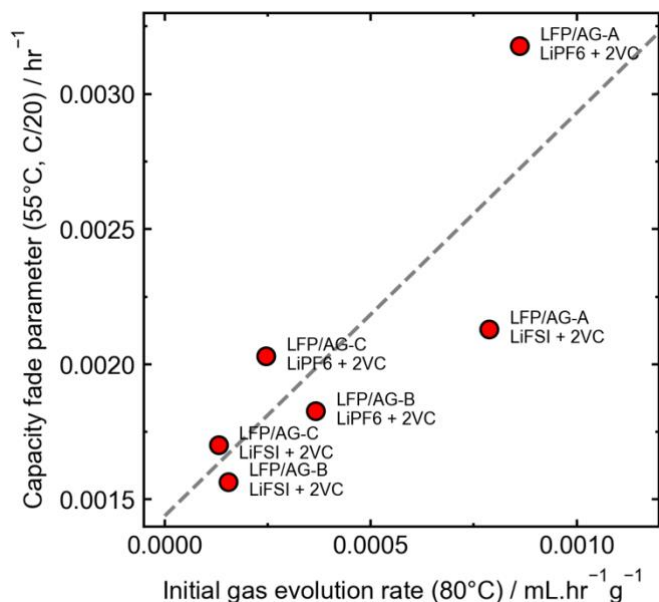


Figure 6.16: Correlating capacity fade in full LFP/AG pouch cells to initial specific gas evolution rate in negative electrode pouch bags aged at 80°C. Full pouch cells were cycled at 55°C at a rate of C/3. Fits were made to the C/20 checkup cycles using the equation  $Q = Q_0(1 - At^{1/2})$ . The dashed line is a linear regression the data.

Similarly, the capacity fade in full cells was also correlated to IMC results at 40°C (results shown in Figure 6.13). Figure 6.17 shows the fitted capacity fade parameter  $A$  for LFP/AG cells cycled at 55°C versus the average parasitic heat flow measured in graphite pouch bags at 40°C. Note that AG-B results are not shown in Figure 6.17 because they were not run in the microcalorimeter. Like in Figure 6.16, a clear correlation between full cell capacity fade and parasitic reactions in negative electrode pouch bags is seen. The correlation with the calorimetry measurements is arguably better than the gas evolution in the 80°C pouch bags, but this cannot be said with any statistical certainty. The benefits of the IMC method are that it is done at much lower temperature (40°C), and the parasitic heat flow was obtained in much less time (~150 hr) compared to the initial gas production value in the pouch bags (~1000 hours). In cells where Li inventory loss is expected to dominate

capacity fade in a full cell, this method may be valuable for screening different electrode/electrolyte combinations for long lifetimes.

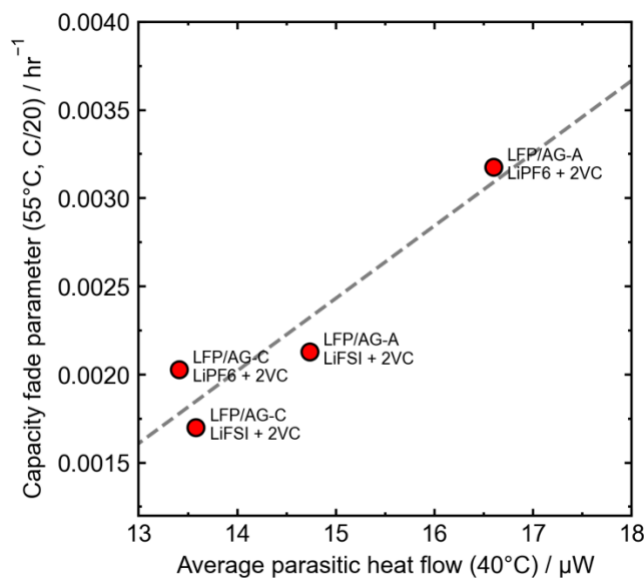


Figure 6.17: Correlating capacity fade in full LFP/AG cells to parasitic heat flow in graphite pouch bags using IMC. Parasitic heat flow was calculated in graphite pouch bags at 40°C using the method described in CHAPTER 5. Full pouch cells were cycled at 55°C at a rate of C/3. Fits were made to the C/20 checkup cycles using the equation  $Q = Q_0(1 - At^{1/2})$ . The dashed line is a linear regression the data.

### 6.3.3 Conclusion

In this chapter, the dependence of different positive electrode materials, graphite materials, and electrolyte salts on parasitic reactions in Li-ion cells was explored. Long-term, high temperature (60°C) OCV storage of LFP/AG and NMC811/AG pouch cells were completed, serving as an extension of the OCV storage experiments that have been presented throughout this thesis so far. In these experiments, different results were seen in LFP/AG and NMC/AG cells. In LFP, cells with AG-B and AG-C negative electrodes had the best capacity retention, and cells with LiFSI electrolyte performed better than cells with LiPF<sub>6</sub> electrolyte. These results were not unexpected given the results in Chapter 5, but it

was valuable to see these results hold for longer storage times. In NMC, cells with AG-B and AG-C negative electrodes and LiPF<sub>6</sub> electrolyte showed increasing capacity fade after 1000 hr of storage. This rapid capacity fade was not observed in NMC cells with either AG-A or LiFSI electrolyte, suggesting a complex interaction between these various components. This rapid capacity fade in NMC/AG-B and AG-C cells was accompanied by an associated increase in gas evolution in the full cells. Contrary to the cycling comparisons presented in CHAPTER 4 and CHAPTER 5, the LFP cells had better capacity retention than the NMC811 cells in these storage experiments, presumably because they were stored at a lower cell voltage.

In addition to the full cell storage experiments, pouch bags from this matrix of positive/negative/electrolyte combinations were constructed and aged at different temperatures, monitoring for gas evolution periodically. The expected Arrhenius temperature dependence of gas evolution was observed, especially in charged NMC811 positive electrodes. Additionally, differences in gas production in graphite negative electrodes were observed depending on both the electrolyte used and the positive electrode originally used in the full cell. Graphite pouch bags from NMC811/AG cells produced less gas than graphite pouch bags from LFP/AG cells when LiPF<sub>6</sub> electrolyte was used. The trend was less clear in LiFSI electrolyte.

Pouch bag isothermal microcalorimetry (IMC) experiments were carried out at 40°C for different cell chemistries with different electrolytes. In these experiments, it was found that NMC811 positive electrodes had considerably higher parasitic heat flow than LFP positive

electrodes, which was expected given the much larger gas volumes evolved in NMC pouch bags. Parasitic heat flows in graphite pouch bags were marginally higher when they originally came from NMC811 pouch cells, and similarly the parasitic heat flow in full cells (in open circuit) were higher in NMC cells compared to LFP cells. The difference between full cell parasitic heat flow and pouch bag parasitic heat flows,  $\Delta\dot{q}$ , were higher in NMC cells, indicating a higher degree of cross-talk reactions in this chemistry at the specified cell voltages.

Finally, the capacity fade of full LFP/AG cells were correlated to parasitic reactions occurring at the negative electrode only, indicating capacity fade dependent on SEI growth at the negative electrode. Fitted capacity fade parameters to LFP/AG cells cycled at 55°C correlated well with both the initial gas evolution rate of graphite pouch bags aged at 80°C, and the parasitic heat flow of graphite pouch bags measured at 40°C in the microcalorimeter. Both the pouch bag gas evolution experiments and pouch bag calorimetry experiments took considerably less time than the full cell cycling experiments, possibly allowing for these techniques to be used to screen electrolytes or graphite materials for use in constructing long-lifetime LFP cells.

The results in this chapter serve as a preliminary survey of the complex parasitic reactions in Li-ion batteries that depend on all components of the cell (positive electrode, negative electrode, electrolyte), and in turn contribute to the determination of the lifetime of a cell. Much more work is required to determine the specific mechanisms that lead to the different results that were found here. No analysis of the gas products or changes in the electrolyte

were done here. These kinds of analyses will be required to fully understand the complex degradation pathways that have been explored here. This future work will be discussed more in the next chapter.

## CHAPTER 7 CONCLUSIONS

All work in this chapter was carried out by the author of this thesis, with the exception of the blended LFP-NMC pouch cells (Figure 7.2b), which were filled by Connor Aiken. Assistance in building cells and pouch bags was provided by Ethan Eastwood, Helena Hebecker, and Animesh Dutta.

### 7.1 CONCLUSION

In this thesis, the degradation modes of  $\text{LiFePO}_4$  (LFP)/graphite cells were studied, and LFP cells with improved lifetimes were developed. One of the primary non-destructive techniques that was used was Li-ion isothermal microcalorimetry (IMC), measuring the parasitic heat flow due to parasitic reactions in cells. Starting with IMC techniques developed by Glazier<sup>119</sup>, these methods were first applied to LFP/graphite cells. Later, new methods were used to separate the contributions of positive and negative electrodes to the parasitic heat flow and infer the degree of cross-talk reactions in a given cell setup.

Preliminary studies of LFP/graphite pouch cells were carried out in CHAPTER 4. Cells were tested with and without water contamination, and with different electrolyte additives. Very poor performance was seen when LFP cells were made without electrolyte additives. This poor performance could be mitigated somewhat when water contamination was removed, but these cells still performed much worse than cells with electrolyte additives. In LFP cells with electrolyte additives, water contamination had a limited impact on capacity retention. Scanning micro X-ray fluorescence ( $\mu\text{XRF}$ ) spectroscopy



measurements of aged graphite electrodes extracted from pouch cells revealed trends in Fe deposition as a function of electrolyte additive and cycling temperature. Fe deposition was always high in cells with Control electrolyte, and Fe deposition was virtually eliminated with the use of appropriate electrolyte additives.

Also in CHAPTER 4, Li-ion isothermal microcalorimetry (IMC) techniques were applied to the LFP/graphite chemistry. The contribution of graphite entropy changes with Li (de)intercalation to the heat flow was estimated using mean field theory approximations, finding good agreement with experimental measurements. Parasitic heat flows found in LFP/graphite cells with different additives agreed well with long-term cycling results. Parasitic heat flow values for cells with different water contamination levels did not necessarily agree with long-term cycling results, but were consistent with UHPC results. Comparing cycle lifetimes in LFP cells with NMC532 cells found that NMC532 cells had better capacity retention at 40°C and 55°C, even though NMC cells operated at a higher voltage.

Several different approaches were taken to improve the long-term performance of LFP/graphite cells in CHAPTER 5. Studies of LFP materials with different particle size and surface area found that low surface area LFP suffered from particle fracturing issues, which led to more parasitic reactions, Fe dissolution and deposition, and higher capacity fade in long-term cycling experiments. High surface area LFP had the best lifetime in these experiments.

Next, the use of LiFSI as an alternative to LiPF<sub>6</sub> salt in the electrolyte was investigated. LFP cells with LiFSI electrolyte showed superior capacity retention compared to LiPF<sub>6</sub> electrolyte in both storage and cycling experiments. These improvements with the use of LiFSI were seen both in Control electrolyte (no electrolyte additives) and electrolytes with 2% vinylene carbonate (VC). Cells with LiFSI had less deposited Fe on the negative electrode after cycling as measured by  $\mu$ XRF spectroscopy. This improvement with the use of LiFSI over LiPF<sub>6</sub> in Control electrolyte was definitively supported by advanced characterization techniques; cells showed higher coulombic efficiency (CE) and lower charge endpoint capacity slippage in ultra-high precision coulometry (UHPC) experiments and significantly lower parasitic heat flow in IMC experiments. However, in cells with 2VC in the electrolyte, these metrics did not agree with the benefits seen in long-term cycling with the use of LiFSI. Specifically, LFP cells with LiFSI and 2VC in the electrolyte had lower CE, higher charge endpoint capacity slippage, higher parasitic heat flow, and higher reversible capacity loss in OCV storage than counterparts with LiPF<sub>6</sub> + 2VC electrolyte. “Pouch bag” experiments that monitor parasitic reactions occurring at one electrode only revealed that graphite negative electrodes were less reactive when LiFSI + 2VC electrolyte was used. These experiments were carried out using the existing Archimedes gas evolution technique, as well as in the TAM microcalorimeter. The discrepancy between long-term cycling and UHPC, full cell IMC, and OCV storage experiments was attributed to a redox shuttle reaction that is unique to the LiFSI electrolyte and does not irreversibly consume lithium. Comparing the difference between parasitic heat flow values in LFP full cells and separated pouch bags measured using IMC allowed for the magnitude of shuttle activity for different electrolytes to be inferred.

Finally, realizing that the majority of capacity loss in LFP/graphite was due to Li inventory loss at the negative electrode, different artificial graphites (AGs) were tested in LFP/graphite pouch cells. AGs with lower surface area (and lower electrochemical surface area) had higher first cycle efficiencies (FCE) and evolved less gas on the first cycle, indicated lower reactivity of the graphite negative electrode. Cells with low surface area AG had better capacity retention in cycling and storage experiments and had lower parasitic heat flow in IMC experiments. Combining the various improvements discussed in CHAPTER 5 led to an LFP/graphite cell with very long cycle life at high temperature. However, these cells still performed worse than comparable high voltage NMC/graphite cells in most cases.

In CHAPTER 6, the different interactions between positive electrodes, negative electrodes, and Li salts in the electrolyte were investigated. Long term OCV experiments were carried out with LFP/AG and NMC811/AG cells, using different AG negative electrodes and either LiPF<sub>6</sub> or LiFSI electrolytes. In these storage experiments, cells with LiFSI electrolyte showed superior capacity retention in both LFP/AG and NMC811/AG cells. As well, LFP cells with low surface area AG (AG-B and AG-C) performed better in these experiments. However, NMC811 cells with AG-B and AG-C negative electrodes exhibited rapid capacity fade in storage experiments after several storage periods. The exact mechanism for this capacity fade is not known at this moment, but the reader must remember that LFP cells were stored at only 3.65 V while the NMC811 cells were stored at 4.06 V. In contrast

to the previous results in this thesis, LFP cells had better capacity retention than NMC811 cells in the 60°C OCV storage experiments.

A systematic study of gas evolution and parasitic heat flow in pouch bags aged at temperatures ranging from 40°C – 80°C was also done in CHAPTER 6. NMC811 positive electrode pouch bags produced significant amounts of gas that largely followed Arrhenius kinetics as a function of temperature. LFP positive electrode pouch bags produced virtually zero gas over several thousand hours of testing, even at 80°C. Graphite pouch bags originally in NMC811 cells generally produced less gas than graphite pouch bags from LFP cells, and graphite pouch bags with LiFSI electrolyte generally generated less gas than pouch bags with LiPF<sub>6</sub> electrolyte. Graphite pouch bag gas generation also depended strongly on temperature.

Pouch bags measured at 40°C in the microcalorimeter revealed some interesting trends. NMC811/graphite cells in open circuit had higher parasitic heat flow than LFP/graphite cells, and graphite pouch bags had higher parasitic heat flow when originally paired with NMC811 compared to LFP. NMC811 pouch bags also had high parasitic heat flow, consistent with the large gas evolution that was observed. Finally, comparing pouch cell parasitic heat flow to pouch bag parasitic heat flow suggested that NMC811/graphite cells have a higher degree of cross-talk reactions between electrodes compared to LFP/graphite cells.

Finally, comparing gas evolution between LFP/graphite cells and NMC811/graphite cells and their respective pouch bags revealed some differences between the LFP and NMC chemistries. LFP full cell gas evolution was always larger than the sum of the pouch bags, while NMC full cell gas volumes were typically less than the sum of the pouch bags. This again points to the existence of complex cross-talk interactions that are highly dependent on the choice of positive electrode material.

## **7.2 FUTURE WORK**

There are several interesting research directions that can be taken based on the results of this thesis. Some of these future directions will be summarized below.

### **7.2.1 LFP future directions**

The bulk of this thesis focused on understanding the various degradation modes of LFP/graphite cells. While much progress was made in this work, there are still many directions to be taken to (1) further understand degradation of LFP/graphite cells, and (2) further improve the lifetimes of these cells.

CHAPTER 4 presented studies of LFP cells with various electrolyte additive blends. While several effective electrolyte additives were found (these turned out to be the same additive mixtures that work well in NMC/graphite chemistries), much more work could be done to optimize the electrolyte composition in LFP/graphite cells. Further, once LiFSI was identified as a good alternative to LiPF<sub>6</sub>, no electrolyte additive optimization was done. This kind of work is labour intensive, as countless combinations of electrolyte additives

(and now Li salts as well) can be envisioned. Such systematic studies of electrolyte additives have been done over the years in our lab<sup>292,298,299</sup> in NMC/graphite cells, over time leading to the discovery of electrolyte additive combinations that lead to cells with extremely long lifetimes. Similar systematic studies of electrolyte additives in LFP/graphite cells would be valuable.

This thesis did not contain much destructive analysis of aged Li-ion cells or pouch bags, instead focusing on non-destructive techniques such as IMC, UHPC, and smart storage. However, to truly understand the mechanisms for Li-ion cell degradation, such destructive techniques are required. For example, analyzing the components of evolved gases or electrolyte composition after aging could provide further insight into the various topics studied here. Such studies were developed and applied by Thompson<sup>300</sup>. Surface-sensitive techniques such as X-ray photoelectron spectroscopy (XPS) would be useful to gain understanding into how the graphite SEI composition changes depending on the positive electrode used, or with different Li salts used in the electrolyte. Future studies into the degradation of LFP/graphite cells should use such techniques.

One destructive analysis technique that was used in this thesis was scanning micro X-ray fluorescence ( $\mu$ XRF) spectroscopy measurements of aged graphite negative electrodes. In CHAPTER 4, deposited Fe was measured as a function of cycle number, which provided some valuable insight into the time-dependence of Fe deposition in LFP cells. Due to the COVID-19 pandemic, access to the  $\mu$ XRF spectrometer became limited, so such systematic studies became less feasible. Instead “snapshots” of Fe deposition in aged cells

were shown in CHAPTER 5 in the studies of different surface area LFP and the use of LiFSI. More systematic studies of Fe deposition, specifically in cells with different Li salts, would provide valuable information about when Fe deposition primarily occurs in a cell's life, and if Fe deposition can be correlated with cell failure later in a cell's life.

### 7.2.2 Isothermal microcalorimetry future directions

In this thesis, isothermal microcalorimetry techniques were valuable for understanding parasitic reactions and degradation in LFP/graphite pouch cells. Measuring parasitic heat flows using the “charge-discharge” method based on the work of Glazier<sup>119</sup> was able to correctly rank the lifetimes of LFP/graphite cells with different electrolyte additives in CHAPTER 4, and LFP cells with different artificial graphite negative electrodes in CHAPTER 5. However, the limits of this technique were reached when investigating the impact of water contamination on parasitic heat flow (CHAPTER 5) and the impact of LiFSI-based electrolytes with 2VC added (CHAPTER 5). In both cases, measured parasitic heat flow did not agree with what was observed in long-term cycling experiments. It was proposed that in the case of LiFSI electrolyte especially, reversible redox shuttles may have impacted the measured parasitic heat flow. This led to the experiments where separated electrode pouch bags were measured in the calorimeter. In these experiments, graphite pouch bags with LiFSI electrolyte had lower parasitic heat flow than graphite pouch bags with LiPF<sub>6</sub> electrolyte, agreeing with long-term cycling.

Now that the limits of microcalorimetry techniques have been approached, there are several future directions to improve on and expand the scope of Li-ion isothermal

microcalorimetry. One obvious approach would be to simply increase the temperature at which calorimetry experiments are done. All IMC experiments in this thesis were done at 40°C. In CHAPTER 4, very small differences were seen in the parasitic heat flow of LFP cells with different electrolyte additives, even when significant differences in long-term cycling were observed. Increasing the temperature of the calorimeter should increase the rate of parasitic reactions and hopefully amplify the differences between cells in less time. The TAM III microcalorimeter is rated to 150°C, so stable temperatures above 40°C should be easily attainable.

Some preliminary work on IMC experiments at different temperatures is shown below. Figure 7.1 shows average parasitic heat flow (averaged over the last 5 hours at each temperature) versus inverse temperature for pouch bags originating from different pouch cells (all LiPF<sub>6</sub> + 2VC electrolyte). Parasitic heat flow was measured at 40°C, 60°C, and 70°C. Pouch bags containing electrolyte only (triangle points) are also shown. Clear Arrhenius behaviour can be seen in the electrolyte pouch bags (the LiFSI point at 40°C is reaching the accuracy limit of the calorimeter, 1 μW), and both the positive electrode pouch bags. This may be expected as Arrhenius behaviour was seen in the gas evolution trends in the NMC pouch bags in CHAPTER 6 (Figure 6.8). For the graphite pouch bags, the parasitic heat flow values at 60°C and 70°C were slightly lower than what may be expected. This is likely due to the  $t^{1/2}$  behaviour of SEI formation: throughout this experiment, the SEI was continuously growing, so by the time the 60°C and 70°C temperatures were reached, the SEI would have been thicker and better passivating than when the pouch bag was inserted at 40°C. A more accurate experiment to measure graphite pouch bag parasitic



heat flow would likely require identical fresh electrodes to be used for each temperature. Another issue to consider for these types of experiments is the calibration stability of each of the calorimeter channels. Some channels in this preliminary study read non-realistic values of heat flow when the temperature was changed. It is possible that all calorimeter channels may need to be re-calibrated at each temperature. Further study is required to confirm this.

Isothermal microcalorimetry applied to separated electrode pouch bags was valuable in understanding the complex interactions between positive and negative electrodes, and removing the influence of cross-talk or shuttle reactions that affected full cell IMC and UHPC measurements in CHAPTER 5. Similar techniques were used in the early days of Li-ion IMC by Krause et al. where graphite/graphite symmetric cells were cycled in the calorimeter<sup>121</sup>. The benefits of the pouch bag method is that (1) the amount of active material is much larger, allowing for parasitic heat flows to be resolved much more easily, and (2) no additional high-precision charger equipment was required, as was needed in Krause et al.<sup>121</sup> Additional research directions for pouch bag IMC experiments can be envisioned. For example, studies of electrolyte additives could benefit from this type of experiment. Measurements of parasitic heat flows in full cells and positive and negative electrode pouch bags with and without a new electrolyte additive could easily determine which at which electrode(s) the additive in question acts. IMC measurements of electrode pouch bags at different states of charge (SOC) could determine SOC or voltage dependence of parasitic reactions at separate electrodes, and would nicely complement similar work done in this thesis and the work done by Glazier<sup>119</sup>.

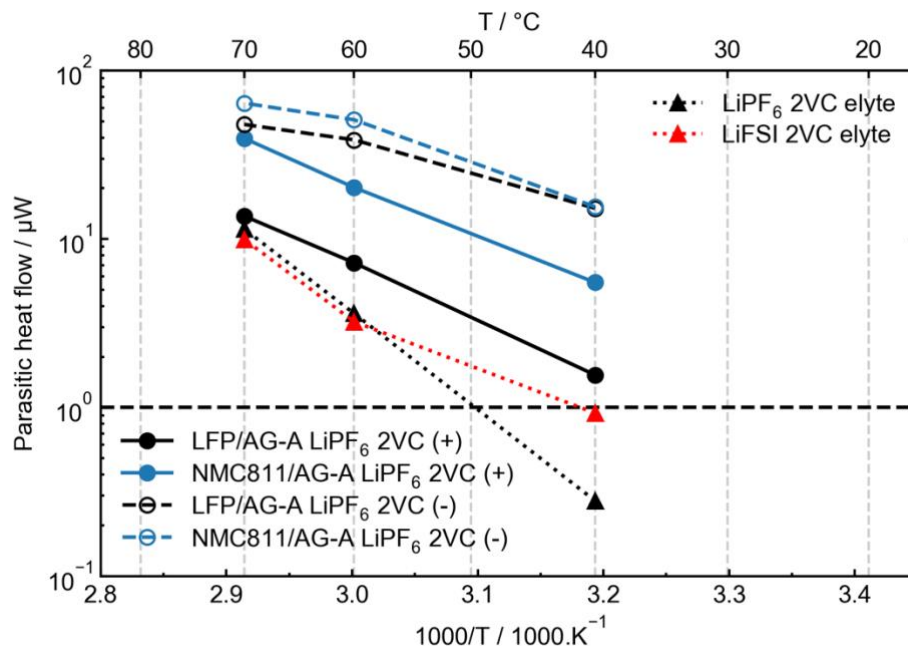


Figure 7.1: Parasitic heat flow versus inverse temperature measured in different pouch bags as a function of temperature. Each point was calculated as the average of the last 5 hours at each temperature. The black dashed line at 1  $\mu\text{W}$  indicates the accuracy limit of the TAM III microcalorimeter.

### 7.2.3 Blended NMC/LFP positive electrodes

Results presented throughout this thesis have suggested that there may be some favorable cross-talk reaction in NMC/graphite chemistries (that does not exist in the LFP/graphite chemistry) that may contribute to superior cycle life. Large gas volumes were detected in NMC pouch bags in CHAPTER 6, likely composed primarily of  $\text{CO}_2$ , while virtually no gas was evolved from LFP pouch bags. In microcalorimetry experiments, relatively high parasitic heat flows were seen in NMC pouch bags, and the degree of cross-talk parasitic heat flow,  $\Delta\dot{q}$ , was higher for NMC cells. Recent work by Aiken et al. has shown

conclusively that NMC/graphite cells show clearly superior performance to LFP/graphite cells<sup>301</sup>.

Some preliminary work has been done to investigate the addition of relatively small amounts (<20% by weight) of NMC active material into LFP positive electrodes. Figure 7.2a shows half-cell voltage curves for a familiar LFP positive electrode (dashed line), as well as a positive electrode containing 90% LFP and 10% NMC811 (solid line). These electrodes were mixed and coated by hand in the lab. Capacity from the NMC811 in the electrode can be seen once the cell is charged beyond the maximum LFP capacity.

Preliminary studies of lab-made blended LFP-NMC/graphite coin cells showed inconclusive results. Later, 402035-size pouch cells (similar to what has been used throughout this thesis) were ordered with blended LFP-NMC positive electrodes and AG-C negative electrodes. These cells were cycled at 70°C to accelerate the parasitic reaction rate and reveal differences between cells quicker than at lower temperatures. Taskovic et al. recently suggested cells cycled at 70°C do not have any additional degradation mechanisms that are not present at lower temperatures, and therefore provide a faster method to screen different Li-ion cells<sup>302</sup>.

Figure 7.2b shows normalized capacity (normalized to cycle 5) versus cycle number for LFP/AG-C and blended LFP-NMC640/AG-C cells with LiPF<sub>6</sub> + 2VC and LiFSI + 2VC electrolytes. LFP cells were cycled between 2.5 V – 3.65 V, and LFP-NMC cells were cycled between 2.5 V – 3.8 V. Both cells were cycled at a nominal rate of C/3 for charge

and discharge. Here it can be seen that the LFP-NMC cells have better capacity retention than the pure LFP cells, both in  $\text{LiPF}_6$  and LiFSI electrolytes. This seems to confirm that the NMC material contributes some unique benefits for long-term cycling in full cells with graphite negative electrodes. Much more work is required to fully understand the benefit that NMC materials contribute, as well as potential difficulties in blended LFP/NMC cells. Both topics are beyond the scope of the discussion here.

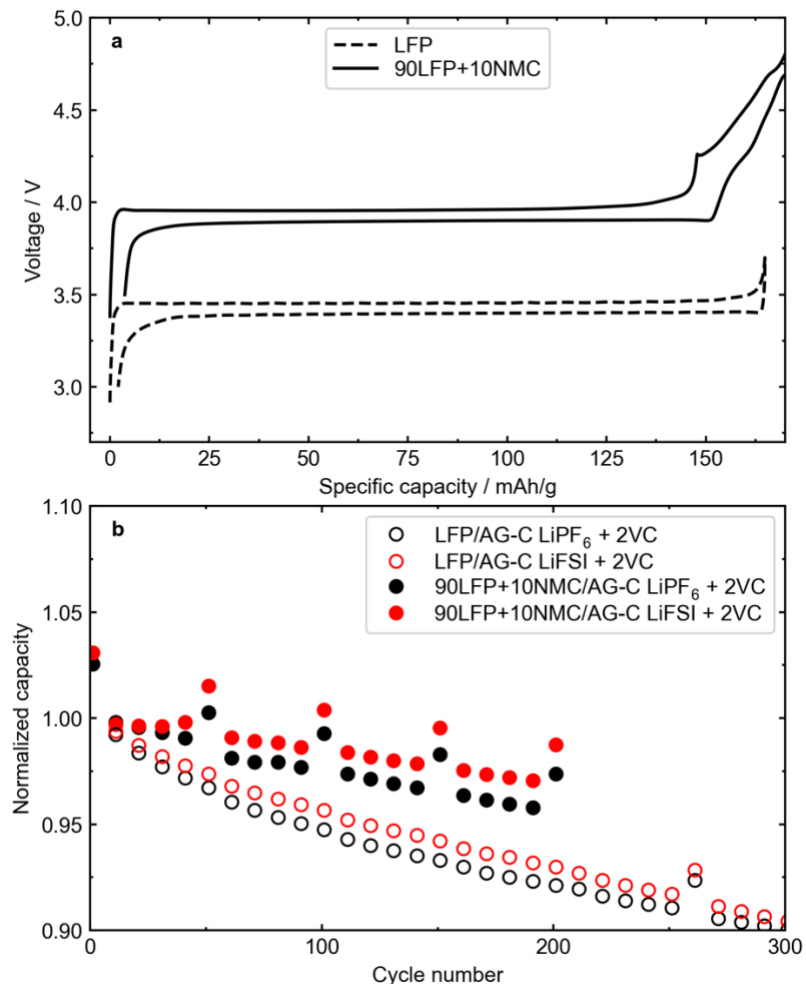


Figure 7.2: Studies of blended LFP-NMC positive electrodes. (a) First cycle voltage versus specific capacity for an LFP/Li half cell (dashed line), and a 90% LFP + 10% NMC811/Li half cell (solid line). Cells were cycled at a nominal rate of C/20 at 40°C. The blended LFP-NMC voltage curve is shifted on the voltage axis for clarity. (b) Normalized capacity (cycle 5) for LFP/AG-C pouch cells and 90% LFP + 10% NMC640/AG-C pouch cells with different electrolytes. LFP cells were cycled to 3.65 V, while LFP-NMC cells were cycled to 3.8 V. Cells were cycled at 70°C at a nominal rate of C/3.

#### 7.2.4 Increasing energy density with LiMn<sub>x</sub>Fe<sub>1-x</sub>PO<sub>4</sub> (LMFP)

Olivine positive electrode materials with transition metals other than Fe were briefly introduced in CHAPTER 1. One of the most common substitutions to Fe in LFP is Mn, making LiMn<sub>x</sub>Fe<sub>1-x</sub>PO<sub>4</sub>, or LMFP. The Mn in LMFP has a higher redox potential than Fe, leading to an electrode with a higher specific energy than pure LFP. However, these

materials have significant capacity fade issues, especially at high temperature. Some preliminary studies were done with LMFP/AG-A cells with 80% Mn and 20% Fe. Figure 7.3 shows normalized capacity versus cycle number for LMFP/AG-A cells with and without 2%VC in the electrolyte, and with LiPF<sub>6</sub> and LiFSI salts in the electrolyte. Cells were cycled at 55°C at a rate of C/3. An optimized (1.5 M LiFSI + 2VC) LFP/AG-A cell is shown for comparison (star markers). Benefits are seen in the LMFP cells going from Control electrolyte to 2VC electrolyte and LiPF<sub>6</sub> electrolyte to LiFSI electrolyte that resemble what was seen in LFP cells in CHAPTER 5, suggesting that some of the degradation mechanisms are similar between LFP and LMFP. However, the LFP cell with LiFSI + 2VC electrolyte had much better capacity retention than the LMFP cell with LiFSI + 2VC electrolyte by a fairly large margin. One possible issue for LMFP cells with LiFSI salt could be corrosion of the Al current collector, since these cells operate at a much higher voltage than LFP cell (up to 4.2 V).

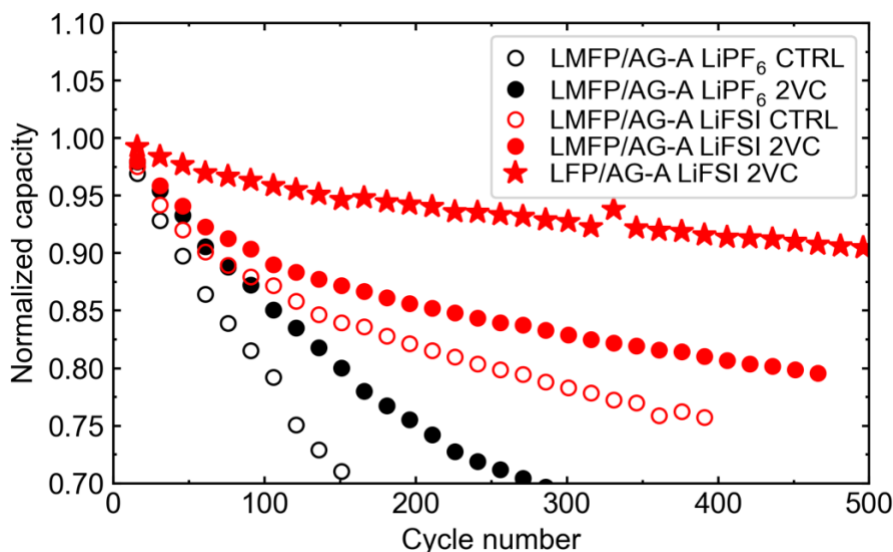


Figure 7.3: Normalized discharge capacity (cycle 5) versus cycle number for  $\text{LiMn}_{0.8}\text{Fe}_{0.2}\text{PO}_4$  (LMFP)/AG-A cells with different electrolytes compared to the best LFP/AG-A cell with LiFSI + 2VC electrolyte. All cells were cycled at  $55^\circ\text{C}$  at a rate of  $C/3$ . LMFP cells were cycled between 2.5 V – 4.2 V and LFP cells were cycled between 2.5 V – 3.65 V.

Isothermal microcalorimetry pouch bag experiments were done on LMFP/AG-A cells and were compared to LFP/AG-A cells. Figure 7.4 shows average parasitic heat flow for full cells and pouch bags measured at  $40^\circ\text{C}$  in the calorimeter after  $\sim 135$  hr. Comparing the LMFP cells to LFP cells, the LMFP positive electrode pouch bags had much higher parasitic heat flow than the LFP pouch bags, even higher than the NMC811 pouch bags shown in CHAPTER 6. Most notable here is the massive  $\Delta\dot{q}$  that is seen in the LMFP/AG-A chemistry, suggesting a large amount of cross-talk reactions occur in this system. Some of this cross-talk could be due to Mn dissolution from the LMFP positive electrode. Notice as well that while the use of LiFSI in LMFP improved cycle performance in Figure 7.3, it increased  $\Delta\dot{q}$  in Figure 7.4 suggesting that a similar shuttle reaction involving LiFSI exists. Further work is required to understand the additional degradation mechanisms in the LMFP chemistry and improve cycle lifetime.

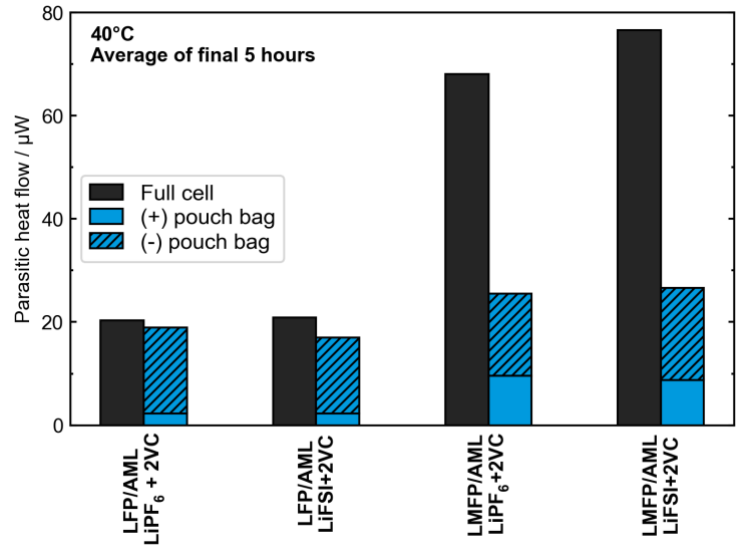


Figure 7.4: Bar graph showing parasitic heat flow measured in full cells and pouch bags in the TAM calorimeter.



## REFERENCES

- (1) Pillot, C. The Rechargeable Battery Market and Main Trends 2018-2030, 2019.
- (2) Hart, D. M.; Bonvillian, W. B.; Austin, N. R., 2018.
- (3) European Environment Agency. *New registrations of electric vehicles in Europe*. (accessed 2022-03-07).
- (4) Carey, N.; Steitz, C. *EU proposes effective ban for new fossil-fuel cars from 2035*. Reuters. (accessed 2022-03-07).
- (5) Office of Governor Gavin Newsom. *Governor Newsom Announces California Will Phase Out Gasoline-Powered Cars & Drastically Reduce Demand for Fossil Fuel in California's Fight Against Climate Change*. (accessed 2022-03-07).
- (6) Scherer, S. *Canada to ban sale of new fuel-powered cars and light trucks from 2035*. Reuters. (accessed 2022-03-07).
- (7) Zhang, S. S. A Review on the Separators of Liquid Electrolyte Li-Ion Batteries. *J. Power Sources* **2007**, *164* (1), 351–364. <https://doi.org/10.1016/j.jpowsour.2006.10.065>.
- (8) Fransson, L.; Eriksson, T.; Edström, K.; Gustafsson, T.; Thomas, J. O. Influence of Carbon Black and Binder on Li-Ion Batteries. *J. Power Sources* **2001**, *101*, 1–9.
- (9) Joachin, H.; Kaun, T. D.; Zaghbi, K.; Prakash, J. Electrochemical and Thermal Studies of Carbon-Coated LiFePO<sub>4</sub> Cathode. *J. Electrochem. Soc.* **2009**, *156* (6). <https://doi.org/10.1149/1.3106121>.
- (10) Chang, Y. C.; Peng, C. T.; Hung, I. M. Effects of Particle Size and Carbon Coating on Electrochemical Properties of LiFePO<sub>4</sub>/C Prepared by Hydrothermal Method. *J. Mater. Sci.* **2014**, *49* (20), 6907–6916. <https://doi.org/10.1007/s10853-014-8395-9>.
- (11) Huang, H.; Yin, S. C.; Nazar, L. F. Approaching Theoretical Capacity of LiFePO<sub>4</sub> at Room Temperature at High Rates. *Electrochem. Solid-State Lett.* **2001**, *4* (10), 170–173. <https://doi.org/10.1149/1.1396695>.
- (12) Pender, J. P.; Jha, G.; Youn, D. H.; Ziegler, J. M.; Andoni, I.; Choi, E. J.; Heller, A.; Dunn, B. S.; Weiss, P. S.; Penner, R. M.; Mullins, C. B. Electrode Degradation in Lithium-Ion Batteries. *ACS Nano* **2020**, *14* (2), 1243–1295. <https://doi.org/10.1021/acsnano.9b04365>.

- (13) Whittingham, M. S. Lithium Batteries and Cathode Materials. *Chem. Rev.* **2004**, *104* (10), 4271–4302. <https://doi.org/10.1021/cr020731c>.
- (14) Mizushima, K.; Jones, P.; Wiseman, P.; Goodenough, J. B.  $\text{Li}_x\text{CoO}_2$  ( $0 < x < 1$ ): A New Cathode Material for Batteries of High Energy Density. *Mater. Res. Bull.* **1980**, *15* (6), 783–789.
- (15) Sovacool, B. K. The Precarious Political Economy of Cobalt: Balancing Prosperity, Poverty, and Brutality in Artisanal and Industrial Mining in the Democratic Republic of the Congo. *Extr. Ind. Soc.* **2019**, *6* (3), 915–939. <https://doi.org/10.1016/j.exis.2019.05.018>.
- (16) Li, B. M.; Lu, J. Cobalt in Lithium-Ion Batteries. *Science* **2020**, *367* (6481), 979–980.
- (17) Azevedo, M.; Campagnol, N.; Hagenbruch, T.; Hoffman, K.; Lala, A.; Ramsbottom, O. Lithium and Cobalt - a Tale of Two Commodities, 2018.
- (18) Kim, J.; Lee, H.; Cha, H.; Yoon, M.; Park, M.; Cho, J. Prospect and Reality of Ni-Rich Cathode for Commercialization. *Adv. Energy Mater.* **2018**, *8* (6), 1702028. <https://doi.org/10.1002/aenm.201702028>.
- (19) Manthiram, A.; Song, B.; Li, W. A Perspective on Nickel-Rich Layered Oxide Cathodes for Lithium-Ion Batteries. *Energy Storage Mater.* **2017**, *6*, 125–139. <https://doi.org/10.1016/j.ensm.2016.10.007>.
- (20) Lu, Z.; MacNeil, D. D.; Dahn, J. R. Layered  $\text{Li}[\text{Ni}_x\text{Co}_{1-2x}\text{Mn}_x]\text{O}_2$  Cathode Materials for Lithium-Ion Batteries. *Electrochem. Solid-State Lett.* **2001**, *4* (12), A200–A203.
- (21) MacNeil, D. D.; Lu, Z.; Dahn, J. R. Structure and Electrochemistry of  $\text{Li}[\text{Ni}_x\text{Co}_{1-2x}\text{Mn}_x]\text{O}_2$  ( $0 < x < 1/2$ ). *J. Electrochem. Soc.* **2002**, *149* (10), A1332–A1336.
- (22) MacNeil, D. D.; Lu, Z.; Chen, Z.; Dahn, J. R. A Comparison of the Electrode/Electrolyte Reaction at Elevated Temperatures for Various Li-Ion Battery Cathodes. *J. Power Sources* **2002**, *108* (1–2), 8–14. [https://doi.org/10.1016/S0378-7753\(01\)01013-8](https://doi.org/10.1016/S0378-7753(01)01013-8).
- (23) Chen, C. H.; Liu, J.; Stoll, M. E.; Henriksen, G.; Vissers, D. R.; Amine, K. Aluminum-Doped Lithium Nickel Cobalt Oxide Electrodes for High-Power Lithium-Ion Batteries. *J. Power Sources* **2004**, *128* (2), 278–285. <https://doi.org/10.1016/j.jpowsour.2003.10.009>.

- (24) Rathore, D.; Geng, C.; Zaker, N.; Hamam, I.; Liu, Y.; Xiao, P.; Botton, G. A.; Dahn, J.; Yang, C. Tungsten Infused Grain Boundaries Enabling Universal Performance Enhancement of Co-Free Ni-Rich Cathode Materials. *J. Electrochem. Soc.* **2021**, *168* (12), 120514. <https://doi.org/10.1149/1945-7111/ac3c26>.
- (25) Liu, A.; Zhang, N.; Stark, J. E.; Arab, P.; Li, H.; Dahn, J. R. Synthesis of Co-Free Ni-Rich Single Crystal Positive Electrode Materials for Lithium Ion Batteries: Part I. Two-Step Lithiation Method for Al- or Mg-Doped LiNiO<sub>2</sub>. *J. Electrochem. Soc.* **2021**, *168* (4), 040531. <https://doi.org/10.1149/1945-7111/abf7e8>.
- (26) Cormier, M. M. E.; Zhang, N.; Liu, A.; Li, H.; Inglis, J.; Dahn, J. R. Impact of Dopants (Al, Mg, Mn, Co) on the Reactivity of Li<sub>x</sub>NiO<sub>2</sub> with the Electrolyte of Li-Ion Batteries. *J. Electrochem. Soc.* **2019**, *166* (13), A2826–A2833. <https://doi.org/10.1149/2.0491913jes>.
- (27) Li, H.; Cormier, M.; Zhang, N.; Inglis, J.; Li, J.; Dahn, J. R. Is Cobalt Needed in Ni-Rich Positive Electrode Materials for Lithium Ion Batteries? *J. Electrochem. Soc.* **2019**, *166* (4), A429–A439. <https://doi.org/10.1149/2.1381902jes>.
- (28) Li, H.; Liu, A.; Zhang, N.; Wang, Y.; Yin, S.; Wu, H.; Dahn, J. R. An Unavoidable Challenge for Ni-Rich Positive Electrode Materials for Lithium-Ion Batteries. *Chem. Mater.* **2019**, *31* (18), 7574–7583. <https://doi.org/10.1021/acs.chemmater.9b02372>.
- (29) Campagnol, N. NMC vs LFP: How Chemistry, Technology, Markets and Politics Shape The Future, 2022.
- (30) Padhi, A. K.; Nanjundaswamy, K. S.; Goodenough, J. B. Phospho-Olivines as Positive-Electrode Materials for Rechargeable Lithium Batteries. *J. Electrochem. Soc.* **1997**, *144* (4), 1188–1194.
- (31) Jiang, J.; Dahn, J. R. ARC Studies of the Thermal Stability of Three Different Cathode Materials: LiCoO<sub>2</sub>; Li[Ni<sub>0.1</sub>Co<sub>0.8</sub>Mn<sub>0.1</sub>]O<sub>2</sub>; and LiFePO<sub>4</sub>, in LiPF<sub>6</sub> and LiBoB EC/DEC Electrolytes. *Electrochem. Commun.* **2004**, *6* (1), 39–43. <https://doi.org/10.1016/j.elecom.2003.10.011>.
- (32) Zaghib, K.; Dubé, J.; Dallaire, A.; Galoustov, K.; Guerfi, A.; Ramanathan, M.; Benmayza, A.; Prakash, J.; Mauger, A.; Julien, C. M. Enhanced Thermal Safety and High Power Performance of Carbon-Coated LiFePO<sub>4</sub> Olivine Cathode for Li-Ion

- Batteries. *J. Power Sources* **2012**, *219*, 36–44. <https://doi.org/10.1016/j.jpowsour.2012.05.018>.
- (33) Pillot, C. The Rechargeable Battery Market and Main Trends 2018-2030. **2019**.
- (34) Delacourt, C.; Poizot, P.; Levasseur, S.; Masquelier, C. Size Effects on Carbon-Free LiFePO<sub>4</sub> Powders. *Electrochem. Solid-State Lett.* **2006**, *9* (7). <https://doi.org/10.1149/1.2201987>.
- (35) Ravet, N.; Chouinard, Y.; Magnan, J. F.; Besner, S.; Gauthier, M.; Armand, M. Electroactivity of Natural and Synthetic Triphylite. In *Journal of Power Sources*; 2001; Vol. 97–98, pp 503–507. [https://doi.org/10.1016/S0378-7753\(01\)00727-3](https://doi.org/10.1016/S0378-7753(01)00727-3).
- (36) Liu, T.; Zhao, L.; Wang, D.; Zhu, J.; Wang, B.; Guo, C. Carbon-Coated Single-Crystalline LiFePO<sub>4</sub> Nanocomposites for High-Power Li-Ion Batteries: The Impact of Minimization of the Precursor Particle Size. *RSC Adv.* **2014**, *4* (20), 10067. <https://doi.org/10.1039/c3ra46975a>.
- (37) Zhou, X.; Wang, F.; Zhu, Y.; Liu, Z. Graphene Modified LiFePO<sub>4</sub> Cathode Materials for High Power Lithium Ion Batteries. *J. Mater. Chem.* **2011**, *21* (10), 3353. <https://doi.org/10.1039/c0jm03287e>.
- (38) Anseán, D.; González, M.; Viera, J. C.; García, V. M.; Blanco, C.; Valledor, M. Fast Charging Technique for High Power Lithium Iron Phosphate Batteries: A Cycle Life Analysis. *J. Power Sources* **2013**, *239*, 9–15. <https://doi.org/10.1016/j.jpowsour.2013.03.044>.
- (39) Wu, X.-L.; Jiang, L.-Y.; Cao, F.-F.; Guo, Y.-G.; Wan, L.-J. LiFePO<sub>4</sub> Nanoparticles Embedded in a Nanoporous Carbon Matrix: Superior Cathode Material for Electrochemical Energy-Storage Devices. *Adv. Mater.* **2009**, *21* (25–26), 2710–2714. <https://doi.org/10.1002/adma.200802998>.
- (40) Wang, Y.; Wang, Y.; Hosono, E.; Wang, K.; Zhou, H. The Design of a LiFePO<sub>4</sub>/Carbon Nanocomposite With a Core–Shell Structure and Its Synthesis by an In Situ Polymerization Restriction Method. *Angew. Chem. Int. Ed.* **2008**, *47* (39), 7461–7465. <https://doi.org/10.1002/anie.200802539>.
- (41) Muraliganth, T.; Manthiram, A. Understanding the Shifts in the Redox Potentials of Olivine LiM<sub>1–y</sub>M<sub>y</sub>PO<sub>4</sub> (M = Fe, Mn, Co, and Mg) Solid Solution Cathodes. *J. Phys. Chem. C* **2010**, *114* (36), 15530–15540. <https://doi.org/10.1021/jp1055107>.

- (42) Wang, D.; Ouyang, C.; Drézen, T.; Exnar, I.; Kay, A.; Kwon, N.-H.; Gouerec, P.; Miners, J. H.; Wang, M.; Grätzel, M. Improving the Electrochemical Activity of  $\text{LiMnPO}_4$  Via Mn-Site Substitution. *J. Electrochem. Soc.* **2010**, *157*, 6.
- (43) Yamada, A.; Takei, Y.; Koizumi, H.; Sonoyama, N.; Kanno, R.; Itoh, K.; Yonemura, M.; Kamiyama, T. Electrochemical, Magnetic, and Structural Investigation of the  $\text{Li}_x(\text{Mn}_y\text{Fe}_{1-y})\text{PO}_4$  Olivine Phases. *Chem. Mater.* **2006**, *18* (3), 804–813. <https://doi.org/10.1021/cm051861f>.
- (44) Park, O. K.; Cho, Y.; Lee, S.; Yoo, H.-C.; Song, H.-K.; Cho, J. Who Will Drive Electric Vehicles, Olivine or Spinel? *Energy Environ. Sci.* **2011**, *4*, 1621–1633. <https://doi.org/10.1039/c0ee00559b>.
- (45) Bak, S.-M.; Nam, K.-W.; Lee, C.-W.; Kim, K.-H.; Jung, H.-C.; Yang, X.-Q.; Kim, K.-B. Spinel  $\text{LiMn}_2\text{O}_4$ /Reduced Graphene Oxide Hybrid for High Rate Lithium Ion Batteries. *J. Mater. Chem.* **2011**, *21* (43), 17309. <https://doi.org/10.1039/c1jm13741g>.
- (46) Amine, K.; Liu, J.; Kang, S.; Belharouak, I.; Hyung, Y.; Vissers, D.; Henriksen, G. Improved Lithium Manganese Oxide Spinel/Graphite Li-Ion Cells for High-Power Applications. In *Journal of Power Sources*; 2004; Vol. 129, pp 14–19. <https://doi.org/10.1016/j.jpowsour.2003.11.007>.
- (47) Li, S.; Xue, Y.; Cui, X.; Geng, S.; Huang, Y. Effect of Sulfolane and Lithium Bis(Oxalato)Borate-Based Electrolytes on the Performance of Spinel  $\text{LiMn}_2\text{O}_4$  Cathodes at 55 °C. *Ionics* **2016**, *22* (6), 797–801. <https://doi.org/10.1007/s11581-015-1611-z>.
- (48) Zhan, C.; Lu, J.; Jeremy Kropf, A.; Wu, T.; Jansen, A. N.; Sun, Y. K.; Qiu, X.; Amine, K. Mn(II) Deposition on Anodes and Its Effects on Capacity Fade in Spinel Lithium Manganate-Carbon Systems. *Nat. Commun.* **2013**, *4* (ii), 1–8. <https://doi.org/10.1038/ncomms3437>.
- (49) Obrovac, M. N.; Chevrier, V. L. Alloy Negative Electrodes for Li-Ion Batteries. *Chem. Rev.* **2014**, *114* (23), 11444–11502. <https://doi.org/10.1021/cr500207g>.
- (50) Dahn, J. R.; Zheng, T.; Liu, Y.; Xue, J. S. Mechanisms for Lithium Insertion in Carbonaceous Materials. *Science* **1995**, *270* (5236), 590–593. <https://doi.org/10.1126/science.270.5236.590>.

- (51) Dahn, J. R. Phase Diagram of  $\text{Li}_x\text{C}_6$ . *Phys. Rev. B* **1991**, *44* (17), 9170–9177. <https://doi.org/10.1103/PhysRevB.44.9170>.
- (52) Zheng, T.; Reimers, J. N.; Dahn, J. R. Effect of Turbostratic Disorder in Graphitic Carbon Hosts on the Intercalation of Lithium. *Phys. Rev. B* **1995**, *51* (2), 734–741. <https://doi.org/10.1103/PhysRevB.51.734>.
- (53) Eldesoky, A.; Bauer, M.; Azam, S.; Zsoldos, E.; Song, W.; Weber, R.; Hy, S.; Johnson, M. B.; Metzger, M.; Dahn, J. R. Impact of Graphite Materials on the Lifetime of NMC811/Graphite Pouch Cells: Part I. Material Properties, ARC Safety Tests, Gas Generation, and Room Temperature Cycling. *J. Electrochem. Soc.* **2021**, *168* (11), 110543. <https://doi.org/10.1149/1945-7111/ac39fc>.
- (54) Glazier, S. L.; Li, J.; Louli, A. J.; Allen, J. P.; Dahn, J. R. An Analysis of Artificial and Natural Graphite in Lithium Ion Pouch Cells Using Ultra-High Precision Coulometry, Isothermal Microcalorimetry, Gas Evolution, Long Term Cycling and Pressure Measurements. *J. Electrochem. Soc.* **2017**, *164* (14), A3545–A3555. <https://doi.org/10.1149/2.0421714jes>.
- (55) Obrovac, M. N.; Christensen, L. Structural Changes in Silicon Anodes during Lithium Insertion/Extraction. *Electrochem. Solid-State Lett.* **2004**, *7* (5), A93. <https://doi.org/10.1149/1.1652421>.
- (56) Qian, J.; Adams, B. D.; Zheng, J.; Xu, W.; Henderson, W. A.; Wang, J.; Bowden, M. E.; Xu, S.; Hu, J.; Zhang, J. G. Anode-Free Rechargeable Lithium Metal Batteries. *Adv. Funct. Mater.* **2016**, *26* (39), 7094–7102. <https://doi.org/10.1002/adfm.201602353>.
- (57) Aurbach, D.; Zinigrad, E.; Teller, H.; Cohen, Y.; Salitra, G.; Yamin, H.; Dan, P.; Elster, E. Attempts to Improve the Behavior of Li Electrodes in Rechargeable Lithium Batteries. *J. Electrochem. Soc.* **2002**, *149* (10), A1267–A1267. <https://doi.org/10.1149/1.1502684>.
- (58) Zhu, G.-N.; Wang, Y.-G.; Xia, Y.-Y. Ti-Based Compounds as Anode Materials for Li-Ion Batteries. *Energy Environ. Sci.* **2012**, *5* (5), 6652. <https://doi.org/10.1039/c2ee03410g>.
- (59) Logan, E. R.; Dahn, J. R. Electrolyte Design for Fast-Charging Li-Ion Batteries. *Trends Chem.* **2020**, *2* (4), 354–366. <https://doi.org/10.1016/j.trechm.2020.01.011>.

- (60) Logan, E. R.; Hall, D. S.; Cormier, M. M. E.; Taskovic, T.; Bauer, M.; Hamam, I.; Hebecker, H.; Molino, L.; Dahn, J. R. Ester-Based Electrolytes for Fast Charging of Energy Dense Lithium-Ion Batteries. *J. Phys. Chem. C* **2020**, *124* (23), 12269–12280. <https://doi.org/10.1021/acs.jpcc.0c02370>.
- (61) Xu, K. Nonaqueous Liquid Electrolytes for Lithium-Based Rechargeable Batteries. *Chem. Rev.* **2004**, *104* (10), 4303–4417. <https://doi.org/10.1021/cr030203g>.
- (62) Xu, K. Electrolytes and Interphases in Li-Ion Batteries and Beyond. *Chem. Rev.* **2014**, *114* (23), 11503–11618. <https://doi.org/10.1021/cr500003w>.
- (63) Campion, C. L.; Li, W.; Lucht, B. L. Thermal Decomposition of LiPF<sub>6</sub>-Based Electrolytes for Lithium-Ion Batteries. *J. Electrochem. Soc.* **2005**, *152* (12), A2327. <https://doi.org/10.1149/1.2083267>.
- (64) Freiberg, A. T. S.; Sicklinger, J.; Solchenbach, S.; Gasteiger, H. A. Li<sub>2</sub>CO<sub>3</sub> Decomposition in Li-Ion Batteries Induced by the Electrochemical Oxidation of the Electrolyte and of Electrolyte Impurities. *Electrochimica Acta* **2020**, *346*, 136271. <https://doi.org/10.1016/j.electacta.2020.136271>.
- (65) Kawamura, T.; Okada, S.; Yamaki, J. Decomposition Reaction of LiPF<sub>6</sub>-Based Electrolytes for Lithium Ion Cells. *J. Power Sources* **2006**, *156* (2), 547–554. <https://doi.org/10.1016/j.jpowsour.2005.05.084>.
- (66) Stich, M.; Göttliger, M.; Kurniawan, M.; Schmidt, U.; Bund, A. Hydrolysis of LiPF<sub>6</sub> in Carbonate-Based Electrolytes for Lithium-Ion Batteries and in Aqueous Media. *J. Phys. Chem. C* **2018**, *122* (16), 8836–8842. <https://doi.org/10.1021/acs.jpcc.8b02080>.
- (67) Terborg, L.; Weber, S.; Blaske, F.; Passerini, S.; Winter, M.; Karst, U.; Nowak, S. Investigation of Thermal Aging and Hydrolysis Mechanisms in Commercial Lithium Ion Battery Electrolyte. *J. Power Sources* **2013**, *242*, 832–837. <https://doi.org/10.1016/j.jpowsour.2013.05.125>.

- (68) Han, H. B.; Zhou, S. S.; Zhang, D. J.; Feng, S. W.; Li, L. F.; Liu, K.; Feng, W. F.; Nie, J.; Li, H.; Huang, X. J.; Armand, M.; Zhou, Z. B. Lithium Bis(Fluorosulfonyl)Imide (LiFSI) as Conducting Salt for Nonaqueous Liquid Electrolytes for Lithium-Ion Batteries: Physicochemical and Electrochemical Properties. *J. Power Sources* **2011**, *196* (7), 3623–3632. <https://doi.org/10.1016/j.jpowsour.2010.12.040>.
- (69) Li, L.; Zhou, S.; Han, H.; Li, H.; Nie, J.; Armand, M.; Zhou, Z.; Huang, X. Transport and Electrochemical Properties and Spectral Features of Non-Aqueous Electrolytes Containing LiFSI in Linear Carbonate Solvents. *J. Electrochem. Soc.* **2011**, *158* (2), A74–A74. <https://doi.org/10.1149/1.3514705>.
- (70) Kerner, M.; Pylahan, N.; Scheers, J.; Johansson, P. Thermal Stability and Decomposition of Lithium Bis(Fluorosulfonyl)Imide (LiFSI) Salts. *RSC Adv.* **2016**, *6* (28), 23327–23334. <https://doi.org/10.1039/c5ra25048j>.
- (71) Li, C.; Zeng, S.; Wang, P.; Li, Z.; Yang, L.; Zhao, D.; Wang, J.; Liu, H.; Li, S. Mechanism of Aluminum Corrosion in LiFSI-Based Electrolyte at Elevated Temperatures. *Trans. Nonferrous Met. Soc. China* **2021**, *31* (5), 1439–1451. [https://doi.org/10.1016/S1003-6326\(21\)65588-7](https://doi.org/10.1016/S1003-6326(21)65588-7).
- (72) Wu, X.; Du, Z. Study of the Corrosion Behavior of LiFSI Based Electrolyte for Li-Ion Cells. *Electrochem. Commun.* **2021**, *129*, 107088. <https://doi.org/10.1016/j.elecom.2021.107088>.
- (73) Abouimrane, A.; Ding, J.; Davidson, I. J. Liquid Electrolyte Based on Lithium Bis-Fluorosulfonyl Imide Salt: Aluminum Corrosion Studies and Lithium Ion Battery Investigations. *J. Power Sources* **2009**, *189* (1), 693–696. <https://doi.org/10.1016/j.jpowsour.2008.08.077>.
- (74) Xu, K.; Zhang, S. S.; Lee, U.; Allen, J. L.; Jow, T. R. LiBOB: Is It an Alternative Salt for Lithium Ion Chemistry? *J. Power Sources* **2005**, *146* (1–2), 79–85. <https://doi.org/10.1016/j.jpowsour.2005.03.153>.
- (75) Xu, M.; Zhou, L.; Dong, Y.; Chen, Y.; Garsuch, A.; Lucht, B. L. Improving the Performance of Graphite/ LiNi<sub>0.5</sub>Mn<sub>1.5</sub>O<sub>4</sub> Cells at High Voltage and Elevated Temperature with Added Lithium Bis(Oxalato) Borate (LiBOB). *J. Electrochem. Soc.* **2013**, *160* (11), A2005–A2013. <https://doi.org/10.1149/2.053311jes>.



- (76) Xu, K.; Zhang, S.; Jow, T. R. LiBOB as Additive in LiPF<sub>6</sub>-Based Lithium Ion Electrolytes. *Electrochem. Solid-State Lett.* **2005**, *8* (7), A365–A368.
- (77) Panitz, J.-C.; Wietelmann, U.; Wachtler, M.; Ströbele, S.; Wohlfahrt-Mehrens, M. Film Formation in LiBOB-Containing Electrolytes. *J. Power Sources* **2006**, *153* (2), 396–401. <https://doi.org/10.1016/j.jpowsour.2005.05.025>.
- (78) Ding, M. S.; Richard Jow, T. How Conductivities and Viscosities of PC-DEC and PC-EC Solutions of LiBF<sub>4</sub>, LiPF<sub>6</sub>, LiBOB, Et<sub>4</sub>NBF<sub>4</sub>, and Et<sub>4</sub>NPF<sub>6</sub> Differ and Why. *J. Electrochem. Soc.* **2004**, *151* (12), A2007–A2007. <https://doi.org/10.1149/1.1809575>.
- (79) Ellis, L. D.; Xia, J.; Louli, A. J.; Dahn, J. R. Effect of Substituting LiBF<sub>4</sub> for LiPF<sub>6</sub> in High Voltage Lithium-Ion Cells Containing Electrolyte Additives. *J. Electrochem. Soc.* **2016**, *163* (8), A1686–A1692. <https://doi.org/10.1149/2.0851608jes>.
- (80) Peled, E. The Electrochemical Behavior of Alkali and Alkaline Earth Metals in Nonaqueous Battery Systems—The Solid Electrolyte Interphase Model. *J. Electrochem. Soc.* **1979**, *126* (12), 2047–2051. <https://doi.org/10.1149/1.2128859>.
- (81) Peled, E.; Menkin, S. Review—SEI: Past, Present and Future. *J. Electrochem. Soc.* **2017**, *164* (7), A1703–A1719. <https://doi.org/10.1149/2.1441707jes>.
- (82) Verma, P.; Maire, P.; Novák, P. A Review of the Features and Analyses of the Solid Electrolyte Interphase in Li-Ion Batteries. *Electrochimica Acta* **2010**, *55* (22), 6332–6341. <https://doi.org/10.1016/j.electacta.2010.05.072>.
- (83) Edström, K.; Gustafsson, T.; Thomas, J. O. The Cathode–Electrolyte Interface in the Li-Ion Battery. *Electrochimica Acta* **2004**, *50* (2–3), 397–403. <https://doi.org/10.1016/j.electacta.2004.03.049>.
- (84) Li, Q.; Wang, Y.; Wang, X.; Sun, X.; Zhang, J.-N.; Yu, X.; Li, H. Investigations on the Fundamental Process of Cathode Electrolyte Interphase Formation and Evolution of High-Voltage Cathodes. *ACS Appl. Mater. Interfaces* **2020**, *12* (2), 2319–2326. <https://doi.org/10.1021/acsami.9b16727>.

- (85) Zhang, Y.; Katayama, Y.; Tatara, R.; Giordano, L.; Yu, Y.; Fraggedakis, D.; Sun, J.; Maglia, F.; Jung, R.; Bazant, M. Z.; Shao-Horn, Y. Revealing Electrolyte Oxidation via Carbonate Dehydrogenation on Ni-Based Oxides in Li-Ion Batteries by in Situ Fourier Transform Infrared Spectroscopy. *Energy Environ. Sci.* **2019**. <https://doi.org/10.1039/C9EE02543J>.
- (86) Parimalam, B. S.; MacIntosh, A. D.; Kadam, R.; Lucht, B. L. Decomposition Reactions of Anode Solid Electrolyte Interphase (SEI) Components with LiPF<sub>6</sub>. *J. Phys. Chem. C* **2017**, *121* (41), 22733–22738. <https://doi.org/10.1021/acs.jpcc.7b08433>.
- (87) Nie, M.; Lucht, B. L. Role of Lithium Salt on Solid Electrolyte Interface (SEI) Formation and Structure in Lithium Ion Batteries. *J. Electrochem. Soc.* **2014**, *161* (6), A1001–A1006. <https://doi.org/10.1149/2.054406jes>.
- (88) Seo, D. M.; Chalasani, D.; Parimalam, B. S.; Kadam, R.; Nie, M.; Lucht, B. L. Reduction Reactions of Carbonate Solvents for Lithium Ion Batteries. *ECS Electrochem. Lett.* **2014**, *3* (9), A91–A93. <https://doi.org/10.1149/2.0021409eel>.
- (89) Heiskanen, S. K.; Kim, J.; Lucht, B. L. Generation and Evolution of the Solid Electrolyte Interphase of Lithium-Ion Batteries. *Joule* **2019**, *3* (10), 2322–2333. <https://doi.org/10.1016/j.joule.2019.08.018>.
- (90) Zhang, B.; Metzger, M.; Solchenbach, S.; Payne, M.; Meini, S.; Gasteiger, H. A.; Garsuch, A.; Lucht, B. L. Role of 1,3-Propane Sultone and Vinylene Carbonate in Solid Electrolyte Interface Formation and Gas Generation. *J. Phys. Chem. C* **2015**, *119* (21), 11337–11348. <https://doi.org/10.1021/acs.jpcc.5b00072>.
- (91) Aurbach, D.; Gofer, Y.; Ben-Zion, M.; Aped, P. The Behaviour of Lithium Electrodes in Propylene and Ethylene Carbonate: The Major Factors That Influence Li Cycling Efficiency. *J. Electroanal. Chem.* **1992**, *339* (1–2), 451–471.
- (92) Zhuang, G. V.; Xu, K.; Yang, H.; Jow, T. R.; Ross, P. N. Lithium Ethylene Dicarboxylate Identified as the Primary Product of Chemical and Electrochemical Reduction of EC in 1.2 M LiPF<sub>6</sub>/EC:EMC Electrolyte. *J. Phys. Chem. B* **2005**, *109* (37), 17567–17573. <https://doi.org/10.1021/jp052474w>.

- (93) Xu, K.; Zhuang, G. V.; Allen, J. L.; Lee, U.; Zhang, S. S.; Ross, P. N.; Jow, T. R. Syntheses and Characterization of Lithium Alkyl Mono- and Dicarbonates as Components of Surface Films in Li-Ion Batteries. *J. Phys. Chem. B* **2006**, *110* (15), 7708–7719. <https://doi.org/10.1021/jp0601522>.
- (94) Nie, M.; Chalasani, D.; Abraham, D. P.; Chen, Y.; Bose, A.; Lucht, B. L. Lithium Ion Battery Graphite Solid Electrolyte Interphase Revealed by Microscopy and Spectroscopy. *J. Phys. Chem. C* **2013**, *117* (3), 1257–1267. <https://doi.org/10.1021/jp3118055>.
- (95) Wang, L.; Menakath, A.; Han, F.; Wang, Y.; Zavalij, P. Y.; Gaskell, K. J.; Borodin, O.; Iuga, D.; Brown, S. P.; Wang, C.; Xu, K.; Eichhorn, B. W. Identifying the Components of the Solid–Electrolyte Interphase in Li-Ion Batteries. *Nat. Chem.* **2019**, *11* (9), 789–796. <https://doi.org/10.1038/s41557-019-0304-z>.
- (96) Haregewoin, A. M.; Wotango, A. S.; Hwang, B.-J. Electrolyte Additives for Lithium Ion Battery Electrodes: Progress and Perspectives. *Energy Env. Sci* **2016**, *9* (6), 1955–1988. <https://doi.org/10.1039/C6EE00123H>.
- (97) Zhang, S. S. A Review on Electrolyte Additives for Lithium-Ion Batteries. *J. Power Sources* **2006**, *162* (2 SPEC. ISS.), 1379–1394. <https://doi.org/10.1016/j.jpowsour.2006.07.074>.
- (98) Qian, Y.; Hu, S.; Zou, X.; Deng, Z.; Xu, Y.; Cao, Z.; Kang, Y.; Deng, Y.; Shi, Q.; Xu, K.; Deng, Y. How Electrolyte Additives Work in Li-Ion Batteries. *Energy Storage Mater.* **2019**, *20* (September 2018), 208–215. <https://doi.org/10.1016/j.ensm.2018.11.015>.
- (99) Ming, J.; Cao, Z.; Wu, Y.; Wahyudi, W.; Wang, W.; Guo, X.; Cavallo, L.; Hwang, J.-Y.; Shamim, A.; Li, L.-J.; Sun, Y.-K.; Alshareef, H. N. New Insight on the Role of Electrolyte Additives in Rechargeable Lithium Ion Batteries. *ACS Energy Lett.* **2019**, *4* (11), 2613–2622. <https://doi.org/10.1021/acsenergylett.9b01441>.
- (100) Michan, A. L.; Parimalam, Bharathy. S.; Leskes, M.; Kerber, R. N.; Yoon, T.; Grey, C. P.; Lucht, B. L. Fluoroethylene Carbonate and Vinylene Carbonate Reduction: Understanding Lithium-Ion Battery Electrolyte Additives and Solid Electrolyte Interphase Formation. *Chem. Mater.* **2016**, *28* (22), 8149–8159. <https://doi.org/10.1021/acs.chemmater.6b02282>.

- (101) Schwenke, K. U.; Solchenbach, S.; Demeaux, J.; Lucht, B. L.; Gasteiger, H. A. The Impact of CO<sub>2</sub> Evolved from VC and FEC during Formation of Graphite Anodes in Lithium-Ion Batteries. *J. Electrochem. Soc.* **2019**, *166* (10), A2035–A2047. <https://doi.org/10.1149/2.0821910jes>.
- (102) Burns, J. C.; Petibon, R.; Nelson, K. J.; Sinha, N. N.; Kassam, A.; Way, B. M.; Dahn, J. R. Studies of the Effect of Varying Vinylene Carbonate (VC) Content in Lithium Ion Cells on Cycling Performance and Cell Impedance. *J. Electrochem. Soc.* **2013**, *160* (10), 1668–1674. <https://doi.org/10.1149/2.031310jes>.
- (103) Nie, M.; Demeaux, J.; Young, B. T.; Heskett, D. R.; Chen, Y.; Bose, A.; Woicik, J. C.; Lucht, B. L. Effect of Vinylene Carbonate and Fluoroethylene Carbonate on SEI Formation on Graphitic Anodes in Li-Ion Batteries. *J. Electrochem. Soc.* **2015**, *162* (13), A7008–A7014. <https://doi.org/10.1149/2.0021513jes>.
- (104) Zhao, W.; Zheng, G.; Lin, M.; Zhao, W.; Li, D.; Guan, X.; Ji, Y.; Ortiz, G. F.; Yang, Y. Toward a Stable Solid-Electrolyte-Interfaces on Nickel-Rich Cathodes: LiPO<sub>2</sub>F<sub>2</sub> Salt-Type Additive and Its Working Mechanism for LiNi<sub>0.5</sub>Mn<sub>0.25</sub>Co<sub>0.25</sub>O<sub>2</sub> Cathodes. *J. Power Sources* **2018**, *380*, 149–157. <https://doi.org/10.1016/j.jpowsour.2018.01.041>.
- (105) Ma, L.; Ellis, L.; Glazier, S. L.; Ma, X.; Liu, Q.; Li, J.; Dahn, J. R. LiPO<sub>2</sub>F<sub>2</sub> as an Electrolyte Additive in Li[Ni<sub>0.5</sub>Mn<sub>0.3</sub>Co<sub>0.2</sub>]O<sub>2</sub>/Graphite Pouch Cells. *J. Electrochem. Soc.* **2018**, *165* (5), A891–A899. <https://doi.org/10.1149/2.0381805jes>.
- (106) Ma, L.; Ellis, L.; Glazier, S. L.; Ma, X.; Dahn, J. R. Combinations of LiPO<sub>2</sub>F<sub>2</sub> and Other Electrolyte Additives in Li[Ni<sub>0.5</sub>Mn<sub>0.3</sub>Co<sub>0.2</sub>]O<sub>2</sub>/Graphite Pouch Cells. *J. Electrochem. Soc.* **2018**, *165* (9), A1718–A1724. <https://doi.org/10.1149/2.0661809jes>.
- (107) Ma, X.; Harlow, J. E.; Li, J.; Ma, L.; Hall, D. S.; Buteau, S.; Genovese, M.; Cormier, M.; Dahn, J. R. Hindering Rollover Failure of Li[Ni<sub>0.5</sub>Mn<sub>0.3</sub>Co<sub>0.2</sub>]O<sub>2</sub>/Graphite Pouch Cells during Long-Term Cycling. *J. Electrochem. Soc.* **2019**, *166* (4), A711–A724. <https://doi.org/10.1149/2.0801904jes>.

- (108) Harlow, J. E.; Ma, X.; Li, J.; Logan, E.; Liu, Y.; Zhang, N.; Ma, L.; Glazier, S. L.; Cormier, M. M. E.; Genovese, M.; Buteau, S.; Cameron, A.; Stark, J. E.; Dahn, J. R. A Wide Range of Testing Results on an Excellent Lithium-Ion Cell Chemistry to Be Used as Benchmarks for New Battery Technologies. *J. Electrochem. Soc.* **2019**, *166* (13), A3031–A3044. <https://doi.org/10.1149/2.0981913jes>.
- (109) Li, J.; Li, H.; Stone, W.; Glazier, S.; Dahn, J. R. Development of Electrolytes for Single Crystal NMC532/Artificial Graphite Cells with Long Lifetime. *J. Electrochem. Soc.* **2018**, *165* (3), A626–A635. <https://doi.org/10.1149/2.0971803jes>.
- (110) Xia, J.; Sinha, N. N.; Chen, L. P.; Dahn, J. R. A Comparative Study of a Family of Sulfate Electrolyte Additives. *J. Electrochem. Soc.* **2014**, *161* (3), A264–A274. <https://doi.org/10.1149/2.015403jes>.
- (111) Madec, L.; Xia, J.; Petibon, R.; Nelson, K. J.; Sun, J.-P.; Hill, I. G.; Dahn, J. R. Effect of Sulfate Electrolyte Additives on  $\text{LiNi}_{1/3}\text{Mn}_{1/3}\text{Co}_{1/3}\text{O}_2$ /Graphite Pouch Cell Lifetime: Correlation between XPS Surface Studies and Electrochemical Test Results. *J. Phys. Chem. C* **2014**, *118* (51), 29608–29622. <https://doi.org/10.1021/jp509731y>.
- (112) Aiken, C. P.; Harlow, J. E.; Tingley, R.; Hynes, T.; Logan, E. R.; Glazier, S. L.; Keefe, A. S.; Dahn, J. R. Accelerated Failure in  $\text{Li}[\text{Ni}_{0.5}\text{Mn}_{0.3}\text{Co}_{0.2}]\text{O}_2$  /Graphite Pouch Cells Due to Low  $\text{LiPF}_6$  Concentration and Extended Time at High Voltage. *J. Electrochem. Soc.* **2020**, *167* (13), 130541–130541. <https://doi.org/10.1149/1945-7111/abbe5b>.
- (113) Logan, E. R.; Tonita, E. M.; Gering, K. L.; Li, J.; Ma, X.; Beaulieu, L. Y.; Dahn, J. R. A Study of the Physical Properties of Li-Ion Battery Electrolytes Containing Esters. *J. Electrochem. Soc.* **2018**, *165* (2), A21–A30. <https://doi.org/10.1149/2.0271802jes>.
- (114) Smart, M. C.; Ratnakumar, B. V.; Surampudi, S. Use of Organic Esters as Cosolvents in Electrolytes for Lithium-Ion Batteries with Improved Low Temperature Performance. *J. Electrochem. Soc.* **2002**, *149* (4), A361. <https://doi.org/10.1149/1.1453407>.

- (115) Li, J.; Li, H.; Ma, X.; Stone, W.; Glazier, S.; Logan, E.; Tonita, E. M.; Gering, K. L.; Dahn, J. R. Methyl Acetate as a Co-Solvent in NMC532/Graphite Cells. *J. Electrochem. Soc.* **2018**, *165* (5), A1027–A1037. <https://doi.org/10.1149/2.0861805jes>.
- (116) Smart, M. C.; Ratnakumar, B. V.; Surampudi, S. Use of Organic Esters as Cosolvents in Electrolytes for Lithium-Ion Batteries with Improved Low Temperature Performance. *J. Electrochem. Soc.* **2002**, *149* (4), A361–A361. <https://doi.org/10.1149/1.1453407>.
- (117) Logan, E. R.; Tonita, E. M.; Gering, K. L.; Li, J.; Ma, X.; Beaulieu, L. Y.; Dahn, J. R. A Study of the Physical Properties of Li-Ion Battery Electrolytes Containing Esters. *J. Electrochem. Soc.* **2018**, *165* (2), A21–A30. <https://doi.org/10.1149/2.0271802jes>.
- (118) Ma, X.; Harlow, J. E.; Li, J.; Ma, L.; Hall, D. S.; Buteau, S.; Genovese, M.; Cormier, M.; Dahn, J. R. Hindering Rollover Failure of Li[Ni 0.5 Mn 0.3 Co 0.2 ]O 2 /Graphite Pouch Cells during Long-Term Cycling. *J. Electrochem. Soc.* **2019**, *166* (4), A711–A724. <https://doi.org/10.1149/2.0801904jes>.
- (119) Glazier, S. L. Isothermal Microcalorimetry As a Tool To Probe Parasitic Reactions in Lithium-Ion Cells, Dalhousie University, Halifax, NS, 2018.
- (120) Downie, L. E. THE APPLICATION OF ISOTHERMAL MICROCALORIMETRY TO THE STUDY OF PARASITIC REACTIONS IN LITHIUM ION BATTERIES, Dalhousie University, 2015.
- (121) Krause, L. J.; Jensen, L. D.; Dahn, J. R. Measurement of Parasitic Reactions in Li Ion Cells by Electrochemical Calorimetry. *J. Electrochem. Soc.* **2012**, *159* (7), A937–A943. <https://doi.org/10.1149/2.021207jes>.
- (122) Krause, L. J.; Jensen, L. D.; Chevrier, V. L. Measurement of Li-Ion Battery Electrolyte Stability by Electrochemical Calorimetry. *J. Electrochem. Soc.* **2017**, *164* (4), A889–A896. <https://doi.org/10.1149/2.1651704jes>.
- (123) Smith, A. J.; Burns, J. C.; Xiong, D.; Dahn, J. R. Interpreting High Precision Coulometry Results on Li-Ion Cells. *J. Electrochem. Soc.* **2011**, *158* (10), A1136–A1136. <https://doi.org/10.1149/1.3625232>.

- (124) Hardwick, L. J.; Marcinek, M.; Beer, L.; Kerr, J. B.; Kostecki, R. An Investigation of the Effect of Graphite Degradation on Irreversible Capacity in Lithium-Ion Cells. *J. Electrochem. Soc.* **2008**, *155* (6), A442. <https://doi.org/10.1149/1.2903882>.
- (125) Hall, D. S.; Allen, J. P.; Glazier, S. L.; Ellis, L. D.; Ma, L.; Peters, J. M.; Hill, I. G.; Dahn, J. R. The Solid-Electrolyte Interphase Formation Reactions of Ethylene Sulfate and Its Synergistic Chemistry with Prop-1-Ene-1,3-Sultone in Lithium-Ion Cells. *J. Electrochem. Soc.* **2017**, *164* (14), A3445–A3453. <https://doi.org/10.1149/2.0181714jes>.
- (126) Rinkel, B. L. D.; Hall, D. S.; Temprano, I.; Grey, C. P. Electrolyte Oxidation Pathways in Lithium-Ion Batteries. *J. Am. Chem. Soc.* **2020**, *142* (35), 15058–15074. <https://doi.org/10.1021/jacs.0c06363>.
- (127) Glazier, S. L.; Li, J.; Louli, A. J.; Allen, J. P.; Dahn, J. R. An Analysis of Artificial and Natural Graphite in Lithium Ion Pouch Cells Using Ultra-High Precision Coulometry, Isothermal Microcalorimetry, Gas Evolution, Long Term Cycling and Pressure Measurements. *J. Electrochem. Soc.* **2017**, *164* (14), A3545–A3555. <https://doi.org/10.1149/2.0421714jes>.
- (128) Smith, A. J.; Burns, J. C.; Zhao, X.; Xiong, D.; Dahn, J. R. A High Precision Coulometry Study of the SEI Growth in Li/Graphite Cells. *J. Electrochem. Soc.* **2011**, *158* (5), A447. <https://doi.org/10.1149/1.3557892>.
- (129) Lawless, K. R. The Oxidation of Metals. *Rep Prog Phys* **1974**, *37*, 231.
- (130) Broussely, M.; Herreyre, S.; Biensan, P.; Kasztejna, P.; Nechev, K.; Staniewicz, R. J. Aging Mechanism in Li Ion Cells and Calendar Life Predictions. *J. Power Sources* **2001**, *97–98*, 13–21. [https://doi.org/10.1016/S0378-7753\(01\)00722-4](https://doi.org/10.1016/S0378-7753(01)00722-4).
- (131) Christensen, J.; Newman, J. A Mathematical Model for the Lithium-Ion Negative Electrode Solid Electrolyte Interphase. *J. Electrochem. Soc.* **2004**, *151* (11), A1977. <https://doi.org/10.1149/1.1804812>.
- (132) Attia, P. M.; Chueh, W. C.; Harris, S. J. Revisiting the  $t^{0.5}$  Dependence of SEI Growth. *J. Electrochem. Soc.* **2020**, *167* (9), 090535. <https://doi.org/10.1149/1945-7111/ab8ce4>.

- (133) Keil, P.; Jossen, A. Calendar Aging of NCA Lithium-Ion Batteries Investigated by Differential Voltage Analysis and Coulomb Tracking. *J. Electrochem. Soc.* **2017**, *164* (1), A6066–A6074. <https://doi.org/10.1149/2.0091701jes>.
- (134) Dahn, H. M.; Smith, A. J.; Burns, J. C.; Stevens, D. A.; Dahn, J. R. User-Friendly Differential Voltage Analysis Freeware for the Analysis of Degradation Mechanisms in Li-Ion Batteries. *J. Electrochem. Soc.* **2012**, *159* (9), A1405–A1409. <https://doi.org/10.1149/2.013209jes>.
- (135) Bloom, I.; Christophersen, J. P.; Abraham, D. P.; Gering, K. L. Differential Voltage Analyses of High-Power Lithium-Ion Cells. *J. Power Sources* **2006**, *157* (1), 537–542. <https://doi.org/10.1016/j.jpowsour.2005.07.054>.
- (136) Sahore, R.; Dogan, F.; Bloom, I. D. Identification of Electrolyte-Soluble Organic Cross-Talk Species in a Lithium-Ion Battery via a Two-Compartment Cell. *Chem. Mater.* **2019**, *31* (8), 2884–2891. <https://doi.org/10.1021/acs.chemmater.9b00063>.
- (137) Bernhard, R.; Metzger, M.; Gasteiger, H. A. Gas Evolution at Graphite Anodes Depending on Electrolyte Water Content and SEI Quality Studied by On-Line Electrochemical Mass Spectrometry. *J. Electrochem. Soc.* **2015**, *162* (10), A1984–A1989. <https://doi.org/10.1149/2.0191510jes>.
- (138) Jung, R.; Metzger, M.; Maglia, F.; Stinner, C.; Gasteiger, H. A. Oxygen Release and Its Effect on the Cycling Stability of  $\text{LiNi}_x\text{Mn}_y\text{Co}_z\text{O}_2$ (NMC) Cathode Materials for Li-Ion Batteries. *J. Electrochem. Soc.* **2017**, *164* (7), A1361–A1377. <https://doi.org/10.1149/2.0021707jes>.
- (139) Glazier, S. L.; Li, J.; Ma, X.; Ellis, L. D.; Allen, J. P.; Gering, K. L.; Dahn, J. R. The Effect of Methyl Acetate, Ethylene Sulfate, and Carbonate Blends on the Parasitic Heat Flow of NMC532/Graphite Lithium Ion Pouch Cells. *J. Electrochem. Soc.* **2018**, *165* (5), A867–A875. <https://doi.org/10.1149/2.0451805jes>.
- (140) Jung, R.; Metzger, M.; Maglia, F.; Stinner, C.; Gasteiger, H. A. Chemical versus Electrochemical Electrolyte Oxidation on NMC111, NMC622, NMC811, LNMO, and Conductive Carbon. *J. Phys. Chem. Lett.* **2017**, *8* (19), 4820–4825. <https://doi.org/10.1021/acs.jpcelett.7b01927>.



- (141) Yamada, A.; Chung, S. C.; Hinokuma, K. Optimized LiFePO<sub>4</sub> for Lithium Battery Cathodes. *J. Electrochem. Soc.* **2001**, *148* (3), A224–A224. <https://doi.org/10.1149/1.1348257>.
- (142) Khakani, S. E.; Rochefort, D.; MacNeil, D. D. ARC Study of LiFePO<sub>4</sub> with Different Morphologies Prepared via Three Synthetic Routes. *J. Electrochem. Soc.* **2016**, *163* (7), A1311–A1316. <https://doi.org/10.1149/2.0801607jes>.
- (143) Zaghib, K.; Dubé, J.; Dallaire, A.; Galoustov, K.; Guerfi, A.; Ramanathan, M.; Benmayza, A.; Prakash, J.; Mauger, A.; Julien, C. M. Enhanced Thermal Safety and High Power Performance of Carbon-Coated LiFePO<sub>4</sub> Olivine Cathode for Li-Ion Batteries. *J. Power Sources* **2012**, *219*, 36–44. <https://doi.org/10.1016/j.jpowsour.2012.05.018>.
- (144) Xiong, D. J.; Ellis, L. D.; Petibon, R.; Hynes, T.; Liu, Q. Q.; Dahn, J. R. Studies of Gas Generation, Gas Consumption and Impedance Growth in Li-Ion Cells with Carbonate or Fluorinated Electrolytes Using the Pouch Bag Method. *J. Electrochem. Soc.* **2017**, *164* (2), A340–A347. <https://doi.org/10.1149/2.1091702jes>.
- (145) Ellis, L. D.; Allen, J. P.; Thompson, L. M.; Harlow, J. E.; Stone, W. J.; Hill, I. G.; Dahn, J. R. Quantifying, Understanding and Evaluating the Effects of Gas Consumption in Lithium-Ion Cells. *J. Electrochem. Soc.* **2017**, *164* (14), A3518–A3528. <https://doi.org/10.1149/2.0191714jes>.
- (146) Betz, J.; Brinkmann, J. P.; Nölle, R.; Lürenbaum, C.; Kolek, M.; Stan, M. C.; Winter, M.; Placke, T. Cross Talk between Transition Metal Cathode and Li Metal Anode: Unraveling Its Influence on the Deposition/Dissolution Behavior and Morphology of Lithium. *Adv. Energy Mater.* **2019**, *9* (21), 1–10. <https://doi.org/10.1002/aenm.201900574>.
- (147) Buhrmester, C.; Moshurchak, L. M.; Wang, R. L.; Dahn, J. R. The Use of 2,2,6,6-Tetramethylpiperinyl-Oxides and Derivatives for Redox Shuttle Additives in Li-Ion Cells. *J. Electrochem. Soc.* **2006**, *153* (10), A1800. <https://doi.org/10.1149/1.2221860>.
- (148) Buhrmester, C.; Chen, J.; Moshurchak, L.; Jiang, J.; Wang, R. L.; Dahn, J. R. Studies of Aromatic Redox Shuttle Additives for LiFePO<sub>4</sub>-Based Li-Ion Cells. *J. Electrochem. Soc.* **2005**, *152*, A2390.

- (149) Pan, F.; Wang, Q. Redox Species of Redox Flow Batteries: A Review. *Molecules* **2015**, *20* (11), 20499–20517. <https://doi.org/10.3390/molecules201119711>.
- (150) Winsberg, J.; Hagemann, T.; Janoschka, T.; Hager, M. D.; Schubert, U. S. Redox-Flow Batteries: From Metals to Organic Redox-Active Materials. *Angew. Chem. Int. Ed.* **2017**, *56* (3), 686–711. <https://doi.org/10.1002/anie.201604925>.
- (151) Harris, O. C.; Lee, S. E.; Lees, C.; Tang, M. Review: Mechanisms and Consequences of Chemical Cross-Talk in Advanced Li-Ion Batteries. *J. Phys. Energy* **2020**, *2* (3), 032002–032002. <https://doi.org/10.1088/2515-7655/ab8b68>.
- (152) Joshi, T.; Eom, K.; Yushin, G.; Fuller, T. F. Effects of Dissolved Transition Metals on the Electrochemical Performance and SEI Growth in Lithium-Ion Batteries. *J. Electrochem. Soc.* **2014**, *161* (12), A1915–A1921. <https://doi.org/10.1149/2.0861412jes>.
- (153) Zhan, C.; Wu, T.; Lu, J.; Amine, K. Dissolution, Migration, and Deposition of Transition Metal Ions in Li-Ion Batteries Exemplified by Mn-Based Cathodes-A Critical Review. *Energy Environ. Sci.* **2018**, *11* (2), 243–257. <https://doi.org/10.1039/c7ee03122j>.
- (154) Blyr, A.; Pasquier, A. D.; Amatucci, G.; Tarascon, J.-M. Origin of Self-Discharge Mechanism in LiMn<sub>2</sub>O<sub>4</sub>-Based Li-Ion Cells: A Chemical and Electrochemical Approach. *Ionics* **1997**, *3*, 321–331.
- (155) Amatucci, G. G.; Schmutz, C. N.; Blyr, A.; Sigala, C.; Gozdz, A. S.; Larcher, D.; Tarascon, J. M. Materials' Effects on the Elevated and Room Temperature Performance of C/LiMn<sub>2</sub>O<sub>4</sub> Li-Ion Batteries. *J. Power Sources* **1997**, *69*, 11–25.
- (156) Sahore, R.; O'Hanlon, D. C.; Tornheim, A.; Lee, C.-W.; Garcia, J. C.; Iddir, H.; Balasubramanian, M.; Bloom, I. Revisiting the Mechanism Behind Transition-Metal Dissolution from Delithiated LiNi<sub>x</sub>Mn<sub>y</sub>Co<sub>z</sub>O<sub>2</sub>(NMC) Cathodes. *J. Electrochem. Soc.* **2020**, *167* (2), 020513–020513. <https://doi.org/10.1149/1945-7111/ab6826>.
- (157) Koltypin, M.; Aurbach, D.; Nazar, L.; Ellis, B. On the Stability of LiFePO<sub>4</sub> Olivine Cathodes under Various Conditions (Electrolyte Solutions, Temperatures). *Electrochem. Solid-State Lett.* **2007**, *10* (2), 40–44. <https://doi.org/10.1149/1.2403974>.

- (158) Amine, K.; Liu, J.; Belharouak, I. High-Temperature Storage and Cycling of C-LiFePO<sub>4</sub>/Graphite Li-Ion Cells. *Electrochem. Commun.* **2005**, *7* (7), 669–673. <https://doi.org/10.1016/j.elecom.2005.04.018>.
- (159) Gallus, D. R.; Schmitz, R.; Wagner, R.; Hoffmann, B.; Nowak, S.; Cekic-Laskovic, I.; Schmitz, R. W.; Winter, M. The Influence of Different Conducting Salts on the Metal Dissolution and Capacity Fading of NCM Cathode Material. *Electrochimica Acta* **2014**, *134*, 393–398. <https://doi.org/10.1016/j.electacta.2014.04.091>.
- (160) Jung, R.; Linsenmann, F.; Thomas, R.; Wandt, J.; Solchenbach, S.; Maglia, F.; Stinner, C.; Tromp, M.; Gasteiger, H. A. Nickel, Manganese, and Cobalt Dissolution from Ni-Rich NMC and Their Effects on NMC622-Graphite Cells. *J. Electrochem. Soc.* **2019**, *166* (2), A378–A389. <https://doi.org/10.1149/2.1151902jes>.
- (161) Li, D.; Danilov, D.; Gao, L.; Yang, Y.; Notten, P. H. L. Degradation Mechanisms of C<sub>6</sub>/LiFePO<sub>4</sub> Batteries: Experimental Analyses of Cycling-Induced Aging. *Electrochimica Acta* **2016**, *210*, 445–455. <https://doi.org/10.1016/j.electacta.2016.05.091>.
- (162) Solchenbach, S.; Hong, G.; Freiberg, A. T. S.; Jung, R.; Gasteiger, H. A. Electrolyte and SEI Decomposition Reactions of Transition Metal Ions Investigated by On-Line Electrochemical Mass Spectrometry. *J. Electrochem. Soc.* **2018**, *165* (14), A3304–A3312. <https://doi.org/10.1149/2.0511814jes>.
- (163) Kassem, M.; Delacourt, C. Postmortem Analysis of Calendar-Aged Graphite/LiFePO<sub>4</sub> Cells. *J. Power Sources* **2013**, *235*, 159–171. <https://doi.org/10.1016/j.jpowsour.2013.01.147>.
- (164) Wu, H.; Su, C.; Shieh, D.; Yang, M. Enhanced High-Temperature Cycle Life of LiFePO<sub>4</sub> -Based Li-Ion Batteries by Vinylene Carbonate as Electrolyte Additive. *Electrochem. Solid-State Lett.* **2006**, 537–541. <https://doi.org/10.1149/1.2351954>.
- (165) Thompson, L. M.; Stone, W.; Eldesoky, A.; Smith, N. K.; McFarlane, C. R. M.; Kim, J. S.; Johnson, M. B.; Petibon, R.; Dahn, J. R. Quantifying Changes to the Electrolyte and Negative Electrode in Aged NMC532/Graphite Lithium-Ion Cells. *J. Electrochem. Soc.* **2018**, *165* (11), A2732–A2740. <https://doi.org/10.1149/2.0721811jes>.

- (166) Thompson, L. M.; Harlow, J. E.; Eldesoky, A.; Bauer, M. K. G.; Cheng, J. H.; Stone, W. S.; Taskovic, T.; McFarlane, C. R. M.; Dahn, J. R. Study of Electrolyte and Electrode Composition Changes vs Time in Aged Li-Ion Cells. *J. Electrochem. Soc.* **2021**, *168* (2), 020532–020532. <https://doi.org/10.1149/1945-7111/abe1da>.
- (167) Nelson, K. J.; d'Eon, G. L.; Wright, A. T. B.; Ma, L.; Xia, J.; Dahn, J. R. Studies of the Effect of High Voltage on the Impedance and Cycling Performance of Li[Ni<sub>0.4</sub>Mn<sub>0.4</sub>Co<sub>0.2</sub>]O<sub>2</sub>/Graphite Lithium-Ion Pouch Cells. *J. Electrochem. Soc.* **2015**, *162* (6), A1046–A1054. <https://doi.org/10.1149/2.0831506jes>.
- (168) Burns, J. C.; Sinha, N. N.; Jain, Gaurav.; Ye, Hui.; VanElzen, C. M.; Lamanna, W. M.; Xiao, A.; Scott, Erik.; Choi, J.; Dahn, J. R. Impedance Reducing Additives and Their Effect on Cell Performance: II. C<sub>3</sub>H<sub>9</sub>B<sub>3</sub>O<sub>6</sub>. *J. Electrochem. Soc.* **2012**, *159* (7), A1105–A1113. <https://doi.org/10.1149/2.078207jes>.
- (169) Weber, R.; Louli, A. J.; Plucknett, K. P.; Dahn, J. R. Resistance Growth in Lithium-Ion Pouch Cells with LiNi<sub>0.80</sub>Co<sub>0.15</sub>Al<sub>0.05</sub>O<sub>2</sub> Positive Electrodes and Proposed Mechanism for Voltage Dependent Charge-Transfer Resistance. *J. Electrochem. Soc.* **2019**, *166* (10), A1779–A1784. <https://doi.org/10.1149/2.0361910jes>.
- (170) Lee, R.-C.; Franklin, J.; Tian, C.; Nordlund, D.; Doeff, M.; Kostecki, R. The Origin of Impedance Rise in Ni-Rich Positive Electrodes for Lithium-Ion Batteries. *J. Power Sources* **2021**, *498*, 229885. <https://doi.org/10.1016/j.jpowsour.2021.229885>.
- (171) Jung, S.-K.; Gwon, H.; Hong, J.; Park, K.-Y.; Seo, D.-H.; Kim, H.; Hyun, J.; Yang, W.; Kang, K. Understanding the Degradation Mechanisms of LiNi<sub>0.5</sub>Co<sub>0.2</sub>Mn<sub>0.3</sub>O<sub>2</sub> Cathode Material in Lithium Ion Batteries. *Adv. Energy Mater.* **2014**, *4* (1), 1300787. <https://doi.org/10.1002/aenm.201300787>.
- (172) Müller, S.; Pietsch, P.; Brandt, B.-E.; Baade, P.; De Andrade, V.; De Carlo, F.; Wood, V. Quantification and Modeling of Mechanical Degradation in Lithium-Ion Batteries Based on Nanoscale Imaging. *Nat. Commun.* **2018**, *9* (1), 2340. <https://doi.org/10.1038/s41467-018-04477-1>.

- (173) Grillet, A. M.; Humplik, T.; Stirrup, E. K.; Roberts, S. A.; Barringer, D. A.; Snyder, C. M.; Janvrin, M. R.; Apblett, C. A. Conductivity Degradation of Polyvinylidene Fluoride Composite Binder during Cycling: Measurements and Simulations for Lithium-Ion Batteries. *J. Electrochem. Soc.* **2016**, *163* (9), A1859–A1871. <https://doi.org/10.1149/2.0341609jes>.
- (174) Kabir, M. M.; Demirocak, D. E. Degradation Mechanisms in Li-Ion Batteries: A State-of-the-Art Review: Degradation Mechanisms in Li-Ion Batteries: A State-of-the-Art Review. *Int. J. Energy Res.* **2017**, *41* (14), 1963–1986. <https://doi.org/10.1002/er.3762>.
- (175) Demirocak, D. E.; Bhushan, B. Probing the Aging Effects on Nanomechanical Properties of a LiFePO<sub>4</sub> Cathode in a Large Format Prismatic Cell. *J. Power Sources* **2015**, *280*, 256–262. <https://doi.org/10.1016/j.jpowsour.2015.01.114>.
- (176) A. Stamps, M.; W. Eischen, J.; Shadow Huang, H.-Y. Particle- and Crack-Size Dependency of Lithium-Ion Battery Materials LiFePO<sub>4</sub>. *AIMS Mater. Sci.* **2016**, *3* (1), 190–203. <https://doi.org/10.3934/matensci.2016.1.190>.
- (177) Santos, D. A.; Andrews, J. L.; Bai, Y.; Stein, P.; Luo, Y.; Zhang, Y.; Pharr, M.; Xu, B.-X.; Banerjee, S. Bending Good Beats Breaking Bad: Phase Separation Patterns in Individual Cathode Particles upon Lithiation and Delithiation. *Mater. Horiz.* **2020**, *7* (12), 3275–3290. <https://doi.org/10.1039/D0MH01240H>.
- (178) Louli, A. J.; Ellis, L. D.; Dahn, J. R. Operando Pressure Measurements Reveal Solid Electrolyte Interphase Growth to Rank Li-Ion Cell Performance. *Joule* **2019**, *3* (3), 745–761. <https://doi.org/10.1016/j.joule.2018.12.009>.
- (179) Kolzenberg, L.; Latz, A.; Horstmann, B. Chemo-Mechanical Model of SEI Growth on Silicon Electrode Particles. *Batter. Supercaps* **2022**, *5* (2). <https://doi.org/10.1002/batt.202100216>.
- (180) Lin, D.; Liu, Y.; Cui, Y. Reviving the Lithium Metal Anode for High-Energy Batteries. *Nat. Nanotechnol.* **2017**, *12* (3), 194–206. <https://doi.org/10.1038/nnano.2017.16>.
- (181) Brissot, C.; Rosso, M.; Chazalviel, J.-N.; Lascaud, S. Dendritic Growth Mechanisms in Lithiumpolymer Cells. *J. Power Sources* **1999**, *81–82*, 925–929.

- (182) Fang, C.; Li, J.; Zhang, M.; Zhang, Y.; Yang, F.; Lee, J. Z.; Lee, M. H.; Alvarado, J.; Schroeder, M. A.; Yang, Y.; Lu, B.; Williams, N.; Ceja, M.; Yang, L.; Cai, M.; Gu, J.; Xu, K.; Wang, X.; Meng, Y. S. Quantifying Inactive Lithium in Lithium Metal Batteries. *Nature* **2019**, *572* (7770), 511–515. <https://doi.org/10.1038/s41586-019-1481-z>.
- (183) Aurbach, D.; Zinigrad, E.; Cohen, Y.; Teller, H. A Short Review of Failure Mechanisms of Lithium Metal and Lithiated Graphite Anodes in Liquid Electrolyte Solutions. *Solid State Ion.* **2002**, *148* (3–4), 405–416. [https://doi.org/10.1016/S0167-2738\(02\)00080-2](https://doi.org/10.1016/S0167-2738(02)00080-2).
- (184) Ng, B.; Coman, P. T.; Faegh, E.; Peng, X.; Karakalos, S. G.; Jin, X.; Mustain, W. E.; White, R. E. Low-Temperature Lithium Plating/Corrosion Hazard in Lithium-Ion Batteries: Electrode Rippling, Variable States of Charge, and Thermal and Nonthermal Runaway. *ACS Appl. Energy Mater.* **2020**. <https://doi.org/10.1021/acsaem.0c00130>.
- (185) Liu, Q.; Petibon, R.; Du, C. Y.; Dahn, J. R. Effects of Electrolyte Additives and Solvents on Unwanted Lithium Plating in Lithium-Ion Cells. *J. Electrochem. Soc.* **2017**, *164* (6), A1173–A1173. <https://doi.org/10.1149/1.3544439>.
- (186) Dahn, J. R.; McKinnon, W. R.; Murray, J. J.; Haering, R. R.; McMillan, R. S.; Rivers-Bowerman, A. H. Entropy of the Intercalation Compound  $\text{Li}_x\text{Mo}_6\text{Se}_8$  from Calorimetry of Electrochemical Cells. *Phys. Rev. B* **1985**, *32* (5), 3316–3318.
- (187) McKinnon, W. R.; Dahn, J. R.; Murray, J. J.; Haering, R. R.; McMillan, R. S.; Rivers-Bowerman, A. H. Entropy of Intercalation Compounds: ii. Calorimetry of Electrochemical Cells of the Chevrel Compound  $\text{Li}_x\text{Mo}_6\text{Se}_8$  for  $0 \leq x \leq 4$ . *J. Phys. C Solid State Phys.* **1986**, *19* (26), 5135–5148. <https://doi.org/10.1088/0022-3719/19/26/013>.
- (188) Saito, Y.; Kanari, K.; Takano, K.; Masuda, T. A Calorimetric Study on a Cylindrical Type Lithium Secondary Battery by Using a Twin-Type Heat Conduction Calorimeter. *Thermochim. Acta* **1997**, *296* (1–2), 75–85. [https://doi.org/10.1016/s0040-6031\(97\)00083-x](https://doi.org/10.1016/s0040-6031(97)00083-x).

- (189) Saito, Y.; Takano, K.; Kanari, K.; Negishi, A.; Nozaki, K.; Kato, K. Comparative Study of Thermal Behaviors of Various Lithium-Ion Cells. *J. Power Sources* **2001**, *97–98*, 688–692. [https://doi.org/10.1016/S0378-7753\(01\)00702-9](https://doi.org/10.1016/S0378-7753(01)00702-9).
- (190) Kobayashi, Y.; Kihira, N.; Takei, K.; Miyashiro, H.; Kumai, K.; Terada, N.; Ishikawa, R. Electrochemical and Calorimetric Approach to Spinel Lithium Manganese Oxide. *J. Power Sources* **1999**, *81–82*, 463–466. [https://doi.org/10.1016/S0378-7753\(99\)00203-7](https://doi.org/10.1016/S0378-7753(99)00203-7).
- (191) Kobayashi, Y.; Miyashiro, H.; Kumai, K.; Takei, K.; Iwahori, T.; Uchida, I. Precise Electrochemical Calorimetry of LiCoO<sub>2</sub>/Graphite Lithium-Ion Cell. *J. Electrochem. Soc.* **2002**, *149* (8), A978. <https://doi.org/10.1149/1.1487833>.
- (192) Krause, L. J.; Jensen, L. D.; Dahn, J. R. Measurement of Parasitic Reactions in Li Ion Cells by Electrochemical Calorimetry. *J. Electrochem. Soc.* **2012**, *159* (7), A937–A943. <https://doi.org/10.1149/2.021207jes>.
- (193) Chevrier, V. L.; Liu, L.; Le, D. B.; Lund, J.; Molla, B.; Reimer, K.; Krause, L. J.; Jensen, L. D.; Figgemeier, E.; Eberman, K. W. Evaluating Si-Based Materials for Li-Ion Batteries in Commercially Relevant Negative Electrodes. *J. Electrochem. Soc.* **2014**, *161* (5), A783–A791. <https://doi.org/10.1149/2.066405jes>.
- (194) Chevrier, V. L.; Yan, Z.; Glazier, S. L.; Obrovac, M. N.; Krause, L. J. Isothermal Calorimetry Evaluation of Metallurgical Silicon as a Negative Electrode Material for Li-Ion Batteries. *J. Electrochem. Soc.* **2021**, *168* (3), 030504–030504. <https://doi.org/10.1149/1945-7111/abe16a>.
- (195) Glazier, S. L. Isothermal Microcalorimetry As a Tool To Probe Parasitic Reactions in Lithium-Ion Cells, Dalhousie University, 2018.
- (196) Downie, L. E.; Dahn, J. R. Determination of the Voltage Dependence of Parasitic Heat Flow in Lithium Ion Cells Using Isothermal Microcalorimetry. *J. Electrochem. Soc.* **2014**, *161* (12), A1782–A1787. <https://doi.org/10.1149/2.0301412jes>.
- (197) Downie, L. E.; Hyatt, S. R.; Wright, A. T. B.; Dahn, J. R. Determination of the Time Dependent Parasitic Heat Flow in Lithium Ion Cells Using Isothermal Microcalorimetry. *J. Phys. Chem. C* **2014**, *118* (51), 29533–29541. <https://doi.org/10.1021/jp508912z>.

- (198) Downie, L. E.; Hyatt, S. R.; Dahn, J. R. The Impact of Electrolyte Composition on Parasitic Reactions in Lithium Ion Cells Charged to 4.7 V Determined Using Isothermal Microcalorimetry. *J. Electrochem. Soc.* **2016**, *163* (2), A35–A42. <https://doi.org/10.1149/2.0081602jes>.
- (199) Glazier, S. L.; Nelson, K. J.; Allen, J. P.; Li, J.; Dahn, J. R. The Effect of Different Li(Ni<sub>1-x-y</sub>Mn<sub>x</sub>Co<sub>y</sub>)O<sub>2</sub> Positive Electrode Materials and Coatings on Parasitic Heat Flow as Measured by Isothermal Microcalorimetry, Ultra-High Precision Coulometry and Long Term Cycli. *J. Electrochem. Soc.* **2017**, *164* (6), A1203–A1212. <https://doi.org/10.1149/2.1121706jes>.
- (200) Glazier, S. L.; Petibon, R.; Xia, J.; Dahn, J. R. Measuring the Parasitic Heat Flow of Lithium Ion Pouch Cells Containing EC-Free Electrolytes. *J. Electrochem. Soc.* **2017**, *164* (4), A567–A573. <https://doi.org/10.1149/2.0331704jes>.
- (201) Glazier, S. L.; Li, J.; Ma, X.; Ellis, L. D.; Allen, J. P.; Gering, K. L.; Dahn, J. R. The Effect of Methyl Acetate, Ethylene Sulfate, and Carbonate Blends on the Parasitic Heat Flow of NMC532/Graphite Lithium Ion Pouch Cells. *J. Electrochem. Soc.* **2018**, *165* (5), A867–A875. <https://doi.org/10.1149/2.0451805jes>.
- (202) Logan, E.; Hebecker, H.; Ma, X.; Quinn, J. B.; HyeJeong, Y.; Kumakura, S.; Paulsen, J.; Dahn, J. R. A Comparison of the Performance of Different Morphologies of LiNi<sub>0.8</sub>Mn<sub>0.1</sub>Co<sub>0.1</sub>O<sub>2</sub> Using Isothermal Microcalorimetry, Ultra-High Precision Coulometry, and Long-Term Cycling. *J. Electrochem. Soc.* **2020**. <https://doi.org/10.1149/1945-7111/ab8620>.
- (203) Smith, A. J.; Burns, J. C.; Trussler, S.; Dahn, J. R. Precision Measurements of the Coulombic Efficiency of Lithium-Ion Batteries and of Electrode Materials for Lithium-Ion Batteries. *J. Electrochem. Soc.* **2010**, *157* (2), A196–A196. <https://doi.org/10.1149/1.3268129>.
- (204) Bond, T. M.; Burns, J. C.; Stevens, D. A.; Dahn, H. M.; Dahn, J. R. Improving Precision and Accuracy in Coulombic Efficiency Measurements of Li-Ion Batteries. *J. Electrochem. Soc.* **2013**, *160* (3), A521–A527. <https://doi.org/10.1149/2.014304jes>.
- (205) Novonix. *Ultra-High Precision Coulometry*. <https://www.novonixgroup.com/bts-ultra-high-precision-coulometry/> (accessed 2022-03-01).



- (206) Ellis, L. D.; Allen, J. P.; Hill, I. G.; Dahn, J. R. High-Precision Coulometry Studies of the Impact of Temperature and Time on SEI Formation in Li-Ion Cells. *J. Electrochem. Soc.* **2018**, *165* (7), A1529–A1536. <https://doi.org/10.1149/2.1091807jes>.
- (207) Sinha, N. N.; Smith, A. J.; Burns, J. C.; Jain, G.; Eberman, K. W.; Scott, E.; Gardner, J. P.; Dahn, J. R. The Use of Elevated Temperature Storage Experiments to Learn about Parasitic Reactions in Wound LiCoO<sub>2</sub>/Graphite Cells. *J. Electrochem. Soc.* **2011**, *158* (11), A1194–A1194. <https://doi.org/10.1149/2.007111jes>.
- (208) Fischer, K. Neues Verfahren Zur Maßanalytischen Bestimmung Des Wassergehaltes von Flüssigkeiten Und Festen Körpern. *Angew. Chem.* **1935**, *48* (26), 394–396.
- (209) Karl Fischer Coulometer C20/C30 Operating Instructions.
- (210) MacLeod, S. K. Moisture Determination Using Karl Fischer Titrations. *Anal. Chem.* **1991**, *63* (10), 557A–566A. <https://doi.org/10.1021/ac00010a001>.
- (211) Liu, Q. Q.; Ma, L.; Du, C. Y.; Dahn, J. R. Effects of the LiPO<sub>2</sub>F<sub>2</sub> Additive on Unwanted Lithium Plating in Lithium-Ion Cells. *Electrochimica Acta* **2018**, *263*, 237–248. <https://doi.org/10.1016/j.electacta.2018.01.058>.
- (212) Buteau, S.; Dahn, J. R. Analysis of Thousands of Electrochemical Impedance Spectra of Lithium-Ion Cells through a Machine Learning Inverse Model. *J. Electrochem. Soc.* **2019**, *166* (8), A1611–A1622. <https://doi.org/10.1149/2.1051908jes>.
- (213) Meddings, N.; Heinrich, M.; Overney, F.; Lee, J.-S.; Ruiz, V.; Napolitano, E.; Seitz, S.; Hinds, G.; Raccichini, R.; Gaberšček, M.; Park, J. Application of Electrochemical Impedance Spectroscopy to Commercial Li-Ion Cells: A Review. *J. Power Sources* **2020**, *480*, 228742. <https://doi.org/10.1016/j.jpowsour.2020.228742>.
- (214) Eldesoky, A.; Logan, E.; Johnson, M.; McFarlane, C.; Dahn, J. R. Scanning Micro X-Ray Fluorescence (MXRF) as an Effective Tool in Quantifying Fe Dissolution in LiFePO<sub>4</sub> Cells: Towards a Mechanistic Understanding of Fe Dissolution. *J. Electrochem. Soc.* **2020**. <https://doi.org/10.1149/1945-7111/abba62>.

- (215) Xiong, D. J.; Petibon, R.; Nie, M.; Ma, L.; Xia, J.; Dahn, J. R. Interactions between Positive and Negative Electrodes in Li-Ion Cells Operated at High Temperature and High Voltage. *J. Electrochem. Soc.* **2016**, *163* (3), A546–A551. <https://doi.org/10.1149/2.0951603jes>.
- (216) Bak, H. J. Thermal Characterization of Liquid Samples with Three-Dimensional On-Chip Micro Calorimeter, Marquette University, 2014.
- (217) TA Instruments. TAM: Thermal Activity Monitor: Basic Theory & Applications Training, 2015.
- (218) Safari, M.; Delacourt, C. Aging of a Commercial Graphite/LiFePO<sub>4</sub> Cell. *J. Electrochem. Soc.* **2011**, *158* (10). <https://doi.org/10.1149/1.3614529>.
- (219) Gandiaga, I.; Villarreal, I. Calendar Ageing Analysis of a LiFePO<sub>4</sub> / Graphite Cell with Dynamic Model Validations : Towards Realistic Lifetime Predictions. *J. Power Sources* **2014**, *272*, 45–57. <https://doi.org/10.1016/j.jpowsour.2014.08.051>.
- (220) Grolleau, S.; Delaille, A.; Gualous, H.; Gyan, P.; Revel, R.; Bernard, J.; Redondo-Iglesias, E.; Peter, J. Calendar Aging of Commercial Graphite/LiFePO<sub>4</sub> Cell - Predicting Capacity Fade under Time Dependent Storage Conditions. *J. Power Sources* **2014**, *255*, 450–458. <https://doi.org/10.1016/j.jpowsour.2013.11.098>.
- (221) Guo, Z.; Chen, Z. High-Temperature Capacity Fading Mechanism for LiFePO<sub>4</sub>/Graphite Soft-Packed Cell without Fe Dissolution. *J. Electroanal. Chem.* **2015**, *754*, 148–153. <https://doi.org/10.1016/j.jelechem.2015.07.009>.
- (222) Kassem, M.; Delacourt, C. Postmortem Analysis of Calendar-Aged Graphite/LiFePO<sub>4</sub> Cells. *J. Power Sources* **2013**, *235*, 159–171. <https://doi.org/10.1016/j.jpowsour.2013.01.147>.
- (223) Naumann, M.; Schimpe, M.; Keil, P.; Hesse, H. C.; Jossen, A. Analysis and Modeling of Calendar Aging of a Commercial LiFePO<sub>4</sub>/Graphite Cell. *J. Energy Storage* **2018**, *17*, 153–169. <https://doi.org/10.1016/j.est.2018.01.019>.
- (224) Paul, N.; Wandt, J.; Seidlmayer, S.; Schebesta, S.; Mühlbauer, M. J.; Dolotko, O.; Gasteiger, H. A.; Gilles, R. Aging Behavior of Lithium Iron Phosphate Based 18650-Type Cells Studied by in Situ Neutron Diffraction. *J. Power Sources* **2017**, *345*, 85–96. <https://doi.org/10.1016/j.jpowsour.2017.01.134>.

- (225) Song, H.; Cao, Z.; Chen, X.; Lu, H. Capacity Fade of LiFePO<sub>4</sub> / Graphite Cell at Elevated Temperature. *J. Solid State Electrochem.* **2013**, 599–605. <https://doi.org/10.1007/s10008-012-1893-2>.
- (226) Li, D.; Danilov, D. L.; Gao, L.; Yang, Y.; Notten, P. H. L. Degradation Mechanisms of the Graphite Electrode in C<sub>6</sub>/LiFePO<sub>4</sub> Batteries Unraveled by a Non-Destructive Approach. *J. Electrochem. Soc.* **2016**, 163 (14), A3016–A3021. <https://doi.org/10.1149/2.0821614jes>.
- (227) Amine, K.; Liu, J.; Belharouak, I. High-Temperature Storage and Cycling of C-LiFePO<sub>4</sub>/Graphite Li-Ion Cells. *Electrochem. Commun.* **2005**, 7 (7), 669–673. <https://doi.org/10.1016/j.elecom.2005.04.018>.
- (228) Li, D.; Danilov, D.; Gao, L.; Yang, Y.; Notten, P. H. L. Degradation Mechanisms of C<sub>6</sub> /LiFePO<sub>4</sub> Batteries: Experimental Analyses of Cycling-Induced Aging. *Electrochimica Acta* **2016**, 210, 445–455. <https://doi.org/10.1016/j.electacta.2016.05.091>.
- (229) Li, W. An Unpredictable Hazard in Lithium-Ion Batteries from Transition Metal Ions: Dissolution from Cathodes, Deposition on Anodes and Elimination Strategies. *J. Electrochem. Soc.* **2020**, 167 (9), 090514. <https://doi.org/10.1149/1945-7111/ab847f>.
- (230) Wang, J.; Yang, J.; Tang, Y.; Li, R.; Liang, G.; Sham, T. K.; Sun, X. Surface Aging at Olivine LiFePO<sub>4</sub>: A Direct Visual Observation of Iron Dissolution and the Protection Role of Nano-Carbon Coating. *J. Mater. Chem. A* **2013**, 1 (5), 1579–1586. <https://doi.org/10.1039/c2ta00521b>.
- (231) Koltypin, M.; Aurbach, D.; Nazar, L.; Ellis, B. On the Stability of LiFePO<sub>4</sub> Olivine Cathodes under Various Conditions (Electrolyte Solutions, Temperatures). *Electrochem. Solid-State Lett.* **2007**, 10 (2), 40–44. <https://doi.org/10.1149/1.2403974>.
- (232) Dupré, N.; Martin, J. F.; Degryse, J.; Fernandez, V.; Soudan, P.; Guyomard, D. Aging of the LiFePO<sub>4</sub> Positive Electrode Interface in Electrolyte. *J. Power Sources* **2010**, 195 (21), 7415–7425. <https://doi.org/10.1016/j.jpowsour.2010.05.042>.

- (233) Hellqvist Kjell, M.; Malmgren, S.; Ciosek, K.; Behm, M.; Edström, K.; Lindbergh, G. Comparing Aging of Graphite/LiFePO<sub>4</sub> Cells at 22 C and 55 C - Electrochemical and Photoelectron Spectroscopy Studies. *J. Power Sources* **2013**, *243*, 290–298. <https://doi.org/10.1016/j.jpowsour.2013.06.011>.
- (234) Wu, H.; Su, C.; Shieh, D.; Yang, M. Enhanced High-Temperature Cycle Life of LiFePO<sub>4</sub>-Based Li-Ion Batteries by Vinylene Carbonate as Electrolyte Additive. *Electrochem. Solid-State Lett.* **2006**, 537–541. <https://doi.org/10.1149/1.2351954>.
- (235) Xu, M.; Zhou, L.; Hao, L.; Xing, L.; Li, W.; Lucht, B. L. Investigation and Application of Lithium Difluoro(Oxalate)Borate (LiDFOB) as Additive to Improve the Thermal Stability of Electrolyte for Lithium-Ion Batteries. *J. Power Sources* **2011**, *196* (16), 6794–6801. <https://doi.org/10.1016/j.jpowsour.2010.10.050>.
- (236) Wu, B.; Ren, Y.; Mu, D. Enhanced Electrochemical Performance of LiFePO<sub>4</sub> Cathode with the Addition of Fluoroethylene Carbonate in Electrolyte. *J. Solid State Electrochem.* **2013**, 811–816. <https://doi.org/10.1007/s10008-012-1927-9>.
- (237) Chang, C. C.; Lee, K. Y.; Lee, H. Y.; Su, Y. H.; Her, L. J. Trimethyl Borate and Triphenyl Borate as Electrolyte Additives for LiFePO<sub>4</sub> Cathode with Enhanced High Temperature Performance. *J. Power Sources* **2012**, *217*, 524–529. <https://doi.org/10.1016/j.jpowsour.2012.05.083>.
- (238) Chang, C.; Chen, T. Tris ( Pentafluorophenyl ) Borane as an Electrolyte Additive for LiFePO<sub>4</sub> Battery. *J. Power Sources* **2009**, *193*, 834–840. <https://doi.org/10.1016/j.jpowsour.2009.04.033>.
- (239) Harlow, J. E.; Ma, X.; Li, J.; Logan, E.; Liu, Y.; Zhang, N.; Ma, L.; Glazier, S. L.; Cormier, M. M. E.; Genovese, M.; Buteau, S.; Cameron, A.; Stark, J. E.; Dahn, J. R. A Wide Range of Testing Results on an Excellent Lithium-Ion Cell Chemistry to Be Used as Benchmarks for New Battery Technologies. *J. Electrochem. Soc.* **2019**, *166* (13), 3031–3044. <https://doi.org/10.1149/2.0981913jes>.
- (240) Li, J.; Li, H.; Stone, W.; Glazier, S.; Dahn, J. R. Development of Electrolytes for Single Crystal NMC532 / Artificial Graphite Cells with Long Lifetime. *J. Electrochem. Soc.* **2018**, *165* (3), A626–A635. <https://doi.org/10.1149/2.0971803jes>.

- (241) Räsänen, S.; Lehtimäki, M.; Aho, T.; Vuorilehto, K.; Karppinen, M. In-Situ Investigation of the Water Absorption/Desorption Behavior of  $\text{LiFePO}_4$ . *Solid State Ion.* **2012**, *211*, 65–68. <https://doi.org/10.1016/j.ssi.2012.01.008>.
- (242) Huttner, F.; Haselrieder, W.; Kwade, A. The Influence of Different Post-Drying Procedures on Remaining Water Content and Physical and Electrochemical Properties of Lithium-Ion Batteries. *Energy Technol.* **2020**, *8*, 1900245. <https://doi.org/10.1002/ente.201900245>.
- (243) Marks, T.; Trussler, S.; Smith, A. J.; Xiong, D.; Dahn, J. R. A Guide to Li-Ion Coin-Cell Electrode Making for Academic Researchers. *J. Electrochem. Soc.* **2011**, *158* (1), A51. <https://doi.org/10.1149/1.3515072>.
- (244) Smith, A. J.; Burns, J. C.; Xiong, D.; Dahn, J. R. Interpreting High Precision Coulometry Results on Li-Ion Cells. *J. Electrochem. Soc.* **2011**, *158* (10), A1136. <https://doi.org/10.1149/1.3625232>.
- (245) Petibon, R.; Rotermund, L.; Nelson, K. J.; Gozdz, A. S.; Xia, J.; Dahn, J. R. Study of Electrolyte Components in Li Ion Cells Using Liquid-Liquid Extraction and Gas Chromatography Coupled with Mass Spectrometry. *J. Electrochem. Soc.* **2014**, *161* (6), A1167–A1172. <https://doi.org/10.1149/2.117406jes>.
- (246) Sinha, N. N.; Smith, A. J.; Burns, J. C.; Jain, G.; Eberman, K. W.; Scott, E.; Gardner, J. P.; Dahn, J. R. The Use of Elevated Temperature Storage Experiments to Learn about Parasitic Reactions in Wound  $\text{LiCoO}_2$ /Graphite Cells. *J. Electrochem. Soc.* **2011**, *158* (11), A1194. <https://doi.org/10.1149/2.007111jes>.
- (247) Thompson, L. M.; Stone, W.; Eldesoky, A.; Smith, N. K.; McFarlane, C. R. M.; Kim, J. S.; Johnson, M. B.; Petibon, R.; Dahn, J. R. Quantifying Changes to the Electrolyte and Negative Electrode in Aged NMC532/Graphite Lithium-Ion Cells. *J. Electrochem. Soc.* **2018**, *165* (11), A2732–A2740. <https://doi.org/10.1149/2.072181jes>.
- (248) Eldesoky, A.; Logan, E. R.; Johnson, M.; McFarlane, C. R. M.; Dahn, J. R. Scanning Micro X-Ray Fluorescence (MXRF) as an Effective Tool in Quantifying Fe Dissolution in  $\text{LiFePO}_4$  Cells: Towards a Mechanistic Understanding of Fe Dissolution. *Prep.* **2020**.

- (249) Dahn, J. R. Phase Diagram of  $\text{Li}_x\text{C}_6$ . *Phys. Rev. B* **1991**, *44* (17), 9170–9177. <https://doi.org/10.1103/PhysRevB.44.9170>.
- (250) Winter, M.; Besenhard, J. O.; Spahr, M. E.; Novák, P. Insertion Electrode Materials for Rechargeable Lithium Batteries. *Adv. Mater.* **1998**, *10* (10), 725–763.
- (251) Kambe, N.; Dresselhaus, M. S.; Dresselhaus, G.; Basu, S.; McGhie, A. R.; Fischer, J. E. Intercalate Ordering in First Stage Graphite-Lithium. *Mater. Sci. Eng.* **1979**, *40* (1), 1–4. [https://doi.org/10.1016/0025-5416\(79\)90002-8](https://doi.org/10.1016/0025-5416(79)90002-8).
- (252) Li, Y.; El Gabaly, F.; Ferguson, T. R.; Smith, R. B.; Bartelt, N. C.; Sugar, J. D.; Fenton, K. R.; Cogswell, D. A.; Kilcoyne, A. L. D.; Tyliszczak, T.; Bazant, M. Z.; Chueh, W. C. Current-Induced Transition from Particle-by-Particle to Concurrent Intercalation in Phase-Separating Battery Electrodes. *Nat. Mater.* **2014**, *13* (12), 1149–1156. <https://doi.org/10.1038/nmat4084>.
- (253) Safran S A. Cooperative Effects and Staging in Graphite Intercalation Compounds. *Synth. Met.* **1980**, *2*, 1–15.
- (254) Ellis, L. D.; Allen, J. P.; Hill, I. G.; Dahn, J. R. High-Precision Coulometry Studies of the Impact of Temperature and Time on SEI Formation in Li-Ion Cells. *J. Electrochem. Soc.* **2018**, *165* (7), A1529–A1536. <https://doi.org/10.1149/2.1091807jes>.
- (255) Burns, J. C.; Sinha, N. N.; Jain, G.; Ye, H.; VanElzen, C. M.; Scott, E.; Xiao, A.; Lamanna, W. M.; Dahn, J. R. The Impact of Intentionally Added Water to the Electrolyte of Li-Ion Cells. *J. Electrochem. Soc.* **2013**, *160* (11), A2281–A2287. <https://doi.org/10.1149/2.101311jes>.
- (256) Bernhard, R.; Metzger, M.; Gasteiger, H. A. Gas Evolution at Graphite Anodes Depending on Electrolyte Water Content and SEI Quality Studied by On-Line Electrochemical Mass Spectrometry. *J. Electrochem. Soc.* **2015**, *162* (10), A1984–A1989. <https://doi.org/10.1149/2.0191510jes>.
- (257) Schwenke, K. U.; Solchenbach, S.; Demeaux, J.; Lucht, B. L.; Gasteiger, H. A. The Impact of  $\text{CO}_2$  Evolved from VC and FEC during Formation of Graphite Anodes in Lithium-Ion Batteries. *J. Electrochem. Soc.* **2019**, *166* (10), A2035–A2047. <https://doi.org/10.1149/2.0821910jes>.

- (258) Stich, M.; Göttliger, M.; Kurniawan, M.; Schmidt, U.; Bund, A. Hydrolysis of LiPF<sub>6</sub> in Carbonate-Based Electrolytes for Lithium-Ion Batteries and in Aqueous Media. *J. Phys. Chem. C* **2018**, *122* (16), 8836–8842. <https://doi.org/10.1021/acs.jpcc.8b02080>.
- (259) Ma, L.; Ellis, L.; Glazier, S. L.; Ma, X.; Dahn, J. R. Combinations of LiPO<sub>2</sub>F<sub>2</sub> and Other Electrolyte Additives in Li[Ni<sub>0.5</sub>Mn<sub>0.3</sub>Co<sub>0.2</sub>]O<sub>2</sub>/Graphite Pouch Cells. *J. Electrochem. Soc.* **2018**, *165* (9), A1718–A1724. <https://doi.org/10.1149/2.0661809jes>.
- (260) Ma, L.; Ellis, L.; Glazier, S. L.; Ma, X.; Liu, Q.; Li, J.; Dahn, J. R. LiPO<sub>2</sub>F<sub>2</sub> as an Electrolyte Additive in Li[Ni<sub>0.5</sub>Mn<sub>0.3</sub>Co<sub>0.2</sub>]O<sub>2</sub>/Graphite Pouch Cells. *J. Electrochem. Soc.* **2018**, *165* (5), A891–A899. <https://doi.org/10.1149/2.0381805jes>.
- (261) Strmcnik, D.; Castelli, I. E.; Connell, J. G.; Haering, D.; Zorko, M.; Martins, P.; Lopes, P. P.; Genorio, B.; Østergaard, T.; Gasteiger, H. A.; Maglia, F.; Antonopoulos, B. K.; Stamenkovic, V. R.; Rossmeisl, J.; Markovic, N. M. Electrocatalytic Transformation of HF Impurity to H<sub>2</sub> and LiF in Lithium-Ion Batteries. *Nat. Catal.* **2018**, *1* (4), 255–262. <https://doi.org/10.1038/s41929-018-0047-z>.
- (262) Verma, P.; Maire, P.; Novák, P. A Review of the Features and Analyses of the Solid Electrolyte Interphase in Li-Ion Batteries. *Electrochimica Acta* **2010**, *55* (22), 6332–6341. <https://doi.org/10.1016/j.electacta.2010.05.072>.
- (263) Edström, K.; Herstedt, M.; Abraham, D. P. A New Look at the Solid Electrolyte Interphase on Graphite Anodes in Li-Ion Batteries. *J. Power Sources* **2006**, *153* (2), 380–384. <https://doi.org/10.1016/j.jpowsour.2005.05.062>.
- (264) Kawamura, T.; Okada, S.; Yamaki, J. Decomposition Reaction of LiPF<sub>6</sub>-Based Electrolytes for Lithium Ion Cells. *J. Power Sources* **2006**, *156* (2), 547–554. <https://doi.org/10.1016/j.jpowsour.2005.05.084>.
- (265) Terborg, L.; Weber, S.; Blaske, F.; Passerini, S.; Winter, M.; Karst, U.; Nowak, S. Investigation of Thermal Aging and Hydrolysis Mechanisms in Commercial Lithium Ion Battery Electrolyte. *J. Power Sources* **2013**, *242*, 832–837. <https://doi.org/10.1016/j.jpowsour.2013.05.125>.

- (266) Andersson, A. M.; Edström, K. Chemical Composition and Morphology of the Elevated Temperature SEI on Graphite. *J. Electrochem. Soc.* **2001**, *148* (10), A1100. <https://doi.org/10.1149/1.1397771>.
- (267) Downie, L. E.; Nelson, K. J.; Petibon, R.; Chevrier, V. L.; Dahn, J. R. The Impact of Electrolyte Additives Determined Using Isothermal Microcalorimetry. *ECS Electrochem. Lett.* **2013**, *2* (10), A106–A109. <https://doi.org/10.1149/2.010310eel>.
- (268) Krause, L. J.; Jensen, L. D.; Chevrier, V. L. Measurement of Li-Ion Battery Electrolyte Stability by Electrochemical Calorimetry. *J. Electrochem. Soc.* **2017**, *164* (4), A889–A896. <https://doi.org/10.1149/2.1651704jes>.
- (269) Boulanger, T.; Buechele, S.; Eldesoky, A.; Taskovic, T.; Azam, S.; Aiken, C.; Logan, E.; Metzger, M. Investigation of Redox Shuttle Generation in LFP/Graphite and NMC811/Graphite Cells. *J. Electrochem. Soc.* **2022**, *169*, 040518.
- (270) Heiskanen, S. K.; Kim, J.; Lucht, B. L. Generation and Evolution of the Solid Electrolyte Interphase of Lithium-Ion Batteries. *Joule* **2019**, *3* (10), 2322–2333. <https://doi.org/10.1016/j.joule.2019.08.018>.
- (271) Joshi, T.; Eom, K.; Yushin, G.; Fuller, T. F. Effects of Dissolved Transition Metals on the Electrochemical Performance and SEI Growth in Lithium-Ion Batteries. *J. Electrochem. Soc.* **2014**, *161* (12), A1915–A1921. <https://doi.org/10.1149/2.0861412jes>.
- (272) Logan, E.; Hebecker, H.; Eldesoky, A.; Luscombe, A.; Johnson, M.; Dahn, J. R. Performance and Degradation of LiFePO<sub>4</sub>/Graphite Cells: The Impact of Water Contamination and an Evaluation of Common Electrolyte Additives. *J. Electrochem. Soc.* **2020**. <https://doi.org/10.1149/1945-7111/abbbbe>.
- (273) Eldesoky, A.; Logan, E.; Johnson, M.; McFarlane, C.; Dahn, J. R. Scanning Micro X-Ray Fluorescence (MXRF) as an Effective Tool in Quantifying Fe Dissolution in LiFePO<sub>4</sub> Cells: Towards a Mechanistic Understanding of Fe Dissolution. *J. Electrochem. Soc.* **2020**. <https://doi.org/10.1149/1945-7111/abba62>.
- (274) Kassem, M.; Delacourt, C. Postmortem Analysis of Calendar-Aged Graphite/LiFePO<sub>4</sub> Cells. *J. Power Sources* **2013**, *235*, 159–171. <https://doi.org/10.1016/j.jpowsour.2013.01.147>.



- (275) Kim, J. H.; Woo, S. C.; Park, M. S.; Kim, K. J.; Yim, T.; Kim, J. S.; Kim, Y. J. Capacity Fading Mechanism of LiFePO<sub>4</sub>-Based Lithium Secondary Batteries for Stationary Energy Storage. *J. Power Sources* **2013**, *229*, 190–197. <https://doi.org/10.1016/j.jpowsour.2012.12.024>.
- (276) Li, W. An Unpredictable Hazard in Lithium-Ion Batteries from Transition Metal Ions: Dissolution from Cathodes, Deposition on Anodes and Elimination Strategies. *J. Electrochem. Soc.* **2020**, *167* (9), 090514–090514. <https://doi.org/10.1149/1945-7111/ab847f>.
- (277) Wang, J.; Yang, J.; Tang, Y.; Li, R.; Liang, G.; Sham, T. K.; Sun, X. Surface Aging at Olivine LiFePO<sub>4</sub>: A Direct Visual Observation of Iron Dissolution and the Protection Role of Nano-Carbon Coating. *J. Mater. Chem. A* **2013**, *1* (5), 1579–1586. <https://doi.org/10.1039/c2ta00521b>.
- (278) Chen, X.; Xu, W.; Engelhard, M. H.; Zheng, J.; Zhang, Y.; Ding, F.; Qian, J.; Zhang, J. G. Mixed Salts of LiTFSI and LiBOB for Stable LiFePO<sub>4</sub>-Based Batteries at Elevated Temperatures. *J. Mater. Chem. A* **2014**, *2* (7), 2346–2352. <https://doi.org/10.1039/c3ta13043f>.
- (279) Li, F.; Gong, Y.; Jia, G.; Wang, Q.; Peng, Z.; Fan, W.; Bai, B. A Novel Dual-Salts of LiTFSI and LiODFB in LiFePO<sub>4</sub>-Based Batteries for Suppressing Aluminum Corrosion and Improving Cycling Stability. *J. Power Sources* **2015**, *295*, 47–54. <https://doi.org/10.1016/j.jpowsour.2015.06.117>.
- (280) Zhang, L. L.; Chai, L.; Zhang, L. L.; Shen, M.; Zhang, X.; Battaglia, V. S.; Stephenson, T.; Zheng, H. Synergistic Effect between Lithium Bis(Fluorosulfonyl)Imide (LiFSI) and Lithium Bis-Oxalato Borate (LiBOB) Salts in LiPF<sub>6</sub>-Based Electrolyte for High-Performance Li-Ion Batteries. *Electrochimica Acta* **2014**, *127*, 39–44. <https://doi.org/10.1016/j.electacta.2014.02.008>.
- (281) Zhang, Z. A.; Zhao, X. X.; Peng, B.; Lai, Y. Q.; Zhang, Z. Y.; Li, J. Mixed Salts for Lithium Iron Phosphate-Based Batteries Operated at Wide Temperature Range. *Trans. Nonferrous Met. Soc. China Engl. Ed.* **2015**, *25* (7), 2260–2265. [https://doi.org/10.1016/S1003-6326\(15\)63839-0](https://doi.org/10.1016/S1003-6326(15)63839-0).

- (282) Eshetu, G. G.; Grugeon, S.; Gachot, G.; Mathiron, D.; Armand, M.; Laruelle, S. LiFSI vs. LiPF<sub>6</sub> Electrolytes in Contact with Lithiated Graphite: Comparing Thermal Stabilities and Identification of Specific SEI-Reinforcing Additives. *Electrochimica Acta* **2013**, *102*, 133–141. <https://doi.org/10.1016/j.electacta.2013.03.171>.
- (283) Burns, J. C.; Kassam, A.; Sinha, N. N.; Downie, L. E.; Solnickova, L.; Way, B. M.; Dahn, J. R. Predicting and Extending the Lifetime of Li-Ion Batteries. *J. Electrochem. Soc.* **2013**, *160* (9), A1451–A1456. <https://doi.org/10.1149/2.060309jes>.
- (284) Burns, J. C.; Jain, G.; Smith, A. J.; Eberman, K. W.; Scott, E.; Gardner, J. P.; Dahn, J. R. Evaluation of Effects of Additives in Wound Li-Ion Cells Through High Precision Coulometry. *J. Electrochem. Soc.* **2011**, *158* (3), A255. <https://doi.org/10.1149/1.3531997>.
- (285) Dahn, J. R.; McKinnon, W. R.; Murray, J. J.; Haering, R. R.; McMillan, R. S.; Rivers-Bowerman, A. H. Entropy of the Intercalation Compound Li<sub>x</sub>Mo<sub>6</sub>Se<sub>8</sub> from Calorimetry of Electrochemical Cells. *Phys. Rev. B* **1985**, *32* (5), 3316–3318.
- (286) Glazier, S. L.; Downie, L. E.; Xia, J.; Louli, A. J.; Dahn, J. R. Effects of Fluorinated Carbonate Solvent Blends on High Voltage Parasitic Reactions in Lithium Ion Cells Using OCV Isothermal Microcalorimetry. *J. Electrochem. Soc.* **2016**, *163* (10), A2131–A2138. <https://doi.org/10.1149/2.0081610jes>.
- (287) Logan, E. R.; Dahn, J. R. Measuring Parasitic Heat Flow in LiFePO<sub>4</sub>/Graphite Cells Using Isothermal Microcalorimetry. *J. Electrochem. Soc.* **2021**, *168* (12), 120526. <https://doi.org/10.1149/1945-7111/ac405b>.
- (288) Parimalam, B. S.; Lucht, B. L. Reduction Reactions of Electrolyte Salts for Lithium Ion Batteries: LiPF<sub>6</sub>, LiBF<sub>4</sub>, LiDFOB, LiBOB, and LiTFSI. *J. Electrochem. Soc.* **2018**, *165* (2), A251–A255. <https://doi.org/10.1149/2.0901802jes>.
- (289) Kang, S. J.; Park, K.; Park, S. H.; Lee, H. Unraveling the Role of LiFSI Electrolyte in the Superior Performance of Graphite Anodes for Li-Ion Batteries. *Electrochimica Acta* **2018**, *259*, 949–954. <https://doi.org/10.1016/j.electacta.2017.11.018>.

- (290) Eldesoky, A.; Logan, E. R.; Louli, A. J.; Song, W.; Weber, R.; Hy, S.; Petibon, R.; Harlow, J. E.; Azam, S.; Zsoldos, E.; Dahn, J. R. Impact of Graphite Materials on the Lifetime of NMC811/Graphite Pouch Cells: Part II. Long-Term Cycling, Stack Pressure Growth, Isothermal Microcalorimetry, and Lifetime Projection. *J. Electrochem. Soc.* **2022**, *169* (1), 010501. <https://doi.org/10.1149/1945-7111/ac42f1>.
- (291) Huang, Q.; Glazier, S. L.; Louli, A. J.; McArthur, M.; Liu, C.; Schrooten, J.; Dahn, J. R. Effects of Graphite Heat-Treatment Temperature on Single-Crystal Li[Ni<sub>5</sub>Mn<sub>3</sub>Co<sub>2</sub>]O<sub>2</sub>/Graphite Pouch Cells. *J. Electrochem. Soc.* **2020**, *167* (8), 080543. <https://doi.org/10.1149/1945-7111/ab9381>.
- (292) Song, W.; Harlow, J.; Logan, E.; Hebecker, H.; Coon, M.; Molino, L.; Johnson, M.; Dahn, J.; Metzger, M. A Systematic Study of Electrolyte Additives in Single Crystal and Bimodal LiNi<sub>0.8</sub>Mn<sub>0.1</sub>Co<sub>0.1</sub>O<sub>2</sub>/Graphite Pouch Cells. *J. Electrochem. Soc.* **2021**, *168* (9), 090503. <https://doi.org/10.1149/1945-7111/ac1e55>.
- (293) Xiong, D. J.; Ellis, L. D.; Nelson, K. J.; Hynes, T.; Petibon, R.; Dahn, J. R. Rapid Impedance Growth and Gas Production at the Li-Ion Cell Positive Electrode in the Absence of a Negative Electrode. *J. Electrochem. Soc.* **2016**, *163* (14), A3069–A3077. <https://doi.org/10.1149/2.1031614jes>.
- (294) Sloop, S. E.; Pugh, J. K.; Wang, S.; Kerr, J. B.; Kinoshita, K. Chemical Reactivity of PF<sub>5</sub> and LiPF<sub>6</sub> in Ethylene Carbonate/Dimethyl Carbonate Solutions. *Electrochem. Solid-State Lett.* **2001**, *4* (4), A42–A44.
- (295) Solchenbach, S.; Metzger, M.; Egawa, M.; Beyer, H.; Gasteiger, H. A. Quantification of PF<sub>5</sub> and POF<sub>3</sub> from Side Reactions of LiPF<sub>6</sub> in Li-Ion Batteries. *J. Electrochem. Soc.* **2018**, *165* (13), A3022–A3028. <https://doi.org/10.1149/2.0481813jes>.
- (296) Dupré, N.; Cuisinier, M.; Martin, J. F.; Guyomard, D. Interphase Evolution at Two Promising Electrode Materials for Li-Ion Batteries: LiFePO<sub>4</sub> and LiNi<sub>1/2</sub>Mn<sub>1/2</sub>O<sub>2</sub>. *ChemPhysChem* **2014**, *15* (10), 1922–1938. <https://doi.org/10.1002/cphc.201400070>.

- (297) Deshpande, R. D.; Bernardi, D. M. Modeling Solid-Electrolyte Interphase (SEI) Fracture: Coupled Mechanical/Chemical Degradation of the Lithium Ion Battery. *J. Electrochem. Soc.* **2017**, *164* (2), A461–A474. <https://doi.org/10.1149/2.0841702jes>.
- (298) Wang, D. Y.; Xia, J.; Ma, L.; Nelson, K. J.; Harlow, J. E.; Xiong, D.; Downie, L. E.; Petibon, R.; Burns, J. C.; Xiao, A.; Lamanna, W. M.; Dahn, J. R. A Systematic Study of Electrolyte Additives in Li[Ni<sub>1/3</sub>Mn<sub>1/3</sub>Co<sub>1/3</sub>]O<sub>2</sub> (NMC)/Graphite Pouch Cells. *J. Electrochem. Soc.* **2014**, *161* (12), A1818–A1827. <https://doi.org/10.1149/2.0511412jes>.
- (299) Ma, L.; Glazier, S. L.; Petibon, R.; Xia, J.; Peters, J. M.; Liu, Q.; Allen, J.; Doig, R. N. C.; Dahn, J. R. A Guide to Ethylene Carbonate-Free Electrolyte Making for Li-Ion Cells. *J. Electrochem. Soc.* **2017**, *164* (1), A5008–A5018. <https://doi.org/10.1149/2.0191701jes>.
- (300) Thompson, L. M. EXTENDED LIFETIME AND INCREASED ENERGY DENSITY STUDIES FOR LI-ION CELLS, Dalhousie University, Halifax, NS, 2021.
- (301) Aiken, C. P.; Logan, E. R.; Hebecker, H.; Oxner, J. M.; Harlow, J. E.; Metzger, M.; Dahn, J. R. Li[Ni<sub>0.5</sub>Mn<sub>0.3</sub>Co<sub>0.2</sub>]O<sub>2</sub> as a Superior Alternative to LiFePO<sub>4</sub> for Long-Lived Low Voltage Li-Ion Cells. *J. Electrochem. Soc.* **2022**, *169*, 050512.
- (302) Taskovic, T.; Eldesoky, A.; Song, W.; Bauer, M.; Dahn, J. R. High Temperature Testing of NMC/Graphite Cells for Rapid Cell Performance Screening and Studies of Electrolyte Degradation. *J. Electrochem. Soc.* **2022**. <https://doi.org/10.1149/1945-7111/ac6453>.

## APPENDIX A ADDITIONAL FIGURES

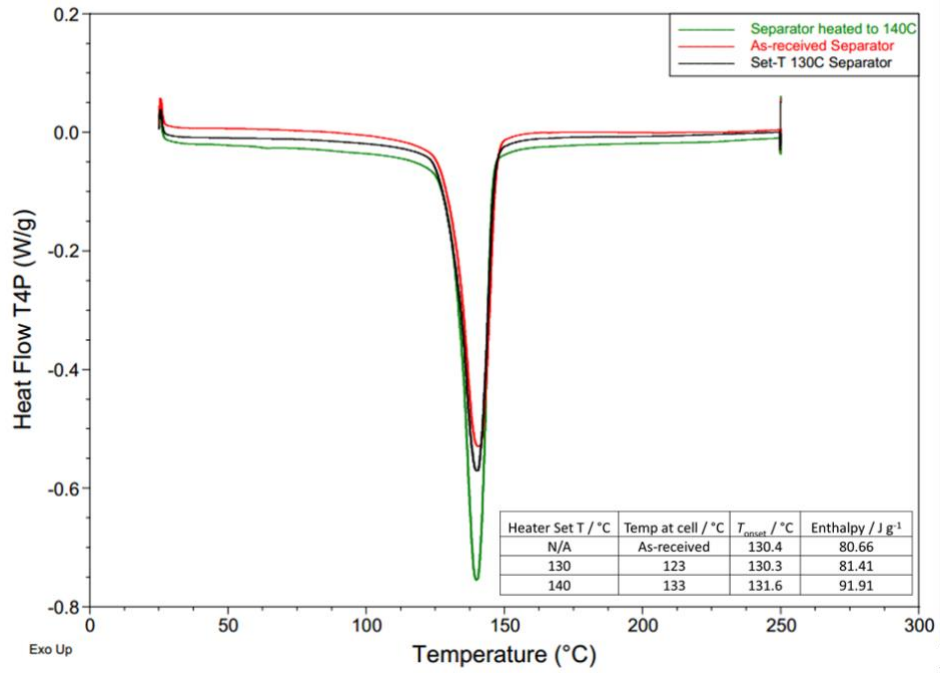


Figure A.1: DSC traces of separator samples taken from pouch cells as received, heated at 130°C and heated at 140°C. Table inset tabulates the onset of the polymer melt and the observed transition enthalpy for each drying condition.

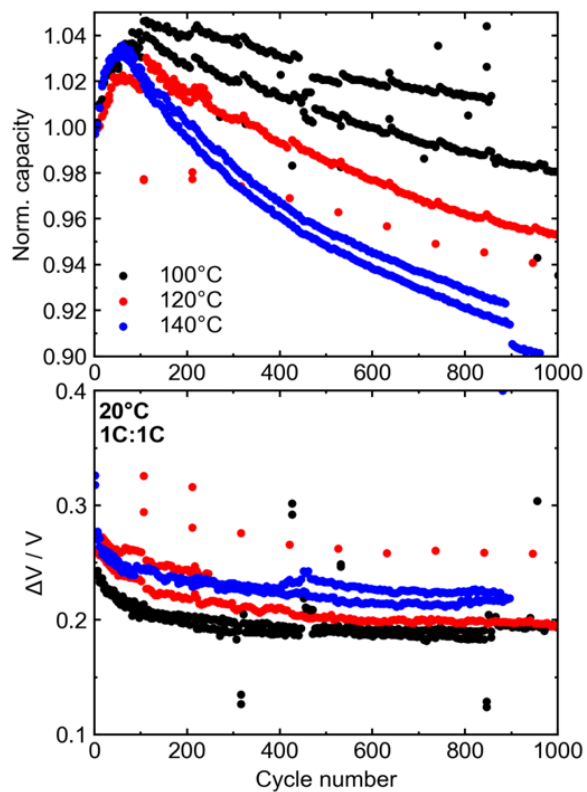


Figure A.2: Capacity retention of LFP/AG cells vacuum dried at different temperatures. All cells have CTRL + 2% VC electrolyte, and are cycled at 20°C at a rate of 1C:1C. (a) Normalized capacity versus cycle number. (b) Absolute voltage hysteresis versus cycle number.

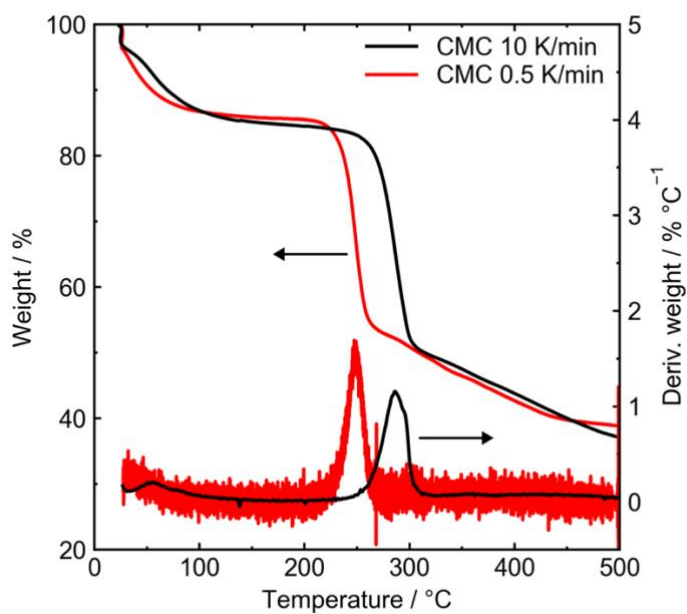


Figure A.3: TGA thermograms of carboxymethylcellulose (CMC) carried out in Ar atmosphere. At low temperatures (<150°C), only loss of surface water was observed. The thermal decomposition onset of CMC was determined to be ca. 250°C from the slow heating rate. The derivative of the weight of each sample with respect to temperature is also shown.

Table A.1: [Fe] detected on the anode, capacity loss, cycle number, and cycle time for the cells disassembled for  $\mu$ XRF measurements referenced in Figure 6 in the main text.

LFP type	Temperature / °C	Electrolyte Additive	# Cycles	Cycle time / hr	[Fe] / $\mu\text{g.cm}^{-2}$	Capacity loss / %
Low BET	20	-	251	1412	$7.0 \pm 0.1$	7.1
Med BET	20	-	259	1412	$9.3 \pm 0.2$	7.2
High BET	20	-	257	1412	$2.97 \pm 0.05$	6.6
Low BET	20	2VC	242	1412	$0.445 \pm$ $0.008$	2.2
Med BET	20	2VC	248	1413	$0.334 \pm$ $0.006$	2.7
High BET	20	2VC	255	1412	$0.299 \pm$ $0.005$	4.0
Low BET	40	-	296	1412	$19.2 \pm 0.3$	32.3
Med BET	40	-	296	1411	$13.7 \pm 0.2$	29.8
High BET	40	-	300	1412	$9.1 \pm 0.2$	31.7
Low BET	40	2VC	250	1412	$0.496 \pm$ $0.009$	5.2
Med BET	40	2VC	255	1412	$0.397 \pm$ $0.007$	6.0
High BET	40	2VC	262	1412	$0.526 \pm$ $0.009$	4.9
Low BET	55	-	135	741	$17.7 \pm 0.3$	40.5
Med BET	55	-	127	719	$14.4 \pm 0.3$	35.7
High BET	55	-	135	740	$12.8 \pm 0.2$	36.8
Low BET	55	2VC	587	3678	$6.3 \pm 0.1$	21.1
Med BET	55	2VC	669	4103	$3.2 \pm 0.1$	18.2
High BET	55	2VC	684	4103	$2.25 \pm 0.04$	17.3



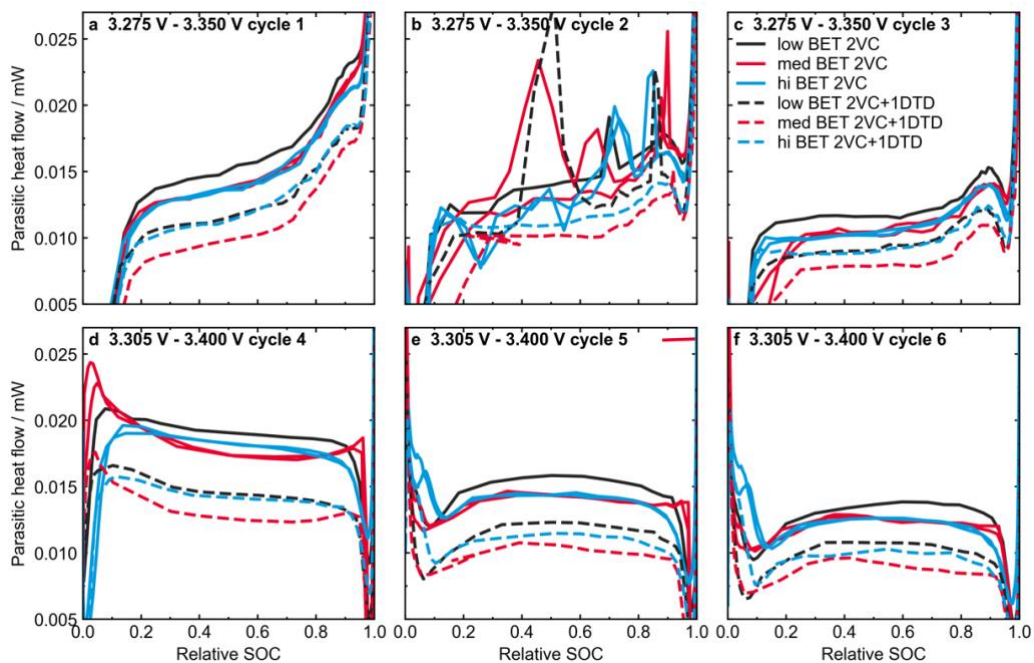


Figure A.4: Parasitic heat flow versus relative state-of-charge (SOC) over the different cycles in the isothermal microcalorimetry protocol. Note that an unplanned power outage during cycle 2 between 3.275 V and 3.350 V caused noisy data and spikes in the heat flow measurement. (a-c) Cycles between 3.275 V and 3.350 V. (d-f) Cycles between 3.305 V and 3.400 V.

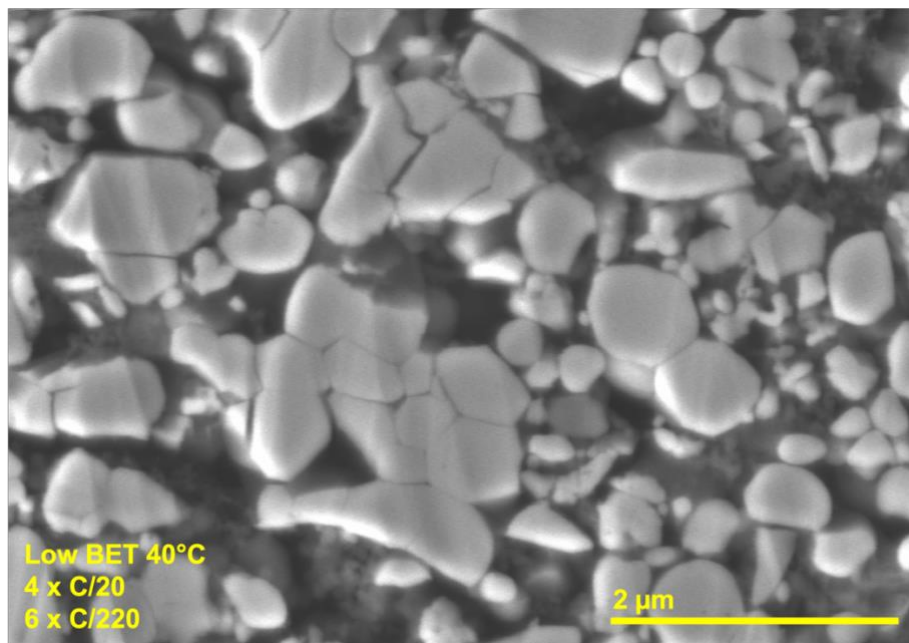


Figure A.5: Cross-sectional SEM image of an LFP electrode extracted from one of the low BET LFP/graphite cells that underwent cycling tests in the microcalorimeter. Cycling conditions are given on the image. The electrode sample was extracted at the top of charge.

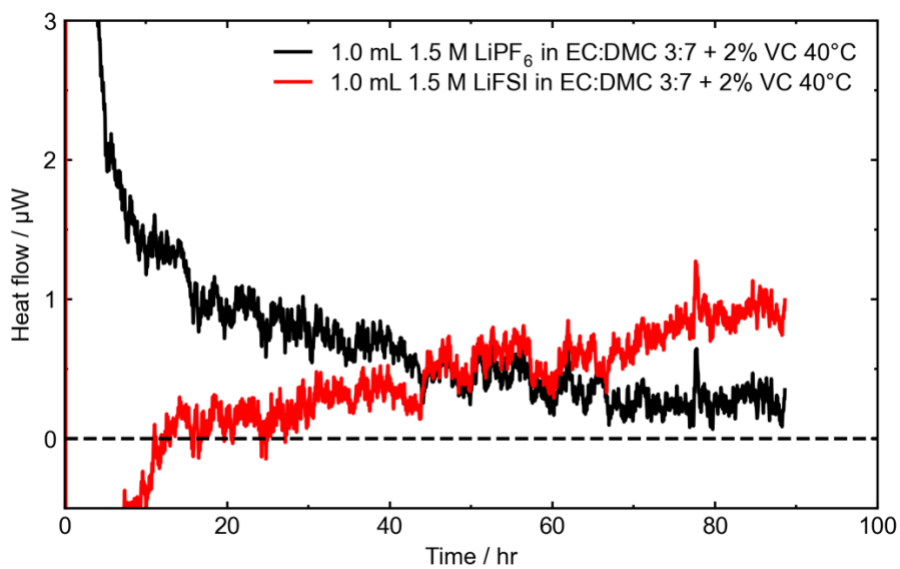


Figure A.6: Heat flow versus time measured in the microcalorimeter for pouch bags filled with 1.0 mL each of electrolyte as indicated. The experiment was done at 40.0000°C.

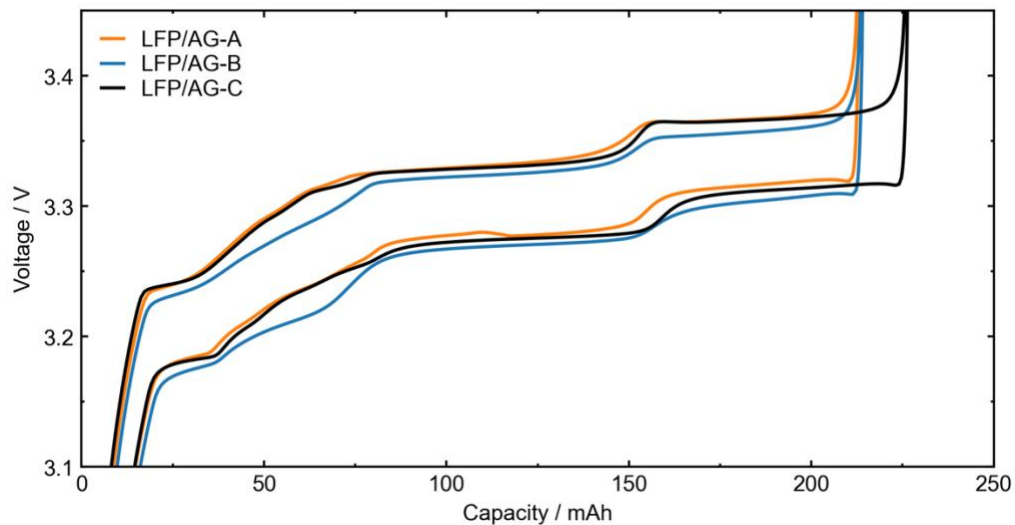


Figure A.7: Voltage versus capacity curves measured at 40°C, C/20 rate for LFP/graphite pouch cells with different artificial graphite negative electrodes.

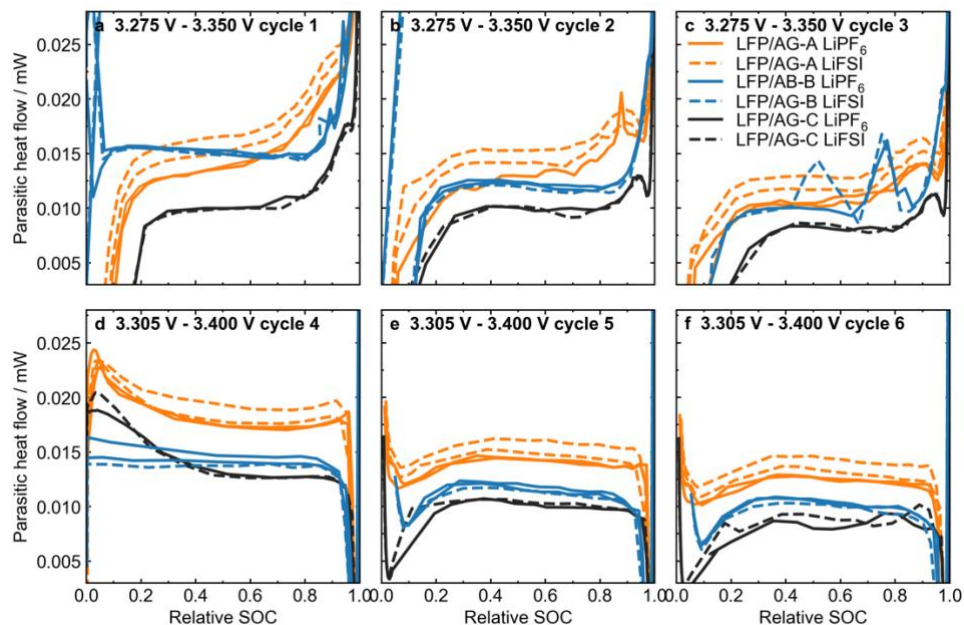


Figure A.8: Isothermal microcalorimetry results for LFP/AG cells with different graphites. (a-c) Parasitic heat flow versus relative SOC for cycles between 3.275 – 3.350 V. (d-f) Parasitic heat flow versus relative SOC for cycles between 3.305 – 3.400 V. Note that these voltage ranges were slightly different for LFP/AG-B cells (3.250 V – 3.335 V, and 3.290 V – 3.400 V).

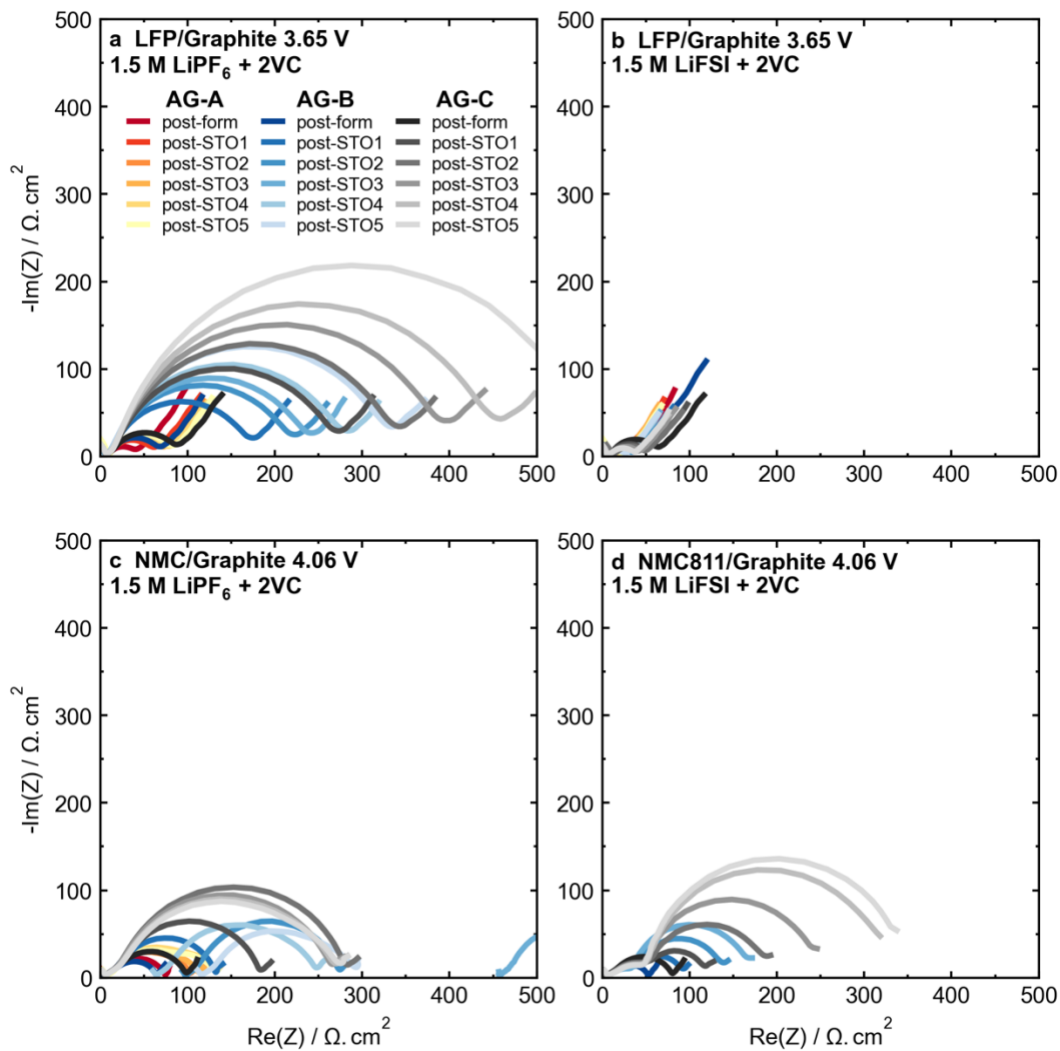


Figure A.9: Nyquist plots for different cells after each storage period. Measurements were completed at 10°C. (a) LFP/AG cells with LiPF<sub>6</sub> + 2VC electrolyte. (b) LFP/AG cells with LiFSI + 2VC electrolyte. (c) NMC811/AG cells with LiPF<sub>6</sub> + 2VC electrolyte. (d) NMC811/AG cells with LiFSI + 2VC electrolyte.

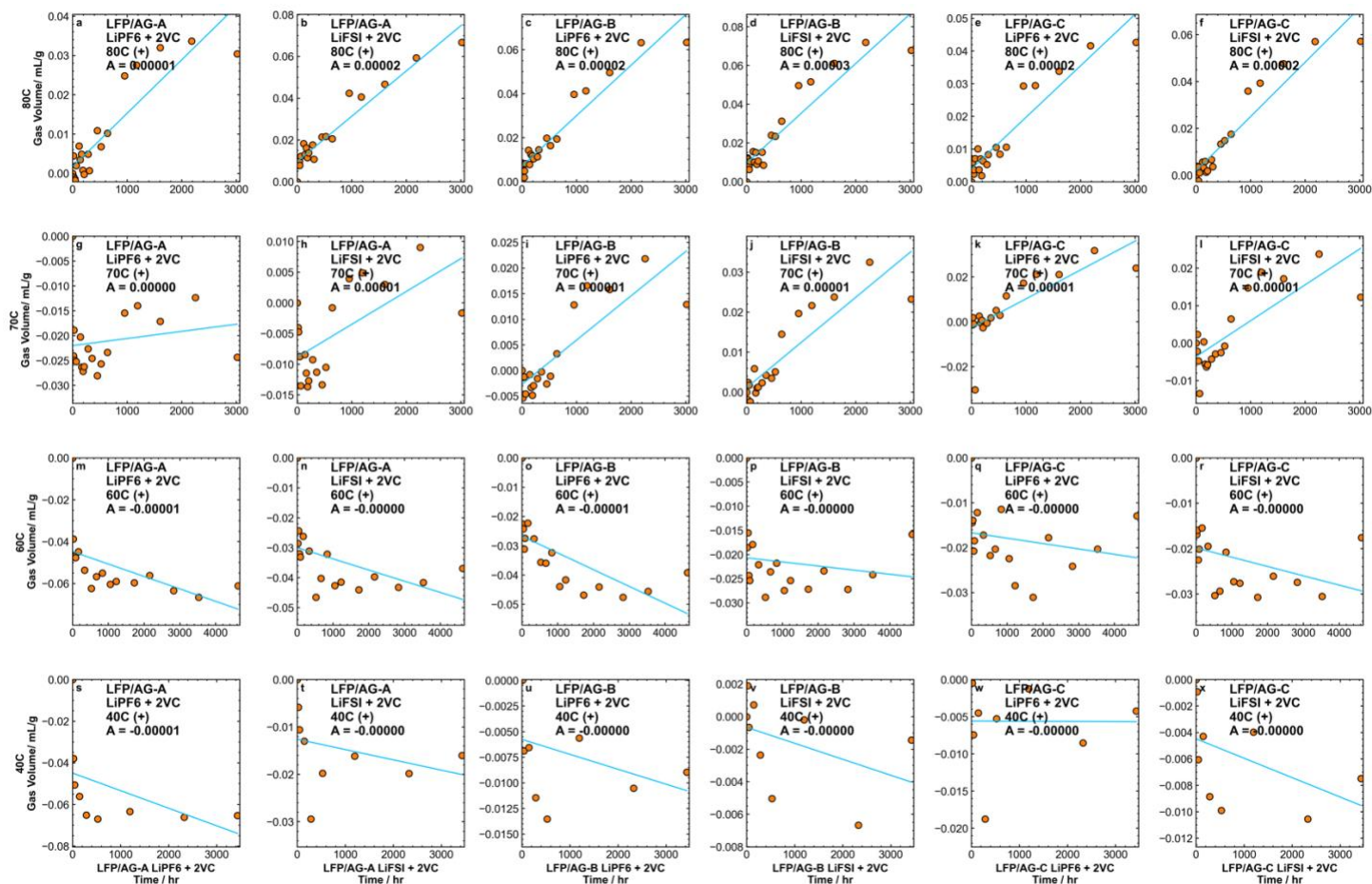


Figure A.10: Measured specific gas volume data for LFP positive electrode pouch bags aged at different temperatures. Linear fits to the initial gas production data are shown. Yellow points specify the data points that were used in the fit. Slopes from each fit are indicated in each individual panel.

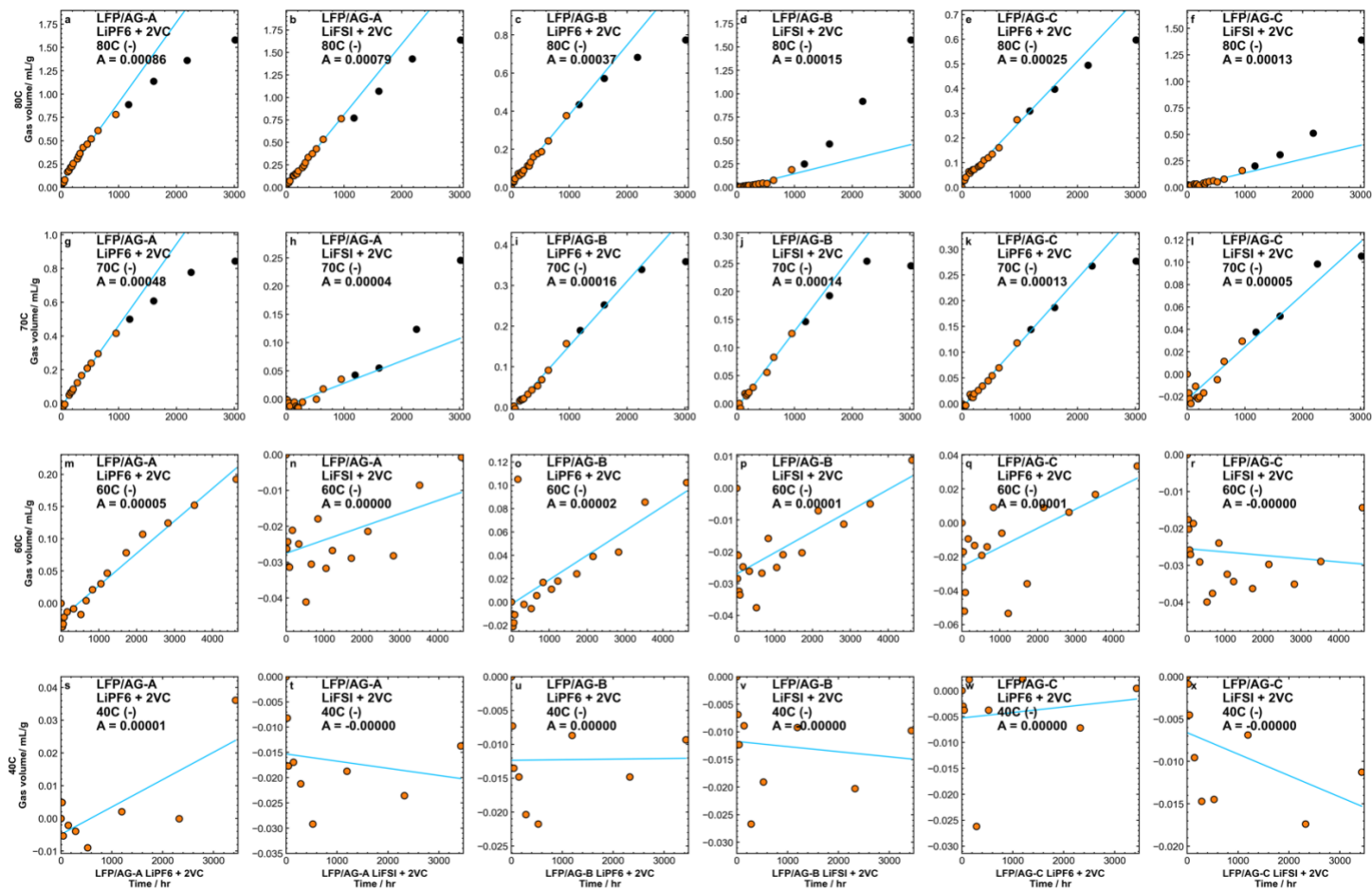


Figure A.11: Measured specific gas volume data for LFP negative electrode pouch bags aged at different temperatures. Linear fits to the initial gas production data are shown. Yellow points specify the data points that were used in the fit. Slopes from each fit are indicated in each individual panel.

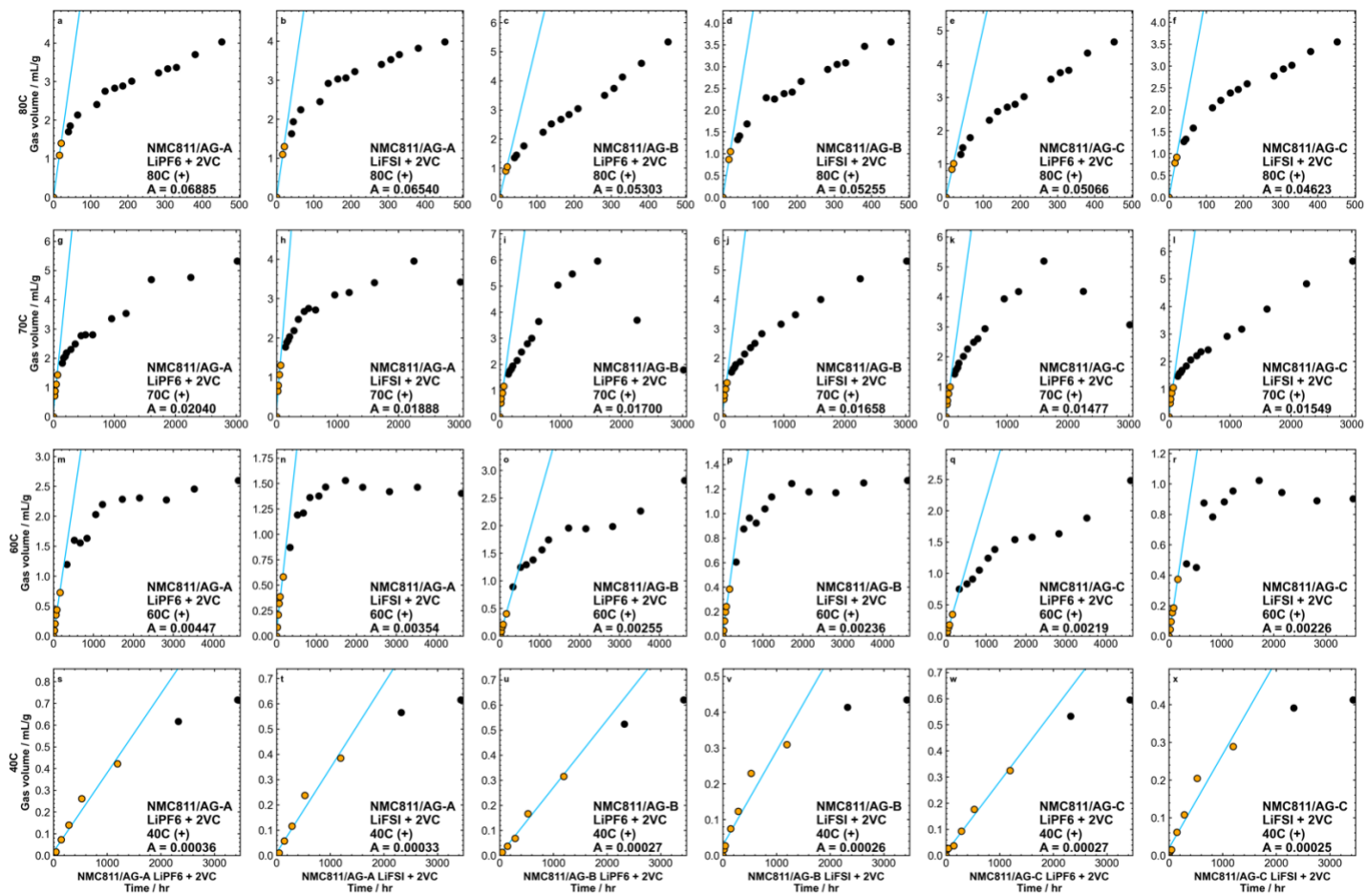


Figure A.12: Measured specific gas volume data for NMC811 positive electrode pouch bags aged at different temperatures. Linear fits to the initial gas production data are shown. Yellow points specify the data points that were used in the fit. Slopes from each fit are indicated in each individual panel.

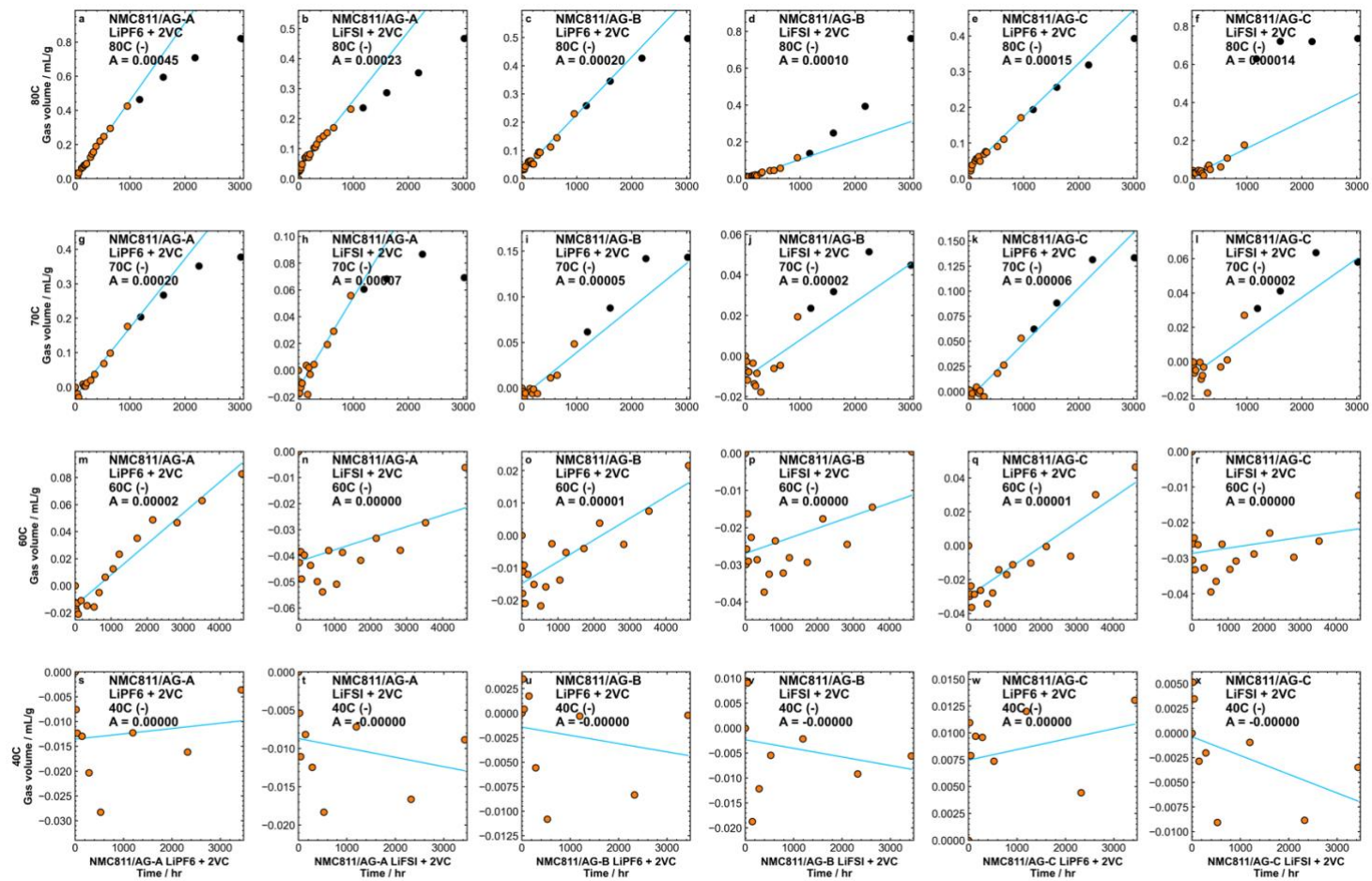


Figure A.13: Measured specific gas volume data for NMC811 negative electrode pouch bags aged at different temperatures. Linear fits to the initial gas production data are shown. Yellow points specify the data points that were used in the fit. Slopes from each fit are indicated in each individual panel.



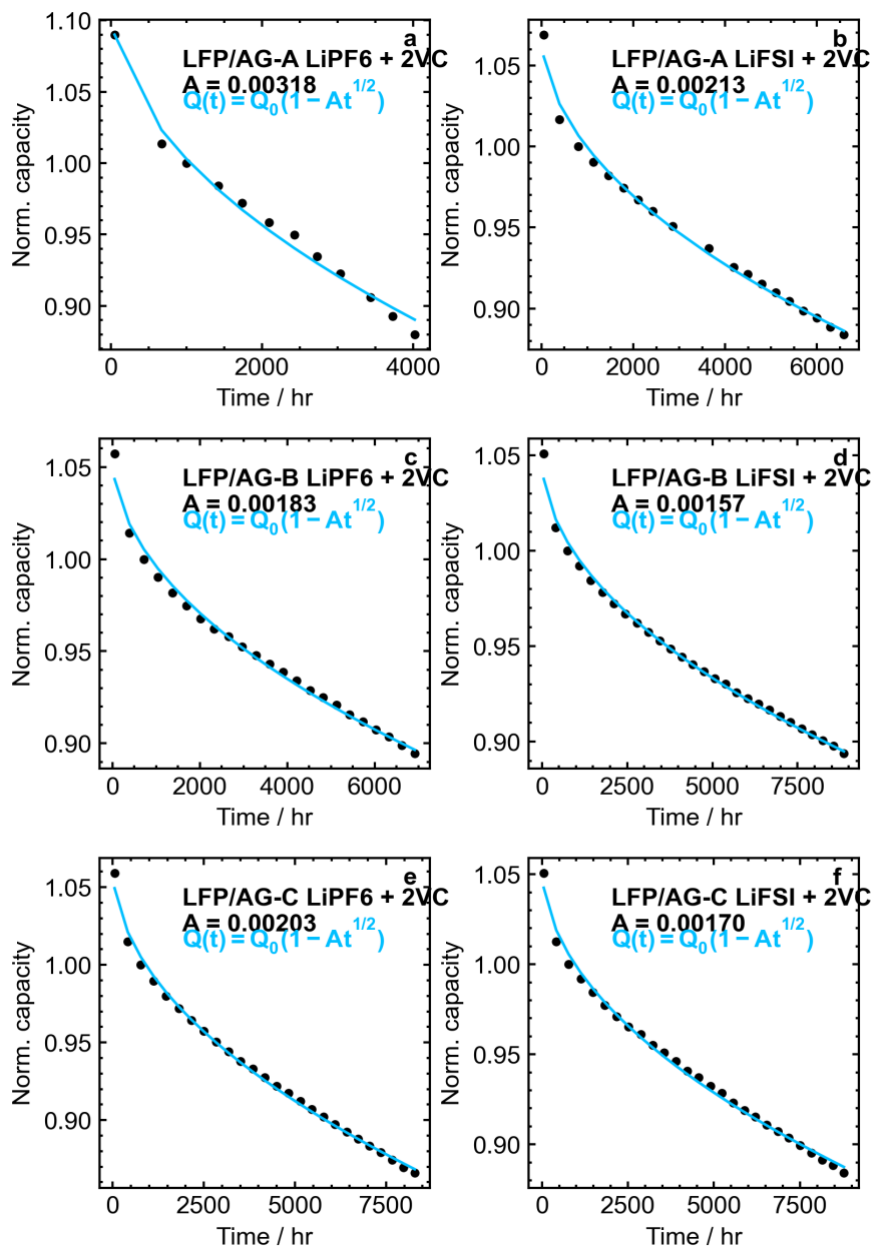


Figure A.14: Fits to normalized capacity versus cycle time for LFP/AG cells cycled at C/3 rate at 55°C. Fits were made to the C/20 check-up cycles only. Fitted values of the capacity fade parameter “A” is indicated in the legend of each panel.

## APPENDIX B COPYRIGHT PERMISSIONS



25-Aug-2022

This license agreement between the American Physical Society ("APS") and Eric Logan ("You") consists of your license details and the terms and conditions provided by the American Physical Society and SciPris.

### Licensed Content Information

**License Number:** RNP/22/AUG/057228  
**License date:** 25-Aug-2022  
**DOI:** 10.1103/PhysRevB.44.9170  
**Title:** Phase diagram of  $\text{Li}_{\mathit{x}}\text{C}_6$   
**Author:** J. R. Dahn  
**Publication:** Physical Review B  
**Publisher:** American Physical Society  
**Cost:** USD \$ 0.00

### Request Details

**Does your reuse require significant modifications:** No  
**Specify intended distribution locations:** Canada  
**Reuse Category:** Reuse in a thesis/dissertation  
**Requestor Type:** Student  
**Items for Reuse:** Figures/Tables  
**Number of Figure/Tables:** 1  
**Figure/Tables Details:** Figure 11  
**Format for Reuse:** Electronic

### Information about New Publication:

**University/Publisher:** Dalhousie University  
**Title of dissertation/thesis:** Understanding and mitigating degradation in Li ion batteries  
**Author(s):** Eric Logan  
**Expected completion date:** Aug. 2022

### License Requestor Information

**Name:** Eric Logan  
**Affiliation:** Individual  
**Email Id:** eric.logan@dal.ca  
**Country:** Canada

**TERMS AND CONDITIONS**

The American Physical Society (APS) is pleased to grant the Requestor of this license a non-exclusive, non-transferable permission, limited to Electronic format, provided all criteria outlined below are followed.

1. You must also obtain permission from at least one of the lead authors for each separate work, if you haven't done so already. The author's name and affiliation can be found on the first page of the published Article.
2. For electronic format permissions, Requestor agrees to provide a hyperlink from the reprinted APS material using the source material's DOI on the web page where the work appears. The hyperlink should use the standard DOI resolution URL, <http://dx.doi.org/{DOI}>. The hyperlink may be embedded in the copyright credit line.
3. For print format permissions, Requestor agrees to print the required copyright credit line on the first page where the material appears: "Reprinted (abstract/excerpt/figure) with permission from [(FULL REFERENCE CITATION) as follows: Author's Names, APS Journal Title, Volume Number, Page Number and Year of Publication.] Copyright (YEAR) by the American Physical Society."
4. Permission granted in this license is for a one-time use and does not include permission for any future editions, updates, databases, formats or other matters. Permission must be sought for any additional use.
5. Use of the material does not and must not imply any endorsement by APS.
6. APS does not imply, purport or intend to grant permission to reuse materials to which it does not hold copyright. It is the requestor's sole responsibility to ensure the licensed material is original to APS and does not contain the copyright of another entity, and that the copyright notice of the figure, photograph, cover or table does not indicate it was reprinted by APS with permission from another source.
7. The permission granted herein is personal to the Requestor for the use specified and is not transferable or assignable without express written permission of APS. This license may not be amended except in writing by APS.
8. You may not alter, edit or modify the material in any manner.
9. You may translate the materials only when translation rights have been granted.
10. APS is not responsible for any errors or omissions due to translation.
11. You may not use the material for promotional, sales, advertising or marketing purposes.
12. The foregoing license shall not take effect unless and until APS or its agent, Aptara, receives payment in full in accordance with Aptara Billing and Payment Terms and Conditions, which are incorporated herein by reference.
13. Should the terms of this license be violated at any time, APS or Aptara may revoke the license with no refund to you and seek relief to the fullest extent of the laws of the USA. Official written notice will be made using the contact information provided with the permission request. Failure to receive such notice will not nullify revocation of the permission.
14. APS reserves all rights not specifically granted herein.
15. This document, including the Aptara Billing and Payment Terms and Conditions, shall be the entire agreement between the parties relating to the subject matter hereof.